19

Magnetic Properties of Metals and Alloys.

19.1 Magnetic Field Quantities and Properties Survey.

19.1.1 Introduction.

This chapter introduces metals and alloys used for soft and hard magnets. Alloy development illustrates the materials paradigm of synthesis $\rightarrow$ structure $\rightarrow$ properties $\rightarrow$ performance relationships. Development is motivated by intrinsic materials properties, such as saturation induction and Curie temperature. Advancement of alloys for applications involves optimizing extrinsic properties, such as *remanent induction* and *coercivity* by processing to achieve suitable microstructures. Magnetic hysteresis is useful in permanent magnets where we wish to store a large metastable magnetization. For soft magnets, small hysteresis losses per cycle are desirable. Metals and alloys for soft and hard magnetic materials now are ubiquitous in many magnetic applications in bulk, powder, nanocrystal and thin film forms.

We begin this chapter by reviewing the magnetic properties which are relevant to soft and hard magnetic materials, respectively. We develop the subject by considering:

(i) A summary of technical magnetic properties of importance for soft and hard magnetic materials in the context of a few illustrative examples.
(ii) Definitions of important magnetic phenomena which are relevant to the determination of these properties.
(iii) A survey of alloys within a historical context as to their development.
(iv) An extrapolation to the future to highlight some emerging areas of magnetic metals and alloys relevant to evolving technological needs with an emphasis on materials important to energy applications.

The magnetization, M, or magnetic induction, B, is an extensive material property and the field, H, is an intensive variable. These form a set of *conjugate variables* which define the *magnetic work* in a thermodynamic analysis. It is a goal to describe the response function $B(H)$ for a material system. This response function can be

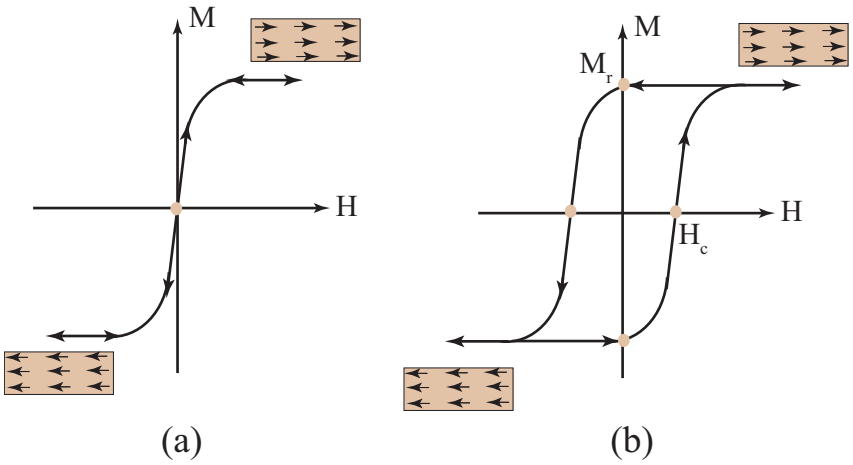

Fig. 19.1. (a) Magnetic response, B(H) for a reversible ferromagnetic system of dipoles and (b) hysteretic magnetic response, B(H), for an irreversible ferromagnetic system of dipoles.

single valued as shown in Fig. 19.1 (a) which would be the case for reversible equilibrium thermodynamics or two-valued (hysteretic) as shown in Fig. 19.1 (b) which is the case for irreversible non-equilibrium thermodynamics. The equilibrium response is generally non-linear and depends on the process by which atomic dipoles rotate into the direction of the field. The *permeability* is the slope of the B(H) curve. The easier it is to magnetize a material for a given applied field, the higher the permeability. The hysteresis curve is the starting point for discussing technical magnetic properties of soft and hard magnetic materials and distinguishing between hard and soft magnets.

Two thermodynamic states exist when all the dipoles are aligned in the direction of a positive field or negative field. The value of the magnetization, M, when all of the dipoles are aligned is called the *saturation magnetization,* M_s A *hysteresis loop* (Fig. 19.1 (b)) is a plot of the magnetization of a material as it is cycled from positive fields to negative and back. Important states on a hysteresis loop include the *remanent induction,* B_r [1] which is the remaining magnetic induction left when the driving field is reduced to zero. The *coercive field,* H_c is the reverse field necessary to drive the magnetization to zero after being saturated.

The value of the coercive field is used to distinguish between hard magnets and soft magnets. Hard or *permanent magnets* require very large fields to switch and are therefore useful for a variety of applications taking advantage of the remanent induction. Soft magnetic materials are characterized by a low coercivity and therefore a narrow loop. Since they are easy to reverse they ideal for high frequency operation.

[1] $B_r = M_r$ (cgs units); $= \mu_0 M_r$ (mksa units)

19.1.1.1 Soft Magnet Introduction.

Box 19.1 summarizes applications and technical properties of soft magnetic materials. **Michael Faraday** (1791- 1867) observed that an applied voltage to one copper coil resulted in a voltage across a second coil wound on the same iron core. Faraday's law of induction (1831):

$$V = N\frac{d\Phi}{dt} \tag{19.1}$$

defines the induced voltage in terms of the number of turns, N, in a primary exciting coil and the rate of change in the magnetic flux, Φ caused by an alternating current. This physical law is the basis for many inductive components including power transformers which are a prototypical application of soft magnetic materials. The 1884 demonstrations of an open (Gaulard and Gibbs) and closed (Deri, Blathy, and Zipperman) core *transformer* was followed by use of closed core transformers to supply power to Edison lamps which illuminated the 1885 Budapest exhibition. Transformers now (1) are key energy conversion devices in power distribution systems, (2) provide the basis for operation of many electromechanical devices, and (3) are components of modern integrated circuits.

Box 19.1 Applications and technical properties of soft magnetic materials.

Important applications of soft magnetic materials include:

(i) inductors and inductive components, low and high frequency transformers,
(ii) alternating current machines, motors and generators,
(iii) magnetic lenses for particle beams and magnetic amplifiers,
(iv) high frequency inductors and absorbers,
(v) magnetocaloric materials
(vi) magnetic sensors.

. The desired technical properties of interest for soft magnetic materials include:

(i) High Permeability: Permeability, $\mu = \frac{B}{H} = (1 + \chi)$, is the material's parameter describing the slope of the flux density, B, as a function of the applied field, H. High permeability materials can produce very large flux changes small fields.
(ii) Low Hysteresis Loss: Hysteresis loss is the energy consumed in cycling a material between $\pm H$. The energy consumed per cycle is the area in the hysteresis loop. The power loss of an AC device includes a term equal to the frequency multiplied by the hysteretic loss per cycle. At high frequencies eddy current losses are intimately related to the materials resistivity, ρ.
(iii) Large Saturation and Remnant Magnetizations: A large saturation induction, B_s, is desirable because it represents the ultimate response of soft magnetic materials.
(iv) High Curie Temperature: The ability to use soft magnetic materials at elevated temperatures depends on the Curie temperature of the material.

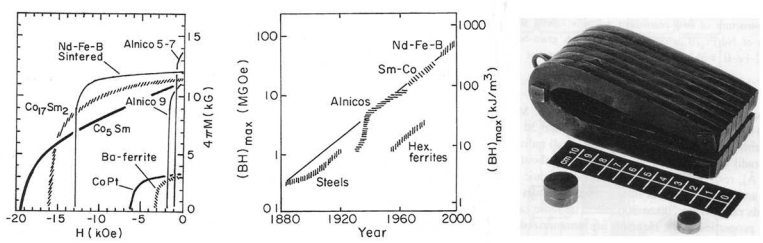

Fig. 19.2. (a) Schematic demagnetization curves for some permanent magnet materials, (b) the evolution of the energy product, $(BH)_{max}$ over time [O'H00].

19.1.1.2 Hard Magnet Introduction.

Permanent magnets provide large fields in a confined space. The strength of a magnet is characterized by the amount of energy it stores. Unlike a battery, this energy is always available as the permanent magnet does no net work. Initially, a field is applied to align domains to obtain a net magnetization. For a permanent magnet, a wide *magnetic hysteresis loop* reflects a large *coercive field* which stabilizes the moment with respect to field fluctuations. In most applications, a large magnetization is also desirable. Figures of merit include the coercive field, *remnant magnetization* and *energy product, (BH)*$_{max}$. A high T_c is desired for a greater operational temperature range. Applications of *permanent magnets* include small motors, loud speakers, electronic tubes, focussing magnets for charged particle beams and mechanical work devices.

The energy product , $(BH)_{max}$, is defined as the maximum value of the product of B and H taken in the second quadrant of a hysteresis curve. This has units of energy per unit volume of the material. For a material with a square hysteresis loop, $(BH)_{max}$ is the product of the remanence and coercivity.

Fig. 19.2 shows schematic demagnetization curves for important permanent magnet materials, and (b) the evolution of $(BH)_{max}$ over time. The first permanent magnets date back to 600 B.C when lodestone, Fe_3O_4, was used as the first compass needles. This was followed by iron. C steel was reported on in 1600 AD in the work *De Magnete* of W. Gilbert [Gil58].

Improvements in $(BH)_{max}$ accompanied development of alloy, oxide and fine particle ferromagnets. Recently, rare earth transition metal (RETM) materials represent a major development . Energy products were $\sim 5\frac{kJ}{m^3}$ for steels available circa 1900 and now approach $\sim 1000\frac{kJ}{m^3}$ in state of the art *rare earth permanent magnet* (REPM) systems. REPM materials have large magnetocrystalline anisotropies which are at the root of large coercivity. Mixtures of rare earth and transition metals species result in large remanent and saturation magnetizations.

19.1.2 Dipoles and Magnetization.

19.1.2.1 Definitions of Field Quantities.

We begin discussing magnetic properties of materials by defining macroscopic field quantities [2] Two fields, the *magnetic induction*, $\vec{B}$, and the *magnetic field*, $\vec{H}$ are vectors. In many cases the induction and the field will be collinear (parallel) and we can treat them as scalar quantities, B and H. [3]

In a vacuum, the magnetic induction, $\vec{B}$, is related to the magnetic field, $\vec{H}$:

$$\vec{B} = \mu_0 \vec{H} \qquad \Big| \qquad \vec{B} = \vec{H} \tag{19.2}$$

where the *permeability of the vacuum*, μ_0 is $4\pi \times 10^{-7} \frac{H}{m}$ in SI (mksa) units. This quantity is taken as 1 in cgs units . In cgs units, the induction and field are the same. In SI (mksa) units we assign a permeability to the vacuum, so the two are proportional.

In a magnetic material the magnetic induction can be enhanced or reduced by the material's *magnetization*, $\vec{M}$, (defined as net dipole moment per unit volume) so that:

$$\vec{B} = \mu_0(\vec{H} + \vec{M}) \qquad \Big| \qquad \vec{B} = \vec{H} + 4\pi\vec{M} \tag{19.3}$$

where the magnetization, $\vec{M}$, is expressed in linear response theory as:

$$\vec{M} = \chi_m \vec{H}. \tag{19.4}$$

The constant of proportionality is called the *magnetic susceptibility*, χ_m. The magnetic susceptibility which relates two axial vector quantities, is a second rank polar tensor. For most discussions (whenever B and H are collinear or when interested in the magnetization component in the field direction) we can view the susceptibility as a scalar.

Considering a scalar induction, field and magnetization, we express $B = \mu_r H$ as:

$$B = \mu_0(1 + \chi_m)H \qquad \Big| \qquad B = (1 + 4\pi\chi_m)H \tag{19.5}$$

and the *relative permeability*, μ_r is defined:

$$\mu_r = \mu_0(1 + \chi_m) \qquad \Big| \qquad \mu_r = (1 + 4\pi\chi_m) \tag{19.6}$$

μ_r thus represents an enhancement factor of the flux density in a magnetic material due to the magnetization which is an intrinsic materials property. If we have $\chi_m < 0$ we speak of *diamagnetic response* and for $\chi_m > 0$ (and no *collective magnetism*) we speak of *paramagnetic response*. A *superconductor* is a material which acts as a *perfect diamagnet* so that $\chi_m = -1$ or $\chi_m = \frac{-1}{4\pi}$.

[2] Selected formulas are introduced in SI (mksa) units followed by cgs units.

[3] For many discussions it will be sufficient to treat field quantities as scalars, when this is not the case, vector symbols will be explicitly used.

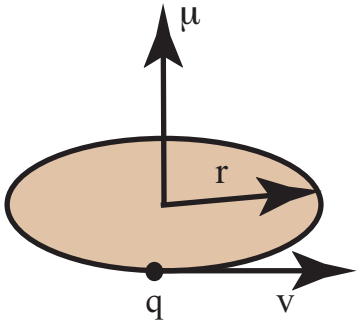

Fig. 19.3. Geometry of a charged particle orbiting at a distance r, with a linear velocity, v. The particle orbit sweeps out an area, A and gives rise to a dipole moment, $\vec{\mu}$.

19.1.2.2 Magnetic Dipole Moments - Definitions

A *magnetic dipole moment* originates from a circulating charge (Fig. 19.3). Concepts relating circulating charge, angular momentum and dipole moments are:

(i) A dipole moment for a circulating charge is defined formally as:

$$\vec{\mu} = IA\vec{u}_{\vec{r}\times\vec{J}} \qquad = \int_V \vec{r}\times\vec{J}dV \tag{19.7}$$

where $\vec{r}$ is the position vector of the charged particle about the origin for the rotation. $\vec{r}$ is the current density of the orbiting charge. I is the current due to the circulating charge, $A = \pi r^2$ is the area swept out by the circulating charge V is the volume. $\vec{u}_{\vec{r}\times\vec{J}}$ is a unit vector normal to the area, A.

(ii) The magnetic dipole moment is proportional to the axial *angular momentum* vector. Let $\vec{\Pi}$ to be a general angular momentum vector. The fundamental relationship between magnetic dipole moment and the angular momentum vector is:

$$\mu = g\frac{e}{2m}\Pi \qquad \Big| \qquad \mu = g\frac{e}{2mc}\Pi \tag{19.8}$$

g is called the *Lande g-factor*. For an orbiting electron the constant $g = 1$. The dipole moment associated with *spin angular momentum* has $g = 2$.

(iii) In quantum mechanics, every electron has a dipole moment associated with it's spinning charge density (spin) and its orbit about the nucleus (orbit). Angular momentum is quantized in units of **Planck's constant** divided by 2π ($\hbar = \frac{h}{2\pi} = 1.05\times10^{-34}J-s = 1.05\times10^{-27}erg-s$). A fundamental unit of

magnetic dipole moment, the *Bohr magneton* is defined:

$$\mu_B = \frac{e}{2m}\hbar \quad \Big| \quad \mu = \mu_B = \frac{e}{2mc}\hbar \tag{19.9}$$

The Bohr magneton has the value:

$$\mu_B = 9.27 \times 10^{-24} Am^2(\frac{J}{T}) \quad \Big| \quad \mu = \mu_B = 9.27 \times 10^{-21}\frac{erg}{G} \tag{19.10}$$

(iv) An atomic dipole moment, μ_{atom}, is calculated by summing all of the electron dipole moments for an atom in accordance with *Hund's rules*.

(v) For a collection of identical atoms the magnetization, M, is:

$$M = N_a \mu_{atom} \tag{19.11}$$

where N_a is the number of dipole moments per unit volume.

(vi) The potential energy of a dipole moment in the presence of a field is:

$$E_p = \vec{\mu} \cdot \vec{B} = \mu B \cos\theta \tag{19.12}$$

where θ is the angle between the dipole moment and $\vec{B}$. The magnetization (or other field quantity) multiplied by another field has units of energy per unit volume. In quantum mechanical systems, the component of the dipole moment vector projected along the field direction is quantized and only particular values of the angle θ are allowed.

19.1.2.3 Magnetization and Dipolar Interactions

We now turn to the definition of the magnetization, M.

Magnetization, M, is the net dipole moment per unit volume.

It is expressed as:

$$M = \frac{\Sigma_{atoms} \times \mu_{atom}}{V} \tag{19.13}$$

where V is the volume of the material [4]. Magnetization is an extrinsic materials property that depends on the constituent atoms in a system, the individual dipole moments, and how the dipole moments add vectorially. Collinear dipoles can add or subtract depending on whether they are parallel or antiparallel. This can give rise to many interesting types of collective magnetism.

A *paramagnet* is a material where permanent local atomic dipole moments are aligned randomly.

[4] Magnetization can also be reported as specific magnetization which is net dipole moment per unit weight

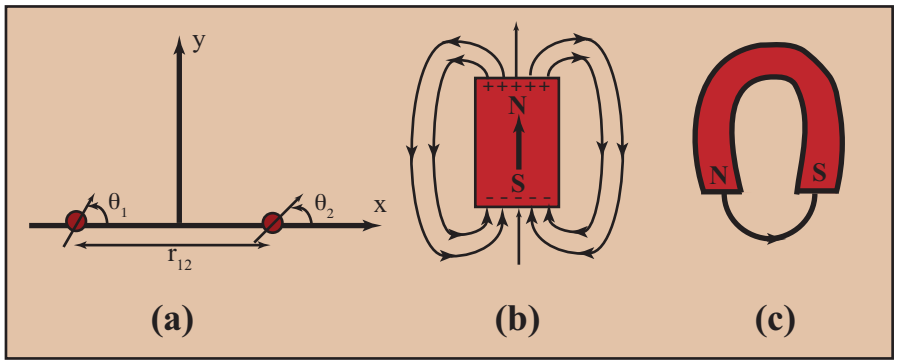

Fig. 19.4. (a) Geometry of two coplanar dipole moments used to define dipolar interactions, (b) net surface dipole moments at the poles of a permanent magnet with a single domain and (c) flux return path for magnetic dipoles in a horseshoe magnet.

In the absence of an applied field, H_a, the magnetization of a paramagnet is precisely zero since the sum of randomly oriented vectors is zero. This emphasizes the importance of the word "net" in the definition of magnetization. A permanent non-zero magnetization does not necessarily follow from having permanent dipole moments. It is only through a coupling mechanism which acts to align the dipoles in the absence of a field that a macroscopic magnetization is possible.

Two dipole moments interact through dipolar interactions that are described by an interaction force analogous to the Coulomb interaction between charges. If we consider two collinear dipoles pointing in a direction perpendicular to $r_{12}^{\rightarrow}$ the potential energy between the dipoles can be expressed:

$$E_p = \frac{\pm\mu_1\mu_2}{4\pi\mu_0 r_{12}^3} \qquad | \qquad E_p = \frac{\pm\mu_1\mu_2}{r_{12}^3} \tag{19.14}$$

which is the familiar Coulomb's law. [5]

Free poles collect at surfaces to form the North and South poles of a magnet (Fig. 19.4(b)). Magnetic flux lines travel from the N to the S pole of a permanent magnet causing a self-field, the *demagnetization field, H_d*, outside the magnet. H_d can act to demagnetize a material for which the magnetization is not strongly tied to an *easy magnetization direction, EMD*.

Most hard magnets have a large *magnetocrystalline anisotropy* which acts to fix the magnetization vector along particular crystal axes. As a result they are difficult to demagnetize. A soft magnet can be used as permanent magnet, if its shape is engineered to control the path of the demagnetization field to not interact with the magnetization

[5] Some authors (Cullity, e.g. use p to denote dipole moment.

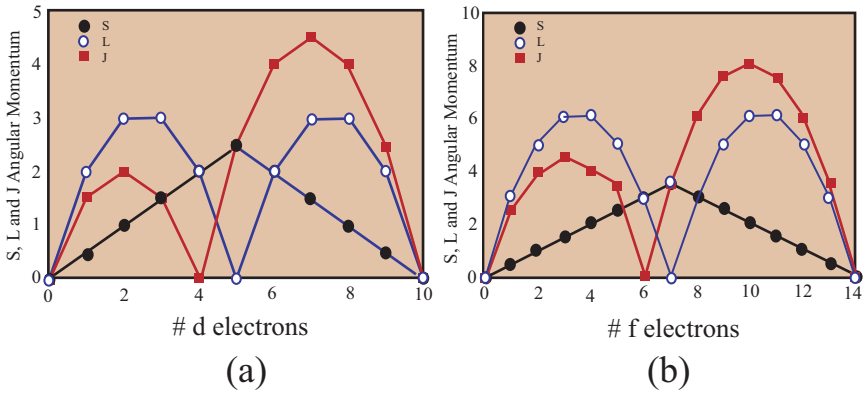

Fig. 19.5. J, L, and S quantum numbers for (a) TM^{2+}, and (b) RE^{3+}, ions.

vector. Fe is an example of a soft magnetic material with a large magnetization. To use Fe as a permanent magnet it is often shaped into a *horseshoe magnet* (Fig. 19.4(c)) where the return path for flux lines are spatially far from the material's magnetization.

19.1.2.4 Magnetic States.

In systems (ionic compounds and rare earths), with localized atomic orbitals responsible for the atomic magnetic dipole moments, discrete magnetic states can be calculated using quantum mechanical rules called *Hund's rules* [Hun27]. Systems with delocalized electrons states are treated within the band theory of solids.

For localized electrons assigned to a particular atom, discrete magnetic states are calculated using quantum mechanical rules. The general angular momentum vector, $\vec{\Pi}$, has contributions from *orbital angular momentum*, $\vec{L}$ and *spin angular momentum*, $\vec{S}$, both quantized in units of $\hbar$. Orbital and spin angular momentum are summed using *Hund's rules* [Hun27] shown in Fig. 19.5 and tabulated in Table 19.1.

The *ground state multiplet* including the m_l and m_s eigenstates allows us to calculate the components of the orbital, L, spin, S, and total angular momentum, J. The magnitudes of orbital and spin angular momenta sum angular momentum over a multielectron shell:

$$L = \sum_{i=1}^{n} (m_l)_i \hbar \qquad S = \sum_{i=1}^{n} 2(m_s)_i \hbar \tag{19.15}$$

The projection of the total angular momentum vector, $\vec{J} = \vec{L} + \vec{S}$ along an applied field direction is subject to quantization conditions that require that ($J = L + S$), J, is $J = |L - S|$ for less than half-filled shells and $J = |L + S|$ for greater than half-filled shells. To determine the occupation of eigenstates of S, L, and J we use Hund's rules:

d-shell electrons	Ion	S	L	J	Term	n_{eff} $g\Big[J(J+1)\Big]^{\frac{1}{2}}$	Obs.	n_{eff} $g\Big[S(S+1)\Big]^{\frac{1}{2}}$
1	Ti^{3+}, V^{4+}	$\frac{1}{2}$	2	$\frac{3}{2}$	$^2D_{\frac{3}{2}}$	1.55	1.70	1.73
2	V^{3+}	1	3	2	$^3F_2$	1.63	2.61	2.83
3	V^{2+},Cr^{3+}	$\frac{3}{2}$	3	$\frac{3}{2}$	$^4F_{\frac{3}{2}}$	0.77	3.85	3.87
4	Cr^{2+},Mn^{3+}	2	2	0	$^5D_0$	0	4.82	4.90
5	Mn^{2+},Fe^{3+}	$\frac{3}{2}$	0	$\frac{5}{2}$	$^5S_{\frac{5}{2}}$	5.92	5.82	5.92
6	Fe^{2+}	2	2	4	$^5D_4$	6.7	5.36	4.90
7	Co^{2+}	$\frac{3}{2}$	3	$\frac{9}{2}$	$^4F_{\frac{9}{2}}$	6.63	4.90	3.87
8	Ni^{2+}	1	3	4	$^3F_4$	5.59	3.12	2.83
9	Cu^{2+}	$\frac{1}{2}$	2	$\frac{5}{2}$	$^2D_{\frac{5}{2}}$	3.55	1.83	1.73
10	Cu^{+}, Zn^{2+}	0	0	0	$^1S_0$	0	0	0
f-shell electrons	Ion	S	L	J	Term	n_{eff} $g\Big[J(J+1)\Big]^{\frac{1}{2}}$	Obs.	n_{eff} $g\Big[S(S+1)\Big]^{\frac{1}{2}}$
1	Ce^{3+}	$\frac{1}{2}$	3	$\frac{5}{2}$	$^2F_{\frac{5}{2}}$	2.54	2.51	
2	Pr^{3+}	1	5	4	$^3H_4$	3.58	3.56	
3	Nd^{3+}	$\frac{3}{2}$	6	$\frac{9}{2}$	$^4I_{\frac{9}{2}}$	3.62	3.3	
4	Pm^{3+}	2	6	4	$^5I_4$	2.68	-	
5	Sm^{3+}	$\frac{5}{2}$	5	$\frac{5}{2}$	$^6H_{\frac{5}{2}}$	0.85 (1.6)*	1.74	
6	Eu^{3+}	3	3	0	$^7F_0$	0 (3.4)*	3.4	
7	Gd^{3+},Eu^{3+}	$\frac{5}{2}$	0	$\frac{5}{2}$	$^8S_{\frac{7}{2}}$	7.94	7.98	
8	Tb^{3+}	3	3	6	$^7F_6$	9.72	9.77	
9	Dy^{3+}	$\frac{5}{2}$	5	$\frac{15}{2}$	$^6H_{\frac{15}{2}}$	10.63	10.63	
10	Ho^{3+}	2	6	8	$^5I_8$	10.60	10.4	
11	Er^{3+}	$\frac{3}{2}$	6	$\frac{15}{2}$	$^4I_{\frac{15}{2}}$	9.59	9.5	
12	Tm^{3+}	1	5	6	$^3H_6$	7.57	7.61	
13	Yb^{3+}	$\frac{1}{2}$	3	$\frac{7}{2}$	$^2F_{\frac{7}{2}}$	4.53	4.5	
14	Lu^{3+}, Yb^{3+}	0	0	0	$^1S_0$	0	-	

Table 19.1. *Ground state multiplets of TM and RE ions from van Vleck (The Theory of Electric and Magnetic Susceptibilities, Oxford Univ. Press, 1932, 243).*

(i) We fill m_l states (which are $2l+1$ - fold degenerate) in such a way as to first maximize total spin.
(ii) We fill m_l states first in such a way as to first maximize total spin.

We consider the ions of transition metal series, TM^{2+}, i.e. ions which have given up 2s electrons to yield a $3d^n$ outer shell configuration in Fig. 19.5 (a). The ground state J, L and S quantum numbers for rare earth, RE^{3+}, ions are shown in Fig. 19.5 (b).

d-electrons	1	2	3	4	5
cations	Ti^{3+},V^{4+}	V^{3+}	V^{2+},Cr^{3+}	Cr^{2+},Mn^{3+}	Mn^{2+},Fe^{3+}
S	$\frac{1}{2}$	1	$\frac{3}{2}$	2	$\frac{5}{2}$
$\mu(\mu_B)$	1	2	3	4	5
d-electrons	6	7	8	9	10
cations	Fe^{2+}	Co^{2+}	Ni^{2+}	Cu^{2+}	Cu^{+},Zn^{2+}
S	2	$\frac{3}{2}$	1	$\frac{1}{2}$	0
$\mu(\mu_B)$	4	3	2	1	0

Table 19.2. *Transition Metal Ion Spin and Dipole Moments (L = 0)*

Defining L, S. and J specifies the ground state multiplet written compactly in the spectroscopic term symbol:

$$^{2S+1}L_J \tag{19.16}$$

where L is the symbol for orbital angular momentum ($L = 0 = S$, $L = 1 = P$, $L = 2 = D$, $L = 3 = F$, etc.) and $2S + 1$ and J are the numerical. Cr^{3+} with $L = 3$, $S = \frac{3}{2}$ and $J = \frac{3}{2}$ would be assigned the term symbol: $^4L_{\frac{3}{2}}$. We can relate the permanent local atomic moment vector with the total angular momentum vector, $\vec{J}$:

$$\vec{\mu} = \gamma\hbar\vec{J} = -g(J, L, S)\mu_B\vec{J} \tag{19.17a}$$

where γ is the *gyromagnetic factor* and $g = g(J, L, S)$ is the *Lande g-factor*:

$$g(J, L, S) = \frac{3}{2} + \frac{1}{2}\Big[\frac{S(S+1) - L(L+1)}{J(J+1)}\Big] \tag{19.17b}$$

Table 19.1 tabulates the ground state multiplets for transition metal and rare earth cation species that are prevalent in interesting ionic systems.

The Lande g factor accounts for precession of angular momentum and quantum mechanical rules for projection onto the field axis [RS25]. For identical ions with angular momentum J we define an effective magnetic moment in units of μ_B:

$$p_{eff} = g(J, L, S)[J(J+1)]^{\frac{1}{2}} \tag{19.18}$$

In many systems the orbital angular momentum is quenched. The *quenched orbital angular momentum* refers to the fact that the orbital angular moment vector is strongly tied to a crystalline *easy magnetization direction, EMD*. For this reason to a good approximation we can take $L = 0$ and $J = S$. In this case $g = 2$ and $p_{eff} = 2[S(S+1)]^{\frac{1}{2}}$. This is true for transition metals and their simple oxides.

Systems with delocalized electron states are treated within the *band theory* of solids. This is important for transition metals, rare earths, and their alloys. In such systems

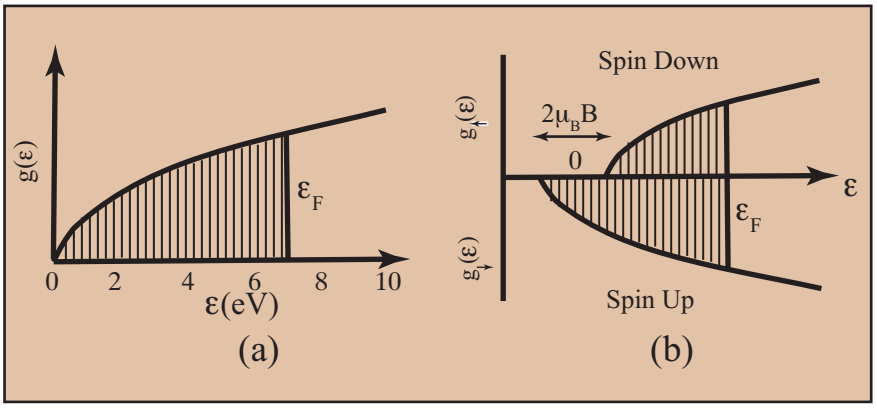

Fig. 19.6. (a) Free electron density of states and (b) free electron density of states where the spin degeneracy is broken by a Zeeman energy due to an applied or internal (exchange) field.

energy levels [6] form a continuum of states over a range of energies called an *energy band*. The *density of states* (per unit volume), $g(\epsilon)$, is defined so that $g(\epsilon)d\epsilon$ represents the number of electronic states (per unit volume) in the energy range from ϵ to $\epsilon + d\epsilon$:

$$g(\epsilon)d\epsilon = \frac{1}{V}\frac{dN_e}{d\epsilon}d\epsilon \tag{19.19}$$

Fig. 19.6 (a) shows the density of states for free electrons with a characteristic $\epsilon^{\frac{1}{2}}$ energy dependence. Many other forms for $g(\epsilon)$ are possible with different potentials.

Fig. 19.6 (b) shows the density of states for free electrons where the spin degeneracy is broken by a *Zeeman energy* due to an applied or internal (exchange) field. We divide the density of states, $g(\epsilon)d\epsilon$, by two, placing half the electrons in *spin-up states* and the other half in *spin-down states*. Spin-up electrons have potential energy lowered by $-\mu_B H$ where H is an applied, H_a, or internal exchange, H_{ex} field. Spin-down electrons have their potential energy increased by $\mu_B H$. We integrate each density of states separately to yield a different number of electrons per unit volume in spin-up and spin-down bands, respectively:

$$n_\uparrow = \frac{N_\uparrow}{V} = \int_0^{\epsilon_F} g_\uparrow(\epsilon)d\epsilon \qquad n_\downarrow = \frac{N_\downarrow}{V} = \int_0^{\epsilon_F} g_\downarrow(\epsilon)d\epsilon \tag{19.20}$$

The magnetization, net dipole moment per unit volume is then :

$$M = (n_\uparrow - n_\downarrow)\mu_B \tag{19.21}$$

The magnetization of elemental ferromagnets can be calculated using atomic dipole

[6] We use ϵ to denote the energy per electron.

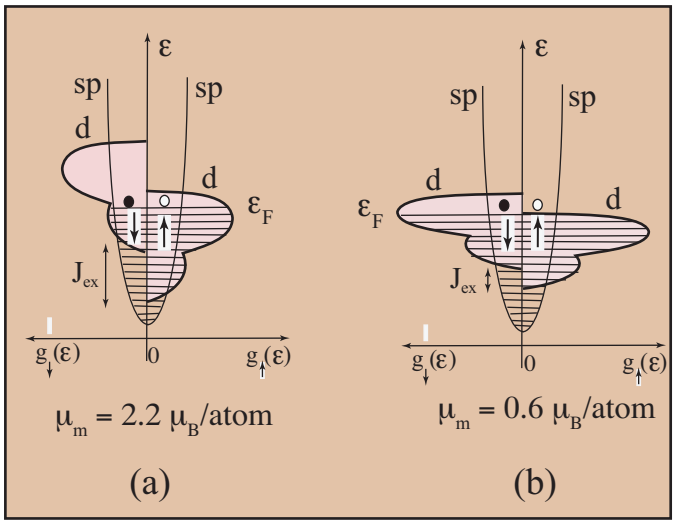

Fig. 19.7. Schematic densities of states for (a) Fe and (b) Ni (adapted from O'Handley [O'H00]) used for the illustration of how to calculate the atomic dipole moment for each.

moments from energy band theory and atomic density from crystallography. Band theory gives the number of spin-up and spin-down electrons per unit volume or per atom. Fig. 19.7 shows schematic densities of states for (a) Fe and (b) Ni (from O'Handley [O'H00]). In each case we have a separate spin-up and spin-down density of states for the s- and d- electrons, respectively. The s-electrons are most important for conduction and have little splitting in energy between their spin-up and spin-down density of states. Thus they do not contribute much to the net dipole moment. The d-electrons have very substantial splitting in energy between their spin-up and spin-down density of states. Thus they have the most contribution to the net dipole moment.

We can integrate the densities of states for (a) Fe and (b) Ni (Fig. 19.7), to determine the net dipole moment per atom and determine the magnetization for each. This is done in Box 19.2. Notice one other feature of the densities of states for Fe and Ni. Ni is an example of a *strong ferromagnet* in that the Fermi level only passes through one of the d-electron spin bands. Fe is an example of a *weak ferromagnet* in that the Fermi level passes through both d-electron spin bands.

In dilute alloy solutions (having a valency difference $\Delta Z \leq 1$) a rigid band model can be employed to explain alloying effects on magnetic moment. Rigid band theory assumes that d-bands do not change much in alloys but just get filled or emptied to a greater or lesser extent depending on composition. The magnetic moment of the solvent matrix remains independent of concentration. A moment reduction of $\Delta Z \mu_B$ is predicted at the solute site. The resulting average magnetic moment per solvent

Box 19.2 Dipole Moments and magnetizations in Fe **and** Ni

For Fe we calculate the number of spin-up and spin-down electrons to be:

$$N_\uparrow = \int_0^{\epsilon_F} g_d^\uparrow d\epsilon = 4.62 \qquad N_\downarrow = \int_0^{\epsilon_F} g_d^\downarrow d\epsilon = 2.42$$

and its net atomic dipole moment is then:

$$\mu_{atom} = (N_\uparrow - N_\downarrow)\mu_B = (4.62 - 2.42)\mu_B = 2.2\mu_B$$

Given that Fe is *bcc*with $a_0 = 0.28664$ nm, the atomic density for *bcc* Fe is:

$$N_a = \frac{2 \quad \frac{atoms}{cell}}{(0.28664 \times 10^{-9})^3 \quad m^3} = 8.49 \times 10^{28} \quad \frac{atoms}{m^3}$$

and the magnetization is therefore calculated to be:

$$M = N_a \mu_{atom} = 8.49 \times 10^{28} \quad \frac{atoms}{m^3} \times 2.2 \times 9.27 \times 10^{-24} A - m^2 = 1.73 \times 10^6 \frac{A}{m}$$

and $\mu_0 M = 2.17T$.
Repeating for Ni we calculate the number of spin-up and spin-down electrons to be:

$$N_\uparrow = \int_0^{\epsilon_F} g_d^\uparrow d\epsilon = 5 \qquad N_\downarrow = \int_0^{\epsilon_F} g_d^\downarrow d\epsilon = 4.4$$

and its net atomic dipole moment is then:

$$\mu_{atom} = (N_\uparrow - N_\downarrow)\mu_B = (5 - 4.4)\mu_B = 0.6\mu_B$$

Given that Ni is *fcc*with $a_0 = 0.3524$ nm, the atomic density for *bcc* Fe is:

$$N_a = \frac{4 \quad \frac{atoms}{cell}}{(0.3524 \times 10^{-9})^3 \quad m^3} = 1.69 \times 10^{29} \quad \frac{atoms}{m^3}$$

and the magnetization is therefore calculated to be:

$$M = N_a \mu_{atom} = 9.14 \times 10^{28} \quad \frac{atoms}{m^3} \times 0.6 \times 9.27 \times 10^{-24} A - m^2 = 0.508 \times 10^6 \frac{A}{m}$$

and $\mu_0 M = 0.64T$.

atom is the concentration weighted average of that of the matrix and that of the solute:

$$\mu = \mu_{matrix} - \Delta Z C \mu_B \tag{19.22}$$

where C is the solute concentration and ΔZ is the valency difference between solute and solvent atoms. This relationship is the basis for explaining the Slater-Pauling curve (Fig. 19.8) [Sla37] [Pau38]. Fig. 19.8 (b) shows a band structure determination of the Slater-Pauling curve for FeCo alloys that is an alloy discussed below. Fig. 19.8 (b) shows a band theory prediction of the average (spin only) dipole moment in FeCo

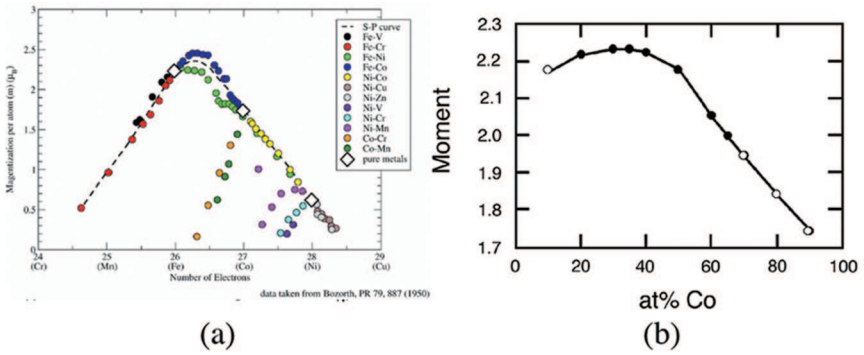

Fig. 19.8. (a) Slater-Pauling curve for Fe alloys and (b) spin-only Slater-Pauling curve for an ordered Fe-Co alloy as determined from LKKR band structure calculations [MSB$^+$98].

as a function of composition is in good quantitative agreement with the experimentally derived Slater-Pauling curve.

For transition metal impurities that introduce a strongly perturbing, highly localized potential, Friedel proposed a *virtual bound state, VBS* [Fri58] model to explain departure from the simple relationship for the compositional dependence of dipole moment above. Friedel suggestsed that when the perturbation due to alloying is strong enough, a bound state will be subtracted from the full d-band majority spin) and moved to higher energies. When the virtual bound state's (VBS) lies below the Fermi energy the moment of the alloy will change slowly with concentration. As the VBS moves above the Fermi level, however, a dramatic change in the magnetic moment is predicted to take place as electrons in the VBS empty into previously empty minority spin states. At this point for every additional solute atom added, a five fold degenerate majority spin 3d VBS will empty into five unoccupied minority spin 3d states. The change in average magnetic moment is predicted to be:

$$\mu = \mu_{matrix} - (\Delta Z + 10) C \mu_B \tag{19.23a}$$

Magnetic moment suppression is given by the VBS as:

$$\frac{d\mu}{dC} = -(\Delta Z + 10)\mu_B \tag{19.23b}$$

The VBS model predicts a moment reduction of -6μ_B for V or Nb additions to Co, e. g. The Friedel model was extended by Malozemoff et al [MWM84]. regarding the effect of the valence of the solute species on the magnetization in late transition metalmetalloid/early transition metal systems. VBS effects have been looked at in amorphous magnets [CO85], [GMO89]. In particular, when early transition metal glass formers are used these reduce the induction of the amorphous phase. Current

efforts discussed below, seek to reduce early transition metal and metalloid glass former concentrations to optimize the inductions in amorphous and nanocomposite systems [MWL$^+$10], [KMS$^+$11]

19.1.3 Temperature Dependent Magnetic Properties.

19.1.3.1 Collective Magnetism

Dipolar interactions are important in defining demagnetization effects. However, they are much to weak to explain the existence of a spontaneous magnetization in a material at any appreciable temperature. This is because thermal energy at relatively low temperature will destroy the alignment of dipoles. To explain a spontaneous magnetization it is necessary to describe the origin of an internal magnetic field or other strong magnetic interaction that act to align dipoles in the absence of a field.

> A *ferromagnet* is a material for which an *internal field* or equivalent *exchange interaction* acts to align atomic dipole moments parallel to one another in the absence of an applied field ($H = 0$).

Ferromagnetism is a *collective phenomenon* since individual atomic dipole moments interact to promote parallel alignment with one another. The interaction giving rise to the collective phenomenon of ferromagnetism has been explained by two models:

(i) *Mean Field Theory*: considers the existence of a non-local internal magnetic field, called the *Weiss field*, which acts to align magnetic dipole moments even in the absence of an applied field, H_a.

(ii) *Heisenberg Exchange Theory*: considers a local (nearest neighbor) interaction between atomic moments (spins) mediated by direct or indirect overlap of the atomic orbitals responsible for the dipole moments. This acts to align adjacent moments in the absence of an applied field, H_a.

Both of these theories help us to explain the T-dependence of the magnetization.

The Heisenberg theory lends itself to convenient representations of other collective magnetic phenomena such as *antiferromagnetism*, *ferrimagnetism*, *helimagnetism*, etc. illustrated in Fig. 19.9.

> An *antiferromagnet* is a material for which dipoles of equal magnitude on adjacent nearest neighbor atomic sites (or planes) are arranged in an antiparallel fashion in the absence of an applied field.

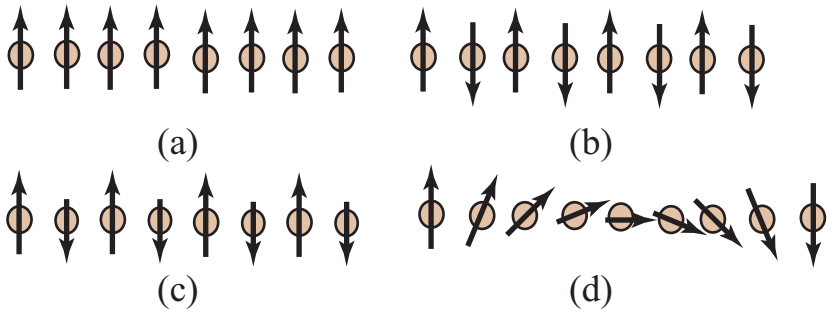

Fig. 19.9. Atomic dipole moment configurations in a variety of magnetic ground states: (a) ferromagnet, (b) antiferromagnet, (c) ferrimagnet, and (d) non-collinear spins in a helimagnet.

Antiferromagnets have zero magnetization in the absence of an applied field because of the vector cancellation of adjacent moments. They exhibit temperature dependent collective magnetism, though, because the arrangement of the dipole moments is not random but precisely ordered.

> A *ferrimagnet* is a material having two (or more) sublattices, for which the magnetic dipole moments of *unequal* magnitude on adjacent nearest neighbor atomic sites (or planes) are also arranged in an antiparallel fashion.

Ferrimagnets have non-zero magnetization in the absence of an applied field because their adjacent dipole moments do not cancel. [7] All of the collective magnets described thus far a *collinear magnets*, meaning that their dipole moments are either parallel or antiparallel. It is possible to have ordered magnets for which the dipole moments are not randomly arranged, but are not parallel or antiparallel. The *helimagnet* of Fig. 19.9 (d) is an example of a non-collinear ordered magnet. Other examples of non-collinear ordered magnetic states include the triangular spin arrangements in some ferrites [YK52].

The temperature dependence of the magnetization in a system with collective magnetic response is calculated within the context of statistical mechanics. We consider the ordering effect of an applied and internal field and the disordering effect of thermal fluctuations. We illustrate this for ferromagnetism in terms of mean field theory as introduced by Pierre Weiss in 1907 [Wei07]. Weiss postulated an *internal magnetic field* (the Weiss field), $\vec{H}_{int}$, which acts to align atomic dipole moments even in the absence of an external applied field, H_a. The of mean field theory is that the internal

[7] ferrimagnets are named after a class of magnetic oxides called ferrites.

field is directly proportional to the magnetization of the sample:

$$\vec{H}_{int} = \lambda \vec{M} \tag{19.24a}$$

The constant of proportionality , λ, is called the *Weiss molecular field constant*.

A statistical mechanical treatment (the canonical ensemble) of the quantum theory of paramagnetism describes the magnetization as a function of $\frac{H}{T}$ in terms of a *Brillouin function*:

$$M = NgJ\mu_B B_J(x) \quad x = \frac{gJ\mu_B B}{k_B T} \tag{19.24b}$$

with:

$$B_J(x) = \frac{2J+1}{2J}\coth\Big[\frac{(2J+1)x}{2J}\Big] - \frac{1}{2J}\coth\Big[\frac{x}{2J}\Big] \tag{19.24c}$$

For spin only angular momentum, $J = S$ this reduces to:

$$M = N\mu\frac{\exp x - \exp(-x)}{\exp x + \exp(-x)} = N\mu\tanh x \quad x = \frac{\mu_B(\mu_0 H)}{k_B T}$$

and in the classical limit, $J = \infty$ reduces to:

$$M = M_s\Big(\coth(x) - \frac{1}{x}\Big) = M_s L(x) \qquad x = \frac{\mu_{atom}\mu_0 H}{k_B T}$$

where L(x) is the *Langevin function*. To consider a ferromagnet we treat the problem in analogy to a paramagnet but now consider the superposition of applied and internal magnetic fields. We conclude:

$$M = M_s\Big(\coth(x') - \frac{1}{x'}\Big) = M_s L(x') \qquad x' = \frac{\mu_0\mu_{atom}}{k_B T}\Big[H_a + \lambda M\Big] \tag{19.24d}$$

for a collection of classical dipole moments. Similarly, $M = N_m < \vec{\mu}_{atom} >$ and:

$$\frac{M}{N_m\mu_{atom}} = \frac{M}{M_s} = L\Big(\frac{\mu_0\mu_{atom}}{k_B T}\Big[H_a + \lambda M\Big]\Big) \tag{19.24e}$$

This transcendental equation has solutions with a non-zero magnetization (*spontaneous magnetization*) in the absence of an applied field. We show this graphically considering $M(H = 0)$ the variables:

$$b = \frac{\mu_0\mu_{atom}}{k_B T}\Big[\lambda M\Big] \quad T_c = \frac{N_m\mu_0(\mu_{atom})^2\lambda}{3k_B} \tag{19.24f}$$

Notice that T_c has units of temperature. Notice also that:

$$\frac{b}{T_c} = \frac{3}{T}\Big[\frac{M(0)}{M_s}\Big] \quad \frac{M(0)}{M_s} = \frac{bT}{3T_c} = L(b) \tag{19.24g}$$

The two equations for the reduced magnetization (i.e., $\frac{M(0)}{M_s} = \frac{bT}{3T_c}$ and $\frac{M(0)}{M_s} = L(b)$) can be solved graphically, for any choice of T by considering the intersection of

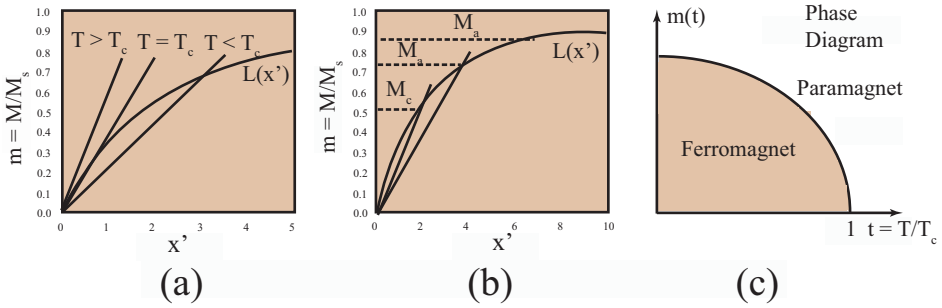

Fig. 19.10. (a) Intersection between the curves, $\frac{b}{3}(\frac{T}{T_c})$, and L(b) for $T < T_c$ gives a non-zero, stable ferromagnetic state and (b) the locus of M(T) determined by intersections at temperatures $T < T_c$, (c) reduced magnetization, m, vs. reduced temperature, $t = \frac{T}{T_c}$, as derived from (b)

the two functions $\frac{b}{3}(\frac{T}{T_c})$, and L(b). For $T \geq T_c$ the only solutionis for $M = 0$, i.e. paramagnetic response.

For $T < T_c$ we obtain solutions with a non-zero, spontaneous, magnetization, the defining feature of a ferromagnet. For $T = 0$ to $T = T_c$ we can determine the spontaneous magnetization graphically as the intersection of our two functions $\frac{b}{3}(\frac{T}{T_c})$, and L(b). This allows us to determine the zero field magnetization, $M(0)$ as a fraction of the spontaneous magnetization as a function of temperature. Fig. 19.10(c) shows $\frac{M(0,T)}{M_s}$ to decrease monotonically from 1, at 0 K, to 0 at $T = T_c$, where T_c is called the *ferromagnetic Curie temperature*. At $T = T_c$, we have a higher order phase transformation from a ferromagnetic phase to paramagnetic phase. In summary, mean field theory for ferromagnets predicts:

(i) For $T < T_c$ collective magnetic response gives rise to a spontaneous magnetization even in the absence of a field. This spontaneous magnetization is the defining feature of a ferromagnet.
(ii) For $T > T_c$, the misaligning effects of temperature serve to completely randomize the direction of the atomic moments in the absence of a field. The loss of the spontaneous magnetization defines the return to paramagnetic response.
(iii) In zero field the ferromagnetic to paramagnetic phase transition is higher order (first order in a field).

19.1.3.2 Landau Theory of Magnetic Phase Transitions.

The *Landau theory* also describes collective magnetism in systems that undergo paramagnetic to ferromagnetic *phase transitions* in terms of an *order parameter*.

> The order parameter, η, quantifies a new physical property of the system that arises from a phase transformation.

The order parameter is defined such that it is zero on one side of the transformation (disordered) and finite and positive on the other side of the transformation. It approaches unity when the transformation nears completion. The order parameter is determined from the condition that the free energy is a minimum. In 1937, [Lan37] was the first to expand the *Free energy* in a Taylor's series about the *Curie temperature* T_C in a ferrromagnet:

$$G = G_0 + \Big(\frac{\partial G}{\partial \eta}\Big)_{\eta=0}\eta + \frac{1}{2}\Big(\frac{\partial^2 G}{\partial \eta^2}\Big)_{\eta=0}\eta^2 + \frac{1}{6}\Big(\frac{\partial^3 G}{\partial \eta^2}\Big)_{\eta=0}\eta^3 + \ldots \tag{19.25a}$$

This can also be written as:

$$G = G_0 + a\eta + b\eta^2 + c\eta^3 + \ldots \tag{19.25b}$$

where it may be assumed that the expansion is valid away from the transition temperature. To express equilibrium, it is required that:

$$\Big(\frac{\partial G}{\partial \eta}\Big) \quad and \quad \Big(\frac{\partial^2 G}{\partial \eta^2}\Big) > 0 \tag{19.25c}$$

and therefore $a = 0$. For magnetic materials the order parameter is related to the magnetization, M. Above the Curie temperature this value goes to zero and below the Curie temperature, M rises until it reaches its maximum value at 0 K, which can be written as M(0). M(0) is also called the *spontaneous magnetization*. In order to define an order parameter which varies from 0 to 1 we can define the *reduced magnetization*:

$$m(T) = \frac{M(T)}{M(0)} \tag{19.26}$$

The value of m(T) thus is 0 above the Curie temperature and unity at 0 K. This is the order parameter for magnetic materials. It can further be remembered that the magnetization is a vector. In this case the order parameter can be written as:

$$m(T) = m_x\vec{i} + m_y\vec{j} + m_z\vec{k} \tag{19.27}$$

where the components of the magnetization, m_x, m_y and m_z represent the direction cosines of the magnetization vector with respect to a reference coordinate system. This distinction will become important in a discussion of *magnetic anisotropy* later in the course. For now we continue our discussion using a scalar order parameter, m. The free energy (in light of equilibrium conditions) can be expressed:

$$G = G_0 + \frac{a}{2}m^2 + \frac{b}{4}m^4 + \ldots \quad b > 0 \tag{19.28a}$$

there are no odd order terms in this expansion because the free energy must be invariant with respect to *time reversal symmetry*. Time reversal symmetry refers to the fact that

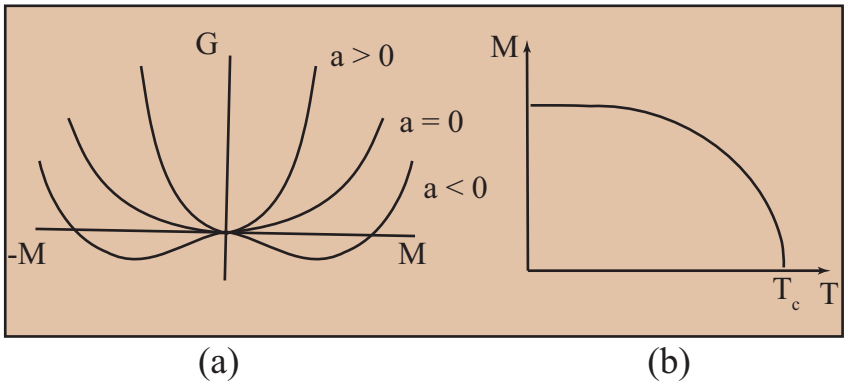

Fig. 19.11. (a) Gibb's free energy functional dependence on m for a paramagnet, ferromagnet and at T_c, (b) resulting temperature dependence of the spontaneous magnetization within the Landau theory.

changing the direction (sign) of the magnetization must yield the same free energy. We now consider the conditions for thermodynamic equilibrium:

$$\left(\frac{\partial G}{\partial m}\right) = am + bm^3 = 0 \quad \left(\frac{\partial^2 G}{\partial m^2}\right) = a + 3bm^2 \tag{19.28b}$$

which can be true for $m = 0$, the paramagnetic state ($\alpha > 0$) and for $m^2 = -\frac{a}{b}$ the ordered state for which a spontaneous magnetization exists and $a < 0$. Examination of the second derivative allows us to infer that for $a < 0$ m is non-zero (ferromagnetic), for $a > 0$ m is zero (paramagnetic) and $a = 0$ at T_c. Fig. 19.11 (a) shows the Gibb's free energy functional dependence on m for a paramagnet, ferromagnet and at T_c and Fig. 19.11 (b) shows temperature dependence of the spontaneous magnetization To first order we can reflect the sign change occurring at T_c by writing:

$$a = a_\theta(T - T_c) \quad and \quad m^2 = \frac{a_\theta(T_c - T)}{b} \quad m = \left(\frac{a_\theta}{b}\right)^{\frac{1}{2}}(T_c - T)^{\frac{1}{2}} \tag{19.28c}$$

The free energy can thus be rewritten:

$$G = G_0 - \left(\frac{a_\theta^2}{4b}\right)(T_c - T)^2 + \ldots \tag{19.28d}$$

The magnetic phase transition (ferromagnetic to paramagnetic) that occurs at the Curie temperature is an example of a *second order phase transition*.

The Landau expansion can be expanded to include the conjugate thermodynamic parameters (including applied fields) of the order parameter. When the order parameter is the magnetization, we can write:

$$G = G_0 + \frac{a}{2}m^2 + \frac{b}{4}m^4 + \ldots - \mu_0 MH \tag{19.29}$$

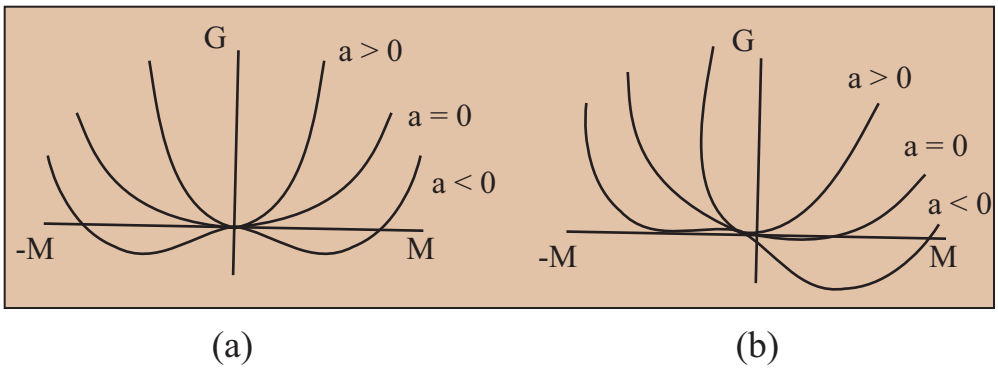

Fig. 19.12. (a) Gibb's free energy functional dependence on m (b) the same with the inclusion of a field (Zeeman) energy term.

where in a scalar formalism we take M and H as parallel. This is an example of a free energy functional that gives rise to a *first order phase transition* in field.

It is often of interest to determine the Curie temperature of a magnetic material from magnetization vs. temperature data taken in a constant applied field. There are a variety of fitting procedures for this including taking the temperature at which an inflection point in such a curve occurs as an estimation of T_c. A more satisfying method for determining the Curie temperature is in terms of the *Arrott plot* [Arr57], [Bel56] which is rooted in a consideration of the first order phase transition in the presence of an applied field, H. Taking the derivative of the function above with respect to m and setting it equal to zero yields:

$$a(T)m + b(T)m^3 = \mu_0 H = a_\theta(T - T_c)m + b(T)m^3 \tag{19.30}$$

At T_c, a plot of m^3 vs. H is therefore predicted to be linear.

The influence of an applied field on the magnetic transition can be rationalized as follows. Fig. 19.12 (a) shows the previous Gibb's free energy functional dependence on m. Fig. 19.12 (b) shows the same with the the inclusion of a field (Zeeman) energy term. In zero applied field, both domains ($\pm M$) have equal free energies, thus either or both domains may form. In the presence of an applied field, one domain (that with its magnetization parallel to the applied field) is favored over the other.

The Landau theory can be extended in several ways to consider other types of phase transitions. These include:

(i) Explicitly considering the magnetization as a vector order parameter (magnetic anisotropy);
(ii) considering spatial derivatives of the magnetization in the expansion (micromagnetics); and

(iii) including additional work terms in the free energy with or without coupling terms to the magnetization (magnetostriction, e.g.).

These are the subject of several of the discussions below.

19.1.4 Angularly Dependent Magnetic Properties: Magnetic Anisotropy.

Anisotropy refers to the phenomenon that certain properties of single crystal materials depend of the the direction in which they are measured. *Magnetic anisotropy* includes: (i) *Magnetocrystalline anisotropy*; (ii) *Shape anisotropy*;(magnetostatic); (iii)*Induced Anisotropy* (a) Stress; (b) Annealing; (c) Deformation; (d) Irradiation.

Only magnetocrystalline anisotropy is intrinsic, depending only on the symmetry of the magnetic material. Most ferromagnetic materials derive from cubic or uniaxial materials. The magnetic free energy is expressed in a tensor formalism:

$$E_a = k_{mn}M_mM_n + k'_{mnop}M_mM_nM_oM_p + k'_{mnopqr}M_mM_nM_oM_pM_qM_r + \ldots \tag{19.31}$$

where the k's are 2nd, 4th, 6th, etc. rank tensors. M's are axial vectors.

Only even powers of M occur in the expansion since E_a is invariant to the *time reversal operation, R*. We express the magnetization in direction cosines:

$$M_i = M_s\cos\alpha_i = M_s\Big(\cos\alpha_1\vec{i} + \cos\alpha_2\vec{j} + \cos\alpha_3\vec{k}\Big) \tag{19.32a}$$

and we can construct the *dyadic product* of M_i with itself to be:

$$M_mM_n = M_s^2\begin{pmatrix} \cos^2\alpha_1 & \cos\alpha_1\alpha_2 & \cos\alpha_1\alpha_3 \\ \cos\alpha_2\alpha_1 & \cos^2\alpha_2 & \cos\alpha_2\alpha_3 \\ \cos\alpha_3\alpha_1 & \cos\alpha_3\alpha_2 & \cos^2\alpha_3 \end{pmatrix} \tag{19.32b}$$

If the paramagnetic phase is cubic, the second rank tensor is a scalar as shown:

$$k'_{mn}M_mM_n = k_1M_s^2\Big(\cos^2\alpha_1 + \cos^2\alpha_2 + \cos^2\alpha_3\Big) = k_1M_s^2 \quad = k'_{mn}\delta_{mn} \tag{19.32c}$$

where δ_{mn} is the *Kronecker delta*. For cubic materials, the first term in the expansion is constant and we must go to the 4th order to obtain information on anisotropy.

For hexagonal symmetry, the 2nd rank anisotropy tensor has the form:

$$k'_{mn} = \begin{pmatrix} k_1 & 0 & 0 \\ 0 & k_1 & 0 \\ 0 & 0 & k_3 \end{pmatrix} \tag{19.33a}$$

$$k'_{mn}M_mM_n = M_s^2k_1 + M_s^2(k_3 - k_1)\cos^2\alpha_3 \tag{19.33b}$$

Thus in hexagonal, or any *uniaxial materials*, we need to include 2nd order terms in

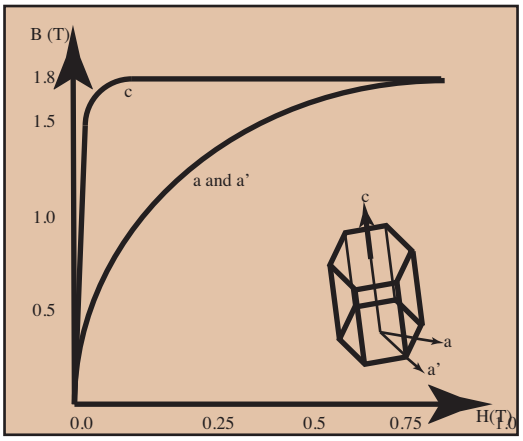

Fig. 19.13. (a) M-H Curves for a single Crystal of *hcp* Co along different directions.

the expansion. Since $\cos^2\alpha_3 = 1 - \sin^2\alpha_3$, the last expression can be written:

$$E_a = K_0 + K_1 \sin^2\theta \tag{19.33c}$$

where $\theta = \alpha_3$ is the more common symbol used in the literature to denote the one unique angle. When 4th order terms are included in the expansion the anisotropy is:

$$E_a = K_0 + K_1 \sin^2\theta + K_2 \sin^4\theta \tag{19.33d}$$

19.1.4.1 Uniaxial Symmetry

The work performed when a field, H, is applied to a magnetic material is HdM with dM the change in magnetization. Fig. 19.13 shows M vs. H plot for hexagonal Co. With H along the $[0001]$ direction M changes more easily than when perpendicular to this direction. Thus the $[0001]$ is the *easy direction of magnetization, EMD*. The area between two H(M) curves (the work difference to saturate) is the *magnetocrystalline anisotropy energy* with units of energy per unit volume. Since a large amount of work must be performed to align M along basal plane directions ($\perp$ to the EMD), these are *hard axes*. Materials with a single easy axis have uniaxial symmetry.

The magnetocrystalline anisotropy energy of a hexagonal material is written to 1st order in 19.33c, where θ is the angle from the $[0001]$ axis . For positive K_1, the minimum energy is for $\theta = 0°$ and the maximum for $\theta = 90°$. If K_1 is negative, the minimum in energy is in the basal plane. The expression for the energy denoted in equation 19.33c is a 1st order expansion in terms of $\sin^2\theta$. If we add the 2nd term we obtain equation 19.33d, where the 2nd order term, K_2, allows more complicated variation of energy with angle. The 3 extrema for this equation are at: $\theta = 0°$, $\theta = 90°$

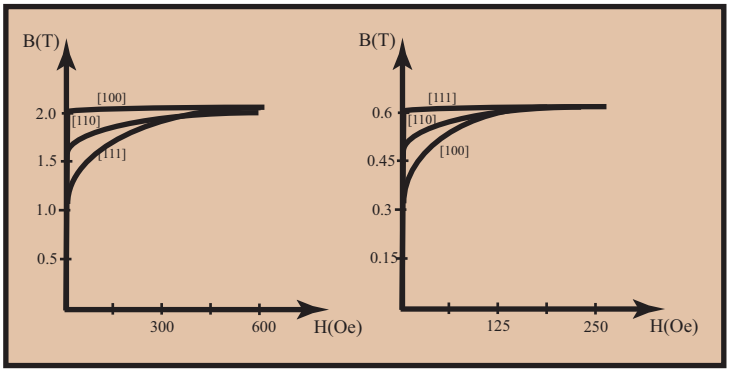

Fig. 19.14. H vs. M plots for Fe and Ni.

and at an intermediate value depending on K_1 and K_2. The third solution allows for easy directions to lie on a cone at an angle from the vertical $[0001]$ direction.

The field associated with magnetic anisotropy is called the *anisotropy field, H_K*:

$$H_K = \frac{2K_1}{M_s} \tag{19.34}$$

Ii $K_2 = 0$. H_K, is the field necessary to saturate the material along the hard direction and serves as an upper bound for the coercivity.

19.1.4.2 Cubic Symmetry

H vs. M plots for Fe and Ni are shown in Fig. 19.14. For Fe, the $\langle 100 \rangle$ directions are the easy axis directions, whereas for Ni the easy axes are the $\langle 111 \rangle$ directions. Thus, Fe has six easy axes ($\pm\langle 100 \rangle$) and Ni has eight easy axes ($\pm\langle 111 \rangle$).

The cubic anisotropy energy is written to sixth order terms in direction cosines as:

$$E_a = K_1\left(\alpha_1^2\alpha_2^2 + \alpha_2^2\alpha_3^2 + \alpha_3^2\alpha_1^2\right) + K_2\left(\alpha_1^2\alpha_2^2\alpha_3^2\right) \tag{19.35}$$

where α's are direction cosines of angles between M and the $\langle 100 \rangle$ axes. For the case where $K_2 = 0$ it can be shown that the minima are along the $\langle 100 \rangle$ if $K_1 > 0$ and along the $\langle 111 \rangle$) if $K_1 < 0$. This is the case of Fe and Ni, respectively. In these cases the intermediate axes are along the $\langle 110 \rangle$ and maxima (hard axes) are $\langle 111 \rangle$ if $K_1 > 0$ and along the $\langle 100 \rangle$) if $K_1 < 0$ (i. e. opposite the easy axes).

Consider Fe with saturation induction, $B_s = 2.2$T and cubic magnetocrystalline anisotropy, with $K_1 = 4.8 \times 10^5 \frac{erg}{cm^3}$. If we consider the magnetization oriented along

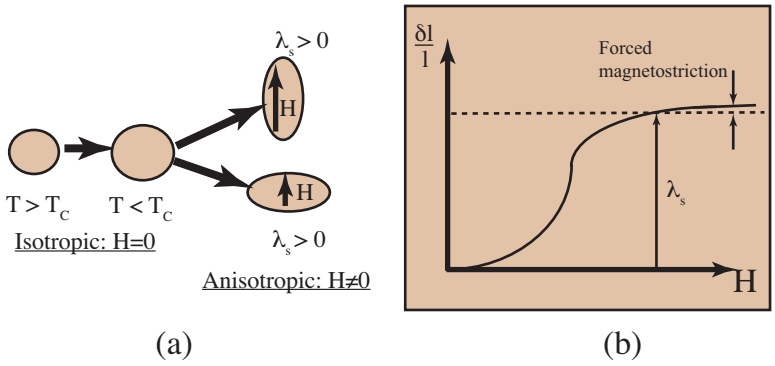

Fig. 19.15. (a) Schematic of isotropic and anisotropic magnetostriction and (b) magnetostrictive strain as a function of the magnitude of the applied field, H.

$[111]$ then $E_a = 1.28 \times 10^5 \frac{erg}{cm^3}$. We can calculate an anisotropy field, H_K:

$$H_K = \frac{2K_1}{M_s} = \frac{9.6 \times 10^5 \frac{erg}{cm^3}}{\frac{21580}{4\pi}} = 559Oe$$

This is the field necessary to saturate when oriented along the hard axis. Recognizing: $B = \mu_r H$, the relative permeability is:

$$\mu_r = \frac{4\pi M_s}{H_K} = \frac{M_s^2}{2K_1} = \frac{21580}{2 \times 559} = 19.3$$

For M $\parallel$ $[100]$, μ_r is unbounded if there aren't impediments to domain wall motion.

19.1.4.3 Coupling of Magnetic Properties to Stress Fields: Magnetostriction.

The coupling of magnetic and mechanical properties is termed *magnetostriction*. Magnetoelastic interactions result from coupling magnetic anisotropy and elastic response. Magnetostriction can cause dissipative energy loss in magnetic materials. Coupling of residual stress in alloys with non-zero *magnetostriction coefficient,* λ (units of strain) results in stress induced anisotropy that can reduce the ease of magnetization, lower μ and increase H_c. [8] In Invar alloys magnetostrictive volume changes cancel the thermal expansion coefficient making material dimensions temperature-independent [Gig95].

A change in dimension during magnetization by an applied field is *anisotropic magnetostriction*. Along the direction of the applied magnetic field the sample elongates or shrinks and perpendicular to the field the sample shrinks or elongates, respectively (Fig. 19.15 (a)). An *isotropic magnetostriction* or *exchange magnetostriction*, arises from coupling of the exchange energy to the interatomic spacing. This occurs during

[8] Strain is defined as the change in length divided by the original length, a dimensionless quantity.

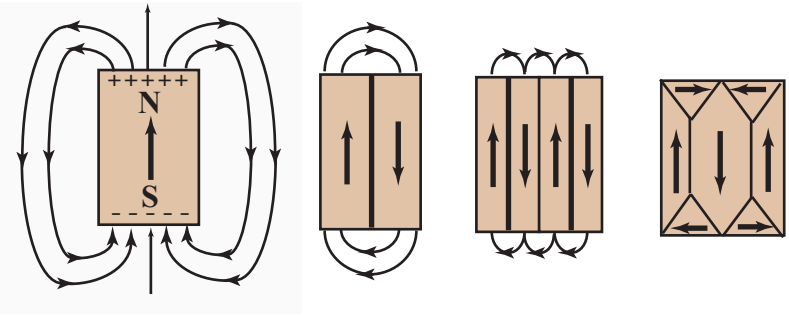

Fig. 19.16. Reduction in the demagnetization field as a result of the introduction of magnetic domains into a ferromagnetic sample.

cooling through T_c without an applied magnetic field. For anisotropic magnetostriction there are both longitudinal and transverse effects that add to zero volume change. A tensor property, magnetostriction is tied to the crystallography.

Magnetostrictive strains, $\frac{\delta l}{l}$, (where δl is the magnetostrictive displacement) for typical transition metal ferromagnets are $\sim 10^{-5} - 10^{-6}$ at saturation. The magnetostriction coefficient in the saturated state is the *saturation magnetostriciton*, λ_s. Beyond saturation there is a small increasing *forced magnetostriction* typically measured on a logarithmic scale with field, H. Co has the largest magnetostriction of the elements with a value of $\frac{dl}{l} \sim 60 \times 10^{-6}$ at room temperature. For interesting alloys $\frac{dl}{l}$ can be large. $\frac{dl}{l} \sim 10^{-3}$ for Terfenol, $Tb_{1-x}Dy_xFe_2$.

19.1.5 Microscopic Magnetization and Domains.

A *magnetic domain* is macroscopic volumes over which atomic magnetic moments are aligned.

For a ferromagnet, when $H_a = 0$, the existence of a spontaneous magnetization requires the existence of domains . It is perhaps surprising, that ferromagnetic materials can exist in a "virgin state" for which the magnetization is zero in the absence of an applied field. This is understood by ferromagnetic domain theory. In a typical magnetic material a macroscopic volume contains many domains. Each domain has a spontaneous magnetization of magnitude, M_s. In the absence of an applied field the magnetization vectors are randomly aligned from domain to domain (just like in a paramagnet atomic dipoles were random). Taking a vector sum of the magnetization over many domains may yield zero sample magnetization because of vector cancellation.

The energetic reasons for domain formation are discussed below. We can qualita-

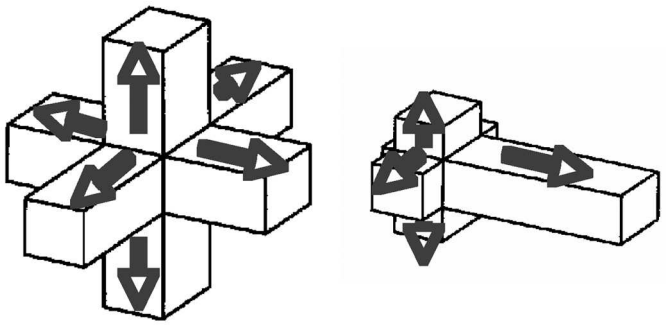

Fig. 19.17. Random domains in a ferromagnetic material, with the $[100]$-type directions as easy direction of magnetization (a) a case where the net magnetization is zero and (b) where the net magnetization is non-zero.

tively understand this by by recognizing that magnetic flux line leave the north pole of a magnet and enter the south pole. This gives rise to a field outside the magnet, the *demagnetization field, H_d* which would like to misalign the dipole moments in the ferromagnet. It requires internal energy to maintain the alignment of the dipoles.

A configuration for which the demagnetization field is reduced will lower the total energy of the system. For two domains (Fig. 19.16) we significantly reduce the return path which is necessary to be taken by fringing fields. By applying successively more domains we can further reduce the *magnetostatic self energy* to nearly zero. In the case where we have two long domains and two closure domains [9] the magnetization makes a nearly circuitous path reducing the demagnetization field to nearly zero. There is no free lunch, though. Each boundary between domains requires that we pay an energy associated with a *domain wall*. The configuration of domains and walls, ultimately depends on the balancing of these two energies.

Magnetic domains were first postulated to exist by P. Weiss in (J. de Phys., 6, 661, 1907) [Wei07]. In his epoch paper he postulated their existence in order to explain how a ferromagnet could exist in a demagnetized state below its Curie temperature. A random array of regions with differing directions of magnetization could be imagined to exist and the regions would align themselves with application of a magnetic field.

Magnetic domains exist because of the lowering of the symmetry of a material when it passes from the paramagnetic state to the ferromagnetic state. However, their specific arrangement in the material is dependent on the various energies associated with the ferromagnetic state. These include:

[9] This often happens in cubic materials with $\langle 100 \rangle$ easy axes

(i) Exchange
(ii) Magnetostatic
(iii) Applied fields
(iv) Magnetocrystalline anisotropy
(v) Magnetostriction

When cooling a cubic material with $\langle 100 \rangle$ easy axes of magnetization from above the Curie temperature, if all domains have equal probability of forming their arrangement may be thought to look like Fig. 19.17.

Fig. 19.17 (a) illustrates an configurations for which) the total magnetization would be zero. If however the arrangement of domains were as shown in Fig. 19.17 (b), the magnetization would be non-zero, with the largest component along the y-axis. The material could magnetize this way if there were a field applied during the cooling process. Such field processing can therefore be important in determining the magnetic remnant state and subsequent magnetization processes.

Breakup into domains is undesirable in *permanent magnet* materials because it reduces the useful *remnant induction*. For this reason permanent maganet materials are engineered to have large magnetic anisotropies and consequently large coercive fields. Magnetic anisotropy can also be developed by judiciously chosen shapes. The shape of a *horseshoe magnet* was developed to prevent the magnetic stray fields from demagnetizing a permanent magnet made from a relatively soft magnetic material.

19.1.6 Energies Determining the Magnetic Domain Size.

It can be seen from the schematic that the stray field in the first configuration of Fig. 19.16. is much larger than the second. The second arrangement of domains lowers this energy. However, a new feature appears, namely the wall between the two domains. This *domain wall* has an energy of its own, so if the material in is to break up into two domains, the decrease in stray field energy must be greater than the increase in energy due to the domain wall.

Further subdivision into more domains is possible as seen in Fig. 19.16. The ultimate size of the domains is determined as calculated below based on the balance between savings of magnetostatic energy and the cost in wall energy. The magnetostatic energy can be further reduced by ensuring *flux closure* through the introduction of *closure domains* at the surface of the sample [LL35] as illustrated in the last frame of Fig. 19.16.

In more complicated domain structures the principles of minimizing the total energy associated with free poles and walls applies. These can be complicated by sample geometries, internal interfaces, surface morphological features and non-magnetic inclusions.

19.1.7 Domain Wall Configurations

There are a variety of configurations for domain walls [SH98] and their geometries depend on a variety of considerations including:

(i) The *exchange stiffness, A* which is a measure of the energy penalty for rotating a spin against the exchange energy in a material. It is defined as:

$$A_{ex} = A = \frac{nJS^2}{a} \tag{19.36a}$$

where n is the number of atoms (dipoles) per unit cell and a is the lattice constant. This derives from the Heisenberg nearest neighbor exchange energy:

$$E_{ex} = -2JS^2 \cos\phi_{ij} = -2A\cos\left(\frac{d\phi}{dx}\right) \tag{19.36b}$$

where the first expression is for a discrete lattice with ϕ_{ij} the angle between adjacent spins. The second expression is the continuum expression.

(ii) The crystal symmetry and the magnetocrystalline anisotropy energy density.

(iii) The material geometry. In particular, domains in bulk samples and thin films are fundamentally different because of demagnetization effects. The magnetostatic energy is often a primary determinant of the wall configurations, especially in thin samples.

(iv) Volume and surface pinning effects.

Fig. 19.18 illustrates a few examples of domain wall configurations in magnetic materials. Fig. 19.18 (a) illustrates a 180° domain wall which accommodates a complete magnetization reversal in a material. Fig. 19.18 (b) illustrates 90° domain walls which provide a closed path for magnetic flux within a sample, minimizing free pole magnetostatic effects. Fig. 19.18 (c) shows curved walls and Fig. 19.18 (d) spike domains. Each of these offer a means of mixing the free pole density on a finer scale which can be of energetic advantage in thin samples. The geometry of the reversal in a wall can also differ from bulk to thin film samples as discussed in the context of *Bloch walls* and *Neel walls*.

19.1.8 Energetics of a 180° Domain Wall.

We now discuss the relative values of energies in determining the geometry of the domain wall. A possible wall structure is one with an abrupt change, (Fig. 19.19 (a)). This abrupt change has a high energy because of the large value of the *exchange energy* across the wall. This energy is estimated using:

$$E_{ex} = -2J_{ex}\vec{S}_i \cdot \vec{S}_j \tag{19.37a}$$

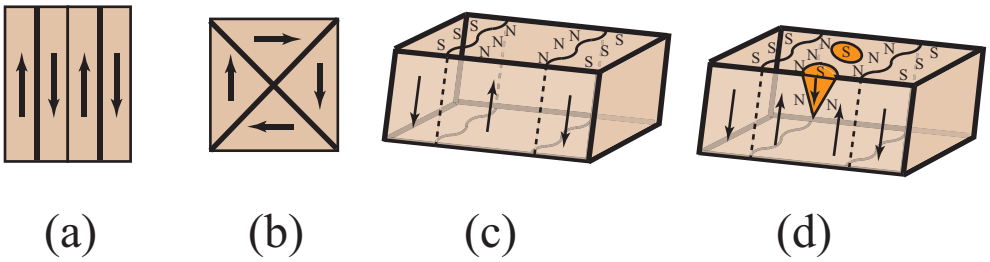

Fig. 19.18. Examples of domain wall configurations in magnetic materials (a) 180°, (b) 90°, (c) curved domain walls and (d) surface spike domains.

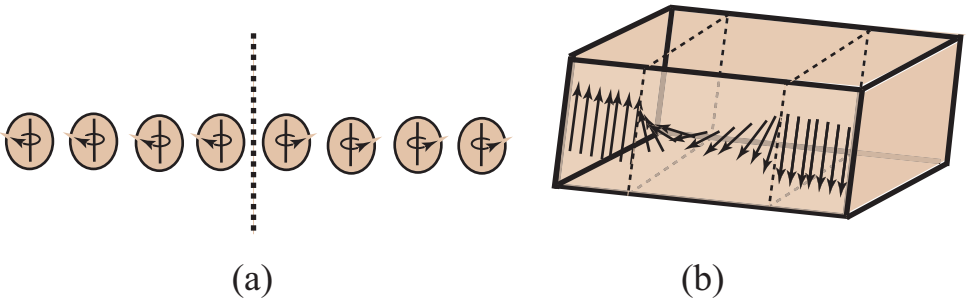

Fig. 19.19. Magnetic domains separated by an atomically sharp domain wall (a) and by a wall with a gradual 180° rotation of the dipole moments in the wall.

and calculating the exchange energy for parallel and antiparallel spins:

$$E_{ex}(\uparrow\uparrow) = -2J_{ex}S^2\cos(0) = -2J_{ex}S^2 \quad E_{ex}(\uparrow\downarrow) = -2J_{ex}S^2\cos(180) = 2J_{ex}S^2$$

The excess energy of the abrupt change wall is proportional to $4J_{ex}S^2$. By spreading the spin reversal over n equal steps of angle $\frac{\pi}{n} = \frac{180}{n}$, a lower wall energy is obtained (Fig. 19.19 (b)). The potential energy between adjacent dipole moments is:

$$E_{ex}(smallangle) = -2J_{ex}S^2\cos(\frac{\pi}{n}) \tag{19.37b}$$

If the angle, θ between nearest neighbor dipole moments is small the we can use the small angle Taylor series expansion for $\cos\theta$:

$$\cos\theta \approx \left(1 - \frac{\theta^2}{2}\right) = \left(1 - \frac{\pi^2}{2n^2}\right)$$

and therefore:

$$E_{ex} = -2J_{ex}S^2\left(1 - \frac{\pi^2}{2n^2}\right) \quad \left(\Delta E_{ex}\right) = 2J_{ex}S^2\left(\frac{\pi^2}{2n^2}\right) = J_{ex}S^2\left(\frac{\pi}{n}\right)^2 \tag{19.37c}$$

and to obtain the total exchange energy over the $n+1$ spins in the wall:

$$U_{ex} = (n+1)\Big(\Delta E_{ex}\Big) = J_{ex}S^2\Big(\frac{\pi}{n}\Big)^2(n+1) \approx \frac{J_{ex}S^2\pi^2}{n} \tag{19.37d}$$

As $n \to \infty$, U_{ex} goes to zero. Thus, if this were the only energy term the wall would be infinitely wide. However, all the spins, in the domain wall, are not aligned in easy axes directions so there will be a magnetocrystalline anisotropy energy term which must be taken into account.

Since we are ultimately interested in normalizing energies per unit area of a domain wall, we can consider the contribution of the exchange energy to the wall energy. The exchange energy per unit area is found by dividing the above energy by a^2, where a is the lattice parameter of the material since a^2 represents the area per spin:

$$\frac{U_{ex}}{a^2} = \frac{J_{ex}S^2\pi^2}{na^2} = \gamma_{ex} \tag{19.37e}$$

Hence the exchange energy is inversely related to the wall thickness. A small exchange energy gives rise to a larger wall width.

The magnetocrystalline anisotropy energy within the wall can be approximated by multiplying the width of the wall times the anisotropy constant, K_1:

$$\gamma_a = naK_1 \tag{19.37f}$$

The total wall energy is then the sum of the contributions from exchange and anisotropy:

$$\gamma_{tot} = \gamma_{ex} + \gamma_a = \frac{J_{ex}S^2\pi^2}{na^2} + naK_1 \tag{19.37g}$$

We can now determine the value of n (and therefore the width of the wall) which minimizes this total energy:

$$\frac{d\gamma_{tot}}{dn} = 0 = -\frac{J_{ex}S^2\pi^2}{n^2a^2} + aK_1 \quad n_{eq} = \Big(\frac{J_{ex}S^2\pi^2}{a^3K_1}\Big)^{\frac{1}{2}} \tag{19.37h}$$

and we can see that increasing JS^2 increases n and increasing K_1 decreases the value of n. The thickness of a domain wall is given as:

$$\delta_w = n_{eq}a = \pi\Big(\frac{J_{ex}S^2}{aK_1}\Big)^{\frac{1}{2}} = \pi\sqrt{\frac{A_{ex}}{K_1}} \tag{19.37i}$$

The total energy of the wall is given as:

$$\gamma_{tot} = \gamma_{ex} + \gamma_a = 2\Big(\frac{J_{ex}S^2\pi^2K_1}{a}\Big)^{\frac{1}{2}} = 2\pi\Big(A_{ex}K_1\Big)^{\frac{1}{2}} \tag{19.37j}$$

The Box 19.3 shows that the wall energy is equally divided between exchange and magnetocrystalline energy and calculates the domain wall width for Fe.

Box 19.3 Calculation of the domain wall thickness for crystalline Fe**.**

The domain wall thickness may be written as:

$$\delta_w = n_{eq} a = \pi \Big(\frac{J_{ex} S^2}{a K_1} \Big)^{\frac{1}{2}}$$

where n_{eq} is the value of n which minimizes the total wall energy. For Fe:

$$J_{ex} S^2 = 2.16 \times 10^{-21} J, \quad K_1 = 4.2 \times 10^4 \frac{J}{m^3} \quad a = 2.86 \times 10^{-10} m$$

and we can calculate δ_w^{Fe} to be:

$$\delta_w^{\mathrm{Fe}} = \pi \Big(\frac{J_{ex} S^2}{a K_1} \Big)^{\frac{1}{2}} = 42 nm$$

This value is $\approx$ 150 lattice spacings.

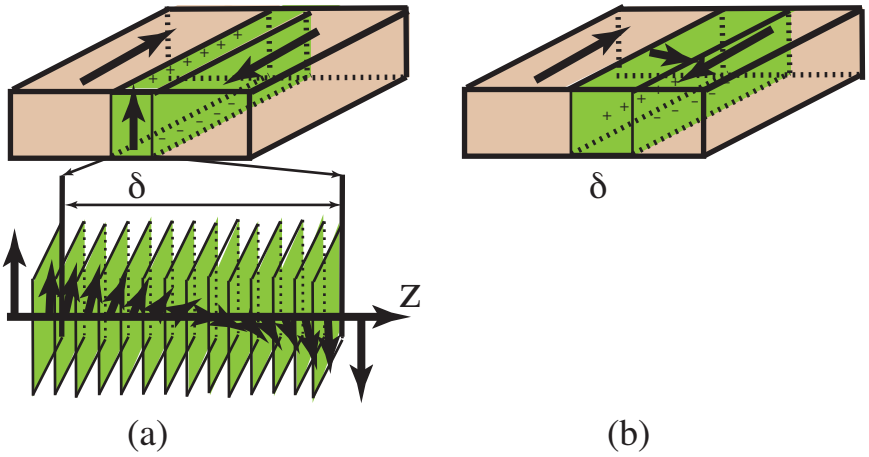

Fig. 19.20. Geometries of 180° domain walls (a) a Bloch wall and (b) a Neel wall.

19.1.9 Energetics of 180° Domain Walls in Thin Films.

In a thin film there are two ways of rotating the magnetization within the wall, as shown in Fig. 19.20. The *Bloch wall*, Fig. 19.20 (a) has a high demagnetization energy since the magnetization vector points out of the thin film. For a Bloch wall, the rotation of the magnetization is parallel to the wall surfaces. An alternative configuration, is shown in Fig. 19.20 (b). Here the magnetization vector rotates in the film, thereby minimizing the demagnetization energy. This type of wall is called a *Neel wall*. For a Neel wall the rotation of the magnetization is normal to the wall surfaces.Typically

the Neel wall is present in films less than ~ 10 nm thick. For thicker films the Bloch wall may be present.

The demagnetization effects in domain walls has important implications for the stability of the domain wall as a function of the thickness of magnetic thin film samples. We consider these stability arguments next. The energies and widths of these walls has been reported by Middelhoek [Mid63]. For a 180° Bloch domain wall parallel to the easy direction, as is illustrated in Fig. 19.20 (a), the direction of magnetization within wall can be expressed as:

$$\theta(x) = \Big(\frac{\pi}{\delta_w}\Big)x \qquad -\frac{\delta_w}{2} < x < \frac{\delta_w}{2} \tag{19.38}$$

where δ_w is the thickness of domain wall and θ is the angle between the magnetization and a direction in the plane of the wall and perpendicular to the plane of the film.

When the thickness of specimens is comparable to the domain wall width, it is not correct to neglect demagnetization effects at intersections of the domain wall and the specimen surface. The importance of this for thin films was first noted by Neel. The lowest energy configuration is the Neel domain wall where the domain wall magnetization rotates from one domain direction to the next without leaving the plane of film. A 180° Bloch domain wall parallel to the easy direction is illustrated in Fig. 19.20 (b). In the Neel domain wall, the magnetization rotates about the axis perpendicular to the plane of film. Box 19.4 considers the energetics and the domain wall thickness for a Bloch and Neel wall.

Fig. 19.21 shows results of calculations of domain wall energies and widths for an $\mathrm{Fe_{40}Co_{40}Nb_4B_{13}Cu}$ nanocomposite alloy. For these calculations, the magnetocrystalline anisotropy energy density is taken as 1 $\frac{J}{m^3}$, the exchange stiffness is 2×10^{11} $\frac{J}{m}$ and the experimentally determined magnetization is 1.088×10^6 $\frac{A}{m}$ Fig. 19.21 (b) shows that when the film thickness is less than 36 nm, the wall energy of Bloch wall is higher than that of Neel wall. Therefore the Neel type domain wall is energetically favored in the thinnest films. The wall width is roughly 28-40 nm in Bloch walls when the film thickness is larger than ~ 36 nm [LMU$^+$08].

19.1.10 Magnetostatic Energy.

To evaluate the magnetostatic energy (stray field energy) it is easier to use spheres, as their demagnetization factor is well known and does not vary with size. Fig. 19.22 shows how the stray field differs between a particle with one domain and one with two domains. The magnetostatic energy in the single domain spherical particle is given as:

$$^1E_{MS} = \frac{2}{9}\mu_0 M_s^2 \pi R^3 \tag{19.39}$$

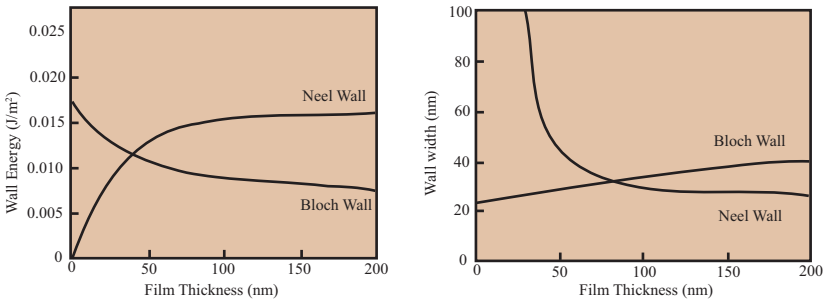

Fig. 19.21. Domain wall calculations: (a) wall energy of a Bloch and Neel wall as a function thickness and (b) domain wall width for an $Fe_{40}Co_{40}Nb_4B_{13}Cu$ nanocomposite alloy.

The magnetostatic energy for the two domain sphere is estimated to be one half that of the single domain particle; hence its total energy is :

$$^2E_{MS} + \gamma\pi R^2 = \frac{1}{9}\mu_0 M_s^2 \pi R^3 + \gamma\pi R^2 \tag{19.40}$$

The *single domain particle size* is the size of the largest particle that can remain single domain, and also known as the *monodomain size*

The single domain particle size is seen to be:

$$R_{SD} = \frac{9\gamma}{\mu_0 M_s^2} = \frac{36\mu_0\sqrt{(AK_1)}}{\mu_0^2 M_s^2} \tag{19.41}$$

Using typical values for these parameters this size is 6 nm for Fe and 16 nm for Ni. Box 19.5 calculates the single domain size for crystalline Fe.

19.1.11 Other Length Scales in Ferromagnets.

19.1.11.1 Equilibrium Size of Domains.

The equilibrium size of domains in a sample depends on among other variables the size of the sample. The relation is given as:

$$D_{eq} = \frac{\sqrt{(\gamma_w L)}}{M_s} \tag{19.42}$$

Where L is a size of the sample. As L decreases the equilibrium domain size decreases but not as rapidly. Eventually a size is reached where there should only be one domain in the particle. This the single domain particle size, R_{SD}.

For Fe, the magnetic domain size in a sample of $L = 10^{-2}$ m is of the order of 5×10^{-6} m or about 5 μm. Since the wall energy depends on K_1 it can be seen

Box 19.4 Calculation the domain wall thickness for a Bloch and Neel walls.

The exchange energy can be expressed as:

$$E_{ex} = A\Big(\frac{d\theta}{dx}\Big) = A\Big(\frac{\pi}{\delta_w}\Big)^2$$

where A is the exchange stiffness. The mean anisotropy energy in the wall is written as:

$$E_K = \frac{1}{\delta_w}\int_{-\frac{\delta_w}{2}}^{\frac{\delta_w}{2}} \delta_w K\cos^2\theta dx = \frac{K}{2}\delta_w$$

where K is the anisotropy constant. The demagnetization energy, is calculated assuming a wall volume approximated by a cylinder with an elliptical cross section, and expressed:

$$E_d = \frac{1}{2}\mu_0 H_d M_{wall} \quad H_d = -N_d M_{wall} \quad N_d = \frac{\delta_w}{\delta_w + D}$$

where H_d is the demagnetization field and M_{wall} is the average magnetization in the cylinder and D is the film thickness and:

$$E_d = \frac{\mu_0}{2}\frac{\delta_w}{\delta_w + D}M_{wall}^2 = \frac{\mu_0}{4}\frac{\delta_w}{\delta_w + D}M_s^2$$

where M_s is the saturation magnetization. The total wall energy density sums the exchange, anisotropy and demagnetization energy densities. Multiplying by the wall width:

$$\gamma = \Big(A\Big(\frac{\pi}{\delta_w}\Big)^2 + \frac{K}{2} + \frac{\mu_0\delta_w}{4(\delta_w + D)}M_s^2\Big)\delta_w = A\frac{\pi^2}{\delta_w} + \frac{K}{2}\delta_w + \frac{\mu_0\delta_w^2}{4(\delta_w + D)}M_s^2$$

as before energy is minimized with respect to the domain wall thickness to yield:

$$\frac{\partial\gamma}{\partial\delta_w} = 0 = -A\Big(\frac{\pi^2}{\delta_w^2}\Big) + \frac{K}{2} + \frac{\mu_0(\delta_w^2 + 2\delta_w)D}{4(\delta_w + D)^2}M_s^2$$

for a thick film, the 3rd term is neglected and the wall energy and wall width are:

$$\gamma_B = 0 = \sqrt{2\pi}\sqrt{AK} \quad \delta_w = \sqrt{2\pi}\sqrt{\frac{A}{K}}$$

The variation of magnetization angle for a Neel wall differs from a Bloch wall in the rotation direction. The total wall energy density is calculated without ignoring the demagnetization term and the expression and solved numerically for the Neel wall width.

that decreasing the magnetocrystalline anisotropy decreases the equilibrium size of a domain.

19.1.11.2 Ferromagnetic Exchange Length.

The ferromagnetic exchange length is the distance over which a perturbation in the spins of a material can be detected due to the changing (flipping) of a single spin. This

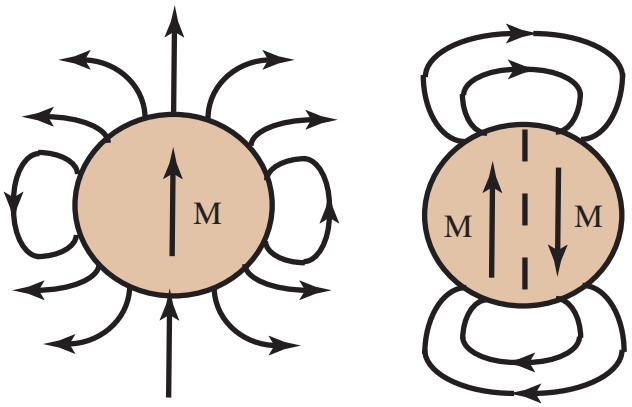

Fig. 19.22. Monodomain spherical particle (a) and break up into two domains to reduce the magnetostatic energy.

Box 19.5 Calculation of the single domain size for crystalline Fe.

The single domain size for crystalline Feis calculated:

$$R_{SD} = \frac{9\gamma}{\mu_0 M_s^2} = \frac{36\mu_0\sqrt{(AK_1)}}{\mu_0^2 M_s^2}$$

$$= \frac{36 \times (4\pi \times 10^{-7})\sqrt{((8.3 \times 10^{-12}) \times (5 \times 10^4))}}{(2.15T)^2} = 6nm$$

value is written as:

$$\Gamma_{ex} = \left(\frac{A_{ex}}{\mu_0 M_s^2}\right)^{\frac{1}{2}} \tag{19.43}$$

19.1.11.3 Magnetic hardness parameter.

The quotient of the ferromagnetic exchange length to the magnetic domain wall width divided by π is a parameter that is called the *magnetic hardness parameter*, κ. It is dimensionless and is given as:

$$\kappa = \left(\frac{K_1}{\mu_0 M_s^2}\right)^{\frac{1}{2}} \tag{19.44}$$

κ is a measure of the relative strengths of the magnetocrystalline anisotropy and magnetostatic energies. For $\kappa > 1$ the material is termed a *permanent magnet*. If $\kappa < 1$ the material is a *soft magnet*.

19.1.11.4 Superparamagnetic Particle Size.

Below a certain size, the thermal energy is greater than the anisotropy energy of a ferromagnetic particle, which causes the magnetization to be unstable in the particle with respect to thermally activated switching. This means that it can take on different orientations with time. The probability per unit time that M switches is given as:

$$P = f_0 \exp\left(\frac{\Delta f V}{k_B T}\right) \tag{19.45}$$

where f_0 is an attempt frequency on the order of 10^9 Hz. The value of Δf depends on whether there is strong shape or strong magnetocrystalline anisotropy. For the former, $\Delta f = \Delta N \mu_0 M_S^2$ and for the latter it equals the anisotropy constant, K_1.

It can be shown that the size of a particle with K_1 of $10^5 \frac{J}{m^3}$ that will prevent switching within one second is about 6 nm whereas the size of a particle with the same K_1 that will prevent switching for one year is about 7.5 nm.

These size particles are easily made, and current magnetic recording media are pushing the limits of superparamagnetism. It can be shown that if the anisotropy constant is raised to 3×10^6 the size of a particle that will prevent switching for one year is about 2.4 nm. The material FePt, with the $L1_0$ structure (Space Group P4/mmm, Pearson Symbol tP2) has this value of a magnetocrystalline anisotropy constant.

19.2 Magnetic Domains and the Magnetization Process.

There are two ways to magnetize a polydomain ferromagnetic material, namely *domain wall displacement* or *rotation of the magnetization vector*. Consider the process as shown schematically in Fig. 19.23.

Considering Fig. 19.23, if the applied field, H, is directed at an arbitrary angle with respect to the magnetization, as shown in (b), for small H magnetic wall displacement occurs. As H increases, the fraction of the domains with M pointing up increases until in (c) only a single domain exists. Going from (d) to (e) occurs by M rotating toward H until saturation at (f). The application of the field H does not change the direction of M anymore but it does increase the magnitude of M until it reaches the value of its saturation at 0 K,. This process, in which the entropy due to finite temperature is overcome by the magnetic field is called the *paraprocess*.

Now consider what happens if H is applied perpendicular to the easy axis. There is no force available to move the magnetic domain wall since it is perpendicular to the field. Thus rotation of the moments occurs from the start and the response as shown in Fig. 19.23 (g). The magnetocrystalline anisotropy tends to keep M_s aligned in the c direction but interaction with H tends to turn M toward H. The total energy is:

$$E = K_1 \sin^2\theta - HM\sin\theta \tag{19.46}$$

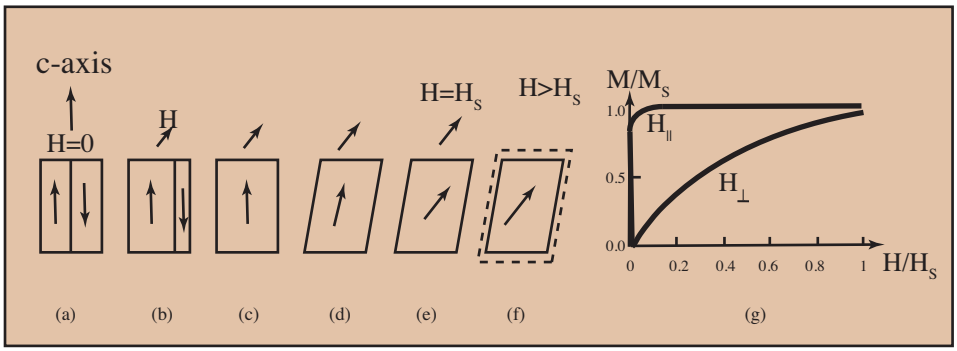

Fig. 19.23. Steps in the magnetization process (a) virgin state, (b) wall motion, (c) monodomain, (d) rotation, (e) saturation and application of a field exceeding that required to saturate.

where θ is measured from the c-axis. To determine the equilibrium configuration, we take the first derivative and obtain:

$$\frac{\partial E}{\partial \theta} = 2K_1 \sin\theta\cos\theta - HM\cos\theta = 0 \quad \sin\theta = \frac{HM}{2K_1} \tag{19.47}$$

The susceptibility in the direction H perpendicular to c equals the component of M along H divided by the magnitude of H, that is:

$$\chi_\perp = \frac{M_s \sin\theta}{H} = \frac{M_s^2}{2K_1} \tag{19.48}$$

At saturation $\theta = 90^0$ and $\sin\theta = 1$. This occurs when:

$$H = H_K = \frac{2K_1}{M_s} \quad H = H_K + \frac{4K_2}{M_s} \tag{19.49}$$

where H_K is called the anisotropy field of the material, the first expression is 1st order (when $K_2 = 0$) the second includes a non-zero K_2.

19.2.1 Frequency Dependent Switching of Magnetic Materials.

19.2.1.1 Bulk Materials.

When a magnetic material is cycled, the area of the hysteresis loop transversed corresponds to the energy loss and consequent heat generated during this cycling process. These energy losses are referred to as *core losses* and are generated due to irreversible magnetization processes occurring in the material. The core losses tend to increase

significantly with increased cycling frequency and maximum saturation induction according to the *Steinmetz equation* [Ste84]:

$$P_{tot} = C f^{\alpha} B_m^{\beta} \tag{19.50}$$

where P_c are the total core losses per unit volume or mass, C is a constant, α and β are called *Steinmetz coefficients*, f is the cycling frequency, and B_m is the maximum induction during magnetic cycling. While these coefficients are material and geometry dependent, typical values are $\alpha \sim 2$ and $\beta \sim 1 - 2$.

Since soft magnetic materials are used in alternating current circuits, the dynamic response as a function of frequency is very important. This response is dictated by magnetic loss mechanism. The total power loss, P_{tot} can be partitioned:

$$P_{tot} = P_h + P_{ec} + P_{an} \tag{19.51}$$

which is the sum of hysteresis, P_h, classical *eddy current* P_{ec}, and excess or anomalous eddy current loss, P_{ec} components. Loss separation is a useful way to analyze each loss term as if they were independent each other. The static part of loss represents that determined by the quasi-static hysteresis loop at a given maximum induction and varies linearly with frequency. Classical eddy current losses depend on the electrical resistivity, sample geometry and dimensions compared to the *skin depth* for EM radiation. These losses increase with the square of frequency. For clockwise eddy currents in a monodomain cylinder uniformly magnetized along the $\pm$z-axis:

$$P_{ec} \sim \frac{(\mu_0 M_0)^2 R^2}{8\rho} f^2 \tag{19.52}$$

where M_0 is the magnetization, R the radius, ρ the resistivity and f, frequency of switching. It can then be seen that eddy currents become increasingly important at higher frequencies and can be mitigated by control of magnet dimension (R) and the material's resistivity. The magnetization is typically required to be large.

Anomalous eddy currents associated with domain walls give rise to losses which increase at a power of frequency that is greater than 2. Ultimately, in a material in which all sources of losses have been minimized, losses will occur at a frequency of an RF magnetic field that corresponding to the precession of atomic dipole moments about a static magnetic field, the *ferromagnetic resonance, FMR* frequency.

19.2.1.2 Relaxation Processes in Magnetic Fluids.

Ferrofluids are colloidal suspensions of magnetic nanoparticles (MNPs) in liquids that have properties important to applications discussed below. Particles in a ferrofluid have a magnetization aligned along the EMD. Dipole moments align in direction of applied field, either by the rotation of the magnetization vector out of the EMD or by the rotation of the particle with the magnetization remaining fixed along the EMD.

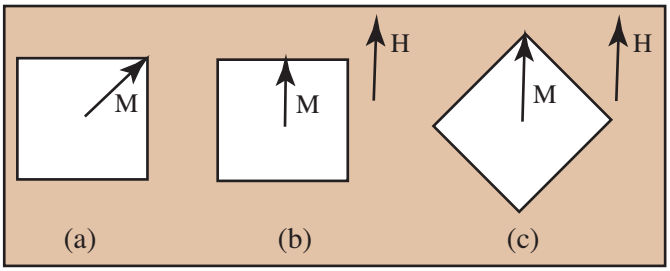

Fig. 19.24. 2-d square nanoparticle with a $[11]$ EMD (a) $H = 0$ equilibrium configuration, (b) Neel rotation of $\vec{M}$ against anisotropy and (c) Brownian rotation with $\vec{M}$ along the EMD.

The magnetization decay with time after field removal occurs by either a *Neel process* associated with magnetization rotation or a *Brownian process* associated with particle rotation. Fig. 19.24 illustrates these processes for a hypothetical 2-dimensional nanoparticle. Both processes have particle size dependent relaxation times: τ_N and τ_B.

For many applications Brownian relaxation controls heat transfer from monodomain MNPs, excited by a time-varying magnetic field. This heat is transferred to the liquid by rotational processes. Of interest is the power dissipation in a ferrofluid. The response to an AC field can be expressed as:

$$B = B_0 \exp(i[\omega t - \delta]) \qquad M = M_0 \exp(i[\omega t + \delta]) \tag{19.53a}$$

where field quantities are collinear scalar quantities and the response functions B and M lag the stimulus H by a phase angle, δ due to dissipative losses in the material. The magnetic permeability and susceptibility in SI units are:

$$\mu = \frac{B}{H} = \frac{B_0}{H_0} \exp(i\delta) = \mu_{DC} \exp(i\delta) \quad \chi = \frac{M}{H} = \frac{M_0}{H_0} \exp(i\delta) = \chi_0 \exp(i\delta) \tag{19.53b}$$

The complex permeability or susceptibility is depicted in an *Argand diagram*. Fig. 19.25 illustrates the complex permeability in an Argand diagram. The complex permeability is:

$$\mu = \mu' + i\mu'' \qquad \mu' = \mu_{DC} \cos(\delta) \qquad \mu'' = \mu_{DC} \sin(\delta) \tag{19.53c}$$

Similarly the susceptibility is expressed as:

$$\chi = \chi' + i\chi'' \qquad \chi' = \chi_0 \cos(\delta) \qquad \chi'' = \chi_0 \sin(\delta) \tag{19.53d}$$

We define a *loss tangent*, $\tan\delta$ and *quality factor*, Q as:

$$\tan\delta = \frac{\mu''}{\mu'} = \frac{\chi''}{\chi'} \qquad Q = \frac{1}{\tan\delta} \tag{19.53e}$$

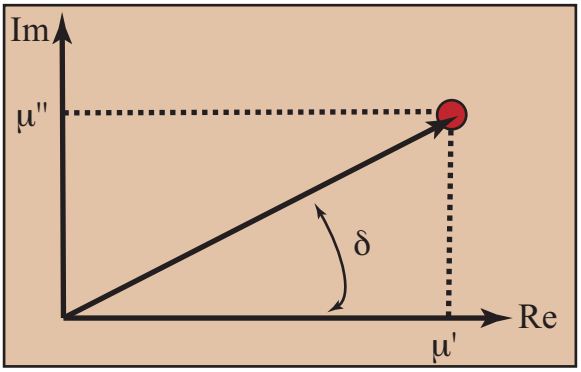

Fig. 19.25. Argand diagram of the complex permeability.

When the magnetization is switched, it relaxes on a time scale called the *magnetic relaxation time*, τ. This is determined by dissipative processes that occur in switching. For an equilibrium DC magnetization, $M_0 = \chi_0 H_0$ and time dependent magnetization $M(t) = M_0 \exp(i[\omega t - \delta])$, with an equilibrium susceptibility, χ_0 the relaxation of the magnetization the first order relaxation of the magnetization is:

$$\frac{\partial M(t)}{\partial t} = \frac{1}{\tau}\Big(M_0(t) - M(t)\Big) \tag{19.54a}$$

Substituting M_0 and $M(t)$ into this partial differential equation yields:

$$i\omega M_0(i[\omega t + \delta]) = \frac{1}{\tau}\Big(M_0 - M_0 \exp(i[\omega t + \delta])\Big) \tag{19.54b}$$

from which we can arrive at:

$$\chi = \frac{\chi_0}{1 + i\omega\tau} = \frac{\chi_0(1 - i\omega\tau)}{1 + (\omega\tau)^2} \tag{19.54c}$$

where:

$$\chi' = Re[\chi] = \frac{\chi_0}{1 + (\omega\tau)^2} \qquad \chi'' = Im[\chi] = -\chi_0 \frac{\omega\tau}{1 + (\omega\tau)^2} \tag{19.54d}$$

The preceding relationships are *Kramers-Kronig relationships* [Kra27] [Kro]. At $\omega = 0$, the real component of the susceptibility reduces to the DC value χ_0 and the imaginary component is zero. The imaginary component reflects frequency dependent losses.

The differential form of the the first law of thermodynamic (conservation of energy) is:

$$dU' = \delta q' - \delta w' \tag{19.55a}$$

where dU' is the differential internal energy, $\delta q' =$ heat absorbed by the system and $\delta w' =$ work done by the system. For an adiabatic process ($\delta q' = 0$) and for work done $\delta w' = -\vec{H} \cdot d\vec{B} = HdB$, where the last scalar expression derives from the assumption of collinear fields H and B. In SI units, ignoring work done on the vacuum:

$$\Delta U' = -\mu_0 \oint MdH \tag{19.55b}$$

and for excitation by a time varying magnetic field, the power dissipation is given by:

$$P = f\Delta U' = -\mu_0 f \oint MdH \tag{19.55c}$$

Consider an alternating magnetic field of the form $H = H_0 \exp(i\omega t)$. We are concerned with the real part of this complex function which is:

$$H(t) = Re[H_0 \exp(i\omega t)] = H_0 \cos(\omega t)] \tag{19.56a}$$

where H_0 is the field amplitude and $f = \frac{\omega}{2\pi}$ is the frequency of the field. Since the magnetization is $M = \chi H$ the time variation of the magnetization is:

$$M(t) = Re[\chi H_0 \exp(i\omega t)] = H_0\Big(\chi' \cos(\omega t) + \chi'' \sin(\omega t)\Big) \tag{19.56b}$$

where χ' and χ'' are the in- and out of phase components of the susceptibility. The adiabatic change in internal energy for one cycle of the magnetization is:

$$\Delta U = -\mu_0 \oint MdH = 2\mu_0 H_0^2 \chi'' \int_0^{\frac{2\pi}{\omega}} \sin^2(\omega t)dt = \mu_0 \pi \chi'' H_0^2 \tag{19.56c}$$

and the power loss is:

$$P = \mu_0 \pi \chi'' f H_0^2 \tag{19.56d}$$

In general, relaxation processes have time constants which can be expressed as:

$$\tau = \tau_0 \exp\left(\frac{-E_A}{k_B T}\right) \tag{19.57a}$$

where E_A is the activation energy barrier appropriate for the physical process equal to the product of an energy density and material volume. The denominator expresses the thermal energy. For rotation of MNPs in the fluid, the *Brownian time constant* is:

$$\tau_B = \frac{3\eta V_H}{k_B T} \tag{19.57b}$$

where η is the fluid viscosity containing the MNPs and the associated volume, V_H is:

$$V_H = \Big(1 + (\frac{\delta}{R})^3\Big)V_M \qquad V_M = \frac{4}{3}\pi R^3 \tag{19.57c}$$

with R the MNP radius and volumeV_M, and δ an incremental surfactant radius.

The Neel time constant energy barrier is the *magnetic anisotropy energy density, K* which determines the easy direction of magnetization (EMD). We define a constant, Γ as the ratio of KV_M to the thermal energy:

$$\Gamma = \frac{KV_M}{k_B T} \tag{19.58a}$$

For rotation of the magnetization out of the EMD, the *Neel time constant* is:

$$\tau_N = \frac{\sqrt{\pi}}{2}\tau_0 \frac{\exp\Gamma}{\Gamma^{\frac{1}{2}}} = \frac{\sqrt{\pi}}{2}\tau_D \frac{\exp\Gamma}{\Gamma^{\frac{3}{2}}} \qquad \tau_D = \Gamma\tau_0 \tag{19.58b}$$

Materials properties that tune the relaxation and therefore dissipation in the ferrofluid are fluid viscosity for the Brownian relaxation and magnetic anisotropy for Neel relaxation. In both cases, a particle volume is a parameter. Parallel Brownian and Neel relaxation processes have an effective relaxation time:

$$\frac{1}{\tau} = \frac{1}{\tau_B} + \frac{1}{\tau_N} \tag{19.58c}$$

if the ferrofluid can be made of monodisperse particles, then the size can be chosen so that relaxation is dominated by the dissipative Brownian motion. The power dissipation for this Brownian motion is given by:

$$P = \pi\mu_0\chi_0 H_0^2 f \frac{2\pi f\tau}{1+(2\pi f\tau)^2} \tag{19.59a}$$

H_0 and χ_0 are experimentally chosen parameters as is the RF frequency of the exciting field. To quantify the power loss, we need a reasonable estimate of initial susceptibility χ_0. For monodomain, superparamagnetic MNPs it obeys the *Langevin relationship*:

$$\chi_0 = \chi_i \frac{3}{\xi}\Big(\coth\xi - \frac{1}{\xi}\Big) \quad \xi = \frac{\mu_0 M_d H V_M}{k_B T} \quad M_d = \frac{M_s}{\phi} \tag{19.59b}$$

M_s is the saturation magnetization in the MNP and ϕ the volume fraction of the magnetic material in the ferrofluid. The initial susceptibility, χ_i is :

$$\chi_i = \frac{\mu_0\phi M_d^2 V_M}{3k_B T} \tag{19.59c}$$

Temperature rise is calculated from a volume average heat capacity of MNPs and fluid, c_p:

$$\Delta T = \frac{P\Delta t}{c_p} \tag{19.59d}$$

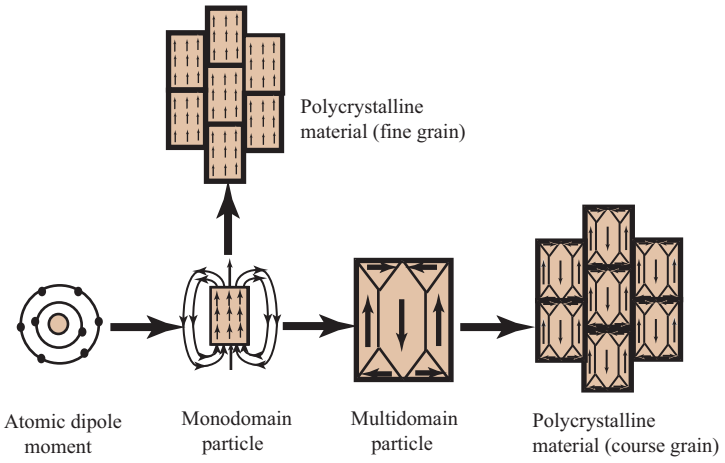

Fig. 19.26. Hierarchy of magnetic length scales.

19.2.2 The Hierarchy of Length Scales in a Magnetic Material.

Describing magnetization curves for a ferromagnet involves discussing equilibrium and non-equilibrium (reversible and irreversible) magnetization processes and several contributions to the magnetic energy density. Fig. 19.26, considers of magnetic dipoles on several different length scales. Collective magnetic phenomena considers the magnitude of the magnetic moments and their coupling with one another (i.e., the direction of the moments). This description is on the atomic scale of the atomic orbital and spin angular momentum and exchange interactions.

In ferromagnets, atomic dipole moments are parallel at 0 K. The next length scale of importance in describing a ferromagnetic material is that of magnetic domains. A magnetic domain is a macroscopic volume which might contain, $\sim 10^{15}$ atoms with magnetic moments aligned. Each domain is a tiny magnet with a dipole moment:

$$\mu = N\mu_{atom} \tag{19.60}$$

where N is the number of atoms in the domain. In a typical polycrystalline material with $\sim 100 - 1000\ \mu$m grains, individual grains will contain $\sim 10^5$ magnetic domains whose moments are randomly oriented in the virgin state. Between two adjacent domains individual atomic dipoles are viewed rotate from the orientation of the dipole moment in one domain to that of the other. The region over which this rotation occurs is called the *domain wall*. In our hierarchy of length scales we might take 1000 or more individual crystalline grains to form a polycrystalline aggregate in 1 cm^3 of material. The sizes chosen here are subject to variation with a variety of materials parameters but give a feel for the order of magnitude of the size of various entities.

Element	*Structure*	M_s *(290 K)* $(\frac{emu}{cm^3})$	M_s *(0 K)* $(\frac{emu}{cm^3})$	n_B (μ_B)	T_c *(K)*
Fe	*bcc*	1707	1740	2.22	1043
Co	*hcp, fcc*	1440	1446	1.72	1388
Ni	*fcc*	485	510	1.72	627
Gd	*hcp*	—	2060	7.63	292
Dy	*hcp*	—	2920	10.2	88

Table 19.3. *Structures, room temperature and 0 K saturation magnetizations and Curie temperatures for elemental ferromagnets [O'H87].*

19.3 Alloy Survey

We next survey important alloys systems with interesting soft and hard magnetic properties. We discuss (a) attractive intrinsic magnetic properties of the alloy system; (b) phase relations in the system; (c) synthesis and processing techniques to develop microstructures of interest for particular technical magnetic properties; and (d) performance issues in some prototypical applications. Table 19.3 summarizes structures, room temperature and 0 K saturation magnetizations and Curie temperatures for elemental ferromagnets [O'H00].

Fe, Co, Ni and Gd are the only elemental ferromagents at room temperature. Elemental Fe and Ni are cubic materials used as soft ferromagnets because of their high symmetry, relatively low values of *cubic magnetocrystalline anisotropy* and low magnetostriction coefficients. All of these can be improved upon by alloying as discussed below. Steels (Fe-C alloys) can serve as reasonably good hard magnetic materials as well if second phase impurities and grain size are controlled to increase *domain wall pinning*. Co has two allotropic forms, *fcc* α-Co, and *hcp* ϵ-Co. α-Co is a relatively soft magnetic material. ϵ-Co has *uniaxial magnetocrystalline anisotropy* with a c-axis *easy direction of magnetization, EMD* making it a hard magnetic material. Both hard and soft Fe were developed early as magnetic materials because of the natural abundance and consequent low cost of Fe and the importance of the mechanical properties of steels in many applications. Fe has $\langle 100 \rangle$ EMDs and Ni has $\langle 111 \rangle$ EMDs.

Gd is also a hexagonal material with uniaxial magnetocrystalline anisotropy. It has an $[0001]$ EMD. It is the only rare earth which is ferromagnetic at room temperature. Because its Curie temperature is close to room temperature, its alloys are widely investigated for magnetocaloric applications as discussed below. Dy is another example of an *hcp* ferromagnet but with a Curie temperature well below room temperature.

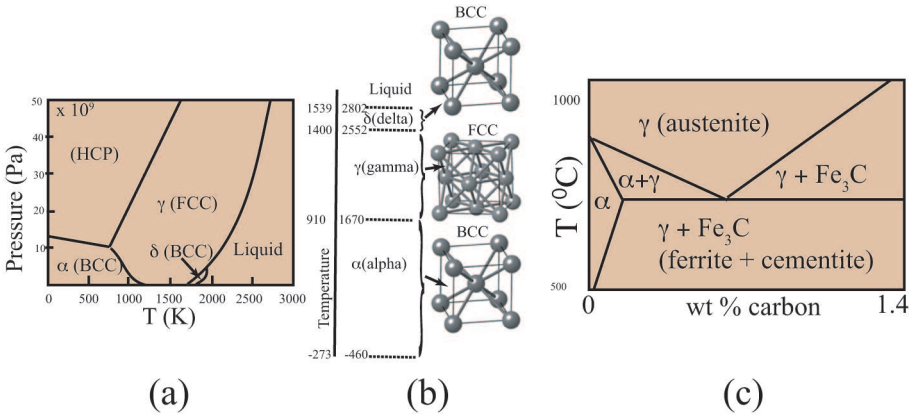

Fig. 19.27. (a) P-T phase diagram for Fe [Din91] and (b) crystal structures at atmospheric pressure [GW74], (c) schematic of the Fe-C eutectoid as a portion of the Fe-C phase diagram.

19.3.1 Fe *and Steels Structure, Properties, and Applications.*

19.3.1.1 Phase Diagram and Physical Properties Survey for Fe

Understanding structure properties relationships in Fe for magnetic applications requires a knowledge of both thermal and physical properties of Fe. We also need to know the phase transformation temperatures and details of the binary phase diagrams of elemental Fe and other alloying additions, e.g. the FeC phase diagram (Fig. 19.27).

Fig. 19.27(a) shows the unary phase diagram for elemental Fe to have several important allotropes (or polymorphs). Allotropes are named with successive letters in the Greek alphabet, e.g. α, β, γ, $\delta \ldots$ Notice that there is no β-iron on the diagram. Before about 1922 the paramagnetic *bcc* iron that formed above the Curie temperature of ferromagnetic *bcc* iron was identified as the β-phase. However, since it was believed that there was no change in the crystal structure after the ferromagnetic magnetic iron transformed to paramagnetic iron, it was concluded that the α to β transformation was not a phase change. Implicit was a definition of phase that only included structure and composition. But paramagnetic *bcc*-Fe is a different phase than ferromagnetic α-Fe since it has different properties and symmetry. See below and T. B. Massalski and D. E. Laughlin [ML09] from which the following discussion is derived.

Fig. 19.27(b) summarizes crystal structures of elemental Fe at atmospheric pressure (this figure ignores the magnetic symmetry). The γ-phase of iron and steels is called *austenite*. Austenite is a high temperature phase and has a *fcc* [close packed] structure. The α-phase is called *ferrite*. Ferrite is a common constituent in steels and has a *bcc* structure (less densely packed than *fcc*). Table 19.4 gives a summary of thermal and physical properties of Fe including phase transformation temperatures [Boz93].

Property	Value
Density, $\rho(\frac{g}{cm^3})$ at 293 K	7.874
Thermal expansion coefficient $\times 10^6$ at 293 K	11.7
Lattice constant, a_0 (nm)	0.2861
Melting Point, T_m, (°C)	1539
$\alpha \rightarrow \gamma$ transition temperature, $T_{\alpha\rightarrow\gamma}$, ($A_3$) on heating (°C)	910
$\gamma \rightarrow \delta$ transition temperature, $T_{\alpha\rightarrow\gamma}$, ($A_4$) on cooling (°C)	1400

Table 19.4. *Selected thermal and physical properties of bcc* Fe *including phase transformation temperatures [Boz93].*

Allotropic transformations in Iron are examples of additional contributions to structure stability from magnetic transitions that can bring about phase changes in a unary system. The temperature/pressure phase diagram for iron indicates that the stable phase, at ambient temperatures and pressures, is the α iron. It has the *bcc* structure and remains stable up to about 910 °C (1183K). On heating above 910 °C, α iron transforms to the *fcc* γ iron, but it reverts again to *bcc*(δ) at 1140 °C. The δ phase is thus a continuation of the α phase in the sequence $\alpha \rightarrow \gamma \rightarrow \delta \rightarrow liquid$. Application of pressure changes the temperatures of these transitions (which can be calculated using the Clapeyron equation). A substantial pressure also makes possible another structure modification, to the *hcp* ϵ-form of Fe, above approximately 15.2 MPa ($\sim$110K bar).

The trends with temperature at ambient pressure of the closest interatomic distances (d) and volumes per atom (Ω) are shown in Fig. 19.28 (a) [BM80]. The d values in the close-packed *fcc* structure are larger than in the *bcc*, but comparable Ω values are slightly smaller. Hence, the *bcc* is more open and allows for more vibrational choices, making the vibrational entropy larger in the *bcc* than in the *fcc* phase. The fact that volume per atom differences between the two structures are quite small indicates that the total energies are similar, and confirms that the bonding between atoms in the two different crystal structures of iron remains essentially metallic.

Several interesting questions about the allotropic changes in Fe include:

(i) Why is the *bcc* form stable at low temperatures? Usually, a close packed allotrope (e.g. *fcc* or *hcp*) is stable at low temperatures because enthalpy is generally lowered by close-packing.

(ii) Why does the bcc phase transform to the close-packed *fcc* phase on heating? This seems backwards because usually on heating a more open, and therefore higher entropy phase, is observed to form at elevated temperatures.

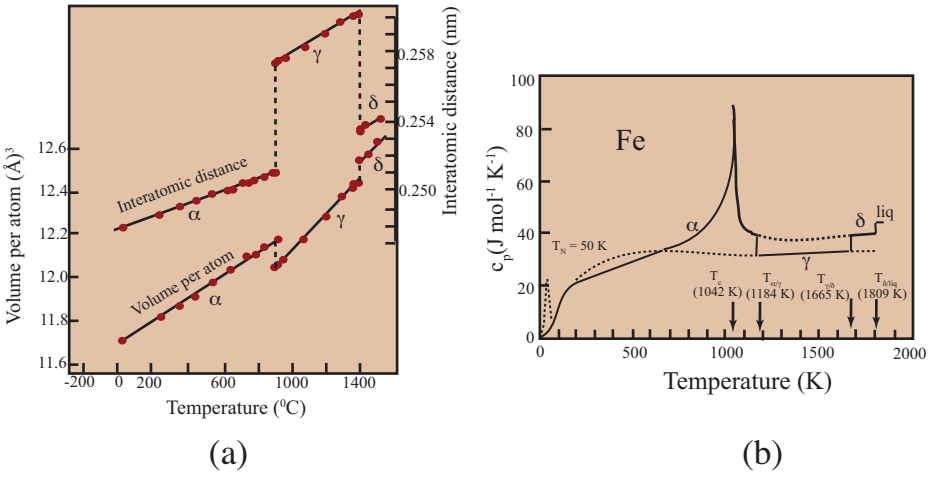

Fig. 19.28. (a) Atomic volumes and lattice spacings and (b) heat capacity as a function of temperature for elemental solid Fe [BM80]

(iii) When the *fcc* γ reverts to the *bcc* δ at even higher temperatures, what is the cause of this? Is the large vibrational entropy of the *bcc* δ the only factor?

(iv) Why is there no β phase in the sequence?

In answering the last question we note that currently both the paramagnetic and ferromagnetic states of *bcc* iron are most commonly designated by the same Greek letter α. However, strictly speaking, it can be argued that the ferromagnetic to paramagnetic transition ($\alpha \rightarrow \beta$) is a phase change because because a symmetry change accompanies the magnetic change. This is so, because the ferromagnetic form is not truly cubic because of its magnetic symmetry; see Fig. 19.29 (a). Considerations of magnetism also explain the free energy vs. temperature curves of Fig. 19.29 (b) discussed below.

The loss of ferromagnetism on heating takes place by what is called a higher order transition, which occurs over a range of temperatures from 600K to nearly 1200K , as can be seen from the large peak in the specific heat curve for α-iron corresponding to the magnetic disordering in Fig. 19.28 (b). The temperature associated with the highest point of the peak corresponds to the largest number of the magnetic moments becoming random (or becoming aligned on cooling) and is designated as the Curie temperature,T_{Curie} ($\sim$1042K (769 °C)). This magnetic transition, and the accompanying increase in entropy contributes to the reappearance of the *bcc* form of Fe at higher temperatures (δ).

The *fcc* γ-phase undergoes a magnetic change below about 50 K, namely a antiferromagnetic transition. The temperature of this transition is called the *Neel tempera-*

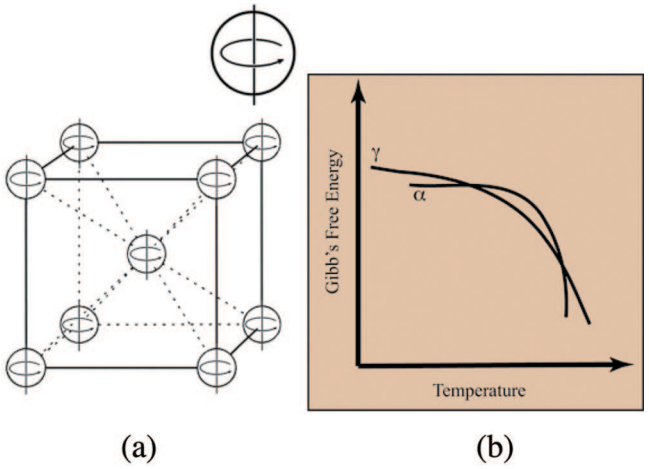

Fig. 19.29. (a) A *bcc* arrangement of atoms with $[001]$ oriented magnetization, showing that its symmetry is I4/mmm. [LWM00]; (b) G(T) curves for α and γ Fe

ture, T_N. In antiferromagnetically (AF) ordered materials, the atomic dipoles become aligned in opposite directions with respect to neighboring spins. This has been demonstrated in micron-size metastable γ-iron particles embedded in Cu which remain *fcc* on cooling. In an antiferromagnetic arrangement the opposite magnetic moments cancel with the overall magnetization equal to zero. However, this antiferromagnetic arrangement contributes to the structure energy, and heat is needed to remove it. The transition is indicated by the small peak in the curve for the γ-phase in Fig. 19.28 (b). This figure shows the trends for both the *fcc* and *bcc* Fe phases, with extrapolations into metastable regions (shown by dashed lines), which seem quite reasonable. Both magnetic states stabilize the respective crystal structures at low temperatures.

Question 1 can be addressed as follows. At 0K, the ferromagnetic ordering in the *bcc* α phase causes the internal energy (and enthalpy) to be lower than the internal energy (and enthalpy) of the antiferromagnetic (and paramagnetic) fcc phase. This is so because the large exchange energy of the aligned magnetic moments of the ferromagnetic *bcc* iron greatly reduces its internal energy. Thus, even though the ferromagnetic *bcc* iron is less close-packed than *fcc* γ, it is the equilibrium phase at low temperatures.

The answers to questions 2 and 3 are more complex and involve the influence of entropy of each of the phases, as well as their internal energies. Here, we need to consider the behavior of the specific heats with temperature for the α and γ phases in more detail (see Fig. 19.28 (b)). Both curves show a peak corresponding to a magnetic transition. We consider two aspects of the entropy of the α and γ phases, namely their vibrational entropy and their magnetic spin entropy. The vibrational entropy usually is

larger for *bcc* structures than for *fcc* structures because the atoms vibrate with a higher frequency in the more close packed structures. This is the reason that *bcc* structures are usually more stable than *fcc* ones at the high temperatures. In the case of Fe, we must also take into account the entropy due to the disordering of the spins.

The low temperature antiferromagnetic to paramagnetic transition in γ-Fe increases its configurational spin entropy to the extent that the overall entropy for the close packed γ phase becomes greater than that of the more loosely packed ferromagnetic α phase. This excess entropy (due to the disordering of the magnetic spins at the Neel temperature) is the cause of the appearance of the γ phase at higher temperatures, as can be seen considering the following for the γ phase:

$$G^{\gamma} = H_0^{\gamma} + \int_0^T C_p dT - T \int_0^T \frac{C_p}{T} dt \tag{19.61}$$

From this equation and Fig. 19.28(b),we conclude that the TS term eventually causes the γ phase to have a lower Gibbs Energy at higher temperatures, since this term continues to decrease as the temperature increases. Hence the *fcc* phase replaces the *bcc* one at about 910 °, that is the $\alpha \rightarrow \gamma$ structural transformations occurs (or better $\beta \rightarrow \gamma$). This *bcc* to *fcc* transformation on heating is opposite to the more usual *fcc* to *bcc* one, because, in the case of iron, it is the entropy due to the spin disordering that determines the equilibrium phase, not the vibrational entropy term.

Fig. 19.29 (b) shows free energy versus temperature curves of these transformations. At 910 °C the G_γ curve crosses below the G_α curve, producing a phase change. However, the excess specific heat of the α phase in the vicinity of T_c makes the α-phase TS term important and, thus, the G_α curve re-crosses the G_γ at 1400 °C. The large entropy due to the randomizing of the spins in the α phase along with its larger vibrational entropy allows the *bcc* phase to reappear, this time labeled as the δ phase.

If the ferromagnetic to paramagnetic transition of the α phase were slightly lower in temperature, its large negative TS term would stabilize the α- relative to the γ-phase and *fcc* iron might never form at elevated temperatures. Also, although the exact form of the c_p trends at very low temperatures has not been determined experimentally, it can be argued that if γ-Fe were not AF at the very low temperatures, it might never be stable enough to form as the higher temperature phase because ferromagnetic *bcc*-Fe has low enthalpy and paramagnetic *bcc*-Fe has higher entropy. This demonstrates the importance of magnetic transformations in iron in determining the equilibrium phase stability. If the antiferromagnetic Neel transition temperature in γ iron were higher, or if the ferromagnetic to paramagnetic T_c in α iron were a little lower, *fcc* iron would never be a stable phase! In terms of Fig. 19.29, the G_α curve may shift to the left, making the *bcc* structure stable at all temperatures.

19.3.1.2 Fe *Properties and Performance*

The magnetic softness of Fe is related to the purity of Fe. For very pure, $\langle 100 \rangle$ oriented single crystals of Fe magnetic permeabilties of 10^6 have been attained in the laboratory. Typical commercial alloys have permeabilities less that 10^4, though this can be increased to 10^5 by annealing in vacuum or hydrogen. Such annealing serves to remove most of the C,S,N and O impurities in Fe. These elements are relatively insoluble in solid Fe but form second phase carbides, sulfides, nitrides and oxides, respectively, which can act as impediments to the motion of magnetic domain walls.

Prototypical soft Fe has a saturation induction, $B_s = 2.1$T, a cubic magnetocrystalline anisotropy energy density, $K_1 = 4.8 \times 10^4 \frac{J}{m}$ and a magnetostriction coefficient, $\lambda_{111} \sim -20 \times 10^{-6}$ (20 ppm). Coercivities of ~ 1 Oe are achievable in commercially rolled Fe. A typical commercial alloy is Armco iron which is Fe sheet rolled from ingot with typical impurity levels of 0.014 wt % C, 0.007 wt % N, 0.15 wt % O, 0.003 wt % Si, 0.005 wt % P, 0.025 wt % S, 0.03 wt % Mn, and 0.003 wt % Al. The biggest disadvantages of soft Fe for many applications is that it is also mechanically soft and has low electrical resistivity. The latter makes it unattractive for high frequency applications for which eddy current losses are prohibitive. Mechanical strength can be improved by reducing the grain size but at a cost of coercivity because of consequent grain boundary pinning of domain walls.

Understanding domain wall pinning is fundamental to understanding coercivity in soft Fe The *Herzer curve*, which will be discussed in the context of amorphous and nanocomposite materials below, shows the important relationship between the coercivity and the grain size of crystalline magnetic material. Notable for understanding alloy development in soft magnetic Fe is the $\frac{1}{D_g}$ dependence of the coercivity on D_g at large grain sizes. Box 19.6 develops a relationship between pinning and grain diameter for large grained materials.

Box 19.6 Pinning of domain walls by grain boundaries.

A domain wall can be viewed as a planar defect with an energy per unit area, γ_{wall} and a thickness, δ w. It will be ideally pinned by a grain boundary of similar thickness, δg. If $\delta g > \delta w$ then the pinning force, $f_p \sim \frac{\delta w}{\delta g}$. The coercivity, H_c of the material will be proportional to the summed pinning force in a unit volume. This will depend linearly on grain boundary area per unit volume. For grains of diameter, D_g:

$$H_c \sim f_p \sim \frac{\delta w}{\delta g} \frac{4\pi \frac{D_g}{2}^2}{\frac{4}{3}\pi \frac{D_g}{2}^3} = \frac{\delta w}{\delta g} \frac{6}{D_g}$$

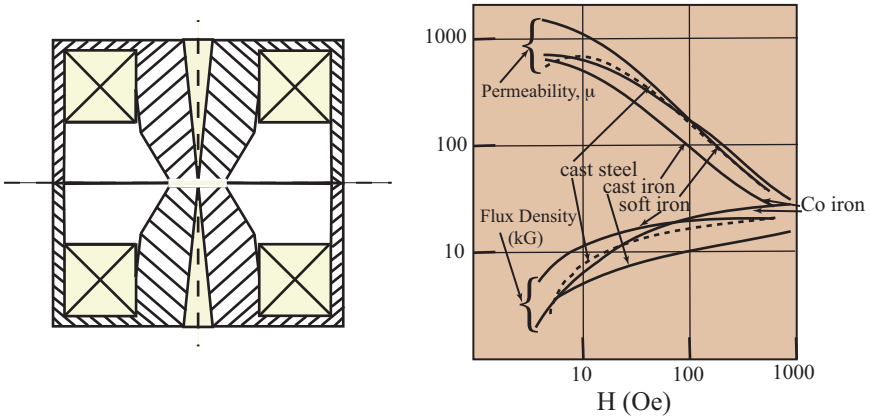

Fig. 19.30. (a) Schematic of a symmetrical objective lens of an electron microscope and (b) magnetic properties of commercial materials used for magnetic lens circuits [Rei82].

19.3.1.3 Materials Application: Soft Fe *for Magnetic Lenses.*

A magnetic lens consists of a coil of Cu or superconducting wires within Fe pole pieces. Current through the coils creates an exciting field in the bore of the pole pieces. Electrons (or other charge particles) are deflected by a *Lorentz force*:

$$\vec{F} = -e\left(\vec{v} \times \vec{B}\right) \tag{19.62}$$

where e is the electron charge and $\vec{v}$ is the electron velocity. Pole piece design is aimed at providing a rotationally symmetric magnetic field that is inhomogeneous in such a way that it is weak in the center of a gap and stronger close to the bore. This causes electrons close to the central axis of the lens to be less strongly deflected than those passing far from the axis, allowing a beam of parallel electrons to be focused into a spot. This requires that large magnetic fields and their distributions are confined to narrow regions comparable to the lens focal length. Electron lenses quality suffers from aberrations resulting from geometrical lens precision and inhomogeneous magnetic properties of pole materials. Aberrations limit the spatial resolution of an image in the image plane of a transmission electron microscope, e.g.

Magnetic lens design for electron microscopy depends on the operating mode of the lens. The fundamental operating modes in electron microscopy require *objective lens*, *projector lens* and *condenser lens*. Fig. 19.30 (a) shows a schematic of a symmetrical objective lens of an electron microscope. Rotationally symmetric magnetic fields can be used to focus electrons in a manner similar to how glass lenses focus light [Rei82].

The first design of objective lenses for electron microscopy [Bus26], [RR66] used high permeability pole pieces which were tapered to concentrate the magnetic flux in the working area of the lens. Fe-shrouded lenses are a commonly adopted magnetic lens.

Although details of the lens design can differ for different operating modes, the design invariably considers flux concentration at the lens working point, geometrical optical aberrations (which result from inhomogeneity in the flux distribution) and general concerns as to flux paths in the magnetic circuit as a whole. The components of a lens include the pole pieces systems with casing, the lens coil, stigmators, aperture alignment systems and exchange systems for control of vibrations and stray fields.

Electron optical design of a magnetic lens has the following considerations [Rei82]:

(i) Specifying the field which differs for objective, projector and condenser lenses.
(ii) Specifying focal length and acceptable values for geometrical aberrations.
(iii) Choice of *gap width, s*, and *bore diameter, D* and the number of *ampere-turns, NI* for the exciting field.
(iv) Design of the shape of the magnetic circuit to prevent saturation of the pole pieces and achieve tolerable stray fields.
(v) Provide alignment apertures, stigmators and beam deflection systems.
(vi) Design to avoid environmental disturbance including shielding AC stray fields and mechanical decoupling to avoid vibrations.

The issues of intended field, gap geometry, and shape of the magnetic circuit pose the most restrictions on the magnetic materials.

Ferromagnetic materials for lens components are chosen so that none of the materials in the magnetic circuit saturate and their relative permeabilities can be maintained at ~ 100. A characteristic parameter for the scaling of the magnetic circuit is $\frac{I}{\sqrt{V}}$ where I is the field generating current and V is the relativistically corrected beam voltage, the dispersion of which is related to the flux in the magnetic circuit. For an objective lens geometrical aberration results from spherical, chromatic and diffraction aberrations. The latter two of these depend on the fluctuations in V and therefore the uniformity of the field.

The choice of ferromagnetic materials for the magnetic circuit is quite important and distinctly different considerations are made for the *pole pieces* and the *lens core*. For the pole pieces, high saturation inductions are the primary consideration and therefore Co-Fe alloys such as *Permendur* are chosen as they provide maximum flux densities. For the lens core, where lower magnetizations and higher permeabilities are desirable soft Fe is chosen. Fig. 19.30 (b) shows the field dependence of the magnetic properties of some commercial materials used for magnetic lens circuits [Rei82]. Specification of the field dependence of the induction and permeability for fields less than saturating fields are required for magnetic circuit design. Predictable magnetic response is of paramount importance.

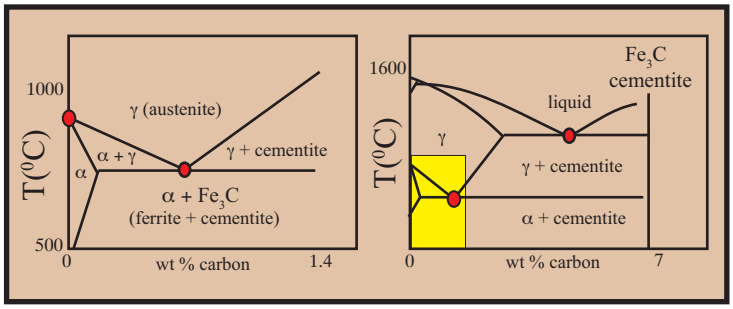

Fig. 19.31. (a) Portion of the Fe-C phase diagram relevant to processing low C and ultra-low C steels [CW86] and (b) Schematic I-T diagram illustrating the onset of various types of ferrite precipitation and (c) diagram of the dominant type of ferrite precipitation for various temperatures and compositions in the Fe-C system. GBA corresponds to grain boundary allotriomorphs, W corresponds to Widmanstatten side-plates and/or intergranular plates, and M corresponds to massive ferrite [PE00].

19.3.1.4 Steels

19.3.1.5 Phase Diagram the Binary Fe-C *System*

The Fe-C phase diagram is shown in Fig. 19.27(c) for compositions in the in the eutectoid portion of the phase diagram. If extended to 6.7 wt. % C (corresponding to 25 at. %) the intermetallic phase Fe_3C, called **cementite** is observed. Steels are restricted to C concentrations of up to 1.4 wt % and the portion of the Fe-C phase diagram pertaining to steels and technical or pure Fe is the simpler one illustrated in Fig. 19.27(c). Fe_3C is called *cementite* and has an orthorhombic crystal structure. Cementite is a magnetically hard phase. Carbides are magnetic hardening agents in technical Fe.

Fig. 19.31(a) shows the portion of the Fe-C phase diagram relevant to processing low C and ultra-low C steels [CW86]. The *maximum solubility, 0.0218 wt %* of C in α-Fe occurs at the *eutectoid transition temperature, 727 °C*. Typically low C and ultra-low C steels are kept to concentrations near or below this solubility limit so as to limit the amounts of second phase carbides in the steel. In the discussion of steel microstructures, it is important to define several other important metastable phases and phase mixtures which are observed in steel. The first, *pearlite*, is a two-phase, lamellar structure having alternating layers of ferrite (88 wt %) and cementite (12 %). Pearlite forms by a eutectoid reaction:

$$\gamma(\mathrm{Fe}) \rightarrow \alpha(\mathrm{Fe}) + \mathrm{Fe_3C} \tag{19.63}$$

when austenite is slowly cooled below 727 °C. In this reaction, austenite of *eutectoid*

composition, 0.77 wt % transforms to the 2-phase, equilibrium mixture where the alternating layers (lamellae) of α-ferrite and cementite grow cooperatively .

19.3.1.6 Phase Diagram and Physical Properties of Low C *Steels*

Low-carbon steels are FeC alloys for which the C concentration is kept to less than ~ 0.1 wt % so that the maximum C content lies close to or within the single phase α-ferrite (ferromagnetic, *bcc*) phase field at the eutectoid temperature (Fig. 19.27(c)). ASTM A848 is an example of an ultra-low-carbon steel ($\mathrm{C} <\sim 0.02$ wt %), where C content allows the eutectoid transformation to be completely avoided. Thus, the characteristic pearlite and bainite obtained in medium and high carbon steels are not typically observed in low-carbon steels used for magnetic applications. This choice minimizes non-magnetic second phases which is important from the standpoint of both induction and structure sensitive properties such as permeability and coercive force.

Alloying and impurity elements in low carbon steels have a variety of effects on the overall performance of the material. From the standpoint of technical magnetic properties, the nonmetallic elements which are present interstitially such as C, O, S, and N have the largest effect. Removal of such impurity atoms can result in higher permeabilities and reduced coercive force and several strategies for purifying the iron exist [CW86]. The allowable degree of purity is dictated primarily by the material requirements of the intended application. Compositional additives that can be used for controlling the magnetic aging behavior can be found in the discussion on magnetic aging below. Although impurity elements typically degrade the technical magnetic properties of freshly prepared (before magnetic aging) magnetic iron alloys, such impurities may be desirable in order to tailor the features of the microstructure for other design purposes. In particular, impurities or alloying elements such as Cr, Mo, and Mn can help to achieve a refined grain size due to a solute drag effect. The presence of P can result in improved machinability.

19.3.2 AlNiCo *Permanent Magnets: Precipitation and Spinodal Decomposition.*

Fe and subsequenty C steels were used as permanent magnets [Gil58]. Hardening mechanisms in C steels are largely associated with pinning of domain walls by carbide precipitates. W and Cr steels were developed in mid- to late 1800's. The 1917 development of Co steels [HS20] permanent magnets was followed by the discovery of AlNiCo permanent magnets [Mis31]. This major breakthrough realized the potential for refining microstructures through *spinodal decomposition*. Alloys near the composition $\mathrm{Fe_2NiAl}$ and alloys with Co substituted for Fe are called *Alnico magnets*. Alnico magnets still have significant markets today. $\mathrm{Fe_2NiAl}$ has a *pseudo-binary phase diagram* described in terms of a single composition variable as illustrated in Fig. 19.32. Alnico alloys typically contain $8-12\%$ Al, $15-26\%$ Ni, $5-24\%$

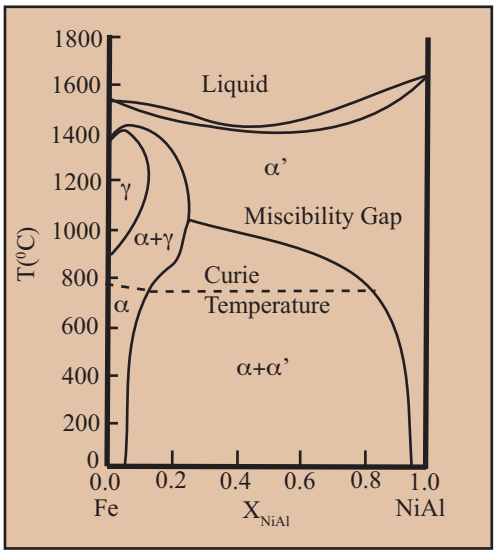

Fig. 19.32. Pseudobinary phase diagram for $\mathrm{Fe_2NiAl}$ [McC82]

Co, $< 6\%$ Cu, < 1 % Ti, with the remainder Fe. The low cost of raw materials makes these particularly economical permanent magnet materials. Alnico magnets can have remanent inductions as large as 1 T, coercivities as large as 2000 Oe and energy products as large as ~ 10 MGOe.

The pseudo-binary PD for Alnico exhibits a miscibility gap between the Fe and NiAl components. NiAl is a near stoichiometric compound due to strong Ni-Al bonds. Alloys below the maximum in the gap will decompose into an Fe-rich α and NiAl-rich α phase. The α phase has some Fe solubility to low temperature it therefore designates the low temperature NiAl-rich phase and the high temperature solution. This decomposition reaction can be written: $\alpha' = \alpha' + \alpha$ where it is implied that the new α' is of a different composition. Spinodals (not shown), from regular solution theory exist in a system that exhibits tendency to cluster (in this case into Fe and NiAl rich regions). The Ni and Al rich regions subsequently order to the B2 phase. This phase forms coherently with *bcc* Fe. The fine microstructures which can be developed by spinodal decomposition give rise to development of regions of monodomain Fe separated by regions providing excellent pinning by the weakly magnetic NiAl phase.

Permanent magnets require large *magnetic anisotropy* to develop significant H_c. In Alnico magnets, much of the anisotropy is derived from *shape anisotropy*, by controlling the free pole distribution of the high moment particles in the alloy. Alnico magnets are further drawn so that the high moment particles deform to take acicular

shapes from which significant shape anisotropy can be derived. Box 19.7 calculates typical values of the shape anisotropy [O'H00] for Fe in Alnico magnets. Spinodal decomposition and thermomechanical processing then allow Alnico magnets to take advantage of shape anisotropy effects originally used in Fe horseshoe magnets to retain hard magnetic properties. In this case it is the nanostructures which retain single domains.

Box 19.7 Calculation of Shape Anisotropy in Alnico Magnets.

Shape anisotropy in Alnico magnets derives from acicular particles of the high moment phase and the difference in demagnetization factors along long and short particle dimensions. The magnetostatic anisotropy energy density, E_{ms} can be calculated:

$$E_{ms} = \frac{\mu_0 \Delta N < M > \Delta M_s}{2}$$

for typical Alnico magnets $\mu_0 < M >\sim 2.1$ T for Fe particles. $\Delta N \sim 0.5 and \mu_0 \Delta M_s \sim 2.1$ T, considering the typical aspect ratios for the particles and differences in the saturation magnetizations of the particles and the NiAl matrix. Using these parameters a value of the magnetic anisotropy can be calculated:

$$K = E_{ms} = 1.1 \times 10^5 \frac{J}{m^3} = 1.1 \times 10^6 \frac{ergs}{cm^3}$$

It is instructive to estimate an upper bound for this anisotropy, if the even larger magnetization differences and particle aspect ratios were possible. For this we consider the case of FeCo particles in a non-magnetic matrix for which needle like particles with $\delta N = 1.0$ could be developed. For such materials, $\mu_0 < M >\sim 2.5$ T for FeCo particles and $\mu_0 \Delta M_s \sim 2.5$ T could be achieved in a non-magnetic matrix and:

$$K = E_{ms} = 2.5 \times 10^5 \frac{J}{m^3} = 2.5 \times 10^6 \frac{ergs}{cm^3}$$

19.3.3 Fe-Si *alloys.*

19.3.3.1 Si *steels*

Silicon steels are alloys of Fe and Si having important electrical applications (motors, transformers, etc.). With low C steels, *non-oriented (NO) steels* and *grain oriented (GO)* Si *steels* are referred to as *electrical steels*. NO silicon steels have applications in rotating machinery, GO silicon steels are used in devices (e.g. transformers) where an easy direction of magnetization parallel to a roll direction is desired. GO silicon steels are further subdivided into *regular grain oriented (RGO)* and *high permeability grain-oriented (HGO)* materials [Bol94]. The drive to develop Si steels was motivated by the large increase in the resistivity of Fe with Si additions, Fig. 19.33(a). Fig. 19.33(b) shows the variation of properties with Si content in Fe-Si steel.

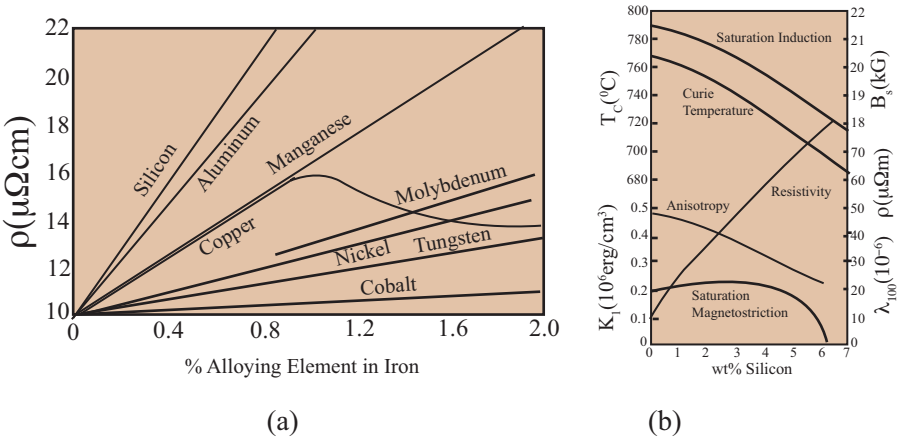

Fig. 19.33. (a) Effect of alloying additions on the resistivity of Fe, and (b) the variation of magnetic properties with Si concentration in Si-steels.

Studies of Fe-Si dates back to 1885 [Hop85]. Fe-Si alloys with 2 - 4.5 wt % Si were the most important soft magnetic material in both volume and market value by 1934 [Che86]. Before 1950 electrical sheet for transformers was produced by melting, ingot casting and hot rolling. By 1951 [Boz93], Si-Fe transformer sheet was produced by cold rolling. Polycrystalline NO Fe-Si materials were followed by the GO materials first with $(110)/[001]$ (Goss texture) and later $(100)/[001]$ texture. Efforts to reduce losses in transformer grade Si steels has focussed on (1) improving Goss texture in GO steel and (2) reducing eddy current losses by decreasing thickness and surface treatment.

Si steels are commonly rated on the basis of core loss (the combined power lost due to (a) magnetic hysteresis, (b) eddy currents and (c) anomalous losses). Limiting hysteresis losses requires a magnetically soft material. Magnetic softness is rooted in (1) low magnetocrystalline anisotropy, (2) low magnetostrictive coefficients, and (3) maximizing the magnetic domain wall mobility. Eddy current losses are limited, along with (3) by having large electrical resistivities. Si additions to Fe have beneficial effects that include: (1) improved magnetic softness and (2) increase in electrical resistivity; [Che86]. This is coupled with the disadvantageous: (1) decrease in Curie temperature and saturation magnetization and (2) embrittlement in alloys with $> 2\%$Si. Embrittlement increases approaching the Fe_3Si intermetallic with the DO_3 structure, Fig. 19.34. Thermomechanical processing is used to develop a texture that aligns magnetic easy axes. Impurity removal (e.g. C, N, S, O and B) reduce impediments to magnetic domain wall motion by second phase impurities. Surface modification of Si-Fe sheet decreases domain size, and reduces anomalous eddy current losses.

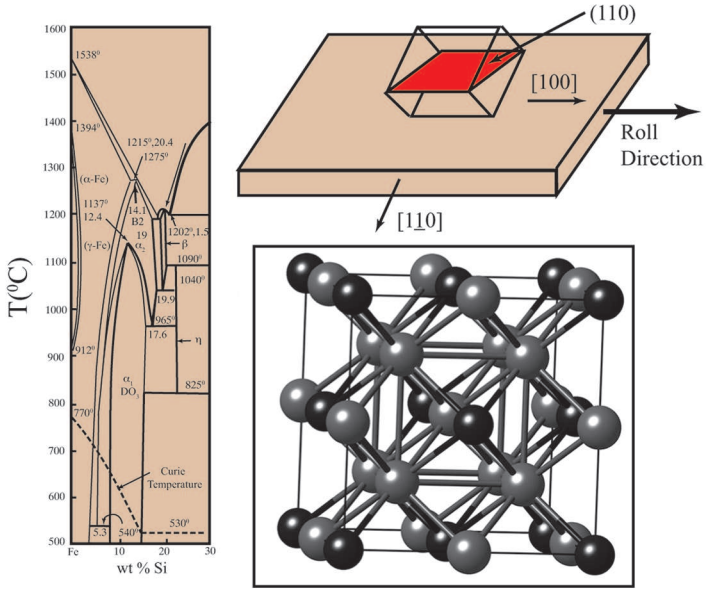

Fig. 19.34. (a) Fe-Si phase diagram, (b) Goss texture schematic and (c) DO_3 structure of Fe_3Si

In Fe-Si alloys, magnetic moment reduction with Siconcentration, (from 2.2 μ_B per atom) can be predicted from dilutional arguments. T_c decreases gradually up to 2 wt % and at an increasing rate for > 2 wt % Si. The first cubic magnetocrystalline anisotropy constant, K_1 decresaes linearly for < 5 wt% Si concentration. For Fe-Si, with 3.2 wt. % Si, at RT,$[100]$ is the EMD. For Fe-Si with 3.5 wt. % Si, $\lambda_{100} = 24 \times 10^{-6}$ and $\lambda_{111} = -2.3 \times 10^{-6}$. Both λ_{100} and λ_{111} decrease in magnitude with Si concentration with a zero crossing in λ_{111} occurring at ~ 5 wt. % Si.

Processing developments for GO Si steel include promoting polycrystalline Goss $(110)/[001]$ recrystallization texture. This not ideal, but is practically and economically viable. A figure of merit is the average deviation angle of the $[100]$ axis from the roll direction of cold reduced materials. Evolution of GO Sisteels have focussed on efficient primary crystallization grain growth inhibitors, e.g. MnS [McC82]. Improved GO laminates have MnS and AlN grain growth inhibtors and achieve 7-9 mm grain diameters and 30 the average deviation angles (as compared to 2-4 mm and 70).

GO silicon steel has a glass film with the main component being forsterite (Mg_2SiO_4) produced prior to secondary recrystallization. This is an electrical insulator and induces a tensile stress in the Fe-Si core. The latter reduces magnetostrictive losses (and transformer hum), decreases domain wall spacing, and promotes favorable domain orientations with respect to the roll axis (limiting anomalous losses). GO silicon

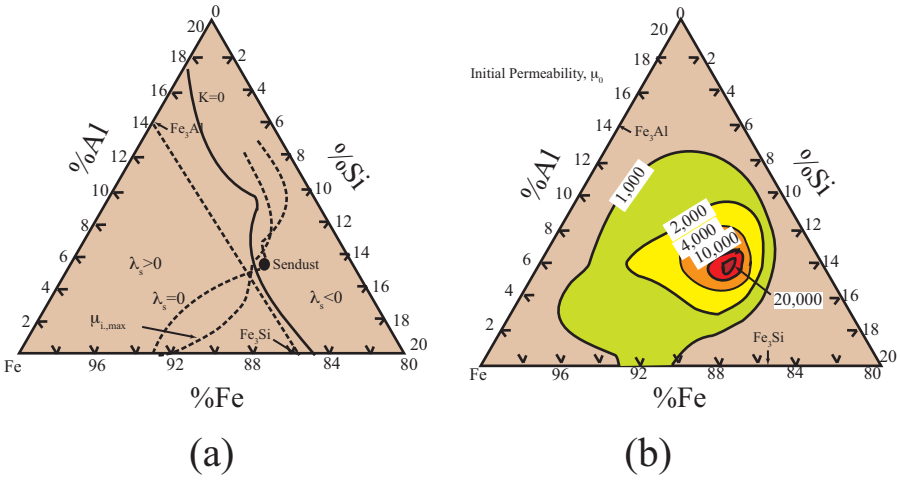

Fig. 19.35. Magnetic anisotropy (a) and magnetostriction (b) in an Fe-Si-Al ternary [O'H87].

steel processing to reduce eddy current and anomalous losses includes: (1) a reduction in sheet thickness from the original 0.35 mm to 0.23 mm now standard, and scratching or laser scribing to form $180°$ magnetic domain walls parallel to the roll direction.

Sendust has composition $\mathrm{Fe}_{1-x-y}\mathrm{Si}_x\mathrm{Al}_y$, with the optimum composition occurring near the zero anisotropy zero magnetostrictive compostion with $x = 0.1$ and $y = 0.05$. Fig. 19.35 shows how these compositions were discovered by determining constant magnetic anisotrpy (a) and (b) magnetostriction contours in the Fe-Si-Alternary system. Because of the appearance of the brittle DO_3 structure in these high Si containing alloys Sendust is very brittle and is used in powder or dust form in applications such as magnetic recording heads.

19.3.4 Fe-Co *alloys.*

FeCo-based alloys are technologically important materials, for soft magnetic applications that require high saturation inductions and high temperature operation. The largest RT saturation induction ($B_s \sim 2.5$T) is documented for bulk FeCo-based binary alloys. This was illustrated earlier within the context of energy band theory and the Slater Pauling curve. Energy band theory predicts well the moment variation in the FeCo alloy system. This alloy system is one for which the peak in the Slater-Pauling occurs, making alloys in this system, those with the highest inductions of transition metal systems. Fig. 19.36 (a) illustrates (courtesy Paul Ohodnicki) within the frame-

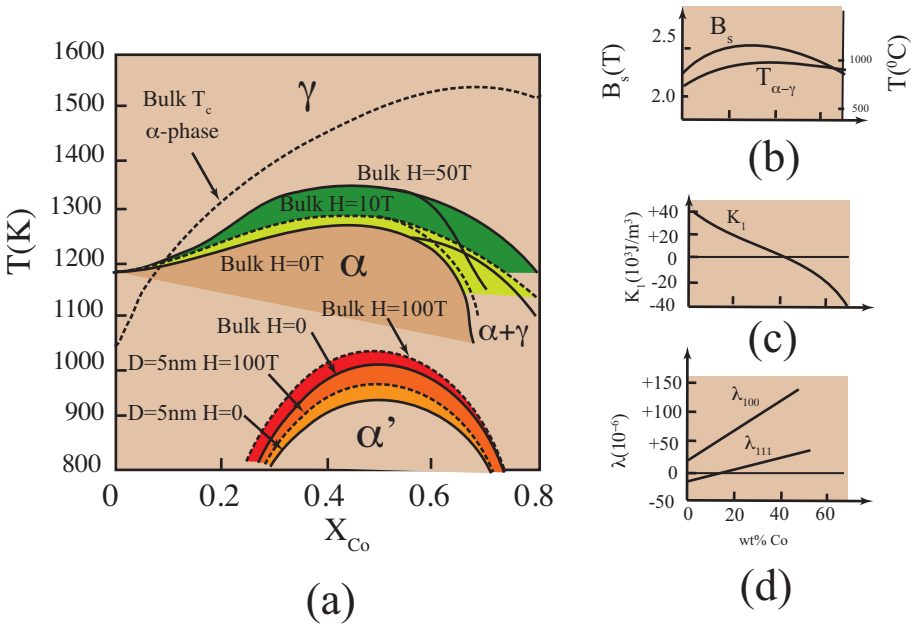

Fig. 19.36. (a) FeCo phase diagram and shifts in phase boundaries in a magnetic field, (b) saturation magnetization and Curie temperature, (c) magnetocrystalline anisotropy, K_1 and (d) magnetostriction, λ, in the FeCo system (reproduced from Pfiefer and Radeloff, 1980) [PR80].

work of the Bragg-Williams model and the shift in phase boundaries in the presence of a large static magnetic field.

Processing magnetic materials in fields can lead to dramatic changes in properties and is used a processing tool in many important magnetic materials. With the ability to generate large magnetic fields it is now possible to contribute enough magnetic work to make significant changes in phase boundaries in magnetic materials systems. Fig. 19.36 (a) shows calculated shifts in the FeCo phase boundaries in experimentally accessible 50 T fields. The shift in phase boundaries can also be realized by including surface energy effects in free energy calculations. Such surface energy terms become noticeable in magnetic nanostructures. Suppression of phase transformations in *metastable nanostructures* can produce materials with properties that are not obtainable in equilibrium structures. Recent examples are found in the suppression of nucleation of the stable γ-phase in Co-Fe-based nanocomposites at compositions where the binary Fe-Co phase diagram would predict that the α and γ- phases should coexist [OML$^+$08], [OPL$^+$08], [OQL$^+$09] FeCo alloys will be discussed below in the context of nanocrytals and nanocomposite systems.

The Curie temperature, T_c, of the low temperature disordered *bcc* α-phase is such that ferromagnetic behavior persists to temperatures approaching 1273 K. At equiatomic composition, the extrapolated T_c of the α-phase is significantly higher than the temperature above which ferromagnetic behavior is no longer observed. The abrupt loss of ferromagnetism results from the structural phase transformation from chemically disordered ferromagnetic *bcc* α-$\mathrm{Fe\,Co}$ to the high temperature paramagnetic *fcc* γ-phase. If the low temperature *bcc* phase could be stabilized relative to the γ-phase, ferromagnetism would persist to higher temperatures. In $\mathrm{Fe\,Co}$, the chemical order-disorder phase transformation is a higher-order transition where the equilibrium value of the chemical order parameter falls continuously to zero with increasing temperature. The phase transition is from an ordered $\mathrm{Cs\,Cl}$ structure to a disordered *bcc* phase.

Fig. 19.36 (b) illustrates the variation of saturation magnetization, T_c, (c) magnetocrystalline anisotropy, K_1, and (d) magnetostriction, λ, in $\mathrm{Fe\,Co}$ alloys. In choosing a binary alloy composition in the binary $\mathrm{Fe}_{1-x}\mathrm{Co}_x$ system it is important to consider the maximum induction which occurs near $x = 0.3$, the minimum magnetocrystalline anisotropy occuring near $x = 0.5$, and finally compositions which minimize magnetostrictive coefficients. In the $\mathrm{Fe\,Co}$ alloys magnetostriction coefficients, λ_{100} and λ_{111} are both substantial near the equiatomic composition where the magnetocrystalline anisotropy vanishes. Across this alloy system, T_c's are larger than Fe or Co).

Consideration of alloy resistivity (important for determining eddy current losses) and alloy additions which influence mechanical properties are used to design alloys for rotor applications in electric aircraft engines. Magnetostriction considerations are also known to be quite important in the design of soft magnetic materials for inductive devices, transformers and a host of other applications. Notable commercial alloys include ***Permendur***^{TM}, an $\mathrm{Fe}_{1-x}\mathrm{Co}_x$ alloy with $x = 0.5$, near the minimum magnetocrystalline anisotropy, ***Supermendur***^{TM} and ***Hiperco-50***^{TM} a similar $\mathrm{Fe}_{1-x}\mathrm{Co}_x$ alloy with $x = 0.5$, but with a 2% V addition to increase strength and electrical resistivity. Small Nb additions to Hiperco-50$^{\mathrm{TM}}$ have led to grain size refinement in the alloy ***Hiperco-50 HS***^{TM} which improves mechanical properties of these materials as well as their degradation in long term ageing at elevated temperatures. [FCT02]

19.3.5 Ni-Fe ***Alloys.***

Fe-Ni alloys are among the most important soft magnetic alloy systems. Ni-rich alloys are called Permalloys. There are three important permalloy compositions. The first is the 78 % Ni Permalloy. This alloy has a zero magnetostriction coefficient. Variations of this alloy are sold under the names, Supermalloy, Mu-metal and Hi-mu 80. The second is the 65 % Ni Permalloy. This alloy has $K_1 \sim 0$, and exhibits a

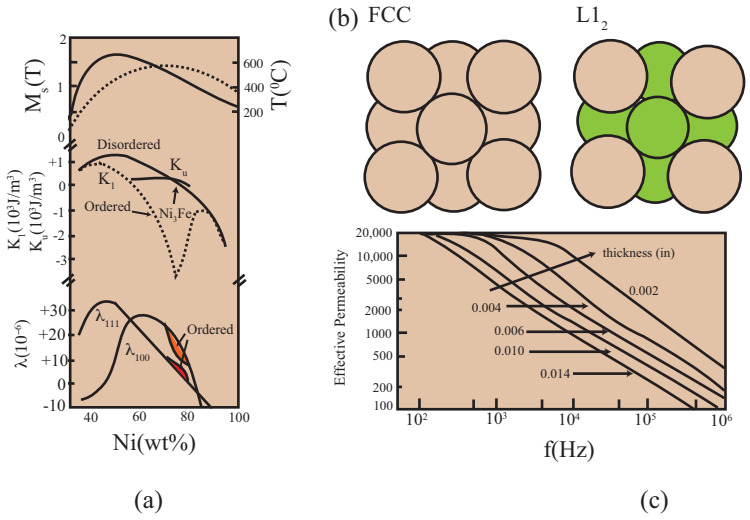

Fig. 19.37. (a) saturation magnetization and Curie temperature, magnetocrystalline anisotropy, K_1 and magnetostriction, λ, in the FeNi system [O'H87]; (b) the disordered *fcc* and ordered superlattice structure of the $L1_2$ Ni_3Fe intermetallic phase and (c) frequency dependence of the effective permeability for permalloy as a function of thickness.

strong response to field annealing. The third is the 50 % Ni Permalloy. This alloy has higher B_s, strong response to field annealing and produces square loop materials.

Fig. 19.37 (a) shows saturation magnetization and Curie temperature, magnetocrystalline anisotropy, K_1 and magnetostriction, λ, in the FeNi system for *fcc* or *fcc*-derivative alloys. Details of the magnetic properties and response to field annealing to induce anisotropies in permalloys depend on whether the material has a disordered *fcc* or ordered $L1_2$ Ni_3Fe intermetallic phase structure. These structures are illustrated in Fig. 19.37 (b). Crystallographic texture in permalloys is often developed by suitable *themomechanical processing* to take advantage of the strong variation in properties with direction. These *fcc*-derivative alloys have [111] EMDs and strong anisotropy in magnetostriction coefficients. Rolling can also benefit the high frequency magnetic properties which are limited by eddy current losses. Fig. 19.37 (c) shows the frequency dependence of the effective permeability for permalloy as a function of thickness.

In Fe-Ni-based nanocomposite systems, exhibit similar nanostructure phenomena as noted for FeCo. This is observed in Fe-rich alloys [GW02] where the nucleation of the equilibrium α-phase is suppressed in favor of the metastable γ-phase. This can also have profound effects on technical magnetic properties because on the Fe-rich side of the Fe-Ni phase diagram there is a strong compositional dependence of the Curie temperature, T_c, on composition in the γ-phase [RWG89]. Fig. 19.38 (a) illustrates the

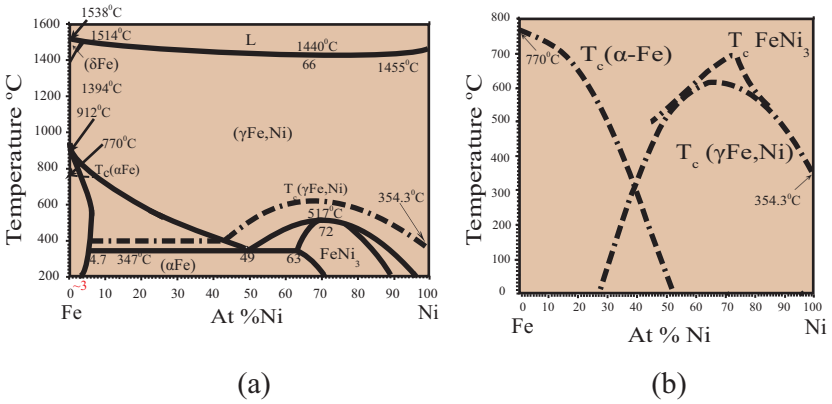

Fig. 19.38. Fe-Ni phase diagram with T_c-composition curves [Mas90] and (b) higher resolution depiction of T_c-composition curves.

Fe-Ni binary phase diagram [Mas90] with Fig. 19.38 (b) showing information on the compositional dependence of the Curie temperature, $T_c(X_{Ni})$. This $T_c(X_{Ni})$ behavior for the γ-phase can be extrapolated to metastable regions of the Fe-Ni phase diagram where desirable T_cs near $100°C$ for magnetocaloric [MSMM10] and biomedical applications [MKLM10] are predicted to occur near the 27 %Ni composition.

It can be seen that the γ-phase of Fe-Ni has appreciable magnetization on the Fe-rich side of the phase diagram. Because of the variations in K_1 and λ with composition interesting variations in properties can be observed as described for the Permalloy alloys. Another important set of alloys in the Ni_xFe_{1-x} family are the *Invar alloys* which are based on the 36% Ni alloys. The *invar effect* or *invar anomaly* occurs because of the magnetoelastic effects near its Curie temperature. Magnetoelastic effects (magnetostriction) gives rise to spontaneous changes in the lattice parameters as a function of temperature. Like the *magnetocaloric effect* these are also largest where the temperature dependence of the magnetization is the largest, i. e. near the Curie temperature. In Invar alloys the magnetostrictive volume change can be tuned to precisely cancel the thermal expansion coefficient, near room temperature, making the material dimensions temperature-independent [Gig95].

19.3.6 Giant Magnetostrictive Materials

19.3.6.1 Terfenol and Galfenol

In soft magnetic materials, magnetostriction can be a deleterious property for certain applications (i.e. it is the source of loss in transformers which is accompanied by "transformer hum"). In other applications, however, a large value of the magnetostric-

tive coefficient is critical to the operation of devices. For example, the generation of magnetostatic waves and consequent magnetoacoustic emission is of paramount importance in sonar applications. Materials with large values of magnetostrictive coefficients are often found by looking for large magnetoelastic coupling coefficients. However, as illustrated in Box 19.8 the magnetostrictive coefficient is also predicted to be large in materials compositions where the mechanical properties are soft and the elastic compliance $C \sim 0$.

Box 19.8 Example calculation of magnetostrictive strain for a tetragonal magnetostrictive material.

Consider a tetragonal material having a $[001]$ easy direction of magnetization (EMD). We can construct a Landau free energy consisting of elastic, $C\epsilon^2$, and magnetoelastic $\alpha B\epsilon m^2$ terms. We take:

$$G = G_0 + C\epsilon^2 + \alpha B\epsilon m^2$$

where α is a geometric constant; $\alpha = 1$ for $m \| [001]$ and $\alpha = -0.5$ for $m \perp [001]$. The elastic compliance constant, $C = \frac{3V_0}{4}(C_{11} - C_{12})$, B is the magnetoelastic coupling constant, m the reduce magnetization and ϵ the strain. Minimizing the free energy with respect to ϵ yields:

$$\frac{\partial G}{\partial \epsilon} = 0 = 2C\epsilon + \alpha B\epsilon$$

and therefore:

$$\lambda = \epsilon_{eq} = \frac{B}{2C}$$

for $m \| [001]$ and:

$$G^{[100]} - G^{[001]} = -\frac{3B\epsilon}{2}$$

and therefore the effective uniaxial anisotropy energy density is:

$$K_u^{eff} = K_u - \frac{3B\epsilon}{2}$$

Large $\frac{dl}{l}$'s are observed in interesting rare earth/transition metal alloys. For the cubic *Laves phase* material *Terfenol,* $\mathrm{Tb}_{1-x}\mathrm{Dy}_x\mathrm{Fe}_2$. *Terfenol-D* $\frac{dl}{l} \sim 10^{-3}$, is an alloy with the composition $\mathrm{Tb}_{0.3}\mathrm{Dy}_{0.7}\mathrm{Fe}_{1.9}$ is a state of the art magnetostrictive material. Terfenol was first developed in the 1970's by the U. S. Naval Ordnance Laboratory and further developed in the 1980's at Ames Laboratory. Terfenol is named after its components terbium (ter), iron (fe), and Naval Ordnance Laboratory(nol). The D in Terfenol-D reflects the dysprosium additions which increase the magnetostrictive coefficients. Terfenol-D has a saturation magnetostrictions as high as 1000 ppm.

The reciprocal effect to magnetostriction is the *Villari effect* or *inverse magnetostriction*. It is the change in a material's magnetization when subjected to a stress,

σ. For a material with a non-zero magnetostriction coefficient, a mechanical stress can alter the magnetic domain structure of a material. This in turn influences the effective magnetic anisotropy, the permeability and the coercivity of a magnetic material.

Magnetostrictive strain is observed to saturate as a function the applied field, H, in Terfenol [Cla80]. Because the effective anisotropy constant is strongly dependent on stress, the approach to saturation of the magnetostriction follows the magnetization of Terfenol-D at room temperature for compressive preloads from 4 to 39 MPa [WFRLC99]. A theory of the mechanism of magnetostriction in Terfenol-D has been presented by James and Kinderlehrer [JK94].

Changes in magnetization with stress can be predicted based on *Le Chatelier's principle*. A material with a positive magnetostriction coefficient will elongate along the axis of magnetization and one with a negative magnetostriction coefficient will contract. Therefore a material with a positive magnetostriction coefficient, under a tensile stress along the direction of magnetization, will exhibit an increased magnetization and under a compressive stress a decreased magnetization in the direction of a field at a fixed non-saturating value of the field. These conclusions are true for all but the virgin remnant state where the magnetization is zero.

Terfenol has a saturation magnetization is approximately 1.0 T at room temperature. Many of Terfenol's material constants vary widely depending on the initial and final magnetic states. Terfenol's initial applications were in sonar systems but has since been applied in magnetomechanical sensors, actuators, and acoustic and ultrasonic transducers. It has also been considered for use in fuel injectors for diesel engines because of the high stresses that can be produced. It is also employed in devices for which passive energy absorption is desired.

Another alloy of recent interest is the shape memory alloy *galfenol* with compositions near $\mathrm{Fe_3Ga}$ [CHWF$^+$03]. Again, galfenol is named after its components gallium (gal), iron (fe), and Naval Ordnance Laboratory (nol). Galfenol is a more recently invented magnetostrictive and is currently under active development. Galfenol has magnetostrictions only 25-33 % that of Terfenol-D, but because it doesn't have rare earth components, it is much less susceptible to corrosion. It can therefore more robust be used in more challenging environments. Galfenol is also of interest for sonar applications. This interesting magnetostrictive behavior in galfenol results from a maximum in the magnetoelastic coupling constant of $\mathrm{Fe}$with increasing Ga concentration, combined with a temperature dependent elastic shear modulus that becomes small near 27% Ga [CHWF$^+$03].

19.3.6.2 Ferromagnetic Shape Memory effects in Heusler Alloys.

The *shape memory effect* has been explored for a variety of applications, including notable applications in dentistry and biomedicine [VMCR$^+$98]. A *shape memory alloy, SMA* is one that can undergo large plastic deformations and then return to its

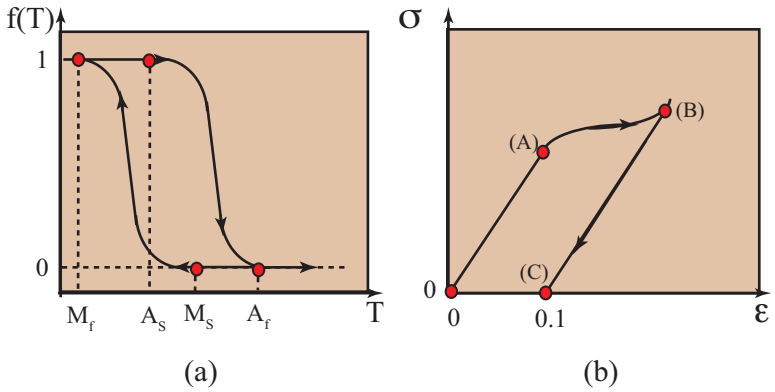

Fig. 19.39. (a) Thermal hysteresis and temperatures in a martensitic phase transformation and (b) shape memory effects in a stress strain curve for an SMA.

original shape upon heating. SMAs can exhibit both *superelasticity* and the *shape memory effect*. Superelasticity referrs to materials for which strains exceeding 10 % can be recovered elastically. Superelasticity is a strain induced transformation. Shape memory effects were first noted in AuCd alloys in 1932 [Ola32] and then again in CuZn alloys in 1956 [Hor56]. Of widespread current interest is the NiTi alloy Nitinol. This alloy was also discovered at the Naval Ordnance Laboratory in 1962, by William Buehler and Frederick Wang.

Shape memory effects derive from *martensite* to *austenite* phase transformations. These terms derive from phases of Fe, which are used generically to describe a low temperature, low symmetry deformed phase and a high temperature, high symmetry undeformed phase. This phase transformation is a *diffusionless*. Since it doesn't require long range atomic movement, it can be made potentially reversible with temperature. In practice, there is *thermal hysteresis* in these transformations and four temperatures are used to define this response as illustrated in Fig. 19.39 (a). f(T) is the volume fraction of martensite in the material. Starting with pure martensite, $f = 1$, at low temperature on heating to the temperature A_s the transformation to austenite starts and finishes at A_f. On cooling pure austenite, $f = 0$, at high temperature the transformation to martensite begins at the temperature M_s and finishes at M_f.

The shape memory effect is described with reference to Fig. 19.39 (b). In the elastic region the $\sigma(\epsilon)$ response is linear until the elastic limit (A) after which non-linear plastic deformation occurs until (B). At point (B) the stress is released and the material returns to a zero stress state with the permanent plastic deformation (C) caused by martensitic distortions. This plastic deformation can then be removed through thermal treatment to arrive back to (0,0).

There has been much recent interest in the development of actuator materials capable of large strains, appreciable thrust and rapid response time. Some representatives of the *Heusler alloy* family exhibit a cubic to tetragonal martensitic phase transformation (MPT). Since this transformation can occur between two ferromagnetic states, and involves large strains, these materials belong to a class called *ferromagnetic shape memory alloys, FSMA* . Unlike magnetostrictive materials (e.g., Terfenol-D), which derive their magnetostrictive strains from large magnetoelastic coupling coefficients, FSMAs can have vanishing elastic compliance upon approaching the MPT temperature and correspondingly large strains.

Magnetic field induced strain of several percent in $\mathrm{Ni_2Mn\,Ga}$ Heusler alloys [UHK$^+$96], [JTW99] are attributed to the motion of martensitic twin boundaries. The mechanism for the large strains in FMSA is explained in terms of the response of martensitic twin boundaries to a magnetic field pressure as illustrated schematically in Fig. 19.40 [O'H00]. At high temperatures, the materials exist in a high symmetry *austenite* phase and undergoes a *displacive phase transformation, DPT* at the martensitic phase transformation temperature, T_M. At low temperatures the material has transformed into a low symmetry *martensite* phase. T his DPT is accompanied by a large crystallographic distortion. Fig. 19.40 (a) shows a schematic crystal structure in the austenite. Fig. 19.40 (b) shows a configuration of distorted cells in the martensite phase.

The crystallographic distortion can involve large strains and large strain energies. The strain energies can be accommodated by slip Fig. 19.40 (b) or twinning Fig. 19.40 (c). In a material where the strain of the martensitic phase transformation is accommodated in twins, mechanical response to a stress can take place by twin boundary motion. Fig. 19.40 (d) shows such a deformation in a material subjected to mechanical shear. Since the martensitic phase is lower symmetry, there will typically be a uniaxial magnetocrystalline anisotropy determining the direction of the magnetization in the martensite as illustrated in Fig. 19.40 (e). For fields, $H < H_K$, the normal component of the field will exert a magnetic pressure on the twin boundary in a manner similar to the magnetic pressure on a domain wall. If the boundaries are mobile then this pressure will cause one of the twin variants to grow at the expense of others (Fig. 19.40 (e)). This can result in large field induced deformation of the material.

The temperature of ferromagnetic (T_c) and structural martensitic (T_M) phase transitions of the FSMAs are important to determining the temperature dependent magnetoelastic properties of the materials. The magnetic and structural phase transformations can be characterized by discontinuities in the temperature and/or field dependence of its properties. Such properties include strain, magnetization, resistivity, enthalpy and magnetocrystalline anisotropy energy. When ferromagnetic materials undergo a symmetry lowering structural phase transformation, the crystallographic orientation of the magnetization vectors within the domains displays a corresponding

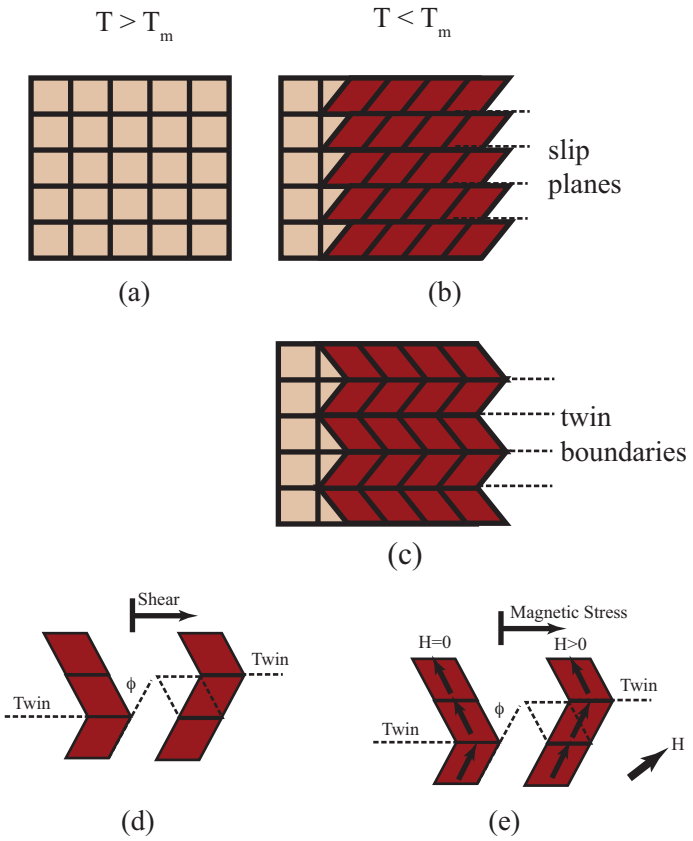

Fig. 19.40. (a) Magnetostrictive strain as a function of the magnitude of the applied field, H, in Terfenol [Cla80] and (b) magnetostriction and magnetization of Terfenol-D at room temperature for compressive preload from 4 to 39 MPa [WFRLC99].

change. Thus the magnetic anisotropy and other properties of the magnetic material can be used as a probe of the change in state in an FMSA [CCDG$^+$00], [CGGM01].

The temperature dependence of the magnetization of the as-grown and post-annealed single crystals with a nearly stoichiometric $\mathrm{Ni_2MnGa}$ composition is shown in Fig. 19.41 (a) [CGGM01]. An experimental protocol was employed where : (1) the sample was first cooled from 385 K to 5 K in zero field; (2) then its DC magnetic moment was measured as a function of increasing temperature as the sample was heated above the ferromagnetic T_c in a applied field of 0.08 T; (3) finally the crystal was cooled to 5 K under the same applied field. In comparison with the as-grown sample, the onset temperatures of the austenite to martensite, T_M, and martensite to austenite, T_A, tran-

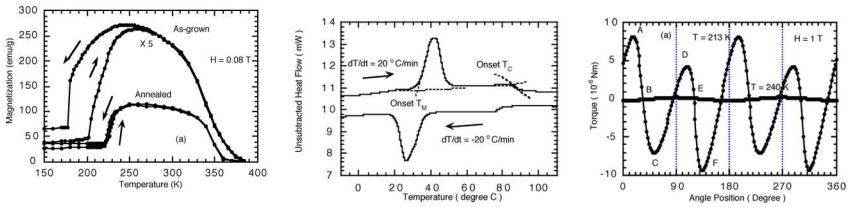

Fig. 19.41. (a) Temperature dependence of the magnetization of the as-grown and post-annealed single crystals with a nearly stoichiometric $\mathrm{Ni_2MnGa}$ composition; (b) shows a differential scanning calorimetry (DSC) curve for a crystal of composition $\mathrm{Ni_{52.7}Mn_{22.6}Ga_{24.7}}$ and (c) magnetic torque curves for a stoichiometric crystal in the austenite and martensite phases, respectively.

sitions in the post-annealed sample were significantly enhanced from 177.5 to 221.5 K and from 202.5 to 224.5 K, respectively.

A post-annealing process reduces the temperature hysteresis for the structural phase transition from 25 K to less than 4 K. This is a signature of the mobility of the twin boundaries in the as-grown and annealed states. Both the hysteresis in the magnetomechanical response and the field induced strain rate reflect this mobility. The post-annealing effect can be interpreted in terms of a reduction of compositional fluctuations and/or second phase in the as-grown sample. High temperature annealing made the sample more homogenous in composition and microstructure. A sharp step in a magnetization curve is a signature of a cooperative phase transition. The elimination of a possible contamination phase may result in a decrease of the magnetic coercivity because an impurity phase in a ferromagnetic material can serve as a pinning phase and increase the coercivity. A magnetic hysteresis measurement in the post-annealed sample shows its coercivity to be 50 Oe which is much smaller than the 250 Oe coercivity of the as-grown sample.

Fig. 19.41 (b) [CGGM01] shows the temperature hysteresis as well as the heat evolved during the structural transition as measured by differential scanning calorimetry (DSC). Again the calorimetric results probe the hysteresis in the martensitic phase transformation. Evidence for a spin reorientation in a stoichiometric sample was also obtained by magnetic torque measurements (Fig. 19.41 (c)). Following a zero field cooling, the torque is shown as a function of angle between the applied field (1 T) and a reference orientation. A large value from peak to peak on the torque curve implies that in comparison with the cubic austenite structure (at 340 K) the tetragonal martensite structure (at 213 K) exhibits a strong magnetic anisotropy.

Vasil'ev et. al. [VBKea99] have constructed a free energy functional that describes the energy behavior of a magnetoelastic material that undergoes a cubic to tetrago-

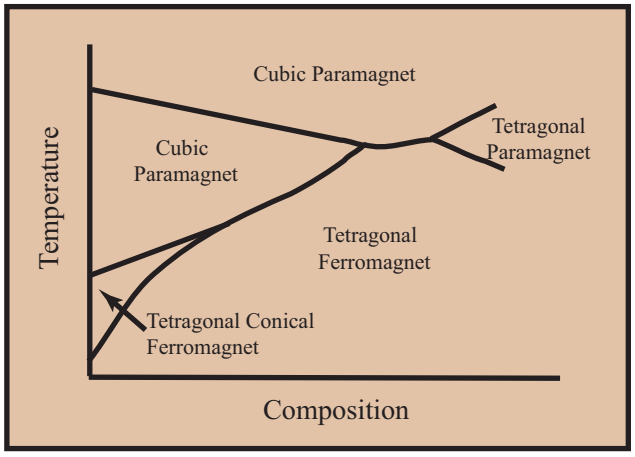

Fig. 19.42. Magnetic phase diagram for $\mathrm{Ni}_{2-x}\mathrm{Mn}_x\mathrm{Ga}$ [VBKea99].

nal martensitic transformation. This functional uses two order parameters, the elastic strain tensor and the magnetization vector and has been used to predict a magnetic phase diagram for $\mathrm{Ni}_{2-x}\mathrm{Mn}_x\mathrm{Ga}$. This phase diagram is illustrated in Fig. 19.42 and has five phase fields. These are a tetragonal paramagnet, an axial tetragonal ferromagnet, a conical tetragonal ferromagnet, a cubic paramagnet and cubic ferromagnet.

For stoichiometric $\mathrm{Ni_2MnGa}$ the ferromagnetic cubic phase with the $\mathrm{L2_1}$ Heusler structure has $\langle 111 \rangle$ easy axes. The low temperature tetragonal phase has $\langle 001 \rangle$ easy axes with 3 possible orientations of the tetragonal phase with respect to the cubic parent phase. There is a close correlation between crystallographic twins and magnetic domain walls in the martensitic state.

Magnetic domain configurations in the $\mathrm{Ni_2MnGa}$ FMSA have been observed by means Lorentz microscopy and noninterferometric phase reconstruction methods [DWMZ01]. So-called *cross-tie walls* were observed in the thinnest sections of the cubic austenite phase. In thicker regions for the cubic austenite phase 180° domain walls are most prevalent, along $\sim$ 300 nm spaced regular arrays of 71° domain walls. The observations indicate that there is a critical thickness below which the nature of the magnetic domains changes consistent with the observations of *Bloch wall* and *Neel wall* transitions as a function of thickness. In the low temperature tetragonal martensite phase the domain configurations correlated with the EMDs for this uniaxial material.

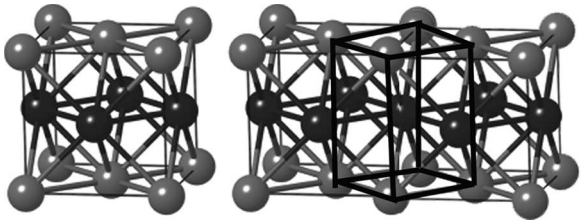

Fig. 19.43. $L1_0$ prototype structure [DM07].

19.3.7 $L1_0$ Permanent Magnets.

Binary FePt and CoPt alloys are studied as magnetic materials for both bulk and thin film magnetic recording applications. Alloys with low symmetry crystal structures possess large K_u's that can be exploited to yield H_c's in appropriate microstructures. Equiatomic FePt and CoPt possess large K_u's (for CoPt : $K_u = 4.9 \times 10^7 \frac{ergs}{cm^3}$ and for FePt: $K_u = 6.6 \times 10^7 \frac{ergs}{cm^3}$) due to their tetragonal $\mathrm{L1_0}$ crystal structures. Metastable hexagonal derivative structures in CoPt thin films also possess large uniaxial magnetic anisotropies in alloys with less of the expensive Pt [HWR$^+$93].

FePt CoPt and other alloys crystallizing in the $L1_0$ structure have hard magnetic properties deriving from a tetragonal crystal structure. FePt adopting the $L1_0$ prototype structure has the $P4/mmm$ space group with Fe in the 1a $[(0,0,0)]$ and 1c $[(\frac{1}{2},\frac{1}{2},0)]$ and Pt in the 2c $[(0,\frac{1}{2},\frac{1}{2})]$ special positions in a 4 atom supercell. Fig. 19.43 illustrates the relationship between the ordered tetragonal $L1_0$ and *fcc* phases. Anisotropy is derived from atomic ordering and variation of the tetragonal $\frac{c}{a}$ ratio.

This $L1_0$ structure has alternate stacking of (001) planes of Fe(Co) and Pt atoms. Elemental Pt exhibits Stoner enhance paramagnetic susceptibility but in structures, where Pt is in contact with a ferromagnetic species Pt can also have an appreciable moment [MM91] [MMC91]. The dipole moment for Pt atoms is induced by polarization effects mediated both by conduction electrons through direct exchange interaction with Co or Fe atoms. Further large spin-orbit interactions ascribed to Pts outer shell electrons gives rise to the high magnetocrystalline anisotropy of such materials.

The FePt and CoPt systems were first studied by Jellinghaus [Jel36] who observed the highest energy products known at the time [Boz93]. Engineering interest in FePt and CoPt thin films arise from applications in extremely high density recording (EHDR) and permanent magnets . The magnetic properties of FePt and CoPt alloys strongly depends on annealing temperature, time and composition due to the influence of each on the atomic ordering fraction of the anisotropic tetragonal phase. Recent efforts have concentrated on developing optimum microstructures to harness the large

magnetic anisotropies in FePt and CoPt alloys to develop coercivities. A focus is on nanometer sized, exchange decoupled grains approaching monodomain sizes.

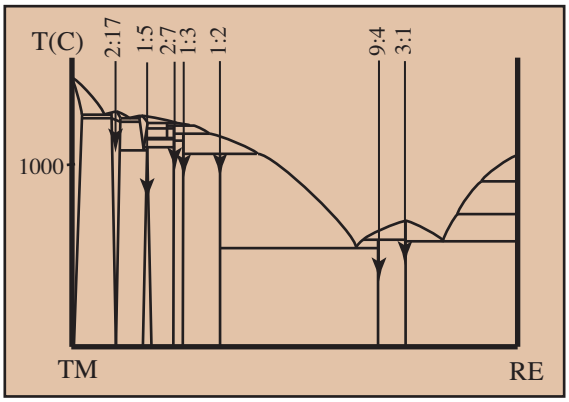

Fig. 19.44. Schematic RT phase diagram (approximating the Sm–Co system).

19.3.8 RT Permanent Magnets

Important *rare earth-transition metal (RT) alloy* permanent magnets have properties that depend on the T to R ratio. Alloys where the ratio is 2, often adopt a cubic Laves phase structure which does not promote permanent magnetic properties. For alloys with ratios above 2, low symmetry crystal structures can result in large uniaxial magnetocrystalline anisotropy impacting the coercivity, H_c, of permanent magnets. The magnitude of the coercivity depends further on the microstructure of the magnet. The *magnetocrystalline anisotropy* must be understood with respect to crystal structure.

R metals (Dy, Nd, Pr, Sm, etc.) have metallic radii of $\sim 0.175-0.185$ nm, $\sim$30 % larger than early and $\sim 50-60$ % larger than late transition metals. Crystal structures exist in RT systems with stoichiometries of RT_2, RT_3, R_6T_{23}, RT_5, R_2T_{17}, R_3T_{29}, RT_{12}, etc. RT phase diagrams often contain many line compounds (with limited solubilities). Fig. 19.44 shows a schematic RT phase diagram (approximating the Sm-Co system.). Near line compounds occur at the stoichiometries: R_2T_{17}, RT_5, R_2T_7, RT_3, RT_2, R_9T_4, and R_3T. In state of the art Sm-Co permanent magnets a 2-phase microstructure relies on the large magnetic anisotropy of $\mathrm{Sm\,Co_5}$ and the high moment of $\mathrm{Sm_2Co_{17}}$. Alloys of composition $\mathrm{Sm\,Co_{7.7}}$ have achieved the largest magnetic energy products (highest stored magnetic energy) in this system .

Properties of RT permanent magnets derive from the magnetic ground states of the rare earth species. Other properties derive from the low symmetry crystal structures and the separation of the T-atom planes. It is important to understand how the coupling between the dipoles on the R and T sites are influenced by the choice of R and T species and constituents. Just as in strengthening in steels *interstitial modification* can be used to great benefit in optimizing properties in hard magnets.

19.3.8.1 Magnetic Dipole Moments and Coupling.

The magnetic dipole moments in RT permanent magnets depend on several significant variables related to the two species, the atomic spacings and the coupling between the dipoles. These aspects are summarized:

(i) R atom moments derive from the localized 4f electrons and thus R dipole moments are well described by the Hund's rule ground state which do not differ from the R^{3+} species tabulated above.

(ii) T dipole moments derive from T d-bands. Since rare earth planes push T planes further apart, this narrows the T bands, decreasing band widths, W, in comparison with respect to their exchange splitting, J_{ex}. This serves to increase the T dipole moments in cases where weak ferromagnetic bands are transformed into strong bands.

(iii) The large R species require larger volumes. Since magnetization is net dipole moment per unit volume, this larger volume reduces the magnetization.

(iv) R and T dipole coupling changes from ferromagnetic for *light rare earths* (< 7 f electrons) to antiferromagnetic for *heavy rare earths* (> 7 f electrons).

The coupling between the dipole moments can be transmitted by direct or RKKY exchange interactions. RKKY exchange is mediated through the conduction electron gas associated, for example, with sp conduction electrons of the magnetic atoms in rare earths. This indirect exchange is transmitted by polarization of the free electron gas and influences the coupling to the local f-electron dipoles.

For atoms with open shells, however, the occupation of angular momentum states in accordance with Hund's rules can lead to anisotropic charge distributions. This is especially pronounced in rare earth species. Depending on the details of the filling of the 4f states the resulting charge density can be oblate, prolate or nearly spherical (i.e. for Gd^{3+}). For a material to exhibit magnetic anisotropy, both the orbital angular momentum (L_z) and the crystalline electric field need to have less than spherical symmetry. The crystal field causes the orbital angular momentum to be strongly tied to particular crystallographic directions. The coupling of spin angular momentum to the orbital angular momentum comes about through thef *spin-orbit interaction*. Spin-orbit interactions give rise to an interaction energy, the *spin-orbit energy*:

$$E_{so} = -\lambda \vec{L} \cdot \vec{S} \tag{19.64}$$

where λ is a phenomenological parameter called the *spin-orbit coupling constant*. For $\lambda > 0$ the lowest spin-orbit energy occurs for spin's aligning parallel to the orbits and for $\lambda < 0$ for spin's aligning anti-parallel to the orbits. The spin-orbit interactions can lead to an energy lowering for spin dipole moments aligned with the orbitals and consequently with specific crystallographic directions! This lower energy for dipoles in particular crystallographic directions is the origin of *magntocrystalline anisotropy*.

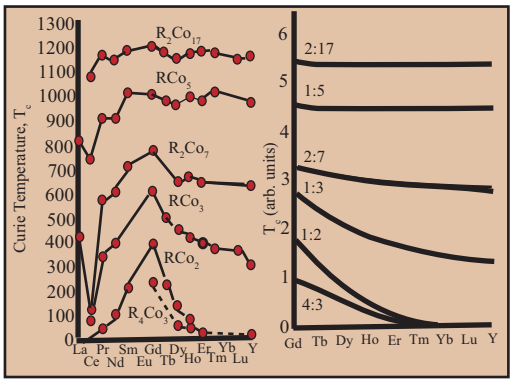

Fig. 19.45. Variation of the Curie temperature in R-Co and R-Y compounds and those predicted from Wohlfarth's [Woh79] Landau theory formalism.

19.3.8.2 Curie Temperatures.

T_c's for RT permanent magnets depend on the composition and the sign of the coupling between the R and T species dipoles. Wohlfarth [Woh79] considered the variation of T_c with R species in R-Co compounds using a Landau theory (discussed above). The model was modified to account for the large R dipole moments and the coupling between the R and Co species by replacing the first Landau coefficient, a(T) with a coefficient a′(T) defined as:

$$a'(T) = a(T) - \frac{\alpha}{T} \quad \alpha = \frac{N\mu_B^2 J_{R\mathrm{Co}}^2 \left[g-1\right]^2 J(J+1)}{3k_B} \tag{19.65}$$

where N R atoms have moments $gJ\mu_B$ and $J_{R\mathrm{Co}}$ is the R-Co exchange constant which changes sign on moving from light to heavy rare earth species. In general, J_{RT}, the $R-T$ exchange constant to changes sign on moving from light to heavy rare earths due to the change in spin-orbit interactions between oblate and prolate 4f electron distributions. .The parameter α can equivalently be expressed more compactly in terms of the *DeGennes factor, D*:

$$\alpha = \frac{N\mu_B^2 J_{R\mathrm{Co}}^2 D}{3k_B} \quad D = \left[g-1\right]^2 J(J+1) \tag{19.66}$$

The scale for the T_c's was set by considering Y-Co compounds for which $D = 0$ since Y has an empty f-shell. Fig. 19.45 shows the variation of T_c in R-Co and R-Y compounds and those predicted from Wohlfarth's [Woh79] Landau theory. T_c's are largest in the compounds with the largest Co-content. Gd gives the strongest coupling to Co. Unfortunately Gd is not a good choice for permanent magnet systems because

its half-filled f-shell does not allow for magnetocrystalline anisotropy because there f-electron energy can not be decreased by a symmetry lowering distortion.

19.3.8.3 Magnetocrystalline Anisotropy.

There are also several considerations necessary to understand the origin of magnetocrystalline anisotropy in RT permanent magnets. For the large magnetic anisotropies required to develop high coercivities in permanent magnets, these include:

(i) The compound's crystal system should be uniaxial rather than cubic.
(ii) The anisotropy should give rise to an easy axis ($K_u > 0$) rather than an easy plane ($K_u < 0$), since for an easy plane the magnetization can rotate without rotating through a hard direction! It is therefore easier to demagnetize.
(iii) The anisotropy associated with the R species depends on the 4f-electron charge distribution. RE^{3+} ions have oblate or prolate ellipsoidal charge distributions depending on whether the f-shell is more or less than half-filled [Coe91].
(iv) The anisotropy associated with the R species depends on the details of the *crystalline electric field* seen by the R species in their special positions.
(v) The anisotropy associated with the T species can be greatly enhanced if the structure has planes for which are 2- as opposed to 3-d. T planes can be isolated by the incorporation of the large R species in the structure or through interstitial modifications which can serve to expand the lattice anisotropically.

In a quantum mechanical framework the energy of electronic states for atoms experiencing a crystal field can be summarized in terms of a *crystal field Hamiltonian*:

$$H = H_0 - eV_{el} + \lambda \vec{L} \cdot \vec{S} \tag{19.67}$$

where H_0 is the Hamiltonian giving rise to electronic energy levels in the absence of the crystal field. V_{el} is the electrostatic Coulomb potential due to ions (viewed as point charges) surrounding the ion for which crystal field energy levels are to be calculated and $\lambda \vec{L} \cdot \vec{S}$ is the aforementioned *spin-orbit coupling*. The electrostatic potential at an ion of interest and the resulting total electrostatic energy is written:

$$V(r,\theta,\phi) = \sum_j \frac{q_j}{|(\vec{R}_j - \vec{r}|} \quad V(r,\theta,\phi) = \sum_i \sum_j \frac{q_i q_j}{|(\vec{R}_j - \vec{r}|} \tag{19.68a}$$

where $\vec{r}$ is the position vector to the ion of interest, $\vec{R}_j$ is the position of the jth ion surrounding the ion of interest and q_j is the charge of the jth surrounding ion. The total energy involves summing over all ions in the structure ($\sum_i$) where q_i is the charge of the ith reference ion. The solution to crystal field problems is aided by expanding in terms of powers of r and *spherical harmonics* or *tesseral harmonics*, since the potential

must be a solution to *Laplace's equation*. An expansion in spherical harmonics is:

$$V(r,\theta,\phi) = \sum_{l,m} C r^l Y_l^m(\theta,\phi) \tag{19.68b}$$

where C is a constant and $Y_l^m(\theta,\phi)$ are spherical harmonics.

19.3.8.4 Extrinsic Magnetic Properties.

For applications, it is the extrinsic properties, coercivity, remnant induction and the derivative energy product that are most important as figures of merit. These are determined by the intrinsic properties and the the magnetization reversal mechanism. The reversal mechanism is intimately related to the microstructure. Processes involved in the reversal of the magnetization in the second quadrant of the hysteresis loop include: nucleation of a reverse domain(s) at a defect, reversible growth of a reverse domain, irreversible motion of domain walls passed pinning centers.

In real materials reversal takes place by nucleation of reverse domains on microstructural imperfections or Inhomogeneities such as defects, surfaces, interfaces, etc. and coercivity is less than that predicted by a rotational mechanism alone.

> *Brown's paradox* states that only a fraction of the anisotropy field is practically realizable in coercivity.

Values of the coercivity do not typically exceed 50 % of the anisotropy field in the best permanent magnet microstructures.

Microstructural development is very important to determining the ultimate properties of a permanent magnet. Microstructural development can be thought of as attempting to control two distinct aspects of the magnetic microstructure. These are:

(i) Engineering the free pole distribution (demagnetization factors) in the microstructure. This was seen in the discussion of Alnico magnets above.

(ii) Engineering the spatial variation of magnetic anisotropy by the distribution and texture of low and high K phases. Domain wall pinning is maximized in regions of low K and isolated particles can be forced to reverse by rotation. Texture is important for achieving optimal alignment of easy and hard axes.

As a practical limitation, these are very difficult microstructural features to control and require clever applications of phase relations and phase diagrams coupled with state of the art processing techniques.

Kronmuller's formalism parameterizes the contributions to the coercivity as follows:

$$H_c = \alpha \frac{2K_u}{\mu_0 M_s} - N_d M_s \tag{19.69}$$

Type	*System*	*Space Group*	*Z*	*a, c* (nm)
$SmCo_5$	hex	P6/mmm	1	0.51, 0.41
β-Sm_2Co_{17}	hex	$P6_3$/mmm	2	0.84, 0.82
α-Sm_2Co_{17}	rhom	$R\overline{3}m$	3	0.843, 1.2222
$Nd_2Fe_{14}B$	tetra	$P4_2$/mnm	4	0.88, 1.22
Nd_3Fe_{29}	mono	A2/m	2	1.05, 0.97 (b=0.85)
α-$Sm_2Fe_{17}N_3$	rhom	$R\overline{3}m$	3	0.843, 1.222
$Sm(Fe,Ti)_{12}N$	tetra	I4/mmm	2	0.893, 0.522

Table 19.5. *Summary of structural information for some non-cubic RT phases.*

where K_u is the uniaxial anisotropy and N_d is a spatially averaged effective demagnetization factor associated with the switching entities (i.e. isolated particles). α is a microstructural parameter that can further be expressed as $\alpha = \alpha_K \alpha_\psi$ where α_K describes spatial variations in the anisotropy and α_ψ describes texture variations.

19.3.8.5 Selected Low Symmetry RT systems.

Table 19.5 summarize structural information for some non-cubic *R-T* phases.

19.3.8.6 $SmCo_5$

$SmCo_5$ is a premiere permanent magnet. This hexagonal material (Fig. 19.46), with the largest value of magnetocrystalline anisotropy, was first reported in 1967, by Strnat, et. al. [SHO$^+$67]. Non-magnetic RT_5 compounds were first synthesized by of W. E. Wallace et. al. [Wal60] of the University of Pittsburgh and subsequently Carnegie Mellon University. In many applications Sm_2Co_{17} with larger T fractions and larger inductions are more attractive. However, the Sm_2Co_{17} phases do not achieve magnetocrystalline anisotropy comparable to $SmCo_5$.

In state of the art Sm-Co permanent magnets a 2-phase microstructures rely on the large magnetic anisotropy of the $SmCo_5$ and the high moment of the Sm_2Co_{17} materials. Alloys of composition $SmCo_{7.7}$ have achieved the largest magnetic energy products (highest stored magnetic energy) in this system . In these non-stoichiometric 2-phase materials some Co is substituted for by Fe, Cu and/or Zr [Bus88].

$SmCo_5$ is a template for many important permanent magnets. $CaCu_5$, with the hexagonal P6/mmm (#191) space group, is the prototype for $SmCo_5$ [WG59]. Fig. 19.46, shows a formula unit of $SmCo_5$ in the unit cell [DM07], to have 8 Ca atoms in each cell each shared with 8 other cells for a total of one Ca. There are $1 + 8(\frac{1}{2}) = 5$

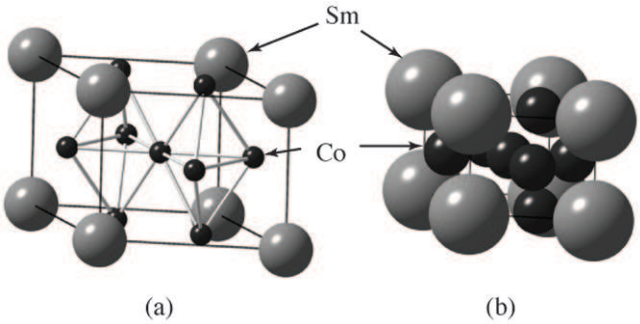

Fig. 19.46. Hexagonal unit cell of $\mathrm{CaCu_5}$ (a) ball and stick and (b) space filling depictions. Reproduced from DeGraef and McHenry [DM07].

Cu atoms per unit cell. The tetrahedral interstices in $\mathrm{SmCo_5}$ are empty. Rare earth intermetallics are important for H storage in these tetrahedral interstices.

19.3.8.7 Dumbell Substitutions: α-$\mathrm{Sm_2Co_{17}}$ and β-$\mathrm{Sm_2Co_{17}}$.

Other important REPM's are related to the $\mathrm{SmCo_5}$ structure through *dumbell substitutions* replacing a R atom with a pair of T atoms. The stoichiometry is changed to enrich the T content at the expense of the R species. Stadelmeier [Sta84] proposed the formula, $R_{m-n}T_{5m+2n}$ where m and n are integers, to describe RT compounds formed dumbell transformations. When $\mathrm{m} = 1$ and $\mathrm{n} = 0$ we describe the parent RT_5 structure. For other structures m represents the number of RT_5 formula units and n the number of dumbell substitutions within the m units. A stoichiometry of R_2T_{17} is obtained for $\mathrm{m} = 3$ and $\mathrm{n} = 1$. If $\mathrm{m} = 2$ and $\mathrm{n} = 1$, a RT_{12} is compound is obtained. If $\mathrm{m} = 5$ and $\mathrm{n} = 3$, a R_3T_{29} compound is obtained. The transformation by which $\frac{1}{3}$ of the R atoms in the $\mathrm{CaCu_5}$ structure of $\mathrm{SmCo_5}$ are replaced with pairs of transition metal atom *dumbells*, is represented:

$$3RT_5 - R + 2T = R_2T_{17} \tag{19.70}$$

where a single rare earth (Sm) is removed from 3 units of $\mathrm{SmCo_5}$ and replaced by a transition metal (Co) dumbell, $2T$, to yield the $\mathrm{Sm_2Co_{17}}$ compound. Phases with this stoichiometry exist in both hexagonal and rhombohedral variants. Pairs of T atoms are arranged along the c-axis at dumbbell sites (Fig. 19.47).

The $\mathrm{Th_2Ni_{17}}$ structure ($\mathrm{P6_3/mmc}$ #194), shown in Fig. 19.47. It is the structure of the β-$\mathrm{Sm_2Co_{17}}$ phase. β-$\mathrm{Sm_2Co_{17}}$ has lattice constants $\mathrm{a} = 0.84$ and $\mathrm{c} = 0.81$ nm respectively. Fig. 19.47 shows the structure of the β-$\mathrm{Sm_2Co_{17}}$, a single unit cell depicted in (a) space filling and (b) ball and stick formats.

$2-17$ phase magnet microstructures are multiphase microstructures with each phase

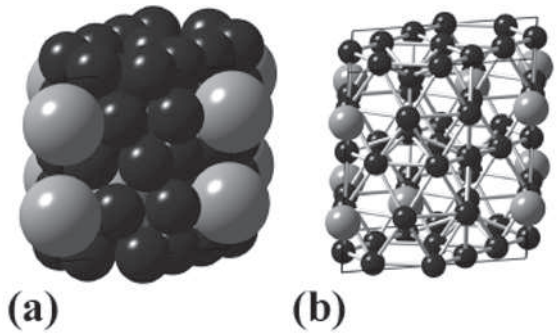

Fig. 19.47. β-Sm_2Co_{17} phase unit cell, depicted in (a) space filling and (b) ball and stick formats. The hexagonal prismatic representation with 3 cells is shown projected along the $[001]$ direction. Reproduced from DeGraef and McHenry [DM07].

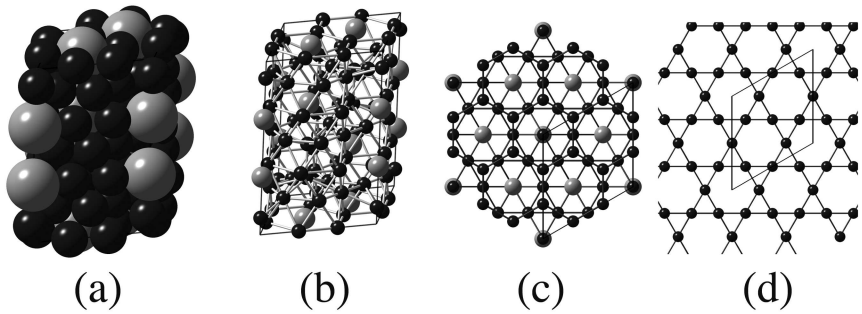

Fig. 19.48. The structure of the α-$\mathrm{Sm_2Co_{17}}$ phase, a single rhombohedral unit cell depicted in (a) space filling and (b) ball and stick formats. The hexagonal prismatic representation projected along $[001]$ is shown in (c) and (d) shows the Co atom Kagome net in the z $= \frac{1}{6}$ plane. Reproduced from DeGraef and McHenry [DM07].

having an important role in developing hard magnetic properties. The $\mathrm{SmCo_5}$ phase develops on the 6 equivalent pyramid planes of the $2:17$R phase. A small amount of Zr stabilizes the $2:17$ phase with Fe substitutions (partial substitution of Fe for Co increases the magnetization of the material, but a corresponding $\mathrm{Sm_2Fe_{17}}$ does not possess a large T_c). The presence of Fe is also thought to promote the formation of a *cellular structure* illustrated in Fig. 19.49. $\mathrm{SmCo_5}$ is metastable at room temperature, but can generally be retained. $\mathrm{Sm_2Co_{17}}$ takes the $2:17$R at room temperature, but the $2:17$H can be retained by rapid quenching.

In magnetic systems, it is often interesting to look mix Fe and Co as the transition metal species. This is motivated by the binary Fe–Co systems, where a magnetization

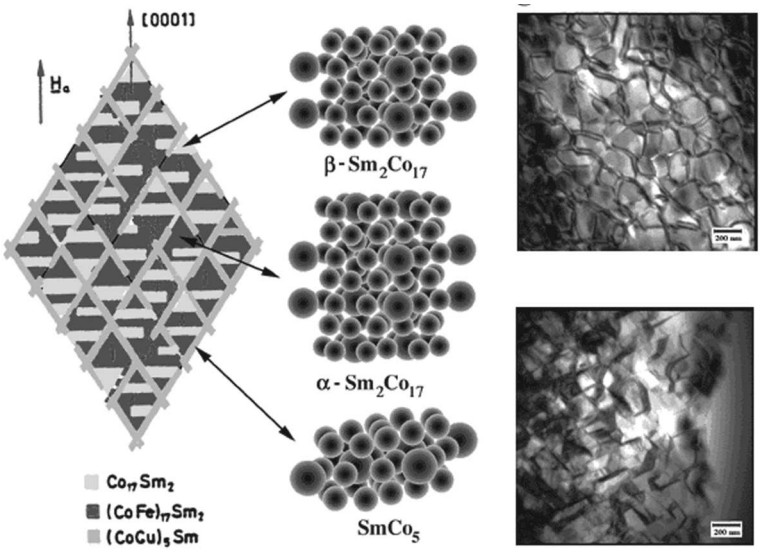

Fig. 19.49. Cartoon and typical microstructures of $\mathrm{Sm_2Co_{17}}$ magnetic materials with a cellular structure along with an actual TEM micrograph showing the cell structure. Reproduced from DeGraef and McHenry [DM07].

larger than pure Fe or pure Co is attainable. Also, since $\mathrm{Fe}$is cubic and Co has an *hcp* structure, their alloys can often be engineered to show preferences for low symmetry phases, influencing the resulting magnetocrystalline anisotropy. Studies have been performed in phases with the $\mathrm{Sm_2Co_{17}}$ structure. Deportes, et al. [DGL$^+$76] studied $\mathrm{Y}_2(\mathrm{Co}_{1-x}\mathrm{Fe}_x)_{17}$ alloys and Herbst, et al. [HCL82] studied T site selection in $\mathrm{Nd}_2(\mathrm{Co}_{1-x}\mathrm{Fe}_x)_{17}$ alloys.

19.3.8.8 The tetragonal $\mathrm{Nd_2Fe_{14}B}$ *Phase.*

The $\mathrm{Nd_2Fe_{14}B}$ $(2:14:1)$ phase is the most important tetragonal permanent magnet material because of its large magnetocrystalline anisotropy and large magnetic induction [HCP84], [GLM84]. It is also less costly than the SmCo-based magnets. $\mathrm{Nd_2Fe_{14}B}$ has an $P4_2/mmm$ ($D_{4h}{}^{14}$, #136) space group with a $= 0.88$ nm and c $= 1.22$ nm. Since it has four formula units per unit cell, the $\mathrm{Nd_2Fe_{14}B}$ cell contains 68 atoms. Herbst et al. [HCP84] solved the magnetic structure by *neutron diffraction*. Fig. 19.50 shows the $\mathrm{Nd_2Fe_{14}B}$ single tetragonal unit cell. For a review of properties the reader is referred to Herbst, 1991 [Her91].

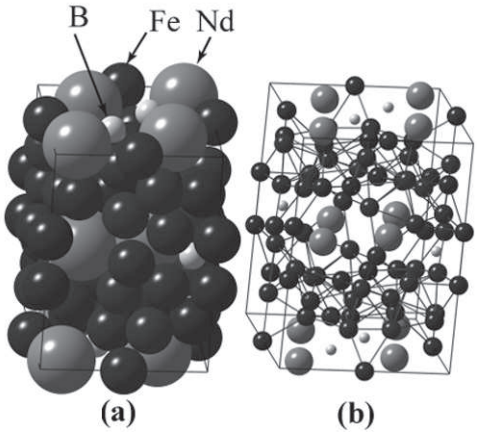

Fig. 19.50. $Nd_2Fe_{14}B$ unit cell depicted in (a) space filling and (b) ball and stick formats. Reproduced from DeGraef and McHenry [DM07].

19.3.8.9 Monoclinic $R_3(Fe, Co)_{29}$ Phases.

The monoclinic $R_3(Fe, Co)_{29}$ phase is a lower symmetry RT magnets for which the hard axis is not orthogonal to a basal plane because the crystal system has all non-orthogonal basis vectors [CLM$^+$94]. Their structures result form the dumbell substitution:

$$5RT_5 - 2R + 4T = R_3T_{29} \tag{19.71}$$

The R_3T_{29} prototype has a A2/m (#12) space group with two inequivalent R sites and 11 inequivalent T sites, respectively. Relationships between the A, B and C lattice constants in the monoclinic unit cell and a, b and c lattice constants in the unit cell of the similar 1:5 derivative structure exist:

$$B = 3^{\frac{1}{2}}a; \qquad A = (4a_2 + c_2)^{\frac{1}{2}}; \qquad C = (a_2 + 4c_2)^{\frac{1}{2}} \tag{19.72}$$

A single cell of the R_3T_{29} phase has 2 formula units (64 atoms). This structure is formed by alternative stacking of $1:12$ and $2:17$ type segments. The R_3T_{29}'s are an example of a phase that is stabilized by ternary additions. The composition of the phases are reported as $R_3(Fe,M)_{29}$ with M being a larger early transition metal. Substitution of other magnetic transition metals for Fe (notably Co) is also possible, but do not impact the stability of the phase.

For the example of $Nd_3Fe_{27.5}Ti_{1.5}$, illustrated in Fig. 19.51 the phase has lattice constants a = 1.06382 nm, b = 0.85892 nm, and c = 0.97456 nm, respectively. A monoclinic tilting angle, β =arctan($\frac{2a}{c}$), for the structure illustrated is 96.93 °. Fig. 19.51 illustrates the structure of the $Nd_3Fe_{27.5}Ti_{1.5}$ with a monoclinic unit cell.

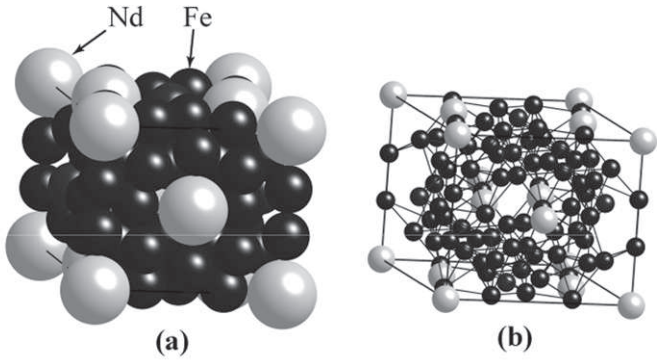

Fig. 19.51. The structure of $Nd_3(Fe,Ti)_{29}$, a single unit cell depicted in (a) space filling and (b) ball and stick formats. Reproduced from DeGraef and McHenry [DM07].

The $R_3(Fe,TE)_{29}$ (3:29) (TE (early transition metal) $= Ti$, etc.) compounds have been reported as potential high temperature permanent magnet applications. Synthesis structure and properties of the 3:29 phase magnets [SMRR$^+$98], [SMRR$^+$99], were examined in the ($Pr_3(Fe_{1-x}Co_x)_{27.5}Ti_{1.5}$ (x $= 0, 0.1, 0.2, 0.3, 0.4$ and 0.5) system with up to 50% Co substitution for Fe . Co substitutions in alloys of composition ($Pr_3(Fe_{1-x}Co_x)_{27.5}Ti_{1.5}$ have been shown to increase T_c, induction and anisotropy field in these magnets. With larger T content the magnetic exchange and consequent T_c's of these magnets can be increased. The attractiveness of a high T:R ratio in this phase is mitigated by the fact that 1.5 of 29 T atoms are replaced by Ti to stabilize the metastable phase.

Site selection with substitution of Ti for Fe in ($Pr_3(Fe_{1-x}Co_x)_{27.5}Ti_{1.5}$ (x $= 0$, 0.1, 0.2, 0.3, 0.4) magnets was studied [HHS$^+$99] using EXAFS and neutron diffraction showing that Ti substitutes in the 4g and 4i special positions, consistent with the observations [HYKP96] in ($Pr_3Fe_{27.5}Ti_{1.5}$ materials. The distribution of Ti between the 4g and two 4i sites agreed with observations [YH96] on ($Pr_3Fe_{27.5}Ti_{1.5}$) materials.

19.3.8.10 Interstitial Modifications.

Interstitial modification can improve properties of REPM materials. Interstitials should have covalent radii less than ~ 0.1 nm [Sko96] to occupy interstitial sites (often octahedral) in the REPM lattice. B has a covalent radii of 0.088 nm, but, it has a strong preference for trigonal prismatic coordination which can dictate the structure as in 2:14:1 magnets. C and N with covalent radii of 0.077 nm and 0.070 nm, often occupy interstitial sites in a REPM structure. These promote volume expansions as large as 8%. Anisotropic volume expansion by interstitial modification can increase K_u.

Dramatic effects on the magnetization and T_c's of interstitially modified REPM

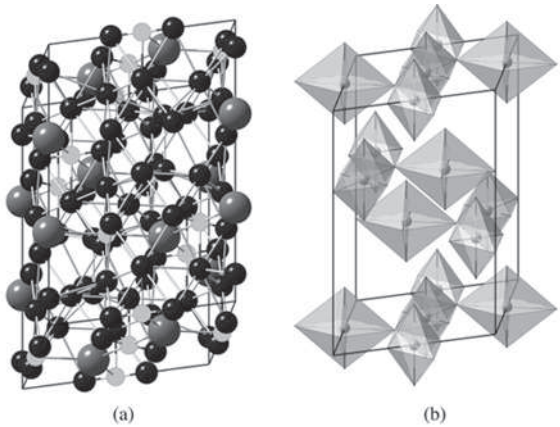

Fig. 19.52. $Sm_2Co_{17}N_3$ structure (a) single unit cell, with 3 formula units of the rhomahedral Sm_2Co_{17} and 9 N atoms (highlighted) in octahedral interstices; (b) polyhedral setting, illustrating N octahedral coordination polyhedra. Reproduced from DeGraef and McHenry [DM07].

materials, are observed especially for those containing Fe as the T species. Larger spacing between the Fe atoms causes narrowing and closing of the majority spin Fe d-band, increasing Fe's dipole moment. The increased separation of Fe atoms also favorably influences exchange and increases T_c.

For N interstitial modification [CS90] of the Sm_2Fe_{17} phase, gas-phase reaction with fine particles is a typical synthesis route. A nitrogenation reaction is:

$$2Sm_2Fe_{17} + (3-\delta)N_2 = 2Sm_2Fe_{17}N_{3-\delta} \tag{19.73}$$

The nitride disproportionates, above 720 K, by the reaction:

$$2Sm_2Fe_{17}N_3 = 2SmN + Fe_4N + 13Fe \tag{19.74}$$

N occupies large octahedral interstices in the nitrides. Structural features of the modification in the rhombohedral Sm_2Fe_{17} phase are explained considering a volume expansion of the parent α-Sm_2Co_{17} phase lattice with occupation of octahedral interstitial sites. Fig. 19.52 (a) shows three formula units in the single unit cell of the rhombahedral Sm_2Co_{17} phase. Here, nine N atoms (highlighted) are incorporated into octahedral interstices to yield the compound $Sm_2Co_{17}N_3$.

The N interstitials sit at the 9e special positions in the $R\overline{3}m$ space group with the sites of the R and T atoms the same as in the parent phase. Fig. 19.52 (b) shows a polyhedral setting, illustrating the N octahedral coordination polyhedra. Notice the vertex sharing polyhedra connected along $[100]$ and $[010]$ directions, in this structure.

Table 19.6. *Classification of materials by range and type of atomic order.*

SRO	*Range of SRO*	*LRO LRO*	*Range of LRO*	*Material Classification*
Crystalline	$\geq 10\mu$m	Crystalline	$\geq 10\mu$m	Macrocrystalline
Crystalline	100 nm - 10μm	Crystalline	$\geq$ 100 nm	Microcrystalline
Crystalline	$\leq$ 100 nm	Crystalline	$\leq$ 100 nm	Nanocrystalline
Crystalline	$\sim$ 1 nm	No LRO		Amorphous I
Non Cryst.	$\sim$ 1 nm	No LRO		Amorphous II
Non Cryst.		Quasiperiodic	$\sim 1\mu$m - 0.1 m	Quasicrystalline

Interstitial modification with C to form $\mathrm{Sm_2Fe_{17}C}_x$ has been demonstrated. Solid state diffusion is used for interstitial modification [SC93].

Interstitial modification of the $\mathrm{Sm(Fe,Ti)_{12}}$ phase structures has been investigated by Yang, et al., [YPZ$^+$93]. Here N occupies large octahedral interstices. The $\mathrm{Sm(Fe,Ti)_{12}}$ phase requires one of the 12 T sites be occupied by Ti in order to stabilize the Fe containing compound. The structural features of the modification in the tetragonal $\mathrm{Sm(Fe,Ti)_{12}}$ phase can also be explained by considering a volume expansion of the parent phase with occupation of octahedral interstitials.

Interstitial modification of the $\mathrm{Sm_3(Fe,Ti)_{29}}$ phase structures [CLM$^+$94] includ hydrogen, nitrogen and carbon interstitial modifications. $\mathrm{Sm_3(Fe,Ti)_{29}N_5}$ alloys have been synthesized with notable increase in the anisotropy fields, saturation magnetization and T_c's.

19.3.9 Amorphous and Nanocomposite Materials.

Amorphous and more recently nanocomposite materials have been investigated as magnetically soft materials for many applications. The term *nanocomposite* will be used for alloys that have a majority of grain diameters in the range from $\sim 1 - 50$ nm embedded in an amorphous matrix. Interest in nanocomposite soft magnetics derives from synergy in the properties of the amorphous and crystalline phases from which it is composed. Interesting properties in amorphous and nanocomposite materials derive from chemical and structural variations on a nanoscale which are important for developing unique magnetic properties. We review structure $\rightarrow$ properties relationships in amorphous and nanocomposite material. Nanocomposites are discussed further below.

Amorphous alloys are topologically disordered. Crystalline alloys have long range (periodic) order in their atomic and (usually) spin positions. The magnitudes of the spin dipole moments are typically uniform and exchange interactions are discrete as a result of the periodicity. Amorphous alloys have short range atomic order but lack

long range order and have disordered spin positions, spin magnitudes and exchange interactions. Attributes of amorphous alloys which derive from disorder are:

(i) More possible spin configurations, including non-collinear arrangements.
(ii) More free volume in the amorphous state than in the crystalline state influences the size of dipoles and net magnetization.
(iii) The metastable thermodynamic state is promoted by alloying with glass formers which reduce net dipole moments by dilution and/or bonding.
(iv) Magnetic species can have different coordination polyhedra and different nearest neighbor symmetries than in their crystalline counterparts.
(v) Strong positional disorder cause large fluctuations in exchange. There can be competing ferromagnetic and antiferromagnetic exchange interactions.
(vi) Amorphous alloys possess random magnetic anisotropy.

These contribute to rich magnetic phase diagrams.

19.3.9.1 The Structure of Amorphous Materials.

Table 19.6 classifies amorphous and nanocrystalline alloys by *short-range order*, *long-range order*, and the ordering length scales [O'H87]. Crystalline alloys are designated macrocrystalline, microcrystalline, or nanocrystalline. Amorphous alloys with local order similar to crystalline counterparts are known as Amorphous I alloys, whereas amorphous alloys with non-crystalline local order belong to the Amorphous II type.

In *amorphous solids*, atomic positions lack crystalline (periodic) or quasicrystalline order but have short-range order. Amorphous metals are usually structurally and chemically homogeneous, which gives them isotropic properties attractive for many applications. Chemical and structural homogeneity can lead to isotropic magnetic properties that are important in materials for many inductive components.

In amorphous metals, atomic correlations extend only to a few coordination shells (0.1 to 0.5 nm out from the central atom), resulting in significant broadening of peaks and fewer features in x-ray diffraction patterns. In *nanocrystalline alloys*, finite size effects give rise to *Scherrer broadening* of the XRD peaks. For a particle size of 1 nm (i.e., about 4 unit cells) the peaks have broadened so much that they overlap and the high angle peaks are no longer resolved. The peak broadening is a signature of the *nanocrystalline structure*.

Atomic distances in an amorphous solid can be described by the *pair correlation function*, $g(r)$. The pair correlation function is defined as the probability that a pair of atoms are separated by a distance, r. We consider N atoms in a volume Ω; let $\mathbf{r}_1, \mathbf{r}_2, \ldots \mathbf{r}_N$ represent the positions of these atoms with respect to an arbitrary origin. The distance $r = |\mathbf{r}_i - \mathbf{r}_j|$ is the length of the vector connecting atoms i and j. Related

is the spatially dependent atomic density, $\rho_{\text{atom}}(r)$, defined as:

$$\rho_{\text{atom}}(r) = \frac{N}{\Omega} g(r), \tag{19.75a}$$

and the *radial distribution function*, RDF(r), defined in terms of the atomic density:

$$\text{RDF}(r) = 4\pi r^2 \rho_{atom}(r) \mathrm{d}r, \tag{19.75b}$$

The radial distribution function, RDF(r), represents the number of atoms between the distances r and $r + \mathrm{d}r$.

The functions $\rho_{\text{atom}}(r)$ and $g(r)$ are determined from scattering experiments using wavelengths on the order of atomic distances. A completely structurally disordered material (e.g. a gas) has a uniform probability of finding neighboring atoms at all possible distances (larger than twice the atomic radius), leading to a featureless $g(r)$. In a crystalline solid, $g(r)$ is represented by a set of $delta$ functions related to the discrete distances between pairs of atoms (i.e., a diffraction pattern). In amorphous alloys, broad peaks in $g(r)$ reflect the presence of short range order.

19.3.9.2 Amorphous Metal Synthesis

Fig. 19.53(a) illustrates that it is possible to cool alloys fast enough to avoid the nose of the liquid to solid phase transformation in a *TTT diagram*. This requires solidification fast enough to preclude nucleation of the stable crystalline phase. In this case an amorphous structure. Such a material is called a *metallic glass*. Eutectic alloys where the liquid phase is already stable to low temperatures are ideal. Also of interest is the return to thermodynamically stable phases (or intermediate metastable phases) in the process of crystallization (or nanocrystallization) in Fig. 19.53(b).

The pioneering work of Duwez [DWW60] was followed by discovery of many metallic glass sytems produced by rapid solidification. Amorphous alloy synthesis typically require cooling rates $> 10^4 \ \frac{K}{s}$ [MWL99]. Rapid solidification techniques include *splat quenching*, *melt spinning*, etc. In melt spinning, alloys at temperatures typically greater than 1300 K are cooled to room temperature in 1 ms, at cooling rates of $\sim 10^6 \ \frac{K}{s}$. Fig. **??** illustrates the melt-spinning process where an alloy charge is placed in a crucible with a small hole at one end. The alloy is typically induction melted. Surface tension keeps the melt in the crucible until an inert gas overpressure pushes the melt through the hole onto a rotating Cu wheel. The stream rapidly solidifies into $\sim 20\mu$m thick amorphous ribbons. Reviews of melt spinning include those by Liebermann [Lie83] by Davies [Dav85] and by Boettinger and Perepezko [BP85].

Many other techniques have been used in amorphous metal synthesis including:

- *Rapid Solidification Processing:* Amorphous alloys can be produced by rapid solidification processing routes, typically requiring cooling rates $\geq 10^4$ K/s. Examples of these techniques include splat quenching, melt spinning, etc.

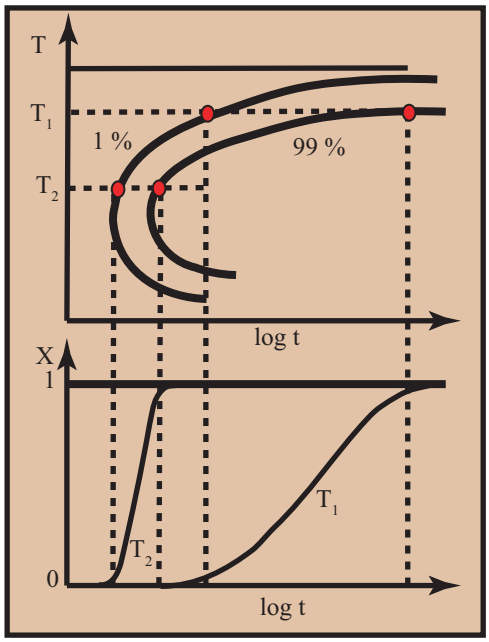

Fig. 19.53. TTT diagram for a hypothetical eutectic alloy [MB01].

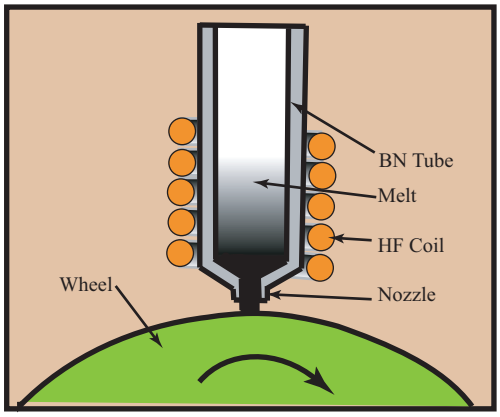

Fig. 19.54. Schematic of melt spinning, illustrating flow of molten metal onto rotating wheel.

- *Solidification of Bulk Amorphous Alloys: Bulk amorphous alloys* are formed by conventional solidification with slow cooling rates. A *large glass forming ability* allows producing amorphous materials with much larger dimensions (up to cm).

- *Powder Synthesis:* Amorphous metals may be synthesized as powders or compacted to form bulk alloys with an amorphous structure. Techniques include *plasma torch synthesis* [Tur99] , *gas atomization*, and *mechanical milling*. Rapid solidification in the gas phase (e.g. ultrasonic gas atomization) or splatting on a substrate can lead to the formation of nanometer-sized glassy droplets, *nanoglasses* [Gle89].
- *Solid State Mechanical Processing:* In *mechanical alloying*, the energy of the milling process and constituent thermodynamic properties determine whether amorphization will occur. Mechanical alloying is also a means of synthesizing amorphous alloys by solid state reaction of two crystalline elemental metals in multilayer systems with a fine interlayer thickness [JAVR$^+$85].
- *Amorphization by Irradiation:* Crystalline alloys can be made amorphous by irradiation by energetic particles beam [MN82]. Amorphization is an effect that is often observed at high particle fluences in radiation damaged materials [Sut94].
- *Thin Film Processing: Thin film deposition* techniques were shown as early as 1963 [MWdN63] to produce amorphous alloys.

19.3.9.3 Thermodynamic and Kinetic Criteria for Glass Formation

Glass forming ability (GFA) involves suppressing crystallization by preventing nucleation and growth of the stable crystalline phase. The solidification of a eutectic liquid involves partitioning of the constituents so as to form the stable crystalline phase. GFA can be correlated with the *reduced glass forming temperature,* T_{rg} , defined as:

$$T_{rg} = \frac{T_g}{T_L} \tag{19.76}$$

where T_L and T_g are the liquidus and glass transition temperatures, respectively. Below the glass transition temperature, T_g, the atomic mobility is too small for diffusional partitioning of alloy constituents.

The thermodynamic condition for glass formation is described by the T_0 construction illustrated in Fig. 19.55, for an $A-B$ eutectic system. For compositions between the T_0 curves the liquid phase can lower its free energy only through the partitioning of the chemical components, nucleating an A-rich or B-rich region that expels the other (B or A) constituent as it grows. This nucleation and growth process requires long range diffusion to continue. If an alloy can be quenched below its glass transition temperature, T_g in the region of compositions between two T_0 curves, then the atomic motion necessary for this partitioning will not be possible and the material will retain the configuration of the liquid. The glass forming ability is increased for materials where the reduced glass forming temperature, T_{rg}, is large.

Massalski [1981] [Mas81] presented thermodynamic and kinetic considerations for the synthesis of amorphous metals. The criteria suggested for *partionless freezing* (no composition change) of a liquid to form a metallic glass are:

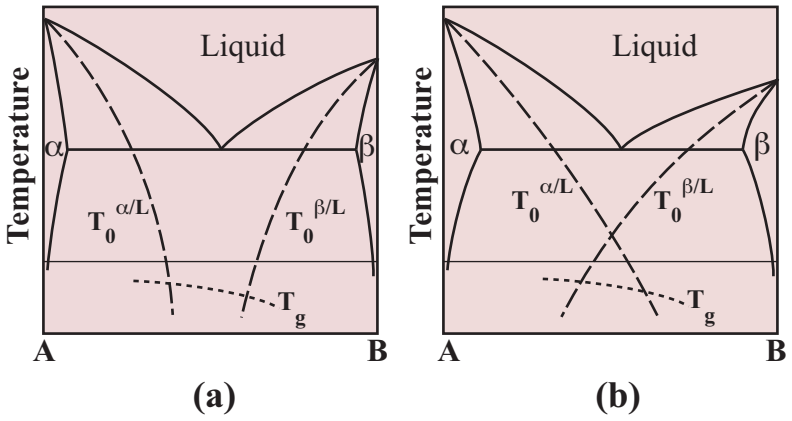

Fig. 19.55. (a) T_0 construction for an AB binary alloy with a deep eutectic. (b) In an alloy for which the T_0 curves intersect above T_g partitionless solidification is not possible [Wil00].

(i) *Quenching to below the T_0 curve:* The T_0 curve is the temperature below which there is no thermodynamic driving force for partitioning and the liquid freezes into a solid of the same composition. The T_0 curve is the locus of T-composition points where the liquid and solid phase free energies are equal.

(ii) *Morphological stability:* depends on the comparison of imposed heat flow and the velocity of the interface between the amorphous and liquid phases.

(iii) *Heat flow:* To prevent segregation, liquid supercooling must exceed $\frac{L}{C}$ where L is the latent heat of solidification and C is the specific heat of the liquid.

(iv) *Kinetic Criteria:* A critical cooling rate, R_c, for quenching of the liquid is empirically known to depend on the *reduced glass forming temperature, T_{rg}*.

(v) *Structural*: Atomic size ratios with difference exceeding $\sim$13 % (consistent with *Hume-Rothery rules*) retard the diffusion necessary for partitioning.

Fig. 19.56 illustrates examples of two alloy systems that exhibit relatively deep eutectics and can be rapidly solidified to form a metallic glass. The Fe-Zr, system is an example of a eutectic in a late transition metal/early transition metal system. The Fe-B system is an example of a eutectic in a (transition) metal/metalloid system.

Criteria i is a condition on the supercooling of the liquid. Criteria iii requires that heat must be transported quickly enough from the moving solidification front. This is determined by heat transfer between the amorphous solid phase and the wheel and depends on the wheel conductivity, speed and the degree of wetting by the liquid. Criteria iv defines a critical cooling rate required to prevent the *nucleation and growth* of the crystalline phase. Deep eutectics occur in systems with large positive heats of mixing and consequent atomic size differences motivating the criteria v

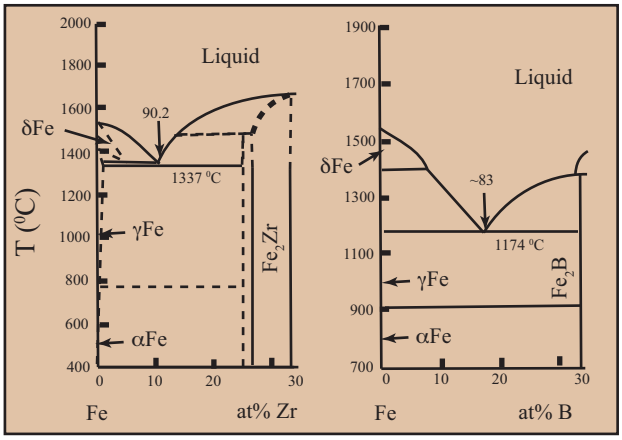

Fig. 19.56. Eutectic phase diagrams for the (a) Fe-B and (b) Fe-Zr sytems. In both cases the alloys can be rapidly solidified to form a metallic glass [Wil00].

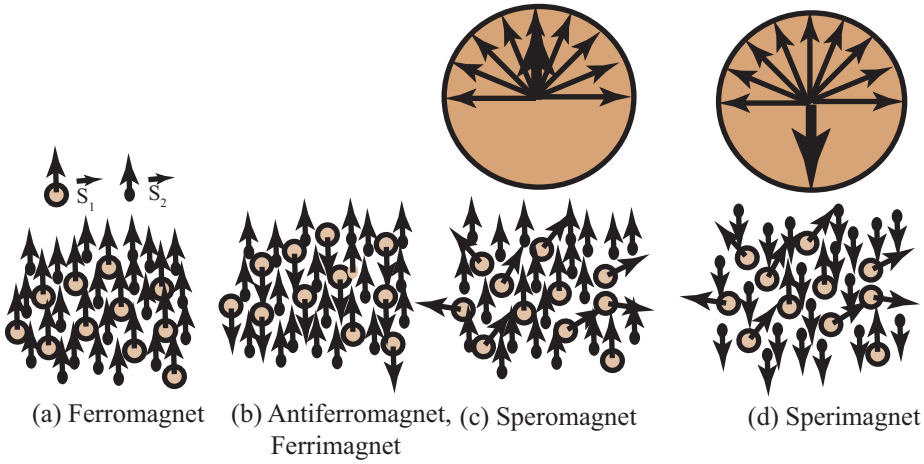

Fig. 19.57. Spin configurations possible in amorphous magnets, (a) ferromagnet, (b) antiferromagnet or ferrimagnet, (c) speromagnet and (d) sperimagnet.

19.3.9.4 Magnetic Dipole Moments and Their Ordering.

The most important determinant in the magnitude of magnetic dipole moments in amorphous alloys is alloy chemistry and then positional disorder. The issue of the influence of alloy chemistry on magnetic dipole moments and magnetization, previously illustrated in the Slater-Pauling curve, can be addressed in a more quantitative

manner in a variety of empirical models. Weak solutes, as defined by a valence difference $\Delta Z \leq 1$, are explained by the previously discussed *rigid band model* while a *virtual bound state model* is employed when the solute perturbing potential is strong, $\Delta Z \geq 2$. TM moment reduction due to sp-d bonding with metalloid glass formers is in addiition to dilution effects! Therefore amorphous magnet inductions are significantly reduced as compared with elemental counterparts. Moment reduction due to coordination bonding has been discussed by Corb and O'Handley [CO85] and magnetic valence ideas have been developed by Williams [WMMT83]

The absence of crystalline periodicity in amorphous materials leads to distributed local exchange interactions and sometimes competing exchange interactions. This leads to richness in the possible magnetic structures in amorphous materials. The collinear magnetism found in crystals, i.e. ferromagnetism, anti- ferromagnetism and ferrimagnetism are all observed in amorphous materials. In addition, non-collinear magnetism can also be observed in the form of *speromagnetism*, *asperomagnetism* and *sperimagnetism*. Competing exchange interactions can also lead to frustration and spin-glass behavior [Coe78]. These configurations are depicted in Fig. 19.57.

19.3.9.5 Random Exchange

As compared with bulk crystalline materials amorphous alloys typically have reduced Curie temperatures, due to alloying with glass forming elements [O'H87]. Amorphous alloys also have large distributions of interatomic spacings resulting in distributed exchange interactions which alter the mean field description of M(T) [Chi78].

Distributed exchange is predicted on the basis of a distribution of nearest neighbor distances and *Bethe-Slater curve*. Observations of distributed hyperfine fields in *Mossbauer spectroscopy* are consistent with this. Handrich and Kobe incorporated distributed exchange into mean field theory to predict M(T) for amorphous magnets. The mean field theory for the temperature dependence of the magnetization in amorphous alloys was proposed by Handrich and Kobe [Kob69] [Han69].

To consider the effects of positional and chemical disorder in amorphous alloys we are guided by simple Taylor series expansions of the exchange energy:

$$J = J_0 + \Big(\frac{\partial J}{\partial r}\Big)\Delta r \qquad J = J_0 + \Big(\frac{\partial J}{\partial C}\Big)\Delta C \tag{19.77}$$

where the first expression reflects positional (R) and the second chemical disorder (C). The starting point for each of these is a description of J(C) or J(R) in similar crystalline alloys. For J(C) we can be guided by the Slater-Pauling curve and for J(R) we can be guided by the Bethe-Slater curve. In the case of positional disorder, the first order effects can be predicted by recognizing that for Fe, $\left(\frac{\partial J}{\partial r}\right) > 0$, for Co, $\left(\frac{\partial J}{\partial r}\right) \sim 0$ and for Ni, $\left(\frac{\partial J}{\partial r}\right) < 0$ in their pure crystals according to the Bethe-Slater curve.

Considering positional disorder the mean field theory description of the Curie temperature can be modified to yield:

$$T_c = \frac{NS(S+1)}{3k_B} \int J(r)g(r)dr \tag{19.78}$$

where $g(r)$ represents the previously defined pair correlation function. Another approximate method for arriving at the positional disorder (Δr) is to use the Scherrer peak broadening in an amorphous XRD pattern.

The temperature-dependence of the magnetization for amorphous alloys has been fit using a two-parameter exchange fluctuation mean field theory [GWLM99]. This is shown to give better fit m(T) data than a single parameter model for amorphous alloys. The modification made to the Handrich-Kobe [Han69] [Kob69] model defined two δ-parameters, δ_+ and δ_- to yield the mean field equation:

$$m(T) = \frac{1}{2}\Big(B_s[(1+\delta_+)x] + \Big(B_s[(1+\delta_-)x]\Big) \tag{19.79}$$

whereδ_+ and δ_- can differ due to the position on the Bethe-Slater curve. The *Gallagher* model gives a better quantitative fit to the temperature dependence of the magnetization.

19.3.9.6 Random Magnetic Anisotropy

The discussion of an effective magnetocrystalline anisotropy in both amorphous and nanocrystalline materials is deeply rooted in the notion of a random local anisotropy as presented by [ABC78b] [ABC78a]. The original basis for this model is in the problem of averaging over randomly oriented local anisotropy axes. The random anisotropy model leads to a small effective magnetic anisotropy due to the statistical averaging of the magnetocrystalline anisotropy.

In amorphous alloys the notion of a *crystal field* (which determined K in crystalline materials) is replaced by the concept of a short-range local field on the scale of several ~ 1 nm. The symmetry of the local field determines the local magnetic anisotropy, $K_1(r)$. The symmetry of the local field in amorphous alloys depends on local coordination and chemical short-range order in the amorphous alloys. The local anisotropy may large but is averaged out due to fluctuations in the orientation of easy axes. The statistical averaging of the local anisotropy takes place over a length scale equivalent to the ferromagnetic exchange length length, L_{ex}.

As in the macroscopic picture of a domain wall, the local anisotropy correlation length is determined by a balance of exchange and anisotropy energy densities. Considering these two terms in the *magnetic Helmholtz free energy*, F_V (i.e. ignoring field and demagnetization terms) can be expressed as:

$$F_v = \int_V A(r)|\nabla \vec{m}|^2 - K_1(r)[\vec{m}\cdot\vec{n}]^2 \tag{19.80}$$

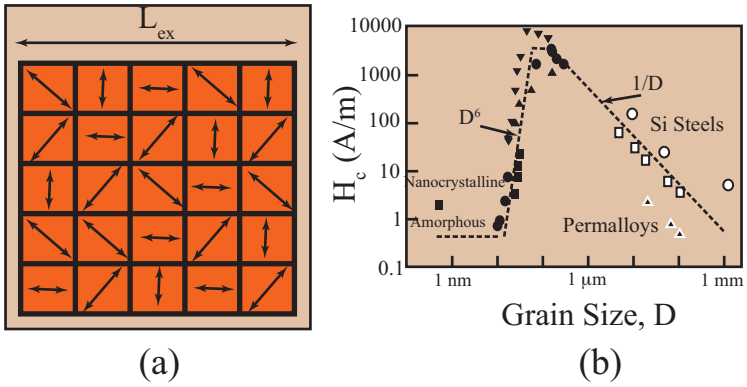

Fig. 19.58. (a) Cartoon illustrating N nanocrystalline grains of dimension D, in a volume L_{ex}^3 and (b) the dependence of coercivity on grain size in the Herzer model.

where $A = A(r)$ is the local exchange stiffness, $\vec{m} = \frac{\vec{M}(r)}{M_s}$ is the reduced magnetization, $\vec{n}$ is a unit vector in the local direction of an easy axis, and $K_1 = K_1(r)$ is the leading term in the expansion of the local magnetic anisotropy. If we denote the length scale of chemical or structural fluctuations in the amorphous material as l (this will be on the order of 1 nm for a typical amorphous material). For this case $L_{ex} >> l$ (or D_g) in soft materials and a statistical averaging of $K_1(r)$ over a volume of $\sim L_{ex}^3$ is warranted. Considering a random walk through a volume L_{ex}^3, which samples all local anisotropies, leads to a scaling of $K_1(r)$ by $(\frac{L_{ex}}{l})^{\frac{3}{2}}$ to arrive at an effective anisotropy K_{eff}. This scaling is responsible for the substantial reduction of the magnetic anisotropy in amorphous alloys. In TM-based amorphous alloys where $K_1(r)$ is small to begin with and $L_{ex} >> l$ then $K_{eff}$is very small in good agreement with experimental observations for amorphous transition metal alloys. On the other hand for amorphous rare earth based materials where $K_1(r)$ is large and L_{ex}^3 may sample only a few fluctuations in n then K_{eff} can remain quite large [ABC78b] [ABC78a]. Amorphous rare earth alloys with substantial coercivities are often observed.

Consideration of the benefits of nanocrystalline alloys for soft magnetic applications include the coercivity and the permeability. Reduction of coercivity and the related increase in permeability are both desirable properties that can be found in select amorphous and nanocrystalline alloys. The extension of the random anisotropy model by Herzer [Her97] to nanocrystalline alloys has also been used as the premise for explaining the soft magnetic properties of these materials (Fig. 19.58). The Herzer argument for effective anisotropies in nanocrystalline materials builds on the arguments of the random anisotropy model for amorphous alloys presented above.

Herzer considers a characteristic volume whose linear dimension is the magnetic

exchange length, $L_{ex} \sim (\frac{A}{K})\frac{1}{2}$. The Herzer argument considers N grains, with random easy axes, within a volume of Lex3 to be exchange coupled. Since the easy axes are randomly oriented, a random walk over all N grains will yield and effective anisotropy which is reduced by a factor of $\left(\frac{1}{N}\right)^{\frac{1}{2}}$ from the value K for any one grain, thus $K_{eff} = \frac{K}{\sqrt{N}}$. The number of grains in this exchange coupled volume is $N = \left(\frac{L_{ex}}{D}\right)^3$, where D is the average diameter of individual grains. Treating the anisotropy self-consistently, then:

$$K_{eff} \sim K D^{\frac{3}{2}} \sim \left[\frac{K_{eff}}{A}\right]^{\frac{3}{2}} \sim \left[\frac{K^4 D^6}{A^3}\right] \tag{19.81}$$

Since the coercivity can be taken as proportional to the effective anisotropy, this analysis leads to Herzers prediction that the effective anisotropy and therefore the coercivity should grow as the 6th power of the grain size: $H_c \sim H_K \sim D^6$ For such a reduction in the coercivity to be realized, Herzer noted that the nanocrystalline grains must be exchange coupled. This is to be contrasted with uncoupled particles that have an exchange length comparable to the particle diameter and are susceptible to superparamagnetic response.

19.3.9.7 Pair Order Anisotropy

Induced anisotropy is also very important in tailoring the properties of amorphous and nanocomposite magnets. Many ferromagnetic materials exhibit an uniaxial anisotropy when they are processed in a magnetic field. An *induced anisotropy* parallel (or perpendicular) to the applied magnetic field direction can be obtained .Controlling the magnetic anisotropy in amorphous soft magnetic materials is important to technical applications of the materials. Induced anisotropy includes: (a) roll-anisotropy, (b) stress annealing anisotropy, (c) field induced anisotropy, etc.

Field induced anisotropy is obtained by annealing in a magnetic field. The mechanism requires the presence of different atomic species that are thought to form ordered atomic pairs aligned with, or perpendicular to the field as illustrated schematically in Fig. 19.59. Fig. 19.59 (a) shows hypothetical atomic arrangements in a random equiatomic A-B alloy. Here the atoms are distributed among sites randomly. Fig. 19.59 (b) shows an ordered equiatomic A-B alloy for comparison. Fig. 19.59 (c) shows the same alloy with directional pair ordering. In directional pair ordering, more atomic pairs A-B pairs point in the direction (or perpendicular to) the field direction.

Field annealing yields induced uniaxial anisotropy in the direction of the applied field as shown in Fig. 19.59 (d). This can be used to tailor the hysteresis loop to influence the permeability (Fig. 19.59 (d)). This can result in the annealing field in a direction transverse to the magnetic path will shear the loop and result in a nearly linear B-H response. The magnetization process is dominated by the rotation of moment

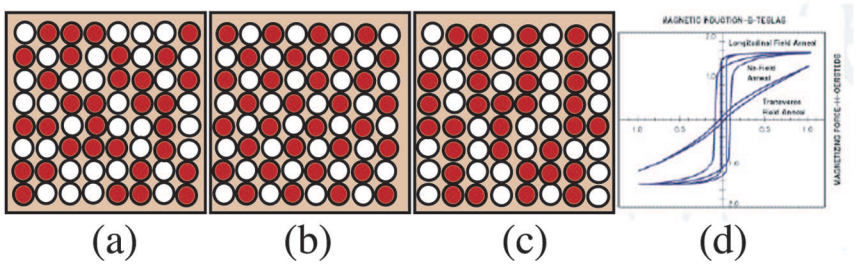

Fig. 19.59. (a) Random atoms in an A-B alloy system, (b) an ordered equiatomic A-B alloy, (c) directional pair ordering and (d) shearing of the hysteresis loop from pair ordering.

vectors within domains, and domain wall motion is minimized. This is important in minimizing the power loss due to irreversible wall motion past defects.

Important technical magnetic properties of amorphous magnetics also derive from *random magnetic anisotropy*. The magnetic anisotropy in amorphous materials is typically low. Interesting properties also derive from zero magnetostriction in Co-based alloys.

19.3.9.8 Examples of Amorphous Metal Alloy Systems.

Common glass forming systems include Group IIa-transition metal, actinide-transition metal, and early transition metal (TE)-Group IIa alloy systems [AE83]. There are several classes of alloy systems that have been shown to have commercial potential. The first of these, *metal-metalloid amorphous systems* include simple metal, early transition metal and late transition metal metalloid systems. The second class are the *rare earth transition metal (RETM) amorphous systems*, and the third class are the *late transition metal (TL) - early transition metal (TE) systems*. In this section, we discuss each of these classes as well as a few interesting multicomponent systems.

Metal - Metalloid Systems.

Metal-metalloid systems include early (TE) or late (TL) transition metals along with *metalloids* (M = C, B, P, Si, etc.). Eutectic compositions are found near 20-30 at% M in typical TL-M systems . The eutectic alloy composition is often bracketed by a solid solution and an intermetallic alloy with composition richer in M. There may also be other M-rich high temperature phases and/or metastable intermetallic phases.

TL-M systems are among the important amorphous systems for magnetic applications. In these alloys, considerations of glass forming abilities and the desire to maintain high early transition metal (typically Fe or Co and sometimes Ni) concentrations are paramount. A series of eutectics that form near the Fe- and Co-rich edges of TL-M binary phase diagrams are summarized in Table 19.7.

Table 19.7. *Glass forming ability parameters (eutectic composition and temperature, and solubility) in binary TL-M systems [MWL99].*

Binary Alloy	x_e (at%)	x_e (wt%)	T_e (°C)	Solubility of X at 600 (°C) (at%)	Terminal Phases
Fe-B	17	3.8	1174	0	Fe, Fe_2B
Co-B	18.5	4.0	1110	0	Co, Co_2B, (Co_3B)
Cr-C	14.0	3.6	1530	0	Co, C_6Cr_{23}
Fe-P	17	10.2	1048	1	Fe, Fe_3P
Co-P	19.9	11.5	1023	0	Co, Co_2P
Fe-Si	33	20	1200	10	Fe, β-Fe_2Si, (Fe_3Si)
Co-Si	23.1	12.8	1204	8	Co, α-Co_2Si, (Co_3Si)

Rare Earth - Transition Metal Systems.

Amorphous *rare earth - transition metal (RETM) systems* have been studied widely, in part because of their importance as *magneto-optic materials*. $Co_{80}Gd_{20}$ amorphous alloys were the first materials considered for magneto-optic recording. [CCG73] discovered the phenomenon of perpendicular magnetic anisotropy (PMA) in amorphous $GdCo$ films. In a presumably isotropic amorphous material, this anisotropy was puzzling. Atomic structure anisotropy (ASA) was proposed as a source of the large PMA. This anisotropy results from preferential ordering of atomic pairs in the amorphous materials. Another model [GC78] proposed selective resputtering to explain the ASA. In 1992, [HS85] employed the polarization properties of EXAFS (see section **??**) to measure and describe the anisotropic atomic structure and relate it to the amplitude of the PMA in amorphous $TbFe$. They reported a direct measure of the ASA in a series of amorphous $TbFe$ films and correlated it with the growth conditions and the magnetic anisotropy energy [HP01].

Early Transition Metal - Late Transition Metal Systems.

Early transition metal - late transition metal binary alloy systems can have eutectics on both the TE- and TL-rich sides of the phase diagram. Of technological importance for magnetic applications are the TL-rich eutectics, since Fe, Co and Ni, the ferromagnetic transition metals, are TL species. The TL-rich eutectics are of interest in that they typically occur at 8-20 at% of the TE species. These alloys do not have as deep a eutectic, making them harder to synthesize, but they do have larger T_{x1} temperatures, making the resulting amorphous alloys more stable.

Eutectics forming near the Fe- and Co-rich edges of TL-TE binary phase diagrams

Table 19.8. *Glass forming ability parameters (eutectic composition and temperature, and solubility) in binary TL-TE systems [MWL99].*

Binary Alloy	x_e (at%)	x_e (wt%)	T_e (°C)	Solubility of X at 600 (°C) (at%)	Terminal Phases
Fe-Zr	9.8	15.1	1337	0	Fe, Fe_3Zr
Co-Zr	9.5	14	1232	0	Co, γ-Co_5Zr, (δ-Co_4Zr)
Fe-Hf	7.9	21.9	1390	0	Fe, λ-Fe_7Hf_3
Co-Hf	11	27.2	1230	0.5	Co, Co_7Hf_2, $Co_{23}Hf_6$
Fe-Nb	12.1	18.6	1373	0	Fe, Fe_2Nb
Co-Nb	13.9	20.3	1237	0.5	Co, Co_3Nb
Fe-Ta	7.9	21.7	1442	0	Fe, Fe_2Ta
Co-Ta	13.5	32.4	1276	3	Co, Co_2Ta

are summarized in Table 19.8. Terminal alloy compounds and other phases in proximity to the eutectic in these systems include Fe_2Zr, Fe_2Hf, Co_2Zr and Co_2Hf phases, which all have the cubic $MgCu_2$ Laves phase structures. The Fe_2Ta, Co_2Ta, Fe_2Nb and λ-Fe_7Hf_3 phases have the hexagonal $MgZn_2$ Laves phase structures. Other compounds include Fe_3Zr, δ-Co_4Zr and $Co_{23}Hf_6$ (with the cubic Th_6Mn_{23} structure).

19.4 Current and Emerging Areas

19.4.1 Nanocomposite Magnets

Magnetic properties stemming from chemical and structural variations on a nanoscale are among those most significantly impacted by amorphous metals. Recent research has focused on *nanocomposite* and *bulk amorphous alloys* for many applications. A *metal/amorphous nanocomposite* is produced by nanocrystallization of a multicomponent amorphous precursor, to yield a nanocrystalline phase embedded in an amorphous matrix. Important nanocomposites have nanocrystalline grains of a (*bcc*, $D0_3$ or CsCl) Fe(Co)X phase, consuming $20-90\%$ oby volume in an amorphous matrix. A typical nanocomposite microstructure [Wil00] is illustrated in Fig. 19.60. Table 19.9 lists magnetic nanocomposite and bulk amorphous systems. Magnetic applications also exist for *bulk amorphous alloys*, which can often be synthesized at cooling rates as low as 1 K/s.

Understanding *primary nanocrystallization* is important in developing nanocomposites [MJO$^+$03]. Fe-based metallic glass crystallization is the most widely studied process [Lub77]. Typical commercial Fe-based metallic glass alloys are *hypoeutectic* (Fe-rich), and are observed to crystallize in a two-step process. A primary crystallization reaction (Am $\rightarrow$ Am$'$ + α-Fe) is followed by secondary crystallization of the glass

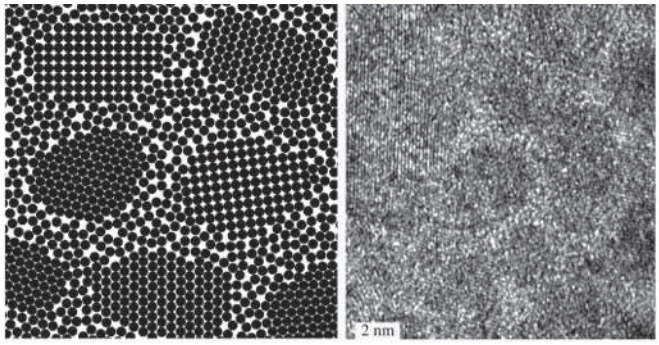

Fig. 19.60. (a) cartoon of a nanocomposite with nanocrystals embedded in an amorphous matrix; (b) high resolution TEM image of a nanocrystallized HITPERM material [WLM$^+$98].

Table 19.9. *Examples of nanocrystalline and bulk amorphous alloy systems.*

Alloy composition	Citation	Alloy composition	Citation
Fe-Si-B-Nb-Cu	[YOY88]	Fe-Si-B-Nb-Au	[KMIM89]
Fe-Si-B-V-Cu	[ST90]	Fe-(Zr,Hf)-B	[SKI$^+$90]
Fe-(Ti,Zr,Hf,Nb,Ta)-B-Cu	[SMK$^+$91]	Fe-Si-B-(Nb,Ta,Mo,W,Cr,V)-Cu	[YY91]
Fe-P-C-(Mo,Ge)-Cu	[FFST91]	Fe-Ge-B-Nb-Cu	[YBYS92]
Fe-Si-B-(Al,P,Ga,Ge)-Nb-Cu	[YBYS92]	Fe-Zr-B-Ag	[KYK$^+$93]
Fe-Al-Si-Nb-B	[WST93]	Fe-Al-Si-Ni-Zr-B	[CIN93]
Fe-Si-B-Nb-Ga	[Tom94]	Fe-Si-B-U-Cu	[SPK$^+$95]
Fe-Si-B-Nd-Cu	[MMK96]	Fe-Si-P-C-Mo-Cu	[LGX$^+$96]
Fe-Zr-B-(Al,Si)	[IG96]	Fe-Ni-Zr-B	[KDS$^+$96]
Fe-Co-Nb-B	[KHD$^+$97]	Fe-Ni-Co-Zr-B	[IZIT97]
Fe-Co-Zr-B-Cu	[WLM$^+$98]		

former enriched amorphous phase, Am′ [KH81]. [LL78] studied the crystallization kinetics of $\mathrm{Fe}_x\mathrm{B}_{1-x}$ alloys using *differential scanning calorimetry (DSC)*. Activation energies for crystallization were determined to be largest for the eutectic compositions.

Amorphous alloy precursors to nanocomposites are typically based on ternary (or higher order) systems. These are often variants of TL/TE/M systems. In many cases, a small amount of a fourth element (making the alloys *quaternary*) such as Cu, Ag, or Au can be added to promote nucleation of the nanocrystalline phase. Five- and six-component systems are also commonplace if more than one metalloid and/or early transition metal species are used as glass formers. A matrix of typical elements in

many amorphous phases is given by [Wil00]:

$$\begin{bmatrix} \mathrm{Fe} \\ \mathrm{Co} \\ \mathrm{Ni} \end{bmatrix} \begin{bmatrix} \mathrm{Ti} & \mathrm{V} & \mathrm{Cr} \\ \mathrm{Zr} & \mathrm{Nb} & \mathrm{Mo} \\ \mathrm{Hf} & \mathrm{Ta} & \mathrm{W} \end{bmatrix} \begin{bmatrix} \mathrm{B} & \mathrm{C} & \\ \mathrm{Al} & \mathrm{Si} & \mathrm{P} \\ \mathrm{Ga} & \mathrm{Ge} & \end{bmatrix} \begin{bmatrix} \mathrm{Cu} \\ \mathrm{Ag} \\ \mathrm{Au} \end{bmatrix}$$

Magnetic metal/amorphous nanocomposites [MWL99] have excellent soft magnetic properties as measured by the figures of merit of combined magnetic induction and permeability, high frequency magnetic response, and retention of magnetic softness at elevated temperatures. Applications have been identified for the patented Fe-Si-B-Nb-Cu alloys (trade-name FINEMET) [YOY88] and $\mathrm{Fe}\,M\,\mathrm{B}\,\mathrm{Cu}$ alloys (trade-name NANOPERM) [SKI$^+$90]. Another nanocomposite $(\mathrm{Fe}_{1-x}\mathrm{Co}_x)_{88}\mathrm{M}_7\mathrm{B}_4\mathrm{Cu}$ (M = Nb, Zr, Hf) soft magnetic material is known as HITPERM [WLM$^+$98]; HITPERM has a superior high temperature magnetic induction.

Two routes are possible for inducing anisotropy in nanocrystalline alloys are possible. The first is *field annealing*, where a previously crystallized alloy is annealed in an applied field at a temperature below the secondary crystallization temperature. In the second, called *field crystallization*, the amorphous precursor is field annealed and the nanocrystalline grains are precipitated in the presence of the field. In addition to pair ordering, the field crystallization technique holds potential for altering the crystalline texture of the precipitated grains. This would allow magnetocrystalline anisotropy as well as induced anisotropy to be controlled.

19.4.1.1 Crystallization of Metallic Glasses.

We categorize *crystallization reactions* from a parent amorphous phase. In analogy with non-diffusional transformations in solids. The discussion of crystallization in amorphous alloys and *micromechanisms of crystallization* follows the work of U. Koster [KH81]. We illustrate transition metal metalloid metallic glasses. We can, however, use this to discuss crystallization of other amorphous alloys. We use the Fe-B-phase diagram (Fig. 19.61) as an example.

Consider a chemically homogeneous amorphous solid. Phase transformations can be diffusional or non-diffusional. Non-diffusional phase transformations can occur where the parent phase and final phase are both amorphous i.e. :

$$\beta(amorphous) \rightarrow \alpha(amorphous) \tag{19.82a}$$

An example is a pseudo-*martensitic phase transformations* in metallic glasses [CO85] where change in local short-range order from *fcc*- to *hcp*-like is inferred from thermal hysteresis in magnetic anisotropy. Diffusional decomposition reactions are reported where the parent phase and final phase are both amorphous i.e.:

$$\alpha'(amorphous) \rightarrow \alpha(amorphous) + \beta(amorphous) \tag{19.82b}$$

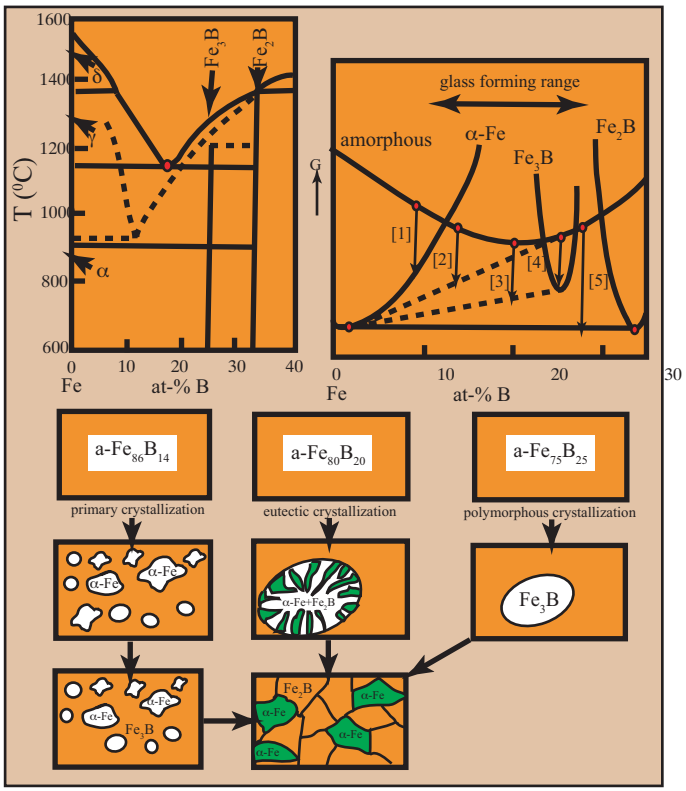

Fig. 19.61. (a) Fe-B phase diagram (b) G(X) curves and crystallization reactions and (c) microstructure development during crystallization or other decomposition reactions.

This can occur by *nucleation and growth* or other mechanisms. An example is amorphous phase *spinodal decomposition* that is observed in Zr-Ti-Be metallic glasses.

Crystallization reactions require the parent phase to be amorphous and one or more of the final phases crystalline. The *polymorphic crystallization* is a non-diffusional phase transformation where an amorphous parent phasecrystallizes to a final phase of the same composition according to the reaction:

$$\beta(amorphous) \rightarrow \alpha(crystalline) \tag{19.82c}$$

The stable crystalline phase could be a supersaturated alloy or a metastable or stable crystalline compound. Polymorphic crystallization is not a common alloy primary crystallization route as they requires compositions that are either close to that of the pure element or compounds. Further decomposition of the crystalline phases, e.g. precipitation form the supersaturated solid, are possible routes to equilibrium structures.

Crystallization reactions that are diffusional can be classified as *primary crystallization* or *eutectoid crystallization*, respectively. Primary crystallization is a diffusional phase transformation where the parent phase is amorphous and the final phases are a crystalline phase and an amorphous phase depleted of the primary component of the crystalline phase. Examples in a simple A-B eutectic system would be:

$$\delta(amorphous) \rightarrow \alpha(A-rich, crystalline) + \beta(amorphous) \quad (19.82d)$$

$$\delta(amorphous) \rightarrow \gamma(B-rich, crystalline) + \beta(amorphous) \quad (19.82e)$$

Equilibrium is achieved through subsequent secondary crystallization of the new amorphous phase.

A diffusional phase transformation where the parent phase is amorphous and the final phases are both crystalline phases and an amorphous phase depleted of the primary component of the crystalline phase is called *eutectoid crystallization*. A typical eutectoid reaction is given by:

$$\gamma(amorphous) \rightarrow \alpha(A-rich, crystalline) + \beta(B-rich, crystalline) \quad (19.82f)$$

Eutectoid crystallization is analogous to eutectic crystallization, in that it requires mutual diffusion between the A-rich α and B-rich β phases. Fig. 19.61(a) illustrates a binary Fe-B phase diagram on the Fe-rich end of the diagram. Fig. 19.61(b) illustrates hypothetical free energy curves for crystalline and amorphous phases in the Fe-B alloy system. Here equilibrium crystalline phases on the iron-rich side of the phase diagram include α-iron, and the compounds $\mathrm{Fe_3B}$ and $\mathrm{Fe_2B}$ (analysis can be made more complicated by considering the possibility of metastable γ-iron, and $\mathrm{Fe_2B}$).

For amorphous alloys of various compositions [1] [5] *crystallization reactions* can be described. Reaction [1] is an example of *polymorphic crystallization* of α-iron. Reaction [4] is an example of *polymorphic crystallization* of $\mathrm{Fe_3B}$. Reaction [2] represents the *primary crystallization* of α-iron. Reaction [3] represents the simultaneous *eutectoid crystallization* of α-iron and $\mathrm{Fe_3B}$. Reaction [5] represents the simultaneous *eutectoid crystallization* of α-iron and $\mathrm{Fe_2B}$.These are examples of *discontinuous reactions*. As can be seen in Fig. 19.61(b) these reactions have the largest driving force and are therefore thermodynamically favored. On the other hand, they require two components to separate into two new phases and therefore should take more time than *polymorphic reactions*, where no diffusion is required, or even *primary crystallization* where solute is expelled to an existing amorphous phase which becomes enriched in glass formers.

The replacement of B by Si increases the activation energy barriers in Fe-based metallic glasses [RF82]. The primary crystallization temperature, T_{x1}, has been studied as a function of transition metal substitution, X, in $\mathrm{M_{78-x}X_xSi_{10}B_{12}}$ compounds [DD78] . Variations in T_{x1} are explained using the *Hume-Rothery rules*, correlating

T_{x1} with the cohesive energies of the pure X species and the atomic size. Two important observations were that: (1) Cu additions, which promote the nucleation of the primary nanocrystals by clustering, resulted in significant reductions in T_{x1}, with additions as small as 0.5-1.0 at %; and (2) early transition metal (e.g. Zr, Hf, Mo) additions impede growth and result in the largest primary crystallization temperatures.

Primary crystallization is important in developing nanocomposite microstructures, as microstructures can be stabilized with nanocrystals embedded in an amorphous matrix that is more stable than the parent phase. Increases in magnetization often accompany primary crystallization which can be probed in thermomagnetic measurements [JHG$^+$01]. Inhomogeneity in the composition of the new amorphous phase after primary crystallization results from the build up of early transition metal species near the nanocrystal amorphous phase interface which can be probed by *atomic probe field ion microscopy, APFIM* [PWH$^+$01] [OQL$^+$09]. Nanocrystallization has been analyzed using Johnson-Mehl-Avrami nucleation and growth kinetics with morphology indices identifying the micromechanisms [HTW$^+$99], [HML$^+$02].

It is only through secondary or higher order transformations that the amorphous phase is completely consumed. Interesting primary and secondary crystallization reactions often yield metastable crystalline phases in pathways toward eventual equilibration. Secondary crystallization can often have sluggish kinetics because of the complicated crystal structures of the product phase. Of particular recent interest has been in phases with stoichiometries $\mathrm{Fe_{23}B_6}$ [ZBC$^+$03], [LOLM07] and $\mathrm{Fe_{23}Zr_6}$ and their stabilities [OCL$^+$08]

19.4.1.2 Figures of Merit for Nanocomposite Magnets.

Fig. 19.62 shows figures of merit for soft magnets [MWL99], the saturation induction and permeability. Permeability is inversely proportional to coercivity, H_c. Improving soft magnetic properties requires tailoring chemistry microstructural optimization, recognizing that H_c decreases with grain size (D_g) for $D_g >\sim 0.1 - 1\mu$m where D_g exceeds the domain wall width (δw). Grain boundaries impede wall motion so Hiperco, etc. are widely used in inductive applications due to high flux density, high permeability and low core losses.

Coercivity mechanisms [MWL99] indicate that for $D_g <\sim 100$ nm, H_c decreases rapidly with decreasing D_g (Fig. 19.58). It is understood that when the domain wall thickness is large fluctuations in magnetic anisotropy on the scale of D_g are irrelevant to wall pinning. $\mathrm{Fe\,Co}$-based nanocomposites (HITPERM) [MWL99] [WLM$^+$98] exhibit excellent soft magnetic properties through exploiting this Herzer model [Her97]. Alloys near equiatomic Fe-Co ratios are standard bearers for high induction with grains much smaller than domains [LQN$^+$07]. The potential for nanocomposites alloys to push the envelope for high-f magnetic components, increasing power densities and allowing smaller volume components is pushing recent soft magnet development.

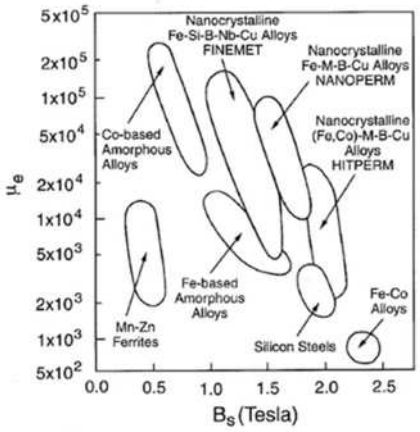

Fig. 19.62. Figures of merit for soft magnets, saturation induction and permeability [MWL99].

The *bcc*-derivative nanocrystals embedded in an amorphous matrix have high saturation induction and low core losses unobtainable in amorphous or large grained crystalline alloys. Increased glass former concentration in the intergranular amorphous phase impede diffusion, prevent grain coarsening and allow nanostructure retention [MWL99]. HITPerm alloys are of particular interest for high temperature applications.

19.4.1.3 Applications of Nanocomposite Magnets.

There is an increasing demand for miniaturization and higher power density in electronics operating at high frequency and high temperature. It is desirable that magnetic materials have improved properties such as low core loss, high saturation magnetic flux density, high Curie temperature, T_c, and linear magnetization as a function of field at high frequencies. Previously mentioned soft magnets do not satisfy these new requirements because of high core losses at high frequencies, relatively low saturation induction, and/or relatively low temperature stability of magnetic properties. Amorphous alloys have properties desirable in applications such as pulse transformers and high frequency inductors but are generally not stable at elevated temperatures.

Materials for power electronic applications must compete with Si-steels and their high saturation flux density ($B_s \sim 2$T). Si-steels, prevalent in 60 Hz transformers, have high losses, at frequencies > 1 kHz. Applications requiring operation at higher frequencies have turned to low loss materials such as FINEMET. FINEMET, however, has a relatively low $B_s \sim 1.24$ T. Nanocomposites can provide high flux density approaching that of Si-steels, tunable permeabilities, and low losses [YOY88],

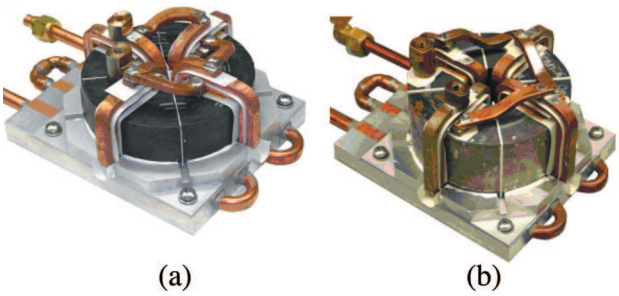

Fig. 19.63. Size comparison of a (4.23 in. OD) converter constructed from (a) HITPERM and (b) FINEMET [LMU$^+$08].

[WLM$^+$98], [ILML99] comparable to ferrites due to unique nanostructures with higher B_s. Fe-based nanocoposites can have large inductions but relatively low T_c's [SKI$^+$90], [SMK$^+$91], [SMIM91], [SKM$^+$91]. Co-additions to Fe-based nanocomposites increases flux density and improves magnetic properties at elevated temperatures.

A promising HITPERM alloy has been reported that exhibited low losses and applicability in a dc-dc converter [Lon08]. Recent developments have shown that the early transition (TE) metal content could be reduced without significantly increasing the core loss to achieve higher flux B_s [MSMM10]. Other alloys, with P-additions, have completely eliminated TE elements in order to compete with Si-steels [MMK$^+$09] but have been targeted for lower frequency applications.

New materials with high B_s and low losses at higher frequencies can reduce inductor size in high frequency applications increasing efficiency through weight reduction for dc-dc converters in electric vehicles [LMU$^+$08]. A HITPERM nanocrystalline alloy was developed for high-power inductors for Army electric vehicle applications [LMU$^+$08]. A core wound (Fig. 19.63) was used to construct a 25μH inductor for use in a 25 kW DC-DC converter with a reduction in the overall size (by ~ 30 %) compared with FINEMET. The nanocomposite's ability to operate at 20 kHz as compared with 1 kHz offers 10-fold or more size reduction compared to Si-steel.

Devices using high induction nanocomposite cores at 20-100 kHz with significant core size reductions can translate directly to cost savings [NV09], [LMU$^+$08], [Rea08]. In addition to power converters, this can impact inverters and power transformers. A high frequency, high power transformer, using a Fe-Si-based (FINEMET) nanocomposite, constructed demonstrated dramatic reductions in weight (300x) and electrical losses (1000x) as compared to Si-steel transformers [Rea08].

State-of-the-art Fe-rich alloys have losses of $500\frac{kW}{m^3}$ (100 kHz, 0.2 T) [KMS$^+$11] comparing favorably to Mn-Zn ferrites (500 kW/m^3,100 kHz, 0.2 T). Benefits of cold- and hot- rolling to reduce ribbon cross-sections may result in increases in operating

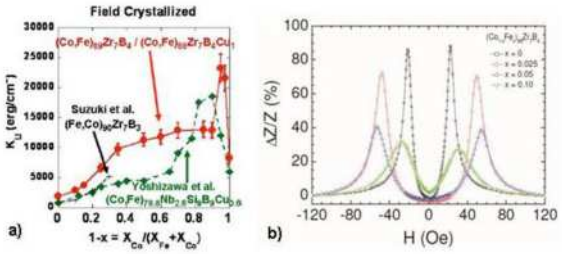

Fig. 19.64. (a) Field induced anisotropy as a function of Fe, Co-ratio for HITPERM nanocomposites [OLL$^+$08] and (b) GMI as a function of field for Co-rich alloys [CLP$^+$11].

frequency. An issue for long-term high temperature material stability is polymorphic secondary crystallization [KMS$^+$11] at reduced glass former concentrations.

Co-rich nanocomposite materials [OML$^+$08], [OPL$^+$08], [OQL$^+$09] also have significant promise for high frequency applications [DMO$^+$11]. They have small magnetostrictions, strong field annealing response [OLL$^+$08], [OML$^+$09] (Fig. 19.64(a)) and superior mechanical properties. They also have promise for sensing applications using the Giant Magnetoimpedance effect [CLP$^+$11], [LCL$^+$11] (Fig. 19.64(b)) .

GMI is a large variation of the impedance of a magnetic conductor in a field. GMI is observed in soft magnets with large electrical conductivities and is largest in materials where the thickness is comparable to the skin depth. Most attention has been paid to improving GMI effect by tuning alloy compositions or thermal annealing in an applied magnetic field. GMI can also be changed by sample shape.

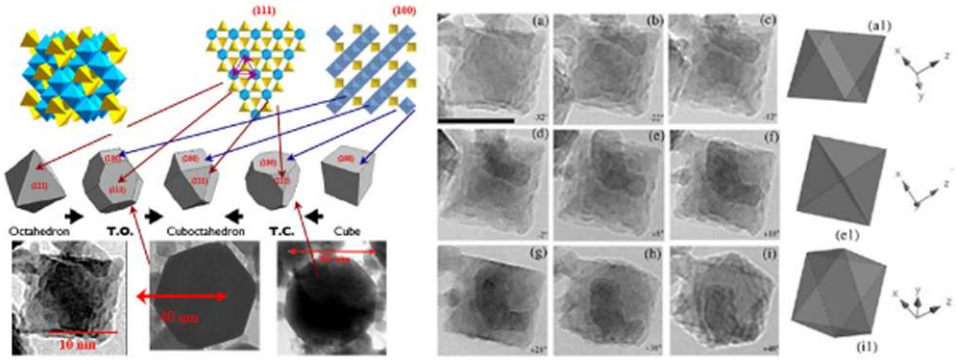

Fig. 19.65. Left: (top) Coordination polyhedral in spinel (Blue = B-site cation, Yellow = A-site cation); (middle) cuboctahedral shapes and (bottom) TEM observations of nanoparticles [Swa05]. Right: 2D projected morphologies [(a)-(i)] at different tilt angles for small octahedral nanoparticle. (a1), (e1) and (i1) are projections of an octahedron. Scale bar on (a) is 20 nm.

19.4.2 Magnetic Nanoparticles and Core Shell Structures

Nanomaterials research impacts many diverse applications [ML00]. Magnetic properties are distinctly different at the nanoscale because many magnetic length scales are on the order of 10 - 100 nm. Engineering magnetic nanostructures allows for tailoring magnetic properties. Magnetic nanoparticles (MNP's) have therefore been studied for a variety of applications over the last decades. Many new applications of MNPs require high frequency switching and power absorption of materials that have oxidation stability. This is achieved in some interesting MNP systems having metallic magnet cores with thin adherent protective oxide shells [TNPM99]. The thin shells not only passivate the particles but the oxide shells are more easily functionalized. MNPs amenable to functionalization for synthesis of aqueous magnetic fluids (ferrofluids) make them attractive for biomedical applications and incorporation into polymer nanocomposites.

Synthesis of MNPs is performed in the solid, liquid or gaseous states. Solid-state synthesis begins with bulk solids (often micron-sized powder precursors) and transforming them to nanostructures by mechanical milling and thermal processing. Other approaches include plasma torch synthesis, chemical vapor deposition, molecular beam epitaxy, focused ion beam milling, and lithography. These methods allow synthesis of large quantities of material but often with polydisperse size distributions.

Plasma torch synthesis has been used to produce large quantities of MNPs. Plasma torch synthesis is a high throughput method for MNP synthesis. Thermal plasma processing [Tur99] has been used to produce a variety of MNP chemistries:

(i) Alloy nanopowders (Fe-Co and Fe-CoV) [THG+97], [TNPM99], [Tur99];

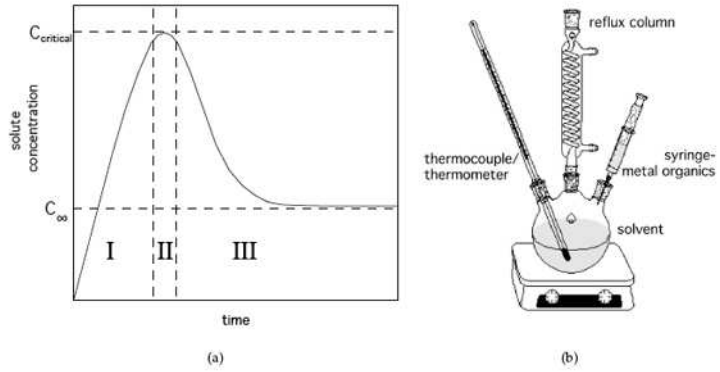

Fig. 19.66. (a) Schematic of the La Mer process (a) (I) prenucleation, (II) nucleation, and (III) growth stages of chemical synthesis and (b) chemical synthesis apparatus. [McN99].

(ii) Carbon-coated nanocrystalline powders (Fe-Co and Fe-Co-V) nanopowders using acetylene as an auxiliary gas source [Tur99];

(iii) Nitrogen martensite (γ-FeN_x) nanoparticles using nitrogen/ammonia as the auxiliary gas source [TFH$^+$99];

(iv) Oxide coated ($CoFe_2O_4$-FeCo) core shell nanoparticles [TNPM99]; and

(v) Mixed ferrites (Fe_3O_4, $MnFe_2O4$, $(MnZn)Fe_2O_4$, $NiFe_{2a}$nd $(NiZn)Fe_2O_4$ for high frequency magnetic applications) [STC$^+$02], [SSM03], [SMCD05].

The crystallography of terminating faces determines the symmetry of atomic environments. In oxides, as the polyhedral environments at the surface differ from the bulk, so do the cationic crystal fields that determine magnetocrystalline anisotropy and ferrimagnetic superexchange interactions. These changes, increased relative importance in MNPs, can influence the magnetic properties and surface activity. Fig. 19.65 illustrates the surface chemistry and facets of some ferrite nanoparticles.

Chemical synthetic approaches involve assembling atoms, molecules and particles to produce materials at a nano- or macroscopic scale [McN99]. These methods are preferred for monodisperse particles to exploit size-dependent properties. Monodisperse particles are are uniform in size, shape and internal structure and have a *coefficient of variation* (standard deviation/mean size) less than about 10%. Chemical synthesis in gas and liquid-states benefits from diffusion coefficients which are orders of magnitude larger than in the solid state, making chemical homogenization much quicker. Liquid-phase chemical synthesis has been conducted in a range of aqueous or non-aqueous solvents. Dissolved metal precursors form thermodynamically unstable supersaturated solutions, from which homogeneous (in solution) or hetero-

geneous (on vessel walls or impurities) nucleation of MNPs takes place. The LaMer process (Fig. 19.66) is a common technique for chemical synthesis of monodisperse MNPs [MKLM10], [McN99].

19.4.2.1 Properties of Magnetic Nanoparticles.

Faceted MNPs with core shell nanostructures [CJM$^+$09] are important for several applications discussed below. For biomedical applications developing chemistries to functionalize with antibodies to promote attachment of the MNPs to body tissues is also desirable. This requires knowledge of: (a) synthesis of core-shell nanoparticles; (b) crystallographic facets of MNPs; (c) orientation relationships oxide shells and metallic cores; (d) properties of the nanocomposites and (e) performance in RF heating and magnetoelastic applications. Applications include the efficient point source heating of metallic nanoparticles [HOC$^+$08], [OHS$^+$09], [SHC$^+$09] for thermoablative cancer therapies, curing polymers and tagging implanted tissue scaffolds to track degradation and changing the shape for regenerative medicine [MSMC$^+$09].

A magnetic property important in many applications is a large saturation magnetization. In particular in biomedical applications concerns over toxicity suggest accomplishing functions with lower concentrations and with particles with passivated surface. The Slater-Pauling curve shows Fe-Co alloys to have the largest M_s (270 emu/g) of transition metal alloys, thus reducing the ferric content required to produce a comparable magnetic response to that of magnetite. Magnetite is also a commonly used magnetic material for applications with a reasonably high M_s (93 emu/g for bulk materials) and polar surfaces that are advantageous for functionalization [McN99].

Important magnetic properties that impact biomedical applications include saturation magnetization, magnetic anisotropy and the exchange interactions. The magnetization of FeCo core shell MNPs is determined by the chemistry and the core/shell volume ratios. Prior work using C-arc methods produced MNPs demonstrating the compositional dependence of the magnetization in $\mathrm{Fe}_x\mathrm{Co}_{1-x}$ C-coated MNPs [GJK$^+$96]. The largest moments were observed at nearly equiatomic compositions with deviation from Slater-Pauling predictions due to carbide formation. Recent work [JMW$^+$10] has shown the decrease in magnetization of MNPs as a function of controlled consumption of the core by the oxide shell. FeCo exchange interactions are also large so that the variation of magnetization with temperature is weak near room temperature.

In ferrites the strength and number of oxygen mediated J_{AB} and J_{BB} superexchange bonds determines the temperature dependence of the magnetization and the collinear or non-collinear [YK52] alignment of cation dipoles. The symmetry of surface polyhedra also determines surface magnetic anisotropy [JMW$^+$10]. In ferrite MNPs and ferrite shells on FeCo, surface and interface anisotropy can be an important means of tuning overall MNP magnetic anisotropies. The overall magnetic anisotropy of FeCo/ferrite MNPs can be tuned by choosing the core composition.

Thus, the core/shell radius ratio can be used as a means of controlling the total magnetic anisotropy.

19.4.2.2 Applications of Nanoparticles in Biomedicine.

An increasing interest in using magnetic nanoparticles for biological and medical applications has developed [PCJD03]. Researcher face new challenges and opportunities for using MNPs in biomedical applications. A highlight of current research are the challenges to functionalizing the materials to achieve biocompatibility for a host of applications. Ferromagnetic as well as superparamagnetic particles coated or encapsulated with polymers or liposomes are used for magnetic labelling.

Magnetite, $\mathrm{Fe_3O_4}$ and hematite $\mathrm{Fe_2O_3}$ have been used most commonly because of their ionic surfaces which aid functionalization and the fact that they are chemically inert contributing to biocompatibilty. Materials optimization for specific applications has demanded further efforts and consideration of a wider variety of materials where metals and alloys can play a role. Emerging techniques, therapies, and tools are made possible by developments in nanotechnology. Topics of current interest include:

(i) MRI Enhancement.
   (a) Principles of NMR.
   (b) Materials for MRI Enhancement.

(ii) Thermoablative Cancer Therapies - RF and Microwave Materials.

(iii) Magnetic Beads for Bioseparation, Cell Sorting and Drug Delivery.
   (a) Magnetic Nanoparticles for Bone Marrow and Blood Detoxification.
   (b) Magnetic Bead Tracking of Blood Flow and Stem Cells.
   (c) Targeted Drug Delivery.

(iv) Magnetoelastic Actuators, Sensors and MNP Cell Tagging.

(v) Nano-capsid Templating of Magnetic Nanoparticles.

(vi) Magnetic Microorganisms.

In this section we review a few selected applications where metallic nanoparticles are playing a significant role. These include MRI enhancement, RF heating applications, cell tagging and magnetoelastic applications. Of interest to several applications of MNPs is the *Neel relaxation* of superparamagnetic nanoparticles in an AC exciting field that allows MNPs to act as point heat sources. The RF power losses can cause local heating useful in *magnetic hyperthermia*. When nanoparticles can be placed near target cells they can be heated from a distance by RF fields generated in a coil assembly. The targeting of cancer cells need not be particularly selective because cancer cells typically die at temperatures $\sim 2^{\circ}\mathrm{C}$ lower than those of normal cells. Current issues

in developing this concept further is the need for highly efficient magnetic nanocrystals, stable under in-vivo conditions for non-invasive cancer therapies. Thermoablative cancer therapy are rooted in the RF heating of ferrofluids dicussed below.

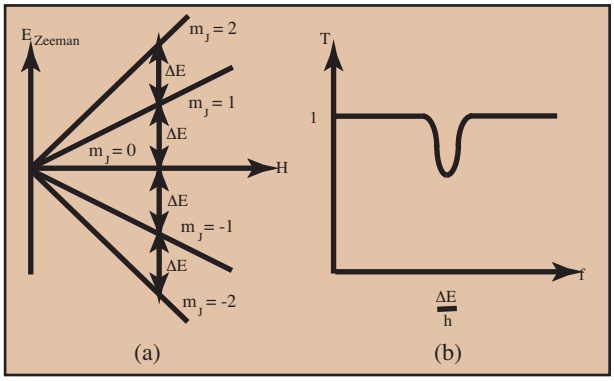

Fig. 19.67. (a) Zeeman splitting of the $2J + 1$-fold degenerate states vs. applied field, H (b) resonant absorption seen in reduced transmission of EM radiation of the resonant frequency.

MRI Enhancement. Neel relaxation of superparamagnetic MNPs in AC fields is used in *magnetic resonance imaging, MRI*. Magnetostatic stray fields of MNPs affect proton relaxation providing enhancement of MRI contrast. Resonance phenomena include *electron paramagnetic resonance, EPR, electron spin resonance, ESR, ferromagnetic resonance, FMR,* and *nuclear magnetic resonance, NMR*. In all absorption of electromagnetic radiation accompanies excitation between quantum states. For EPR the quantum states are the $2J + 1$-fold degenerate ground state of a quantum paramagnet. For ESR the quantum states are the $2S + 1$-fold degenerate states of a atom for which $L = 0$. In FMR, exchange interactions influenc the resonance phenomena. NMR is a resonance phenomena associated with nuclear dipole moments. Just as electrons have spin dipole moments, protons also have dipole moments. Excitation between states of the dipole moments of protons in the nucleus give rise to NMR.

The *Zeeman splitting* lifts the degeneracy of magnetic states and increases linearly with applied field (Fig. 19.67 (a)). Atoms of interest exhibit a transmission coefficient for EM radiation that us a monotonic function of frequency, f. At a resonant frequency, $f = \frac{\Delta E}{h}$ ($\omega = \frac{\Delta E}{\hbar}$) EM radiation is strongly absorbed and the transmission coefficient diminished. Spatially resolved transmission in NMR is used as an imaging tool.

MRI is improved by using contrast agents that increase sensitivity or specificity of MRI processes. A difference in proton density and their relaxation in biological environments provides the mechanism for contrast. Contrast agents include superamagnetic macromolecular compounds, superparamagnetic iron oxide and rare earth metal ion (Gd) complexes [WBPea84]. Paramagnetic metal ions reduce the T_1 relaxation of protons in water. This enhances the intensity of the NMR signal making images brighter. The use of *superparamagnetic iron nanoparticles (SPION)* have been shown to be more effective than Gd contrast agents.

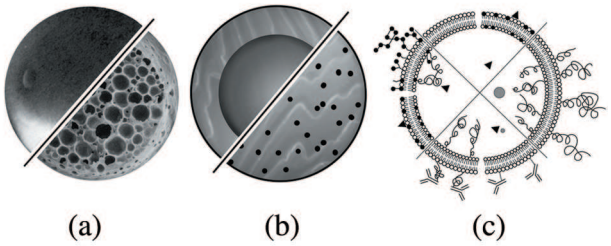

Fig. 19.68. (a) magnetic microspheres, (b) microcapsules and (c) liposomes (courtesy U. Hafeli).

Magnetic Beads for Bioseparation, Cell Sorting and Drug Delivery.

Bioseparation is the isolation of biological substances including molecules, cells and cell components, and organisms. Magnetic bio-separation may be accomplished by two routes. First, the species to be separated may have a large enough magnetic dipole moment (e.g. red blood cells) so as to be directly separated by a magnetic field. Second, non-magnetic cells or biomolecules are modified by attaching MNPs so that they can be manipulated by an external field. In *magnetic bioseparation* a substance that is desired to be isolated is bound to a MNP through suitable surface chemistry. The material responds to a magnetic field used to move the substance.

Magnetic particles of micron size dimensions, called *magnetic beads* can be embedded in other bioactive materials. They serve as a bioactive agent and can be localized or retrieved with a magnet. This can shorten purification steps. Using magnetic bioseparation decreases times needed for target substance recovery. Magnetic separation technologies have also been used for environmental remediation in removing oil spills from waterways. In many bioseparation applications ideal particles are superparamagnetic. Superparamagnetic particles are not hysteretic and don't have a remanant magnetization, so they return to zero magnetization after field removal. Typically, superparamagnetic particles are nanosized and micron-sized beads are composites.

Magnetic particles for biomagnetic applications typically fall into three classes. These are (i) *magnetic microspheres* and *magnetic nanospheres*, (ii) *magnetic microcapsules* and (iii) *magnetic liposomes* illustrated schematically in Fig. 19.68. Magnetic bioseparation-based technologies have applications in mRNA extraction, separation of DNA from solutions or gels, and isolation of plasmid DNA. MNPs have also been used for bone marrow and blood detoxification; tracking of blood flow and stem cells and drug delivery. *Dynabeads*^{TM} are monodisperse polymer beads with a uniform dispersion of superparamagnetic $\gamma - \mathrm{Fe_2O_3}$ or $\mathrm{Fe_3O_4}$ coated with a thin polymer. Dynabeads have well defined surfaces for the adsorption or coupling of bioreactive

molecules and can be added to a suspension and bind to cells, nucleic acids, proteins or other biomolecules. The resulting target-bead complex is removed using a magnet.

Magnetoelastic Actuators, Sensors and MNP Cell Tagging.

A *smart material* is one which is capable of two functions, e.g., a material capable of both actuation and sensing is an example of a smart material. Exciting new biomedical applications of smart materials include magnet-polymer composites which are being used in such applications as artificial muscle. [RL06]. Attempts to synthesize artificial muscles, have ranged from a robot-like metallic actuators to soft actuators. Hydrogels are water swollen crosslinked polymer networks. These are a promising materials class for producing soft actuators.

Since most gels are homogenous and shrink or swell uniformly without a dramatic change in shape efforts have focused on means to promote larger anisotropic shape changes. Szabo, et al. [SSZ98] have reported magnetic field sensitive gels where colloidal magnetic particles are dispersed in the gels. These are called *ferrogels* and constitute composites which combine the magnetic properties of the fillers and the elastic properties of hydrogels. In these materials, an instantaneous shape distortion is observed which disappears quickly when the external field is removed (Fig. 19.69).

When ferrogels are placed into a spatially inhomogeneous magnetic field, forces act on the magnetic particles. Due to the strong mechanical coupling between the particles and polymer chains, the composite responds as a single entity. The coupling of the hydrogel and magnetic particles has applications in soft actuators.

A *superelastic polymer* is an elastomer, silicone, or gel embedded with micro- or nano- magnetic particles. A composite superelastic polymer is capable of responding to a magnetic field with a smooth muscle-like motion. The composite can also be classified as a *smart material* as it is capable of both actuation and sensing it own motion. For every concentration of magnetic particles in the composite, there is a threshold field strength at which the deflection increases rapidly. When the material is elongated it's resistivity is changed remarkably, so that the strain in the actuator can be sensed by the current passed at constant voltage. This sensing response is sensitive both in tension and compression.

An important tissue engineering problem is proving the viability of a scaffold delivery system. This requires determining details about scaffold remodeling such as degradation time and where degradation products travel in the body. The fate of scaffold degradation products can include remaining within local tissue or traveling to extreme locations in the body. It is desirable to monitor the in vivo behavior of scaffold remodeling through suitable tagging of the scaffold cells to monitor their fate over time.

Imaging with the use of magnetic nanoparticles has many advantages. Magnetic nanoparticle tracking also has the added benefit of being bio-inert as well as simple to measure. Magnetic fields do not pose deleterious effects in biological systems. This bio-inert property of magnetic flux is one of the chief advantages of magnetic nanoparticles tracking. Magnetic nanoparticle tracking has additional advantages due

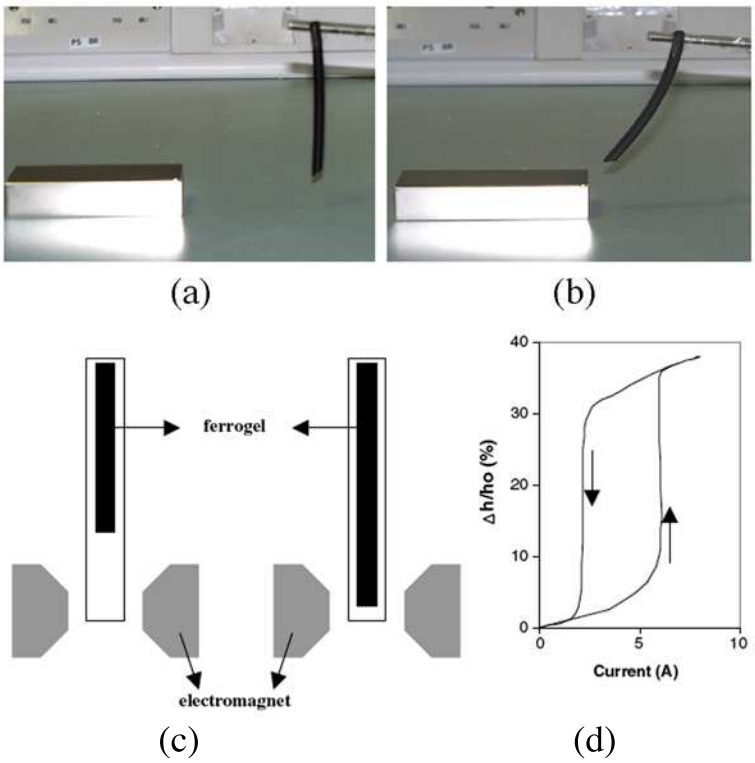

Fig. 19.69. (a) Experimental manifestation of the response of a ferrogel (a) in no field and (b) in a field provided by a permanent magnet [RL06]. (c) Elongation of ferrogel in no magnetic field and in maximal magnetic field; and (d) elongation versus current density (hysteresis)

to ease of measurement. An immediate consequence of the ease with which magnetic information is read is the ability to miniaturize such detection devices. Typical hard disk drives employ materials that exhibit the so called giant magnetoresistive effect (GMR) and can distinguish domains as small as 0.0065 μm^2 [MKGP05]. In order to image domains of this size, the materials composing the sensor must also be on the same order of magnitude in size as well. This miniaturization is the foundation for an ultimate method of imaging.

Once a scaffold has been implanted for regeneration, an array of GMR sensors could be implanted near the scaffold. It has been shown theoretically that the use of a GMR sensor for detection of a magnetic nanoparticle is feasible and is predicted to distinguish particles sizes of down to 10 nm in size [TPL00]. A GMR array would allow adequate resolution for tracking magnetic nanoparticles as the scaffold degraded.

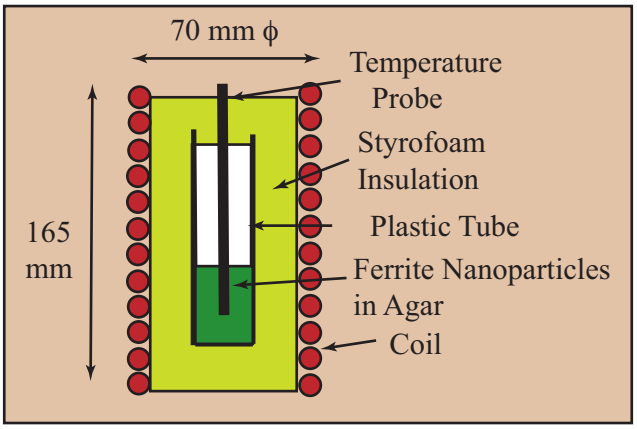

Fig. 19.70. Schematic of an RF coil designed for inductive heating.

MNP's for Thermoablative Cancer Therapies.

An important biomedical application of the RF heating of ferrofluids is in magnetic hyerthermia. The choice of the frequency of the alternating magnetic field is a design consideration. The power dissipation scales linearly (or as a higher power) of frequency. In biomedical applications the frequency is often chosen to be non-invasive. This means that the EM radiation does not interact strongly with body fluids or tissues. Radio frequencies of 100-300 kHz have been chosen for cancer therapies because they are non-invasive but interact strongly with suitably chosen nanoparticles. To the extent that magnetic nanoparticles can be targeted to specific cells or if specific cells die at lower temperatures, this is a viable technique for cancer therapies, for example.

The expression for power dissipation has a H_0^2 dependence and therefore the choice of field amplitude is also an important consideration for promoting dissipation. Typical fields are on the order of ~ 100 Oe. High amplitude (~ 1000 Oe) AC fields have been used in recent therapies. Fig. 19.70 shows an example of an RF coil designed for a high amplitude, RF radiation source for inductive heating.

Most work on ferrofluids for thermoablative cancer therapies have focussed on iron oxides, magnetite, $\mathrm{Fe_3O_4}$, and maghemite, γ-$\mathrm{Fe_2O_3}$. Calculations of Maenosono and Saita [MS06] argue for the efficiency of FePt nanoparticles showing that the comparative heating rates (at non-invasive frequencies, ~ 300 kHz, AC field amplitudes of 50 mT and nanoparticle volume fractions $\phi = 0.1$) that exceed those of magnetite and maghemite. FeCo nanoparticles have significantly larger heating rates but at sizes that are argued to be too large to allow colloidal suspension. However, calculations considered only FeCo alloys with small magnetocrystalline anisotropy ($K = 1.5x10^3 \frac{J}{m^3}$). Fig. 19.71(a) shows comparative heating rates as a function of particle size for the ma-

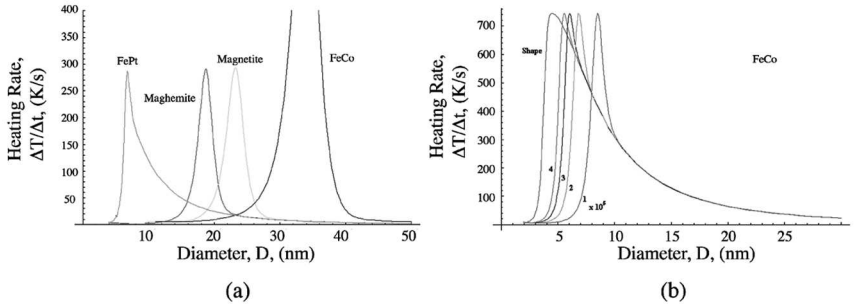

Fig. 19.71. (a) Comparative heating rates as a function of particle size for nanoparticle materials considered in Maenosono and Saita [MS06] and (b) for FeCo nanoparticles of different compositions and acicular equiatomic FeCo nanoparticles with shape anisotropy [HOC$^+$08].

terials considered in Maenosono and Saita [MS06]. Important observations are: (1) the material magnetization sets the scale for heating rate and (2) magnetic anisotropy (entering the expression for Neel relaxation) determines the particle diameter, D, where a maximum heating rate occurs.

Fig. 19.71(b) shows calculations for FeCo alloys with much larger Ks, achievable by varying composition [HOC$^+$08]. In $\mathrm{Fe}_{1-x}\mathrm{Co}_x$ (x = 0.250.5) alloys, K varies between 0 and $4 \times 10^5 \frac{J}{m^3}$, while the induction is relatively constant (2.2-2.5T) These heating rates are twice those of the oxides or FePt and are peaked at smaller particle diameters. The materials are thus predicted to have superior heating rates at sizes appropriate for colloidal suspension. Particles that are too large settle due to gravitational forces.

Magnetic shape anisotropy in acicular FeCo particles offers another possible mechanism for stabilizing colloidal FeCo-based ferrofluids. FeCo-based materials that exploit shape anisotropy were discussed earlier in the context of Alnico magnets. Because of their large magnetization, shape anisotropy on the order of $K_s = 1 \times 10^6 \frac{J}{m^3}$ are achievable in FeCo nanoparticles with moderate aspect ratios. FeCo nanoparticles have other advantages in forming stable protective cobalt-ferrite shells. Cobalt ferrite has been shown to be suitable for water based magnetic fluids, suggesting FeCo /$\mathrm{CoFe_2O_4}$ acicular core shell structures for use in water-based ferrofluids.

Recently, the Rosensweig [Ros02] formalism has been generalized to consider T-dependent material properties in a self-regulated heating theory [OHS$^+$09] For FeCo MNPs this can be ignored because of their high Curie temperatures, T_c's. However, T_c tuning is an important area of recent study [MSMM10], [MKLM10], [MCPM10]. γ-FeNi MNPs have tuneable Curie temperatures which can be employed for self-

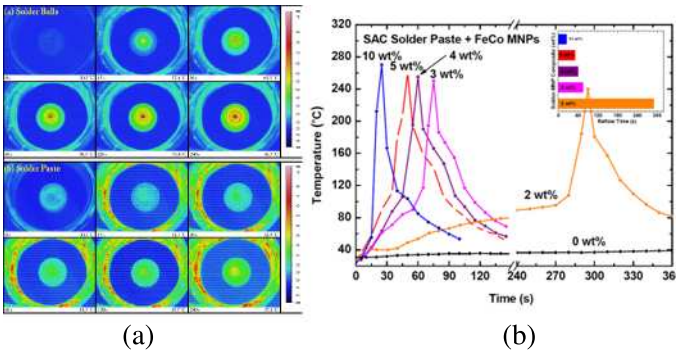

Fig. 19.72. (a) Thermal images showing T-profile in solder balls and (b) T(t) for different wt% solder-MNP composites in AC fields of 500 Oe at 280 kHz, inset shows time to reflow for different wt% samples.

regulated heating in hyperthermia [MKLM10]. This allow for control of heating at a therapeutic target temperature.

19.4.2.3 Applications of Nanoparticles in Microelectronics.

The reflow of small solder volumes is critical to high interconnect densities needed for electronic packages. Efforts to eliminate Pb from consumer electronics due to health concerns of Pb toxicity has led adoption of Pb-free solders for packaging applications. An example is SAC305 (3wt%Ag; 0.5wt%Cu, remaining Sn) which have a higher reflow temperature and longer reflow times, due to higher melting points, and poor wetting compared to Sn-Pb eutectics. This increases risk of printed circuit board (PCB) delamination and blistering.

Localized heating, promoted by MNPs to cause solder reflow can aid efficient processing of Pb-free solders [HOM$^+$10]. MNPs subjected to AC magnetic fields dissipate by the relaxation processes discussed above. Unlike eddy current losses, these result in significant power loss in sub-micron and nano-sized magnetic materials [MSMC$^+$09]. Nanocomposites incorporating magnetic nanoparticles (MNPs) in solder paste have been shown to enhance induction losses [HOM$^+$10].

Fig. 19.72 (a) shows thermal images of the spatial T-profile in solder balls at various time intervals in an AC magnetic field of 500 Oe at 280 kHz. Fig. 19.72 (b) shows temporal T-profiles derived from this data. When MNPs are incorporated into solder paste the resulting composite shows a significant temperature rise in AC magnetic fields sufficient to cause solder reflow. Reflow times vary systematically with MNP concentration in the composite. Reflow of solder-MNP composite paste (~ 5g) at modest MNP loadings on Si, glass and $\mathrm{Ni/Au}$ substrates has been demonstrated. However, for processing of smaller solder volumes (~ 0.05g) higher MNP concentra-

tion and field parameters are required due to the increased fraction of heat lost to the surrounding at smaller volumes.

19.4.3 Magnetocaloric Materials

Applications of thermodynamics to heat engines, refrigerators, heat pumps, etc. rely on efficient use of thermodynamic cycles. Most of these cycles, e.g. *Carnot cycles*, are based on use of PV work in the expansion/compression of a fluid (liquid and/or gas) system. Here we consider magnetic work and the consequent magnetocaloric effect in magnetic refrigeration cycles. The magnetocaloric effect (MCE) was first described Warburg [War81]. MCE provides a ways to realize refrigeration from ultra-low temperatures to room temperature and above. We discuss the following:

(i) Attaining low temperatures by adiabatic demagnetization.
(ii) Magnetocaloric effects with paramagnetic salts.
(iii) Magnetocaloric effects with superparamagnetic particles.
(iv) Magnetocaloric effects using ferromagnetic to paramagnetic phase transitions.
(v) Magnetic Refrigeration Cycles.

19.4.3.1 Attaining low temperatures by adiabatic demagnetization.

The use of paramagnetic salts in adiabatic demagnetization processes dates back to the 1920's and the work of W. F. Giauque [Gia27] and P. Debye [Deb26]. Recall that paramagnetism results from the existence of permanent magnetic moments on atoms. In a paramagnetic material in the absence of a field, the local atomic moments are uncoupled and randomly oriented these dipole moments will align themselves with a magnetic field. The magnetic Susceptibility of a paramagnet obeys the *Curie Law*:

$$\chi = \frac{M}{H} = \Big(\frac{N_m \mu_0 (\mu_{atom})^2}{3k_B T}\Big) = \frac{C}{T} \tag{19.83}$$

with N_m, the dipole density and μ_{atom} the atomic dipole moment. In a paramagnetic system, the spin entropy, S, is: $S = R\ln(n+1)$ where n is the number of unpaired electrons per formula unit. Adiabatic demagnetization has the following steps:

(i) Cool a paramagnetic salt to ~ 1 K using liquid Helium (LHe) using He(g) as a heat transfer medium;
(ii) Isothermally magnetize the salt in fields of ~ 1 T;
(iii) Adiabatically isolate the salt by evacuating i.e. removing the He(g);
(iv) Turn of the field (adiabatic demagnetization).

The entropy change in adiabatic demagnetization of a paramagnetic salt is:

$$\Delta S = \Big(\frac{-C}{T^2}\Big)\int_0^H H dH = -\frac{C}{2}\Big(\frac{H}{T}\Big)^2 \tag{19.84}$$

where since the Curie constant, $C > 0$ then $\delta S < 0$ for adiabatic demagnetization. Spin entropy is decreased on magnetization and increased on demagnetization. In an adiabatic process the spin entropy change is opposed by the thermal(lattice) entropy change.

19.4.3.2 Magnetocaloric effects with superparamagnetic particles.

Superparamagnetic response refers to thermally activated switching of a magnetic fine particle moment. This thermally activated switching is described by an Arrhenius law for which the activation energy barrier is $K_u < V >$ where K_u is the magnetic anisotropy energy density and $< V >$ is the average particle volume. The switching frequency becomes larger for smaller particle size. Above a blocking temperature, T_B, the switching time is less than the experimental time and the hysteresis loops is observed to collapse. For experimental times of ~ 1 hour, the blocking temperature roughly satisfies $T_B = \frac{K_u < V >}{30 k_B}$.

Above T_B, the magnetization scales with H and T in the same way as does a classical paramagnetic material, with the exception that the inferred dipole moment is a particle moment and not an atomic moment but a cluster moment. The magnetization, $M(H,T)$ can be described a Langevin equation of state:

$$\frac{M}{M_s} = L(a) = \coth(a) - \frac{1}{a} \tag{19.85}$$

where $a = \frac{\mu H}{k_B T}$ and moment μ is given by the product $M_s < V >$, where M_s is the spontaneous magnetization and $< V >$ is the average particle volume. A limiting form for the equation of state is the standard Curie law. The associated magnetocaloric effect for superparamagnetic particles is therefore analagous to that of a paramagnetic salt except for two important differences:

(i) We consider a particle rather than atomic dipole moment and the density is a particle rather than atomic density. The Curie constant scales accordingly.
(ii) The largest effect occurs near the blocking temperature, T_B, rather than on approaching 0 K.

The large moment allows for potentially more entropy change associated with the adiabatic demagnetization of the superparamagnetic particles. By tuning the particle size and therefore the blocking temperature one can influence the temperature (range) where the magnetocaloric effect is significant and raise it above the very low (LHe) temperatures typically accessible with paramagnetic salts.

19.4.3.3 Magnetocaloric effects in ferromagnetic to paramagnetic phase transitions.

Many modern day refrigerants take advantage of the entropy change in a phase transition that occurs at or near the temperature at which the refrigerator is to operate. Often this is a liquid to gas phase transition and sometimes a solid/solid phase transition. Another significant phase transition would be the ferromagnetic to paramagnetic phase transition that occurs at the ferromagnetic Curie temperature which will be discussed further in terms of the Landau Theory below. Of the elemental ferromagnets the magnetocaloric effect Gd is of most interest since its Curie temperature is close to room temperature!

A figure of merit for refrigerants is the *refrigeration capacity, RC* which is a measure the effective cooling capacity of a refrigerator, expressed in $\frac{Btu}{hour}$ or in tons of refrigeration (1 ton of refrigeration $= 13,898 \frac{kJ}{hr} = 3.861$ kW). Another measure of the RC for magnetic materials takes the product of the entropy change, dS and multiplies in by the incremental temperature change, dT. The dS is determined from from integrating M(H) isotherms and dT would represent the increment between the hot and cold sides of the refrigerator.

19.4.3.4 Magnetic Refrigeration Cycles.

An example of a thermodynamic cycle that takes advantage of the magnetocaloric effect is the *Joule-Brayton Cycle*. Fig. 19.73 shows an example of a rotary active magnetic liquifier taking advantage of adiabatic demagnetization in a Joule-Brayton Cycle. The steps in the Joule-Brayton Cycle are;

(i) Magnetize and thereby warm the magnetic solid;
(ii) Remove heat with a cooling fluid;
(iii) Demagnetize and thereby cool the magnetic solid;
(iv) Absorb heat from a cooling load (adiabatic demagnetization).

19.4.3.5 Selected Recent Research on Magnetocaloric Effects.

The magnetocaloric effect (MCE) explains the fact that magnetic materials heat when placed in a magnetic field and cool upon removal from the field. This effect was first observed by E. Warburg [War81] in 1881 in iron. The magnitude of the effect in elemental ferromagnets, like Fe is 0.5-2C per T. Recently, Gd-Ge-Si alloys have been shown to have much larger effects of $\sim 3 - 4^{\circ}$C per T. The search for new magnetocaloric effect materials is a very active area of current research.

A large MCE is the figure of merit for the efficacy of a magnetic refrigerant. With an increasing field, the magnetic entropy decreases and heat is transferred from the magnetic system to the environment in an isothermal process. With a decreasing field, the magnetic entropy increases and heat is absorbed from the lattice system to the

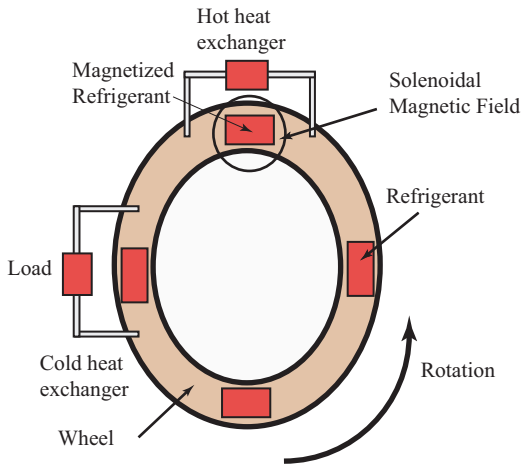

Fig. 19.73. Magnetocaloric Device Example: Rotary Active Magnetic Liquefier

magnetic system in an adiabatic process. Both a large, isothermal entropy change and adiabatic temperature change characterize the prominent MCE [Bru05], [GPT05]. The importance of the lattice system has led much recent literature in MCE to consider MCEs in materials in the vicinity of simultaneously occurring magnetic and structural phase transitions.

Nanocomposite magnetic materials have been among the systems of interest for MCE applications [JS06], [FCBC07]. The ability to tune the Curie temperature by alloying the amorphous phase in these materials makes them of interest for a variety of refrigerant applications at a different temperatures. Fig. 19.74 shows unpublished MCE data for an FeCo-based amorphous alloy. Fig. 19.74 (a) shows M(H) isotherms from 40-400 K; (b) shows the integrated magnetic entropy changes for the curves of (a) with the method for determining the *refrigeration coefficient, RC* shown and the inset shows the RC as a function of applied field (courtesy A. Colletti and K. Miller). The magnetic entropy is determined by integrating the Maxwell relation described above [FCBC07]. The refrigeration coefficient, RC is defined as the specific (maximum) energy that can be absorbed over a range of temperatures in $\frac{J}{kg}$. The RC is a figure of merit for a magnetocaloric material. Values approaching $1\frac{kJ}{kg}$ at $H = 5$ T are observed for this particular material. The largest area under the dS curve from T(hot) to T(cold) is the RC. There are two suggested methods of getting the RC from $\Delta S(T)$ data: 1) Full width at half max of the peak as a function of temperature and 2) finding the largest rectangle which fits under the curve [WP85].

Giant MCE has been observed in materials exhibiting first-order phase transitions, including $\mathrm{Gd_5Si_2Ge_2}$, $\mathrm{LaFe_{13-x}M_x}$ (M = Si, Al), $\mathrm{MnFePAs}$, $\mathrm{MnAs_{1-x}Sb_x}$,

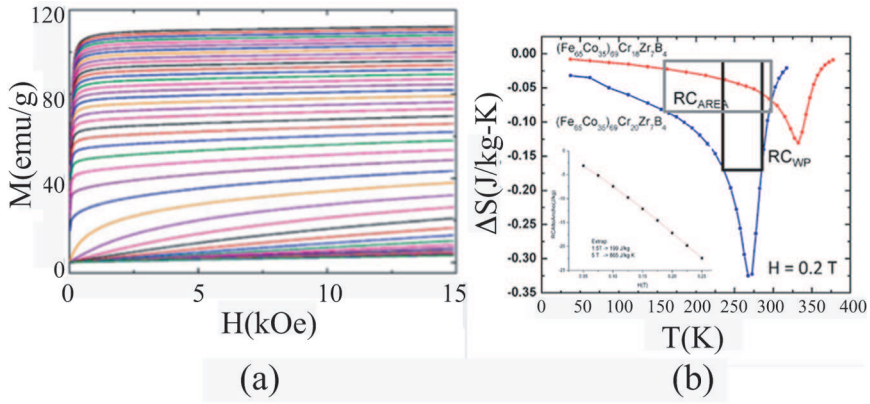

Fig. 19.74. MCE data for an $\mathrm{Fe Co}$-based amorphous alloy. (a) M(H) isotherms from 40-400 K, (b) integrated magnetic entropy changes for the curves of (a) with method for determining RC shown and (inset) RC as a function of applied field. courtesy A. Colletti and K. Miller

$\mathrm{Mn}_{1-x}\mathrm{Fe}_x\mathrm{As}$, and NiMnX (X = Ga, Sn). Large MCEs also are observed in some rare earth metals, alloys, compounds and the manganites [PY07]. Second-order phase transitions are also useful in limiting the hysteresis in the magnetocaloric effect. Over the past few years, the MCE and magnetic refrigeration materials have been investigated extensively and several kinds of magnetic-refrigerant prototype instruments have been demonstrated. This remains a very active area of current research in magnetic materials. Of particular interest is the suspension of magnetic nanoparticles in fluid systems capable of transporting absorbed heat away.

Suppression of phase transformations in metastable nanostructures can be used to produce materials with properties not obtainable in equilibrium. In Fe-rich, Fe-Ni-based nanocomposite systems [11] the nucleation of the equilibrium *bcc*-phase is suppressed in favor of the metastable γ-phase. This has profound effects on technical magnetic properties because on the Fe-rich side of the Fe-Ni phase diagram there is a strong compositional dependence of the Curie temperature, T_c on composition in the γ-phase [12]. For certain Naval applications the T_c of the particles should lie between ambient, ocean water temperature and the desired upper-limit operating temperature of a device. A magnetocaloric thermodynamic cycle can be used for such a exploiting the ferromagnetic to paramagnetic phase transformation in γ-Fe-Ni. New research has focused on the stabilization of γ-phase nanostructures in magnetic nanopowders and nanostructures produced by primary crystallization of amorphous precursors, powdering materials and producing aqueous ferrofluids suitable for magnetocaloric cooling applications near room temperature.

19.4.4 Electromagnetic Interference Absorbers

Materials designed to absorb electromagnetic noise in specific frequency ranges is another active area of new research in *electromagnetic interference (EMI)* absorption. This research requires understanding ways to tune magnetic and dielectric properties of EM absorbers for specific applications. This requires choosing appropriate intrinsic magnetic and dielectric materials properties and the iinfluence of morphology and microstructure on their frequency-dependent absorption spectrum.

Electromagnetic interference (EMI) is electrical noise transmitted by electric motors, machines, generators, circuits and other sources that interferes with the function of another electronic device such as a circuit, computer or transmission line. Electromagnetic radiation is classified by its energy, E, frequency, f, and wavelength, λ, related through *Einstein's formula* relating the photon energy to frequency $\nu = 2\pi f$:

$$E = h\nu = \frac{hc}{\lambda} \tag{19.86}$$

where h is *Planck's constant* ($h = 6.626 \times 10^{-34} J - s = 6.626 \times 10^{-27} erg - s$) and for EM radiation, $\nu = \frac{c}{\lambda}$, and c is the velocity of light $c = 3 \times 10^{10} \frac{cm}{sec} = 3 \times 10^{8} \frac{m}{sec}$.

High frequency electronic devices exacerbate the need for EMI absorbers. Examples of these applications include:

(i) telecommunications;

(ii) consumer applications;

(iii) biomedical applications; and

(iv) military and civilian security applications.

Mechanisms for EMI shielding are *reflection EMI shielding* and *absorption EMI shielding*. In reflection shielding, the mobile charge carriers in metals or conductive polymers interact with the EM field and the radiation is reflected. In absorption shielding, the electric or magnetic dipoles in dielectric or magnetic materials interact with the EM waves and the EM waves are transformed into heat in the absorbing material [Lia07].

Reflection and attenuation properties are determined by the complex permeability ($\mu' - i\mu''$) and permittivity ($\epsilon' - i\epsilon''$). In absorption, the loss is proportional to the product, $\sigma\mu$, of conductivity, σ and permeability, μ. For reflection the loss is a function of the ratio, $\frac{\sigma}{\mu}$. Absorption loss increases with frequency and reflection loss decreases. The sum of all the losses gives the total loss. Good conductors such as Ag and Cu have excellent reflection characteristics, whereas materials like Superpermalloy and Mumetal have excellent absorption characteristics due to their high permeabilities.

19.4.4.1 Principles for Designing EMI Absorbers with Magnetic Materials.

The effectiveness of electromagnetic interference shielding is quantified by the reflection loss, Γ given in dB:

$$\Gamma(dB) = -20\log_{10}\left[\frac{Z_A - Z_0}{Z_A + Z_0}\right] \qquad Z_A = Z_0\sqrt{\frac{\mu_e}{\epsilon_e}}\tanh\left(\frac{2\pi f}{cd\frac{\mu_e}{\epsilon_e}}\right) \qquad (19.87)$$

where, Z_0 is the impedance of free space (377 Ω), Z_A is the absorber impedance at the free space - material interface, μ_e and ϵ_e are the effective permeability ($\mu' - i\mu''$) and permittivity ($\epsilon' - i\epsilon''$) of the absorber medium and d is the absorber thickness. When the absorber impedance is equal to the impedance of air there is no reflection. A reflection loss of -20 dB corresponds to 99 % wave absorption and is considered an impedance matching situation [Liu04] atypical target performance of EMI absorbers. For GHz range absorbers it is favorable to have matching permeability and permittivity. Increasing the permeability or thickness will increase the loss. Changing permeability can change properties without adding additional size and weight. The permeability of the materials depends on composition and microstructural features such as particle size and porosity.

Magnetic materials for EMI shielding include *spinel ferrite* and *hexagonal ferrites*, metallic (and amorphous metallic) magnetic materials, and combinations of both. Desired properties include high *permeability*, a high *Curie temperature*, high *saturation magnetization*, high induction, and a high *resistivity* to limit eddy current losses. High permeability requires considering a variety of other materials and morphological properties including *magnetocrystalline anisotropy*, *shape anisotropy*, *induced anisotropy* and *magnetostriction*. The consideration and matching of magnetic and *dielectric properties* increasingly lead to the consideration of composite and *nanocomposite* structures to exploit attractive properties of two or more engineering materials.

Ferrite materials have many properties which make them useful for EMI wave absorbing applications. Ferrites are ceramics having high permeability, temperature stability, and low cost which provides many design advantages. However, they have low inductions as compared to metals and cubic ferrites do not have sufficient magnetic anisotropy to function at high frequencies. Their high resistivity does allow them to operate without the frequency limitations of eddy current losses. To have superior EMI absorbers at the highest frequencies, it would be desirable to have the large inductions of metals combined with the large resistivities of the ferrites along with the engineering of large magnetic anisotropies. This has spurred the studies of ferromagnetic nanocomposites and *metamaterials* often exploiting high induction metal - high resistivity oxide core shell structures often with morphologies designed to exploit shape anisotropy.

The complex impedance and an EMI absorber depends on the *dielectric permittivity* and the *magnetic permeability*. The complex permeability depends on the chemical

composition of the alloy, as well as microstructure, particle size, and porosity of the compact [Nea00]. The permeability can be described by contributions from domain wall motion and spin rotation processes. Domain wall motion dominates in the initial permeability and is sensitive to the microstructure, particle size, and particle loading in the compact. Spin rotation dominates at frequencies above 100 MHz and depends on the anisotropy field and particle loading. Thus optimizing the microstructure, particle size, anisotropy field, and loading can lead to a large permeability.

To design state of the art absorbers a variety of fundamental considerations must be taken into account. In the following sections we develop the physical principles necessary to tailor the properties of an EMI absorber. These are summarized as follows:

(i) DC Magnetic Shielding: DC shielding of a soft magnetic material is determined by it's permeability. If the fields to be shielded are sufficiently large saturation induction is an issue. At higher frequencies considerations of eddy current and anomalous eddy current losses and resonant absorption are important considerations in assessing the frequency dependent magnetic response.

(ii) *EMI Absorption and Skin Depth*: In general we wish to limit the amount of the material to that required to perform the engineering function. In the case of EMI absorbers the important length scale of note is the *EM skin depth*. The skin depth is the depth to which losses occur in a material and to which the material responds to an oscillating field. The skin depth is a function of the magnetic permeability, the conductivity and the frequency of the exciting EM radiation. Solutions of *Maxwell's equations* for fields penetrating into a permeable medium give rise to an exponential decay of the applied field over the *classical skin depth*, δ which is given by the relationship:

$$\delta = 5030\sqrt{\frac{\rho}{\mu f}} \tag{19.88}$$

where ρ is the resistivity in $\Omega - cm$, μ is the relative permeability and f is the frequency of the EM radiation in Hz. Since most of the losses are confined to the skin depth, it is desirable to design absorbers with dimensions approximating the skin depth at the frequency to be absorbed. This illustrates the importance of high resistivity for high frequency absorbers. For very high frequencies e.g. 1 GHz and reasonable permeabilities of 100-1000, e.g a good insulator will have nanoscale dimensions to match it's skin depth. High frequency absorbers require tailoring microstructures at the nanoscale.

(iii) *Magnetic Anisotropies*: To tune the permeability it is important to engineer magnetic anisotropy . In many state of the art EMI absorption materials the important types of magnetic anisotropy include (a) magnetocrystalline anisotropy, (b) shape anisotropy, (c) magnetoelastic anisotropy and (d) induced anisotropy.

(iv) *Ferromagnetic Resonance Frequency*: The *ferromagnetic resonance frequency*, f_r is a spin resonance at microwave frequencies where transverse EM field energy is absorbed at the precessional frequency of atomic dipoles about a static field. In the absence of magnetic anisotropy this resonance frequency depends on the magnetization of the material as described by *Snoek's Law*:

$$\mu' f_r \sim M_s \tag{19.89}$$

where μ' is real magnetic permeability and M_s the saturation magnetization. In the absence of other loss mechanisms, the FMR frequency represents a material's ultimate EMI absorption frequency. EMI absorber design recognizing the role of the FMR frequency then requires materials with large magnetizations and restricts the permeability. It is desirable to fix the internal magnetization direction with a suitable magnetic anisotropy to ensure that switching takes place by non-lossy rotational mechanisms and the real permeability is :

$$\mu' = \frac{M_s}{H_K} \qquad H_K = \frac{2K}{M_s} \tag{19.90}$$

with H_K the *anisotropy field* and K the *magnetic anisotropy energy density*.

(v) *Magnetic Losses*: Power losses in a ferromagnetic material are described by:

$$P_{Total} = P_{hys} + P_{ec} + P_{anomalous} \tag{19.91}$$

where the first term, the *hysteretic power loss* has a linear dependence on frequency, the second term, the *classical eddy current power loss* has a square dependence on frequency, and the third term, the *anomalous power loss* has a power greater than 1 dependence on frequency. It is apparent that the eddy current losses dominate at high frequencies. Approaches to limiting these losses include: (1) choice of strongly exchange coupled soft magnetic materials to limit hysteretic losses; (2) choice of high resistivity materials or composite structures with insulating coatings and (3) limiting the dimensionality of the material to limit the spatial extent over which eddy currents flow.

(vi) *Morphology and Microstructure*: Often, composites can give better response than a single material. The morphology of the magnetic species and the microstructure of the composite must be carefully engineered to optimize the properties. Morphological and microstructural considerations include (a) skin-depth matching and insulation, (b) monodomain particles, engineering shape anisotropy and/or magnetoelastic anisotropy. To control losses, the eddy current must be confined to run in a dimension comparable to the skin depth. This requires insulating coatings in 3-d structures and insulation parallel to the induction in 2-d or 1-d structures.

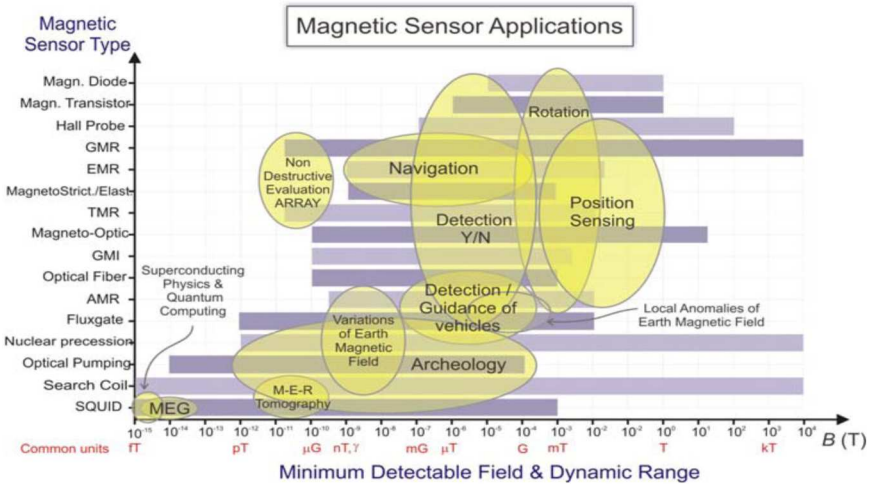

Fig. 19.75. Magnetic sensors technologies and applications categorized by sensor type and magnetic properties (minimum detectable field and dynamic ranges [DM09].

19.4.5 Magnetic Sensors

Magnetic metals and alloys important in sensor applications. Existing magnetic field sensors use a variety of physical phenomena including inductive pick-up coils, Hall probes, magnetoresistive elements, magneto-optic devices, flux-gates and superconducting quantum interference devices (SQUIDs) [Rip01]. Magnetic sensors are classified by their field sensing ranges.

Low-field sensors are typically larger and can require careful and costly sample preparation to correct for demagnetization effects and for the Earth's magnetic field field. A superconducting quantum interference device (SQUID) is the most sensitive low field sensor. SQUID magnetometers can detect fields as low as femtotesla. They require cryogenic cooling, making testing expensive and sizes cumbersome. Other sensitive low field sensors include Alternating Field Gradient Magnetometers (AGM) and Vibrating Sample Magnetometers (VSM).

In many applications, the sensor size is of paramount importance. In space applications, where the price per unit mass of devices launched is a primary concern, sensor size is a critical design issue [DM09]. This is the subject of considerable efforts in miniaturization [Acu02]. The size of current AGMs and VSMs is an obstacle for applications in-orbit measurements, planetary characterizations and space exploration. Similarly, many biomedical applications are limited by sensor size. *In vivo* sensing applications, for example, have significant physical size constraints. Miniaturization of magnetic sensing devices has fueled the rapid increase in data storage capacity.

Fig. 19.75 summarizes current magnetic sensor technologies in terms of minimal detectable field and dynamic range. Applications require measuring fields anywhere from 10^{-15} to 10^4 T, a range of 19 orders of magnitude! A *superconducting quantum interference devices, SQUID* magnetometer, with sensitivities of 1 femtotesla (fT), can be used in such sensitive applications as mapping currents in the brain in the field of *magnetoencephalography, MEG*. MEG signals result from ionic currents flowing in neuron dendrites during synaptic transmission. These measurements are now used in research and clinical settings. MER tomography gives sensitivities of 0.1-1 microGauss (μG). A typical magnetic noise floor in a city environment is 10^8 fT. As a result, measurements of the smallest fields requires sophisticated magnetic shielding and shielded rooms.

Measurement of the earth's magnetic field for mapping and as a navigational tool uses fluxgate magnetometers. Fluxgates measure fields from mT to 10's of pT in DC to 10's of kHz frequencies. Fluxgates for geomagnetic field mapping have dynamical ranges of 64000 nT, and resolutions in the order of tenths of nT to pT and low *noise density* (several $\frac{pT}{\sqrt{Hz}}$ at 1Hz). A typical fluxgate mass is 0.5 kg and 2 W of power consumption [DM09].

Magnetometer design and development has sought smaller size, lower power consumption, and lower cost for similar performance. [LE06]. Recent innovations aimed at improving size, power, and cost, have included the use of piezoresistive cantilevers and magnetometers based on electron-tunneling effects, *magnetic tunnel junctions, MTJ's*. Magnetic fields are vectors with both magnitude and direction. Sensors differ in their ability to measure the magnitude and direction of the field. A scalar sensor measures the field's total magnitude but not its direction, while an omnidirectional sensor measures the magnitude of the component of magnetization that lies along its sensitive axis. Bidirectional sensors include direction in its measurements and vector magnetic sensor incorporates two or three bidirectional detectors.

Detection and measurement of magnetic fields can be classified by distinguishing whether the measurement technique is direct or examines a spatial derivative of the field in question:

(i) A *magnetometer* is a device that detects magnetic fields directly. Typically this uses a simple induction loop.

(ii) An *axial gradiometer* is a device in which two magnetometers placed in series axially. The gradiometer then measures the difference in magnetic flux between those points in space. It is therefore a measure of the first spatial derivative of the field.

(iii) A *planar gradiometer* has two magnetometers placed next to each other in the same plane. It measures the "difference in the differences" in flux between two points. It is therefore a measure of the second spatial derivative.

19.4.5.1 Noise Levels

A goal of recent effort has been development of small, inexpensive, low-power, low-frequency, magnetic sensors to sensitive to fields between 1 nT and 1 pT [EPU$^+$09]. This range of field measurement is currently dominated by fluxgates, optically pumped magnetometers, and SQUIDS. The development of picoTesla magnetic-tunnel-junction (MTJ) sensors requires controlling noise levels. Noise characteristics have been recently modeled based on the contributions to the sensor noise floor. These include amplifier noise, Johnson and shot noise, electronic 1/f noise, thermal magnetic white noise and magnetic 1/f noise [EPU$^+$09]. One $\frac{pT}{\sqrt{Hz}}$ at 1Hz is a current goal which would be a factor of ~ 100 below the current commercial MTJ sensors.

Electrical noise is the random fluctuation in a signal. Noise can be produced by a variety of effects. Thermal noise and shot noise are inherent to all devices, while other types depend on other physical phenomena. We explore a few of these here:

(i) *Johnson-Nyquist noise* is synonymous with *thermal noise* and is generated by the random thermal motion of charge carriers in a conductor. The power spectral density of thermal noise, nearly constant throughout the frequency spectrum, is called *white noise*. Thermal noise can be modeled with Gaussian distribution of amplitudes. The root mean square (RMS) voltage due to thermal noise V_n, generated in a resistance R (ohms) over a bandwidth, Δf (Hz), is:

$$V_n = \sqrt{4k_B T R \Delta f} \tag{19.92}$$

where k_B is Boltzmann's constant ($\frac{J}{K}$) and T is the resistor's absolute temperature (K).

(ii) *Shot noise* is the random fluctuation of current which results from the fact that current is carried by discrete charges.

(iii) *1/f noise* is also called flicker noise. It is the portion of the noise spectrum which falls off at high frequencies. In magnetic sensors this noise results from fluctuations of magnetic properties on a nanoscale. One example of a magnetic 1/f noise source is the random telegraph noise which is generated from the motion of magnetic domain walls through pinning sites. This noise is called *Barkhausen noise*.

The noise level can be quantified (1) as an electrical power in watts or dBm, (2) as a root mean square (RMS) voltage equal to the noise standard deviation in volts, or (3) characterized by a probability distribution and noise spectral density N_0(f) in watts per hertz. The frequency dependence of the noise is expressed in units of $\left(\frac{power}{frequency}\right)^{\frac{1}{2}}$. In a resistor, the power is proportional to V^2 and noise units are $\frac{V}{\sqrt{Hz}}$. In an inductive component power is proportional to B^2 and noise units are $\frac{T}{\sqrt{Hz}}$.

19.4.5.2 Measurement of Fields.

Common field measurement techniques include a Hall sensors, fluxgate magnetometers, and magnetoresistive sensors. Several sensors use the *Lorentz force*, or *Hall effect* which describes the force $\vec{F}_L$ experienced by a particle with charge q moving with velocity $\vec{v}$ in a magnetic field, $\vec{B}$: $\vec{F}_L = q\vec{v} \times \vec{B}$ The measurable transverse voltage in a conductor carrying a longitudinal current in a field results from the *Hall effect* [Hal79]. For a geometry where a current is induced by an electric field, E_x, in the x-direction, a magnetic field is applied in the z-direction and the Hall voltage (and electric field) are along the y-direction the *Hall coefficient, R_{Hall}*, is:

$$R_{Hall} = \frac{E_y}{j_x B_z} \tag{19.93}$$

Measuring a Hall voltage, and determining longitudinal current density from *Ohm's Law*, $j_x = \sigma_0 E_x$, the Hall coefficient can be determined for a material. This depends on the charged conducting particles (electron and hole) densities in a material. The Hall voltage is proportional to the applied field. A material with a known Hall coefficient can be used in a *Hall sensor* to accurately measure the magnitude of a normal applied field. A *Hall effect sensor* is a *transducer* with an output voltage that varies with field. and used in switches, position, speed, and current detection applications.

Magnetoresistive sensors have historically been important sensors for field and magnetization measurements. The *magnetoresistance* is the change in the electrical resistance of a material in response to an applied field. The *magnetoresitive (MR* ratio is the ratio of the change in resistance in a field to the resistance in zero field [Spa03]:

$$MR = \frac{R_H - R_0}{R_0} = \frac{\Delta R}{R_0} \tag{19.94}$$

Positive magnetoresistance ($MR > 0$) is a larger and negative ($MR < 0$) a smaller resistance in a field. Normal magnetoresistance, from the Hall effect, is used to sense fields. Ferromagnetic *anisotropic magnetoresistance, AMR* is discussed below.

A *fluxgate magnetometer* is sensor with good field sensitivity related to the magnetic core material [GB72], [Len24]. A *single axis fluxgate magnetometer* is of a toroidal magnetic core wound with a magnetizing drive coil. Another sensing coil is wound around an axis in which the magnetic field component is measured. A fluxgate compares the current required to saturate a material in one direction with that in the normal direction. The difference in the two currents is proportional to the field. An ideal core will have linear response to saturation. A sense coil detects harmonics of a fundamental drive coil frequency which are stronger at the abrupt permeability change at saturation. Largest sensitivity occurs for a high permeability material. Linear M(H) response is achieved by controlling a uniaxial anisotropy. A uniaxial anisotropy induced by field annealing an amorphous or nanocomposite material serves this purpose.

Fluxgates were developed during World War II to detect submarines from low-flying aircraft. Modern applications include electronic compasses for navigation of aircraft and oil-well borehole measurements to navigate while digging deep oil wells. Because of their sensitivity (typically $\sim 0.5 - 1.0$ nT) fluxgates can be used to follow gradients in the earth's magnetic field. The development of 2-axis and 3-axis fluxgates has led to their use as navigational tools and in magnetic surveying. Variations in the earth's magnetic field result from the geometry of the earth's magnetic poles and the magnetic properties of the materials in the earths core and crust. NASA has employed fluxgates to measure magnetospheric and solar system magnetic fields.

19.4.5.3 Measurement of Magnetization.

Commercial magnetometers [Fon96], can be broadly classified as measuring the magnetization by: (a) direct techniques, including measuring the force on a sample placed in a non-uniform field, e. g. Faraday, Guoy, Kahn balances and (b) indirect techniques, including measurements based on magnetic induction due to relative motion between the sample and the detector, e.g VSMs and SQUIDs [Lon08]. Magnetometers are characterized by their sensitivity and a range of other features such as vector or scalar operation, bandwidth, heading error, size, weight, power, cost and reliability. These characteristics determine the suitable applications for the magnetometer.

Lorentz force magnetometers are simple, small, lightweight, low-cost, and low-power-consumption devices for measuring vector magnetic fields. *Xylophone magnetometers*, based on a classical xylophone resonator, are linear sensors with a wide dynamic range from nT to T. A *search-coil magnetometer* exploits Faraday's law of induction. The sensitivity of a search-coil depends on the permeability of the core and the area and number of turns of the coil. Solenoidal search-coils sense time-varying magnetic fields. This is the principle of operation of a *pick-up coil*. A time varying magnetization, $\frac{dM}{dt}$, is sensed by the induced voltage. Other low-field sensor technologies include nuclear precession, optically pumped, and fiberoptic magnetometers.

An example of the use of a pick-up coil sensor is in the *vibrating sample magnetometer, VSM* or Foner magnetometer [Fon59]. The principle of operation of a VSM is based on placing a magnetic sample in a uniform magnetic field. The sample dipole moment is made to undergo a periodic sinusoidal motion at a fixed frequency (typically 60 Hz, i.e. a loudspeaker frequency), f, using a transducer drive head to vibrate a sample rod. The vibrating magnetic dipole moment (through Faradays law of induction) induces a voltage, V, in a sensitive set of pick-up coils placed between the pole pieces of the electromagnet. This signal, proportional to the magnetization, is amplified and monitored. The VSM is calibrated using a standard sample of known moment such as a Ni (ferromagnetic) or Pt (diamagnetic) sphere.

New applications for atomic magnetometers include detection of biomagnetic signals [BWW03] [XBHR06], nuclear magnetization [LSS$^+$06], [SR05] and magnetic

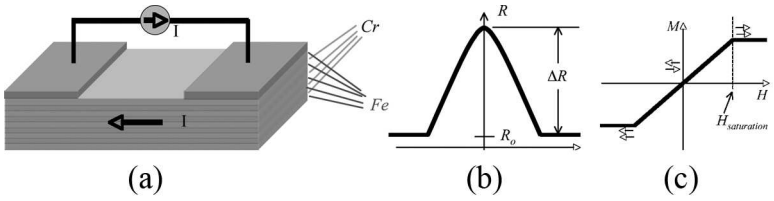

Fig. 19.76. (a) schematic $\mathrm{Fe Cr}\ (001)$ superlattices [BBF$^+$88]; (b) typical resistivity vs. applied field behavior and (c) M(H) response for a GMR sensor.

particles [XDP$^+$06]. The combination of sensitivity with ease of use in atomic magnetometers make them a promising alternative for detecting weak magnetic fields. One of the first chip-scale atomic magnetometer constructed at NIST [SKS$^+$04] was based on magnetically sensitive *coherent population trapping (CPT)* resonances at atomic hyperfine frequencies. Since the CPT resonance is optically driven, there are not magnetic fields applied to the instrument that might interfere with other sensors.

Commercially available magnetoresistive sensors can exploit *anisotropic magnetoresistance, AMR* of ferromagnets. In anisotropic magnetoresistance the change in resistance is different when the field is applied parallel to the current than when normal to the current direction. Anisotropic Magnetoresistive (AMR) sensors can measure both linear and angular position and displacement in the Earth's field. Typical devices are Ni-Fe thin films deposited on a Si wafer using 2%-3% resistance changes, in a field, in patterned resistive strip [CM92].

These types of sensors have found much recent importance after the discovery of *giant magnetoresistance* Fig. 19.76 (a) shows a schematic of $\mathrm{Fe Cr}\ (001)$ superlattices for which giant magnetoresistance was first observed (b) shows a typical resistivity vs. applied field behavior for a GMR material and (c) shows the magnetic state of the material in terms of its field-dependent magnetization, M(H). The term giant refers to values of $MR \geq\sim 25$ % to several 100 %. MR values 10-100 times larger have been observed in oxides and other materials exhibiting *colossal magnetoresistance, CMR*. CMR materials typically require very large bias fields limiting their applicability.

Alternating gradient magnetometers are another sensitive technique which is used to measure magnetization. A thin film AGM has been designed for use in detecting extraterrestrial minerals [SCW$^+$11], [WSV$^+$11] and biomedical applications [JMS$^+$11] of tagging tissue scaffold. The sensor system is shown in Fig. 19.77 (a). The sensor head consists of a permanent $\mathrm{Fe Pt}$ or $\mathrm{Co Cr Pt}$ magnet deposited using a thin film sputtering to create a checkerboard pattern onto a Si substrate. Fig. 19.77 (b) shows the membrane, the checkerboard and Fig. 19.77 (c) the SEM determined chemistry.

The sensor shown in Fig. 19.77 (a) has coils creating a driving field gradient. The correct geometries and spatial arrangement of the coils will generate a magnetic force

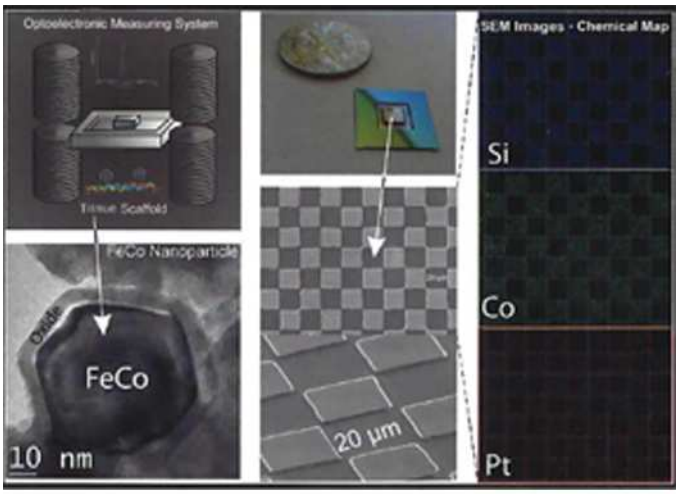

Fig. 19.77. (a) AGM thin film resonator sensor geometry; (b) membrane, the checkerboard and (c) the SEM determined chemistry of the films (April 1, 2011 cover of the J. Appl. Phys.)

on the membrane in the z direction, causing it to vibrate in mechanical resonance. An additional force, proportional to the detected material's magnetic moment and the field gradient is determined from shifts in the mechanical resonance frequency. When excited at the resonance frequency, the membrane deformation is measured using a high resolution optical detection method. Light emitted from an LED is guided through an optical fiber and is reflected on the surface of the magnet. Reflected light is detected by a bundle of PMMA fibers and transmitted to a photodiode. The resulting photocurrent is amplified and a lock-in amplifier is used to measure the detection signal.

Strains can also be the basis for sensing exploiting giant magnetostriction in important rare-earth/Fe alloys like Terfenol-D [$(\mathrm{Dy}_{0.7}\mathrm{Tb}_{0.3})\mathrm{Fe}_2$]. The shape of the magnetostriction-applied field curve yields little magnetostriction at low fields making such materials unsuitable for low-field magnetometry. However, it has been shown that in tension, a significant slope is observed at low fields [SHS$^+$94]. Novel sensors have been developed using surface micromachining of silicon with microelectromechanical system (MEMS) fabrication techniques [BMC95]. In a magnetostrictive magnetometer, a thin Terfenol-D film is deposited on a MEMS cantilever. The magnetostriction of the Terfenol-D causes the cantilever to deflect. The deflection is a function of the field strength and can be measured by optical beam deflection or capacitance changes.

Giant Magnetoimpedance, GMI, as discussed above is observed in materials with large permeabilities including amorphous and nanocomposite materials.

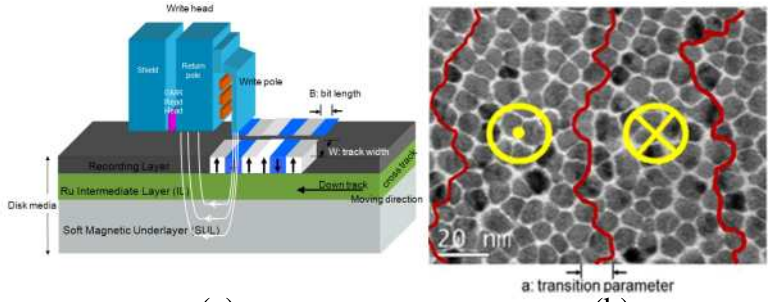

Fig. 19.78. (a) Schematic of perpendicular recording scheme and (b) schematic of a bit drawn on micrograph of an actual thin film media. (courtesy Dr. S. Park) [Par10]

19.4.6 Magnetic Recording.

The rapid development of information technology has been greatly enabled by the rapid growth in the areal recording density of magnetic hard drives [PVEWE01]. This has been made possible by advances in the materials and processing techniques used to produce current recording devices.

Magnetic recording devices consist of two main magnetic systems: the heads which write or read the information and the media on which the information is stored. In todays media, information is written in the perpendicular mode by a single pole write head when it applies a magnetostatic field in the perpendicular direction and reverses the magnetization in the medium. In Fig. 19.78 (a), the magnetization is stored perpendicular to the disk plane because the magnetic easy axis of materials in the recording layer has been aligned in this direction. When the information is read back, a giant magnetoresistance (GMR) (see above) read sensor is moved to where the information is stored and it reads the magnetization in the recording layer.

The information is stored on the media in bits. Fig. 19.78 (b) illustrates two magnetic domains in the opposite direction [Par10]. One bit consists of 50-75 magnetic grains and each of the grains is surrounded by a non magnetic oxide film which magnetically isolates them from each other. The bits are aligned along a track and tracks are configured concentrically on the hard disk. In Fig. 19.78 (b) the transition region between written bits is delineated and it can be seen to be directly related to the grain size of the film. In turn, media noise is directly related to the transition width as well as the grain size distribution [Par10].

The early generations of computers had the information stored on tapes or hard disks that had been coated with a slurry that contained elongated particles of γ-Fe_2O_3 (maghemte). The particles coercivity was determined by shape anisotropy. Later, thin

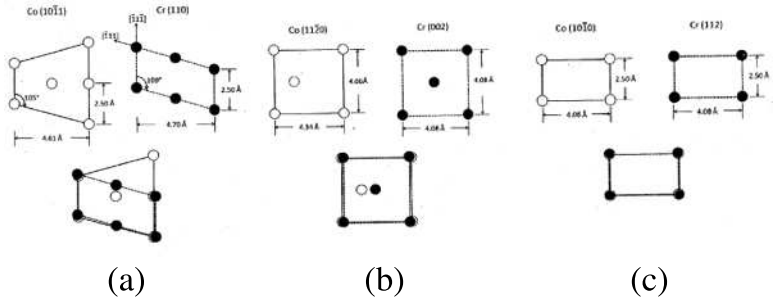

Fig. 19.79. Schematics of the atomic matching of (a) the $(10\bar{1}1)$ planes of *hcp*Co and (110) planes of Cr; (b) $(11\bar{2}0)$ planes of *hcp*Co and (200) planes of Cr and (c) $(10\bar{1}0)$ planes of *hcp*Co and (112) planes of Cr. [LW91]

films of Co alloys were introduced and as of the time writing of this chapter thin Co alloy films are still utilized.

The development of media for magnetic storage is a good example of the use of the basic principals of materials science. The media must consist of small magnetic grains that are strongly oriented (textured) with their easy axes in the plane of the disk for longitudinal recording or normal to the plane of the disk for perpendicular recording. Furthermore, the grains should be of uniform size and should be magnetically isolated from each other.

As mentioned above, particulate media and the first of the thin film hard drives were longitudinal media. In the particulate media the particles had their long axes in the plane of the film. In the first commercialized thin film media the films were produced in such a way that the c-axes of the Co alloy grains were in the plane of the disk. Since the magnetic easy axis of Co alloys is the c-axis, a method had to be devised to grow the Co alloys with the c-axes in (or nearly in) the plane of the disk. This was done by using Cr underlayers. Cr(*bcc*) naturally sputters with a ((110) texture and this gives rise by epitaxy to a $(10\bar{1}1)$ texture of the Coalloy. In this case the c-axes were about 30° out of the plane of the disk. Later it was found that by depositing the Cr films at elevated temperatures (270-300°C) they would obtain the (200) texture, which in turn produced (by epitaxy) the $(11\bar{2}0)$ texture in the Co alloy. This texture allowed for the c-axes to be in the plane of the film (Fig. 19.79) [LW91]. Later the underlayers were grown with the (112) texture (with the help of NiAl seedlayers) [LCF$^+$95] and the Co alloys deposited with the $(10\bar{1}0)$ texture [LYYW09].

Since the turn of the century, information in hard disk media has been stored in the so-called perpendicular mode, in which the easy axes of the magnetic grains in the films are perpendicular to the plane of the disk. Co alloys have the hexagonal close packed (*hcp*) structure and their c axes are usually the magnetically soft axes. Since

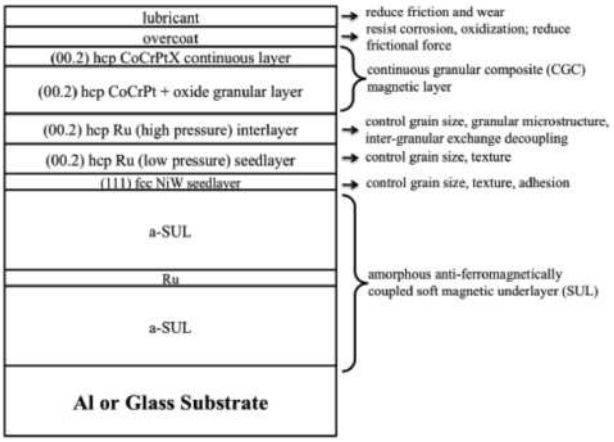

Fig. 19.80. A schematic of the structure of the thin film layers of a typical perpendicular magnetic recording media. (courtesy of Dr. H. Yuan) [Yua09]

the anisotropy of a thin film tends to lie in the plane of the film (because of shape effects), the magnetization of the Co alloy has to be lowered by the addition of Cr. This decreases the magnetization and hence lowers the magnetostatic energy of the film.

A schematic cross section of perpendicular media is shown in Fig. 19.80. Here there are several layers of films, each with their specific purpose. The layer directly under the magnetic layer is Ru (or an alloy of Ru) which has the *hcp* structure and a slightly larger lattice parameter than the Co alloys. When deposited in the perpendicular manner the larger Ru lattice tends to stretch the Co alloy lattice its the basal plane, since this is the plane of epitaxy in perpendicular recording. Since Co alloys have a negative magnetostrictive constant, a perpendicular anisotropy is induced in the Co alloy over and above its already strong magneto-crystalline anisotropy in the same direction.

Another function of the Ru layer is to control the grains size and the positioning of the oxide phase in the recording layer. The deposited Ru films have domes on their surface which controls where the oxide in the recording layer forms (Fig. 19.81). The domes form best in films that are sputtered under a higher Ar pressure. In the Figure the Ru domes can be seen to allow for the oxide to form in the valleys during the deposition of the Co alloy/oxide layer. The oxides then grow around the Co alloy grains magnetically isolating them from other Co alloy grains.

The grain size of the storage layer is controlled by a combination of the percentage of oxide and the grain size of the Ru underlayer. In turn, this is controlled by

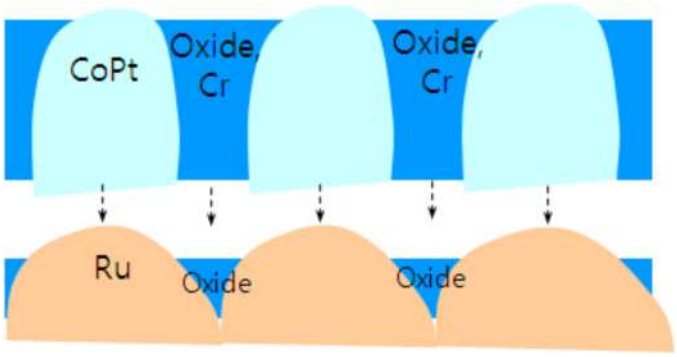

Fig. 19.81. A schematic showing the role of the Ru domes in controlling the microstructure of the Co recording layer. (courtesy of Dr. S. Park) [Par10]

processing variables (sputtering power, Ar back-pressure, etc.) and sometimes by an additional underlayer.

Beneath the Ru layer there is often a layer such as a Ni-W alloy which deposits with a very strong (111) *fcc* texture and because of its similar atomic arrangement increases the subsequent Ru and Co alloy films texture by means of epitaxy. The texture of the Co alloy film is crucial to good recording properties and it is measured by the full width half maximum (FWHM) of a x-ray rocking curve.

In most perpendicular media there exists a *soft magnetic underlayer (SUL)* which acts to close the magnetic flux with the head. Amorphous soft magnetic materials with high permeability, such as CoZrTa are commonly used as the SUL. The thin Ru layer in the middle of the SUL couples the two SULs in an antiferromagnetic fashion and acts to pin any magnetic domains that exist in that layer, thereby minimizing its contribution to the noise (Fig. 19.80).

The type of media described above is often termed *conventional perpendicular magnetic media*. It has been used in hard drives for computers over a decade now. A limit in the lower bound of the Co alloy grain size is approaching since the grains will soon be small enough to become superparamagnetic. This will require the introduction of a new magnetic media: one with larger magnetocrystalline anisotropy [Woo00]. A candidate for this is FePt alloys, which will be able to sustain magnetization down to about 3 nm grains. There are many challenges with FePt. First, since they will need to have very high magnetocrystalline anisotropy, they will be very difficult to write on. Schemes such a heat assisted magnetic recording (HAMR) [RBB+06] may be needed if the new media is used. Another challenge is producing the high anisotropy: to do this the FePt alloy must be highly ordered atomically. This entails high temper-

ature processes, which may not be compatible with the rest of the magnetic recording device. Research on these alloys continues.

This chapter has introduced metals and alloys used for soft and hard magnets and surveyed some current applications. This field has continued to innovate an progress over many decades. The choices of materials and applications is by no means exhaustive and reflects the interest and expertise of the authors. They are convinced that in a decade there will be more new and exciting additions to this field and hope to contribute to its future.

19.5 Further Reading.

Magnetic Materials.:

(i) **Ferromagnetism** by Richard M. Bozorth has been published by the IEEE Press as a classic reissue [Boz93].
(ii) Chen discusses the development of soft magnetic metal alloys. [Che86]
(iii) O"Handley [O'H87] offers a more modern materials perspective.
(iv) Cullity and Graham [CG09] is the update of the classic text on magnetic materials
(v) Coey [Coe10] is a modern text on magnetic materials.
(vi) Coey [Ce96] discusses permanent magnet materials.
(vii) The book edited by Plumer, et al. [PVEWE01] discussed data storage technologie

Structure.:

(i) DeGraef and McHenry [DM07] discusses the structure of materials with many magnetic materials examples.
(ii) Cullity [Cul78] is the classic text on x-ray diffraction by the author of the famous book on magnetic materials.
(iii) Barrett and Massalski [BM80] is a classic text on structure of materials.

Phase Equilibria:

(i) Prince [Pri66] is a classic text discussing phase diagrams.
(ii) Porter and Easterling [PE00] discusses phase equilibria and the kinetics of phase transformations.
(iii) Massalski [Mas90] is the handbook of Bbnary alloy phase diagrams

Current Research and Applications: There are many good journals covering magnetism and magnetic materials. In particular, the Journal of Applied Physics annually publishes the peer reviewed articles from the Magnetism and Magnetic Materials (MMM) Conference, the largest international scientific conference on the subject. The IEEE Transaction on Magnetics similarly publishes peer reviewed articles from the Intermag conferences which are more focussed on applications. The two are held simultaneously every three years as the MMM/Intermag Conference. Many materials societies also have topical groups and symposia dedicated to magnetic materials. The Materials Society (TMS) is one such example.

Bibliography

[ABC78a] R. Alben, J. J. Becker, and M. Chi. "". *J. Appl. Phys.*, 49:1653, 1978.

[ABC78b] R. Alben, J. Budnick, and G. S. Cargill. *"Metallic Glasses."*, page 304. ASM, Metals Park, OH, 1978.

[Acu02] M. H. Acuna. "Space-based Magnetometers.". *Rev. Sci. Instrum.*, 73:3717–3736, 2002.

[AE83] M. Ausleos and R. I. editors. Elliot. *"Magnetic Phase Transitions, Springer Series in Solid State Sciences."*, volume 48. Springer-Verlag, Berlin, Heidelberg, New York, Tokyo, 1983.

[Arr57] A. S. Arrott. "Criterion for Ferromagnetism from Observations of Magnetic Isotherms.". *Phys. Rev.*, 108:1394–96, 1957.

[BBF+88] M. N. Baibich, J. M. Broto, A. Fert, F. Nguyen Van Dau, F. Petroff, Eitenne P., and G. Creuzet. "Giant Magnetoresistance of (001)Fe/(001)Cr Magnetic Superlattices.". *Phys. Rev. Lett*, 61:2472, 1988.

[Bel56] K. P. Belov. "". *Fiz. Met. Metalloved*, 27:261, 1956.

[BM80] C. Barrett and T. B. Massalski. *"Structure of Metals, Crystallographic Methods, Principles and Data", 3rd revised edition, International Series on Materials Science and Technology 35*. Pergamon, Oxford, 1980.

[BMC95] R. C. Benson, J. C. Murphy, and H. K. Jr. Charles. "Miniature Sensors Based on Microelectromechanical Systems.". *Johns Hopkins APL Tech. Dig.*, 16(3):311–318, 1995.

[Bol94] R. Boll. *"Chapter 14: Soft Magnetic Metals and Alloys"*, volume 3B of *Materials Science and Technology, A Comprehensive Treatment (K. H. J. Buschow, Editor).*, page 399. VCH, Weinheim, 1994.

[Boz93] Richard M. Bozorth. *"Ferromagnetism."*. IEEE Press, Piscataway, N. J., 1993.

[BP85] W. J. Boettinger and J. H. Perepezko. "Fundamentals of Rapid Solidification.". In *Rapidly Solified Crystalline Alloys*. Proceedings of a TMS-AIME North East Regional Meeting, May 1-3 1985.

[Bru05] E. Bruck. "Developments in Magnetocaloric Refrigeration.". *J. Phys. D: Appl. Phys.*, 38:R381–391, 2005.

[Bus26] H. Busch. "Berechnung der Bahn von Kathodenstrahlen im Axialsymmetrischen Elektromagnetischen Felde.". *Ann. Phys. (Leipzig)*, 18:974–993, 1926.

[Bus88] K. H. J. Buschow. *in "Ferromagnetic Materials." E. P. Wohlfarth and K. H. J. Buschow, editors*. Elsevier Science Publishers, Amsterdam, 1988.

[BWW03] G. Bison, R. Wynands, and A. Weis. "Dynamical Mapping of the Human Cardiomagnetic Field with a Room Temperature, Laser-optical Sensor.". *Optics Express*, 11:904–909, 2003.

[CCDG+00] S. Y. Chu, A. Cramb, M. De Graef, D. E. Laughlin, and M. E. McHenry. "The

Effect of Field Cooling and Field Orientation on the Martensitic Phase Transformation in a Ni_2MnGa Single Crystal.". *J. Appl. Phys.*, 87:5777–5779, 2000.

[CCG73] P. Chaudhari, J. J. Cuomo, and R. J. Gambino. "Amorphous Films for Magnetic Bubble and Magneto-optic Applications.". *Appl. Phys. Lett.*, 22:337–339, 1973.

[Ce96] J. M. D. Coey and editor. *"Rare Earth Permanent Magnets."*. Oxford Science Publications, Clarendon Press, Oxford, 1996.

[CG09] B.D. Cullity and C.D. Graham. *"Introduction to Magnetic Materials. 2nd Edition."*. IEEE Press, John Wiley and Sons, Hoboken, NJ, 2009.

[CGGM01] S. Y. Chu, R. Gallagher, De Graef, and M. E. McHenry. "Structural and Magnetic Phase Transitions in Ni_2MnGa Ferromagnetic Shape-memory Alloy Crystals.". *IEEE Trans. Mag.*, 37:2666–2668, 2001.

[Che86] Chih-Wen Chen. *"Magnetism and Metallurgy of Soft Magnetic Materials."*. Dover, New York, 1986.

[Chi78] C. L. Chien. "Mossbauer study of a binary amorphous ferromagnet: $Fe_{80}B_{20}$.". *Phys. Rev. B*, 18:1003–15, 1978.

[CHWF+03] A. E. Clark, K. B. Hathaway, M. Wun-Fogle, J. B. Restorff, T. A. Lograsso, V. M. Keppens, G. Petculescu, and R. A. Taylor. "Extraordinary Magnetoelasticity and Lattice Softening in *bcc*Fe-Ga alloys.". *J. Appl. Phys.*, 93:8621, 2003.

[CIN93] T. Chou, M. Igarashi, and Y. Narumiya. Soft magnetic properties of microcrystalline fe-al-si-ni-zr-b alloys. *J. Magn. Soc. Jpn.*, 17:197–200, 1993.

[CJM+09] K. N. Collier, N. J. Jones, K. J. Miller, Y. L. Qin, D. E. Laughlin, and M. E. McHenry. "Controlled Oxidation of $FeCo$ Magnetic Nanoparticles (MNPs) to Produce Faceted FeCo/ferrite Nanocomposites for RF Heating Applications.". *J. Appl. Phys.*, xxx:accepted for publication, 2009.

[Cla80] A. E. Clark. *"Chapter 7: Magnetostrictive Rare Earth-*Fe_2 *Compounds."*, volume 1 of *Ferromagnetic Materials (E. P. Wohlfarth, Editor)*., page 531. North-Holland, Amsterdam, 1980.

[CLM+94] M. Cadogan, H. S. Li, A. Margarian, J. B. Dunlop, Ryan D. H., S. J. Collocott, and R. L. Davis. "New Rare-Earth Intermetallic Phases $R_3(Fe,M)_{29}X_n$ - (R Ce, Pr, Nd, Sm, Gd, M Ti, V, Cr, Mn, and X H, N, C).". *J. Appl. Phys.*, 76:6138, 1994.

[CLP+11] A. Chaturvedi, N. Laurita, M. H. Phan, M. E. McHenry, and H. Srikanth. "Giant Magnetoimpendance and Field Sensitivity in Amorphous and Nanocrystalline $(Co_{1-x}Fe_x)_{89}Zr_7B_4$ (x=0,0.025,0.05,01) Ribbons.". *J. Appl. Phys.*, 109:07B508, 2011.

[CM92] P. Ciureanu and S. Middelhoek. *"Thin Film Resistive Sensors."*. Institute of Physics Publishing, New York, 1992.

[CO85] B. W. Corb and R. C. O'Handley. "Magnetic Properties and Short-range Order in Co-Nb-B Alloys.". *Phys. Rev. B*, 31:7213–7219, 1985.

[Coe78] J. M. D. Coey. "Amorphous Magnetic Order.". *J. Appl. Phys.*, 49:1646–52, 1978.

[Coe91] R. L. Coehorn. *"Supermagnets: Hard Magnetic Materials. Long, G. J. and Grandjean, F., editors "*, chapter 8. Kluwer, 1991.

[Coe10] J. M. D. Coey. *"Magnetism and Magnetic Materials."*. Cambridge University Press, Cambridge, UK, 2010.

[CS90] J. M. D. Coey and H. Sun. "Improved Magnetic Properties by Treatment of Iron-based Rare Earth Intermetallic Compounds in Ammonia.". *J. Magn. Magn. Mater.*, 87:L251–L254, 1990.

[Cul78] B.D. Cullity. *"Elements of X-ray Diffraction."*. Addison-Wesley Publishing Company, Inc., Reading, MA, 1978.

[CW86] G. Y. Chin and J. H. Wernick. *"Soft Magnetic Metallic Materials in Ferromagnetic Materials, Edited by Wohlfarth"*. North-Holland, New York, 1986.

[Dav85] H. A. Davies. *in "Rapidly Quenched Metals." edited by S. Steeb and H. Warlimont*, volume 1. North Holland, Amsterdam, 1985.

[DD78] I. W. Donald and H. A. Davies. "Prediction of Glass Forming Ability for Metallic Systems.". *J. Non-Cryst. Solids.*, 30:77–85, 1978.

[Deb26] P. Debye. "". *Ann. Phys. (Lpz)*, 81:1154, 1926.

[DGL+76] J. Deportes, D. Givord, R. Lemaire, H. Nagai, and Y. J. Yang. "Influence of Substitutional Pairs of Cobalt atoms on Magnetocrystalline Anisotropy of Cobalt-rich Rare-Earth Compounds.". *J. Less-Common Met.*, 44:273–279, 1976.

[Din91] T. Dinsdale. "SGTE Data for Pure Elements.". *CALPHAD*, 15(4):317–425, 1991.

[DM07] M. E.. DeGraef and M. E. McHenry. *"The Structure of Materials."*. Cambridge University Press, Cambridge, 2007.

[DM09] M. Diaz-Michelena. "Small Magnetic Sensors for Space Applications.". *Sensors*, 9:2271–2288, 2009.

[DMO+11] S. Dweyedi, G. Markandeyulu, P. R. Ohodnicki, A. Leary, and M. E. McHenry. "Stress-MI and Domain Studies in Co-based Nanocrystalline Ribbons..". *J. Mag. Mag. Mat.*, 323:1929–1933, 2011.

[DWMZ01] M. E.. DeGraef, M. A. Willard, M. E. McHenry, and Y. Zhu. "In-situ Lorentz TEM Cooling Study of Magnetic Domain Configurations in Ni_2MnGa.". *IEEE Trans. Mag.*, 37:2663–2665, 2001.

[DWW60] P. Duwez, R. H. Willens, and Klement W. "Continuous Series of Metastable Solid Solutions in Silver-Copper Alloys.". *J. Appl. Phys.*, 31:1136–1137, 1960.

[EPU+09] W. F. Egelhoff, P. W. T. Pong, J. Unguris, R. D. McMichael, E. R. Nowak, A. S. Edelstein, J. E. Burnette, and G. A. Fischer. "". *Sensors and Actuators A*, 155:217225, 2009.

[FCBC07] V. Franco, C. F. Conde, J. S. Blazquez, and A. Conde. "Magnetocaloric Effect in Mn-containing Hitperm-type Alloys.". *J. Appl. Phys.*, 102:013908, 2007.

[FCT02] R. T. Fingers, R. P. Carr, and Z. Turgut. "Effect of Aging on Magnetic Properties of Hiperco™ 27, Hiperco™ 50, and Hiperco 50 HS™ Alloys.". *J. Appl. Phys.*, 91:7848, 2002.

[FFST91] Y. Fujii, H. Fujita, A. Seki, and T. Tomida. "Magnetic Properties of Fine Crystalline Fe-P-C-Cu-X Alloys.". *J. Appl. Phys.*, 70 (10):6241–6243, 1991.

[Fon59] S. Foner. "Versatile and Sensitive Vibrating-sample Magnetometer.". *Rev. Sc Instr.*, 30:548–557, 1959.

[Fon96] S. Foner. "The Vibrating Sample Magnetometer: Experiences of a Volunteer (invited).". *J. Appl. Phys.*, 79:4740, 1996.

[Fri58] J. Friedel. "Theory of Magnetism in Transition Metals.". *Nuevo Cim. Suppl.*, 7:287, 1958.

[GB72] D. I. Gordon and R. E. Brown. "Recent Advances in Fluxgate Magnetometry.". *IEEE Trans. Magnetics*, MAG-8:76–82, 1972.

[GC78] R. J. Gambino and J. J. Cuomo. "Selective Resputtering Induced Anisotropy in Thin Films.". *J. Vac. Sci. Tech.*, 15 (2):296–301, 1978.

[Gia27] W. F. Giauque. "Paramagnetism and the third law of thermodynamics. Interpretation of the low-temperature magnetic susceptibility of gadolinium sulfate.". *J. Amer. Chem. Soc.*, 49:1870–77, 1927.

[Gig95] D. Gignoux. *"Magnetic Properties of Metallic Systems."*, volume 3 Ch. 5 of *Materials Science and Technology, A Comprehensive Treatment. Electronic and Magnetic Properties of Metals and Ceramics. K. H. J. Buschow, editor.*, pages 367–453. VCH, Weinheim, 1995.

[Gil58] W. Gilbert. *De Magnete, translated by P. Mottelay*. Dover Publications, Inc., New York, 1958.

[GJK+96] K. A. Gallagher, F. A. Johnson, E. Kirkpatrick, J. H. Scott, S. Majetich, and M. E. McHenry. "Synthesis, Structure, and Magnetic Properties of Fe-Co Alloy Nanocrystals. ". *IEEE Trans. Mag.*, 32:4842–4844, 1996.

[Gle89] H. Gleiter. "Nanocrystalline Materials.". *Prog. Mat. Sci.*, 33:223–315, 1989.

[GLM84] D. Givord, H. S. Li, and J. M. Moreau. "Magnetic Properties and Crystal Structure of $Nd_2Fe_{14}B$.". *Solid State Commun.*, 50:497–499, 1984.

[GMO89] A. M. Ghemawat, M. E. McHenry, and R. C. O'Handley. "Magnetic Moment Suppression in Rapidly Solidified Co-TE-B Alloys.". *J. Appl. Phys.*, 63:3388–90, 1989.

[GPT05] K. A. Gschneidner, V. K. Pecharsky, and A. O. Tsokol. "Recent Developments in Magnetocaloric Materials.". *Reports on Progress in Physics*, 68:1479–539, 2005.

[GW74] A. G. Guy and J. J. Wren. *"Elements of Physical Metallurgy."*. Addison-Wesley, 1974.

[GW02] A. L. Greer and I. T. Whitaker. "Transformations in Primary Crystallites in (Fe,Ni)-based Metallic Glasses. ". *Materials Science Forum*, 386-388:77–88, 2002.

[GWLM99] K. A. Gallagher, M. A. Willard, D. E. Laughlin, and M. E. McHenry. "Distributed Magnetic Exchange Interactions and Mean Field Theory Description of Temperature Dependent Magnetization in Amorphous $Fe_{88}Zr_7B_4Cu_1$ Alloys. ". *J. Appl. Phys.*, 85:5130–32, 1999.

[Hal79] E. Hall. "On a New Action of the Magnet on Electric Currents". *Am. J. Math.*, 2:28792, 1879.

[Han69] K. Handrich. "A Simple Model for Amorphous and Liquid Ferromagnets.". *Phys. Status Solidi*, 32:K55, 1969.

[HCL82] J.F. Herbst, J.J. Croat, and R.W. Lee. "Neutron Diffraction Studies of $Nd_2(Co_xFe_{1-x})_{17}$ Alloys: Preferential Site Occupation and Magnetic Structure.". *J. of Appl. Phys.*, 53:250–256, 1982.

[HCP84] J.F. Herbst, J.J. Croat, and F.E. Pinkerton. "Relationships Between Crystal Structures and Magnetic Properties in $Nd_2Fe_{14}B$.". *Phys. Rev. B*, 29:4176–4178, 1984.

[Her91] J.F. Herbst. "$R_2Fe_{14}B$ Materials: Intrinsic Properties and Technological Applications.". *Rev. Mod. Phys.*, 63:819–898, 1991.

[Her97] G. Herzer. *""*, volume 10 Ch. 3 of *Handbook of Magnetic Materials. K. H. J. Buschow, editor.*, page 415. Elsevier Science, Amsterdam, 1997.

[HHS+99] V. G. Harris, Q. Huang, V. R. Shah, G. Markandeyulu, K. V. S. Rama Rao, M. Q. Huang, K. Sirisha, and M. E. McHenry. "Neutron Diffraction and Extended X-ray Absorption Fine Structure Studies of $Pr_3(Fe_{1-x}Co_x)_{27.5}Ti_{1.5}$ Permanent Magnet Compounds.". *IEEE Trans. Magn.*, 35:3286–88, 1999.

[HML+02] A. Hsiao, M. E. McHenry, D. E. Laughlin, M. J. Kramer, C Ashe, and T. Okubo. "The Thermal, Magnetic and Structural Characterization of the Crystallization Kinetics of Amorphous and Soft Magnetic Materials.". *IEEE Trans. Mag.*, 38:2946–2948, 2002.

[HOC+08] A. Habib, C. L. Ondeck, P. Chaudhary, M. R. Bockstaller, and M. E. McHenry. "Evaluation of Iron-Cobalt/Ferrite Core-shell Nanoparticles for Cancer Thermotherapy.". *J. Appl. Phys.*, 103:07A307, 2008.

[HOM+10] A. Habib, M. G. Ondeck, K. J. Miller, R. Swaminathan, and M. E. McHenry. "Novel Solder-magnetic Particle Composites, Their Reflow using AC Magnetic Fields.". *IEEE Trans. Mag.*, 46:2187–2190, 2010.

[Hop85] J. Hopkinson. "Magnetization of Iron.". *Trans. Roy. Soc. (London) A*, A 176:455, 1885.

[Hor56] E. Hornbogen. "". *Z. Metallkunde*, 47:47, 1956.

[HP01] V. G. Harris and T. Pokhil. "Selective-Resputtering-Induced Perpendicular Magnetic Anisotropy in Amorphous TbFe Films.". *Phys. Rev. Lett.*, 87 (36):067207, 2001.

[HS20] K. Honda and S. Saito. "". *Sci Rep. Tohoku Imp. Univ.*, 9:417, 1920.

[HS85] A. B. Harris and R. Sachidanandam. "Orientational Ordering of Icosahedra in Solid C_{60}.". *Phys. Rev. B*, 46 (8):4944–4957, 1985.

[HTW+99] A. Hsiao, Z. Turgut, M. A. Willard, E. Selinger, M. Lee, D. E. Laughlin, M. E. McHenry, and Hasegawa R. "Crystallization And Nanocrystallization Kinetics of Fe- and

Fe(Co)-based Amorphous Alloys.". *MRS Res. Symp. Proc.*, 577:551, 1999.

[Hun27] F. Hund. *"Linienspektren und periodische system der elemente"*. Springer, Berlin, 1927.

[HWR+93] G. R. Harp, D. Weller, T. A. Rabedeau, R. F. C. Farrow, and M. F. Toney. "Magnetooptical Kerr Spectroscopy of a New Chemically Ordered Alloy - Co_3Pt.". *Phys. Rev. Lett.*, 71 (15):2493, 1993.

[HYKP96] Z. Hu, W. B. Yelon, O Kaligirou, and V. Psycharis. "Site Occupancy and Lattice Changes on Nitrogenation in $Nd_3Fe_{29-x}Ti_xN_y$.". *J. Appl. Phys.*, 80:2955–2959, 1996.

[IG96] A. Inoue and J. S. Gook. "Effect of Additional Elements on the Thermal Stability of Supercooled Liquid in $Fe_{72-x}Al_5Ga_2P_{11}C_6B_4M_x$ Glassy Alloys". *Mat. Trans. JIM.*, 37 (1):32–38, 1996.

[ILML99] H. Iwanabe, B. Lu, M. E. McHenry, and D. E. Laughlin. "Thermal Stability of the Nanocrystalline Fe-Co-Hf-B-Cu Alloy". *J. Appl. Phys.*, 85:4424–6, 1999.

[IZIT97] A. Inoue, T. Zhang, T. Itoi, and A. Takeuchi. "New Fe-Co-Ni-Zr-B Amorphous Alloys with Wide Supercooled Liquid Regions and Good Soft Magnetic Properties.". *jim*, 38 (4):359–362, 1997.

[JAVR+85] W. L. Johnson, M. Atzmon, M. Van Rossum, B. P. Dolgin, and X. L. Yeh. *in "Rapidly Quenched Metals." edited by S. Steeb and H. Warlimont*, volume 1. Elsevier, North Holland, New York, 1985.

[Jel36] W. Jellinghaus. "". *Zeit. Krist.*, 133:33, 1936.

[JHG+01] F. Johnson, P. Hughes, R. Gallagher, M. E. McHenry, and D. E. Laughlin. "Structure and Thermomagnetic Properties of New FeCo-base Nanocrystalline Ferromagnets.". *IEEE Trans. Mag.*, 37:08K909, 2001.

[JK94] R. D. James and M. Kinderlehrer. "Theory of Magnetostriction with Application to Terfenol-D.". *J. Appl. Phys.*, 76:7012–7014, 1994.

[JMS+11] N. J. Jones, K. L. McNerny, V. Sokalski, M. Diaz-Michelena, D. E. Laughlin, and M. E. McHenry. "Fabrication of Thin Films for a Small Alternating Gradient Field Magnetometer for Biomedical Magnetic Sensing Applications.". *J. Appl. Phys.*, 109:07E512, 2011.

[JMW+10] N. J. Jones, K. L. McNerny, A. T. Wise, M. Sorescu, M. E. McHenry, and D. E. Laughlin. "Observations of Oxidation of Oxidation Mechanisms and Kinetics in Facetted FeCo Nanoparticles.". *J. Appl. Phys.*, 107:09A304, 2010.

[JS06] F. Johnson and R. D. Shull. "Amorphous-FeCoCrZrB Ferromagnets for Use as High Temperature Magnetic Refrigerants.". *J. Appl. Phys.*, 99:8, 2006.

[JTW99] R. D. James, R. Tickles, and M. Wuttig. "Large Field-Induced Strains in Ferromagetic Shape Memory Materials.". *Mat. Sci. Eng. A*, A273-275:320–325, 1999.

[KDS+96] K. S. Kim, L. Driouch, V. Strom, B. J. Jonsson, K. V. Rao, and S. C. Yu. "Magnetic Properties of Glassy $Fe_{91-x}Zr_7B_2Ni_x$.". *ieee*, 32 (5):5148–5150, 1996.

[KH81] U. Koster and U. Herold. *"Glassy Metals I." Topics in Physics 46.* Springer-Verlag, Berlin, 1981.

[KHD+97] I. Kraus, V. Haslar, P. Duhaj, Svec P., and V. Studnicka. "The Structure and Magnetic Properties of Nanocrystalline $Co_{21}Fe_{64-x}Nb_xB_{15}$ Alloys.". *Mat. Sci. Eng. A-Struct*, 226:626–630, 1997.

[KMIM89] N. Kataoka, T. Matsunaga, A. Inoue, and T. Masumoto. "Soft Magetic Properties of BCC Fe-Au-X-Si-B (X = Early Transition Metal) Alloys with fine Grain Structure.". *Mat. Trans. JIM*, 30:947–950, 1989.

[KMS+11] S. J. Kernion, K. J. Miller, S. Shen, V. Keylin, J. Huth, and M. E. McHenry. "High Induction Low Loss FeCo-based Nanocomposite Alloys with Reduced Metalloid Content.". *IEEE Trans. Mag.*, 73 (10):to appear, 2011.

[Kob69] S. Kobe. "". *Phys. Status Solidi*, 41:K13, 1969.

[Kra27] R. de L. Kramers. "La diffusion de la lumiere par les atomes.". *Atti Cong. Intern.*

Fisica, (Transactions of Volta Centenary Congress) Como, 2:545557, 1927.

[Kro]

[KYK+93] K.-S. Kim, S.-C. Yu, K.-Y. Kim, T.-H. Noh, and I.-K. Kang. "Low Temperature Magnetization in Nanocrystalline $Fe_{88}Zr_7B_4Cu_1$ Alloy". *IEEE Trans. Mag.*, 29:2679–81, 1993.

[Lan37] L. D. Landau. "theory of phase transformations. i". *Zh. Eksp. Teor. Fiz.*, 7:19, 1937.

[LCF+95] D. E. Laughlin, B. Cheong, Y. C. Feng, D. N. Lambeth, L. L. Lee, and B. Y. Wong. The control of microstructural features of thin films for magnetic recording. *Scripta Metallurgica et Materialia*, 33:1525–1536, 1995.

[LCL+11] N. Laurita, A. Chaturvedi, A. Leary, C. Bauer, C. Miller, M. H. Phan, M. E. McHenry, and H. Srikanth. "Magnetoimpedance Effect in Soft Ferromagnetic Amorphous Ribbons Coated with Magnetic Metals.". *J. Appl. Phys.*, 109, 2011.

[LE06] J. E. Lenz and A. S. Edelstein. "Magnetic Sensors and Their Applications.". *IEEE Sensors Journal*, 6, 2006.

[Len24] J. E. Lenz. "A Review of Magnetic Sensors.". *Proc. IEEE*, 78 (6):973, 1924.

[LGX+96] T. Liu, Y. F. Gao, Z. X. Xu, Z. T. Zhao, and R. Z. Ma. "Compositional Evolution and Magnetic Properties of Nanocrystalline $Fe_{81.5}Cu_{0.5}Mo_{0.5}P_{12}C_3Si_{2.5}$.". *jap*, 80 (7):3972–3976, 1996.

[Lia07] L. Lian. "Effect of Nd Content on Natural Resonance Frequency and Microwave Permeability of $Nd_2Fe_{14}B$/a-Fe Nanocomposites in 26.5-40 GHz Frequency Range.". *J. Alloys and Compounds*, 441:301–304, 2007.

[Lie83] H. H. Liebermann. *Chapter 2 in Amorphous Metallic Alloys. edited by F. E. Luborsky*. Butterworths, London, 1983.

[Liu04] J. Liu. "A GHz Range Electromagnetic Wave Absorber with Wide Bandgap Made of $FeCo/Y_2O_3$ Nanocomposites.". *J. Mag. Mag. Mat.*, 271:L147–152, 2004.

[LL35] L. D. Landau and E. Lifschitz. "on the theory of the dispersion of magnetic permeability in ferromagnetic bodies.". *Phys. Z. Sowjetunion*, 8:153–169, 1935.

[LL78] F. E. Luborsky and H. Lieberman. "Crystallization Kinetics of Fe-B Amorphous Alloys.". *Appl. Phys. Lett.*, 33:233, 1978.

[LMU+08] J. Long, M. E. McHenry, D. Urciuoli, V. Keylin, J. Huth, and T. Salem. "Nanocrystalline Material Development for High-Power Inductors.". *J. Appl. Phys.*, 103:07E705, 2008.

[LOLM07] J. Long, P. R. Ohodnicki, D. E. Laughlin, and M. E. McHenry. "Structural Studies of Secondary Crystallization Products of the $Fe_{23}B_6$-type in a Nanocrystalline $FeCoB$-based Alloy.". *J. Appl. Phys.*, 101:09N114, 2007.

[Lon08] J. Long. "$FeCoB$ *and* $FeZrSi$*-based Nanocomposite Soft Magnetic Alloys and Application.*". Ph.D Thesis, Carnegie Mellon Univ., Pittsburgh, PA, 2008.

[LQN+07] J. Long, Y. Qin, N. T. Nuhfer, M. De Graef, D. E. Laughlin, and M. E. McHenry. "Magnetic Domain Observations in $FeCo$-base Nanocrystalline Alloys by Lorentz Microscopy.". *J. Appl. Phys.*, 101:09N115, 2007.

[LSS+06] S. K. Lee, K. L. Sauer, S. j. Seltzer, O. Alem, and M. V. Romalis. "Subfemtotesla Radio-frequency Atomic Magnetometer for Detection of Nuclear Quadrupole Resonance.". *Appl. Phys. Lett.*, 89:214106, 2006.

[Lub77] F. E. Luborsky. *"Amorphous Magnetism II."*, chapter "Perspective on Application of Amorphous Alloys in Magnetic Devices.", pages 345–68. Plenum Press: New York, 1977.

[LW91] D. E. Laughlin and B. Y. Wong. The crystallography and texture of -based thin film deposited on underlayers. *IEEE Trans. Mag.*, 27(6):4713–4717, 1991.

[LWM00] D. E. Laughlin, M. A. Willard, and M. E. McHenry. *"Phase Transformations and Evolution in Materials. edited by P.Turchi and A. Gonis"*, chapter "Magnetic Ordering: Some Structural Aspects.", pages 121–27. The Minerals, Metals and Materials Society,

2000.

[LYYW09] D. E. Laughlin, H. Yuan, E. Yang, and C. Wang. Application of texture analysis edited by a.d. rollett. *Ceramic Transactions.*, 201, 2009.

[Mas81] T. B. Massalski. "Relationships Between Metallic Glass Formation Diagrams and Phase Diagrams.". In T. Masumoto and K. Suzuki, editors, *Proc. 4th Int. Conf. on Rapidly Quenched Metals*, pages 203–208. The Japan Insitute of Metals, 1981.

[Mas90] T. B. Massalski. *Binary Alloy Phase Diagrams:Second Edition.*, pages 1735–1738. ASM International, 1990.

[MB01] F. Mazaleyrat and F. R. Barrue. *"Soft Amorphous and Nanocrystalline Magnetic Materials."*. Handbook of Advanced Electronic and Photonic Materials and Devices (H. S. Nalwa, Editor) in Nanostructured Materials. Academic Press, 2001.

[McC82] R. A. McCurrie. *Ferromagnetic Materials Structure and Properties.* Academic Press, San Diego, 1982.

[McN99] K. L. McNerny. *"Chemical Synthesis of* α-FeCo *and Metastable* γ-FeNi *Magnetic Nanoparticles with Tunable Magnetic Properties for Study of RF Heating and Magnetomechanical Responses in Polymeric Systems."*. Ph.D Thesis, Carnegie Mellon Univ., Pittsburgh, PA, 1999.

[MCPM10] K. J. Miller, A. Colleti, P. J. Papi, and M. E. McHenry. "Fe-Co-Cr nanocomposites for applications in self-regulated rf heating.". *J. Appl. Phys.*, 107:09A313, 2010.

[Mid63] S. Middelhoek. "Domain Walls in Thin $\mathrm{Ni}-\mathrm{Fe}$ Films.).". *J. Appl. Phys.*, 34:1054, 1963.

[Mis31] T. Mishima. "". *Stahl u. Eisen*, 53:79, 1931.

[MJO+03] M. E. McHenry, F. Johnson, H. Okumura, T. Ohkubo, V. R. V. Ramanan, and D. E. Laughlin. "The Kinetics of Nanocrystallization and Microstructural Observations in FINEMET, NANOPERM and HITPERM Nanocomposite Magnetic Materials.". *Scripta Materialia*, 48:881–887, 2003.

[MKGP05] R. Millen, T. Kawaguchi, M. Granger, and M. Porter. "Giant Magnetoresistive Sensors and Superparamagnetic Nanoparticles: A Chip-Scale Detection Strategy for Immunosorbent Assays.". *Analytical Chemistry*, 77, 2205.

[MKLM10] K. L. McNerny, Y. Kim, D. E. Laughon, and M. E. Mchenry. "Synthesis of Monodisperse γ-Fe-Ni Magnetic Nanoparticles with Tunable Curie Temperatures for Self-Regulated Hyperthermia.". *J. Appl. Phys.*, 107:09A312, 2010.

[ML00] M. E. McHenry and D. E. Laughlin. "Nano-scale Materials Development for Future Magnetic Applications.". *Acta Materialia*, 48:223, 2000.

[ML09] T. B. Massalski and D. E. Laughlin. "The Surprising Role of Magnetism on the Phase Stability of Fe (Ferro). ". *CALPHAD: Computer Coupling of Phase Diagrams and Thermochemistry.*, 33:3–7, 2009.

[MM91] M. E. McHenry and J. M. MacLaren. "Iron and Chromium Monolayer Magnetism in Noble-Metal Hosts: Systematics of Local Moment Variation with Structure.". *Phys. Rev. B*, 43:10611, 1991.

[MMC91] M. E. McHenry, J. M. MacLaren, and D. P. Clougherty. "Monolayer Magnetism of 3d Transition Metals in Ag, Au, Pd, and Pt Hosts: Systematics of Local Moment Variation.". *J. Appl. Phys.*, 70:10611, 1991.

[MMK96] M. Müller, N. Mattern, and U. Kühn. "Correlation between Magnetic and Structural Properties of nanocrystalline Soft Magnetic Alloys.". *J. Mag. Magn. Mat.*, 157/158:209–210, 1996.

[MMK+09] A. Makino, H. Men, T. Kubota, K. Yubuta, and A. Inoue. "New Excellent Soft Magnetic $\mathrm{FeSiBPCu}$ Nanocrystallized Alloys With High B_s of 1.9 T From Nanohetero-Amorphous Phase.". *IEEE Trans. Mag.*, 45:4302–4305, 2009.

[MN82] S. Matteson and M. A. Nicolet. *in Metastable Materials Formation by Ion*

Implantation. edited by S. T. Picraux and W. J. Choyke. Elsevier, New York, 1982.

[MS06] S. Maenosono and S. Saita. "Theoretical Assessment of FePt Nanoparticles as Heating Elements for Magnetic Hyperthermia.". *IEEE Trans. Mag.*, 42:1638–1642, 2006.

[MSB+98] J. M. MacLaren, T. C. Schultess, W. H. Butler, R. A. Sutton, and M. E. McHenry. "Magnetic and Electronic Properties of Fe/Au Multilayers and Interfaces.". *J. Appl. Phys.*, 1998.

[MSMC+09] K. J. Miller, H. B. Soll-Morris, K. N. Collier, R. Swaminathan, and M. E. McHenry. "Induction Heating of FeCo Nanoparticles for Rapid RF Curing of Epoxy Composites.". *J. Appl. Phys.*, 105:07E714, 2009.

[MSMM10] K. J. Miller, M. Sofman, K. McNerny, and M. E. McHenry. "Metastable γ-FeNi Nanostructures with Tunable Curie Temperatures.". *J. Appl. Phys.*, 107:09A305, 2010.

[MWdN63] S. Mader, H. Widmer, F. M. dHuerle, and A. S. Nowick. "Metastable Alloys of Cu-Co and Cu-Ag Thin Films Deposited in Vacuum.". *Appl. Phys. Lett.*, 3 (11):201–203, 1963.

[MWL99] M. E. McHenry, M. A. Willard, and D. E. Laughlin. "Amorphous and Nanocrystalline Materials for Applications as Soft Magnets.". *Prog. Mat. Sci.*, 44:291, 1999.

[MWL+10] K. J. Miller, A. Wise, A. Leary, D. E. Laughlin, M. E. McHenry, V. Keylin, and J. Huth. "Increased Induction in Nanocomposite Materials with Reduced Glass-Formers.". *J. Appl. Phys.*, 107:09A316, 2010.

[MWM84] A. P. Malozemoff, A. R. Williams, and V. L. Moruzzi. "Band-gap Theory of Strong Ferromagnetism: Application to Concentrated Crystalline and Amorphous Fe- and Co-metalloid Alloys.". *Phys. Rev. B*, 29:1620–1632, 1984.

[Nea00] T. Nakamura and et. al. "". *J. Appl. Phys.*, 88(1):348–53, 2000.

[NV09] G. T. Nikolov and V. C. Valchev. "Nanocrystalline magnetic Materials vs. Ferrites in Power Electronics.". *Proc. Earth and Planetary Science*, 1:1357–1361, 2009.

[OCL+08] P. R. Ohodnicki, N. C. Cates, D. E. Laughlin, M. E. McHenry, and M. Widom. "Ab initio Theoretical Study of Magnetization and Phase Stability of $(\mathrm{Fe},\mathrm{Co},\mathrm{Ni})_{23}\mathrm{B}_6$ and $(\mathrm{Fe},\mathrm{Co},\mathrm{Ni})_{23}\mathrm{Zr}$ Structures of $\mathrm{Cr}_{23}\mathrm{C}_6$ and $\mathrm{Mn}_{23}\mathrm{Th}_6$ prototypes.". *Phys. Rev. B*, 78:144414, 2008.

[O'H87] R. C. O'Handley. "Physics of Ferromagnetic Amorphous Alloys.". *J. Appl. Phys.*, 62 (10):R15–R49, 1987.

[O'H00] R. C. O'Handley. *"Modern Magnetic Materials, Principles and Applications."*. John-Wiley and Sons, New York, 2000.

[OHS+09] C. L. Ondeck, A. H. Habib, C. A. Sawyer, P. Ohodnicki, K. J. Miller, P. Chaudhary, and M. E. McHenry. "Theory of Magnetic Fluid Heating with an Alternating Magnetic Field with Temperature Dependent Materials Properties for Self-Regulated Heating.". *J. Appl. Phys.*, 105:07B324, 2009.

[Ola32] A. Olander. An electrochemical investigation of solid cadmium-gold alloys. *J. Amer. Chem. Soc.*, 54:3819–3833, 1932.

[OLL+08] P. R. Ohodnicki, J. Long, D. E. Laughlin, M. E. McHenry, and V. Keylin. "Composition Dependence of Field Induced Anisotropy in Ferromagnetic $(\mathrm{Co},\mathrm{Fe})_{89}\mathrm{Zr}_7\mathrm{B}_4$ and $(\mathrm{Co},\mathrm{Fe})_{88}\mathrm{Zr}_7\mathrm{B}_4\mathrm{Cu}$ Amorphous and Nanocrystalline Ribbons."". *J. Appl. Phys.*, 104, 2008.

[OML+08] P. R. Ohodnicki, H. McWilliams, D. E. Laughlin, M. E. McHenry, and V. Keylin. "Phase Evolution of Three-Phase *fcc*, *hcp*, and Amorphous Soft Magnetic Nanocomposite Alloy $\mathrm{Co}_{89}\mathrm{Zr}_7\mathrm{B}_4$,"". *J. Appl. Phys.*, 103:07E740, 2008.

[OML+09] P. R. Ohodnicki, M. E. McHenry, D. E. Laughlin, V. Keylin, and J. Huth. "Temperature Stability of Field Induced Anisotropy in Soft Ferromagnetic Fe,Co-Based Amorphous and Nanocomposite Ribbons.". *Acta Materialia*, accepted, 2009.

[OPL+08] P. R. Ohodnicki, S. Y. Park, D. E. Laughlin, M. E. McHenry, V. Keylin, and M. A.

Willard. "Crystallization and Thermal-Magnetic Treatment of Co-Rich HiTPerm-type Alloys.". *J. Appl. Phys.*, 103:07E729, 2008.

[OQL+09] P. R. Ohodnicki, Y. L. Qin, D. E. Laughlin, M. E. McHenry, M. Kodzuka, T. Ohkubo, K. Hono, and M. A. Willard. "Composition and Non-Equilibrium Crystallization in Partially Devitrified Co-rich Soft Magnetic Nanocomposite Alloys.". *Acta Materialia*, 57:87–96, 2009.

[Par10] S. Park. *"Extending The Recording Density In Perpendicular Recording Media."*. Ph.D Thesis, Carnegie Mellon Univ., Pittsburgh, PA, 2010.

[Pau38] Linus Pauling. "The Nature of the Interatomic Forces in Metals.". *Phys. Rev.*, 54:899, 1938.

[PCJD03] Q. A. Pankhurst, J. Connolly, S. K. Jones, and J. Dobson. "". *J. Phys. D: Appl. Phys.*, 36:R167, 2003.

[PE00] D. A. Porter and K. Easterling. *"Phase Transformations in Metals and Alloys, 2nd Edition."*. Nelson Thornes Ltd., 2000.

[PR80] F. Pfeiffer and C. Radeloff. "Soft Magnetic Ni-Fe and Co-Fe Alloys-Some Physical and Metallurgical Aspects.". *J. Magn. Magn. Mat.*, 19:190–207, 1980.

[Pri66] A. Prince. *"Alloy Phase Equilibria."*. Elsevier Publishing Company, Amsterdam, 1966.

[PVEWE01] M. Plumer, J. Van Ek, D. Weller, and G. Ertl, editors. *"The Physics of Ultrahigh-Density Magnetic Recording."*, volume 41 of *Springer Series in Surface Sciences*. Springer, Pittsburgh, PA, 2001.

[PWH+01] D. H. Ping, Y. Q. Wu, K. Hono, M. A. Willard, D. E. Laughlin, and M. E. McHenry. "Microstructural Characterization of $Fe_{44}Co_{44}Zr_7B_4Cu_1$ Nanocrystalline Alloys.". *Scripta Mat.*, 45:781–786, 2001.

[PY07] M. H. Phan and S. C. Yu. "Review of the Magnetocaloric Effect in Manganite Materials.". *J. Magn. Magn. Mat.*, 308:325–40, 2007.

[RBB+06] R. E. Rottmayer, S. Batra, D. Buechel, W. A. Challener, J. Hohlfeld, Y. Kubota, L. Lei, B. Lu, C. Mihalcea, K. Mountfield, K. Pelhos, C. Peng, T. Rausch, M.A. Seigler, D. Weller, and X. Yang. "Heat-Assisted Magnetic Recording.". *IEEE Trans. Mag.*, 42:2417–2421, 2006.

[Rea08] W. A. Reass. "Components and Technologies for High Frequency and High Average Power Converters. in High Megawatt Power Converter Technology R&D Roadmap Workshop.". *National Institute of Standards and Technology*, 2008.

[Rei82] W. D. Reicke. *"Practical Lens Design."*, volume 18 of *Topics in Current Physics: Magnetic Electron Lenses (P. W. Hawkes, Editor)*, chapter 4. Springer-Verlag, Berlin, 1982.

[RF82] V. R. V. Ramanan and G. Fish. "Crystallization Kinetics in Fe-B-Si Metallic Glasses.". *J. Appl. Phys.*, 53:2273–2275, 1982.

[Rip01] P. Ripka. *"Magnetic Sensors and Magnetometers"."*. Artech House, Inc., Norwood, MA, 2001.

[RL06] R. V. Ramanujan and L. L. Lao. "The Mechanical Behavior of Smart Magnet-Hydrogel Composites.". *Smart Mater. Struct.*, 15:952–956, 2006.

[Ros02] R. E. Rosensweig. "Heating Magnetic Fluid with Alternating Magnetic Field.". *J. Mag. Mag. Mat.*, 252:370–374, 2002.

[RR66] W. D. Reicke and E. Ruska. "A 100-kV Transmission Electron Microscope with Single-Field Condenser Objective.". *Proc. 6th Int. Cong. Elec. Mic., Kyoto*, 1:19–20, 1966.

[RS25] H. N. Russell and F. A. Saunders. "New Regularites in the Spectra of the Alkaline Earths.". *Astrophys. J.*, 61:38, 1925.

[RWG89] K. B. Reuter, D. B. William, and J. I. Goldstein. Determination of the fe-ni phase diagram below 400 °c. *Metall. Trans. A*, 20:719–725, 1989.

[SC93] R. Skomski and J. M. D. Coey. "Nitrogen Diffusion in Sm_2Fe_{17} and Local Elastic and

Magnetic-Properties.". *J. Appl. Phys.*, 73(11):7602–7611, 1993.

[SCW+11] R. Sanz, M. Cerdan, A. Wise, M. E. McHenry, and M. Daz-Michelena. "Temperature dependent Magnetization and Remanent Magnetization in Pseudo-binary $(Fe_2TiO_4)_x - (Fe_3O_4)_{1-x}$ (0.30¡x¡1.00) Titanomagnetites.". *IEEE Trans. Mag.*, page to appear, 2011.

[SH98] R. Schafer and A. Hubert. *"Magnetic Domains."*. Springer, Heidelberg, 1998.

[SHC+09] C. A. Sawyer, A. H. Habib, K. N. Collier, K. J. Miller, C. L. Ondeck, and M. E. McHenry. "Modeling of Temperature Profile During magnetic thermotherapy for cancer treatment.". *J. Appl. Phys. and issue of Virtual Journal of Biological Physics Research.*, 105:07B320, 2009.

[SHO+67] K. Strnat, G. Hoffer, J. C. Olson, W. Ostertag, and J. J. Becker. "A Family of New Cobalt-base Permanent Magnet Materials.". *J. Appl. Phys.*, 38:1001–, 1967.

[SHS+94] F. Schatz, M. Hirscher, M. Schnell, G. Flik, and H. Kronmuller. "Magnetic Anisotropy and Giant Magnetostriction of Amorphous TbDyFe Films.". *J. Appl. Phys.*, 76:5380–5382, 1994.

[SKI+90] K. Suzuki, N. Kataoka, A. Inoue, A. Makino, and T. Masumoto. "High Saturation Magnetization and Soft Magnetic Properties of bcc Fe-Zr-B Alloys with Ultrafine Grain Structure". *Mat. Trans. JIM*, 31:743–746, 1990.

[SKM+91] K. Suzuki, M. Kikuchi, A. Makino, A. Inoue, and T. Masumoto. "Changes in Microstructure and Soft Magnetic Properties of An $Fe_{86}Zr_7B_6Cu_1$ Amorphous Alloy upon Crystallization". *Mat. Trans. JIM*, 32:961–8, 1991.

[Sko96] R. Skomski. *"Interstitial Modification, Chapter 4 in Rare Earth Permanent Magnets."*. Oxford Science Publications, Clarendon Press, Oxford, 1996.

[SKS+04] P. D. D. Schwindt, S. Knappe, V. Shah, L. Hollberg, J. Kitching, L. A. Liew, and J. Moreland. "Chip-scale Atomic Magnetometer.". *Appl. Phys. Lett.*, 85:6409–6411, 2004.

[Sla37] John C. Slater. "Electronic Structure of Alloys.". *J. Appl. Phys.*, 8:385, 1937.

[SMCD05] R. Swaminathan, M. E. McHenry, S. Calvin, and L. Diamandescu. "Surface Structure Model of Cuboctahedrally Truncated Ferrite Nanoparticles". *J. Am. Cer. Soc.*, 2005.

[SMIM91] K. Suzuki, A. Makino, A. Inoue, and T. Masumoto. "Soft Magnetic Properties of Nanocrystalline bcc Fe-Zr-B and Fe-M-B-Cu (M = Transition Metal) Alloys with High Saturation Magnetization (Invited)". *J. Appl. Phys.*, 70:6232–7, 1991.

[SMK+91] K. Suzuki, A. Makino, N. Kataoka, A. Inoue, and T. Masumoto. "High Saturation Magnetization and Soft Magnetic Properties of bcc Fe-Zr-B and Fe-Zr-B-M (M = Transition Metal) Alloys with Nanoscale Grain Size". *Mat. Trans. JIM*, 32:93–102, 1991.

[SMRR+98] V.R. Shah, G. Markandeyulu, K. V. S. Rama Rao, M. Q. Huang, K. Sirisha, and M. E. McHenry. "Structural and Magnetic Properties of $Pr_3(Fe_{1-x}Co_x)_{27.5}Ti_{1.5}$ (x = 0.0, 0.1, 0.2, 0.3).". *J. Magn. Mag. Mats.*, 190:233, 1998.

[SMRR+99] V.R. Shah, G. Markandeyulu, K. V. S. Rama Rao, M. Q. Huang, K. Sirisha, and M. E. McHenry. "Effects of Co Substitution on Magnetic Properties of $Pr_3(Fe_{1-x}Co_x)_{27.5}Ti_{1.5}$ (x = 0-0.3).". *J. Appl. Phys.*, 85:4678, 1999.

[Spa03] N. Spaldin. *"Magnetic Materials Fundamentals and Device Applications."*. Cambridge University Press, Cambridge, 2003.

[SPK+95] P. Sovák, P. Petrovič, P. Kollár, M. Zatroch, and M. Knoč. "Structure and Magnetic Properties of an $Fe_{73.5}Cu_1U_3Si_{13.5}B_9$ Nanocrystalline Alloy.". *J. Mag. Magn. Mat.*, 140-144:427–428, 1995.

[SR05] I. M. Savukov and M. V. Romalis. "NMR detection with an Atomic Magnetometer.". *Phys. Rev. Lett.*, 94:123001, 2005.

[SSM03] S. Son, R. Swaminathan, and M. E. McHenry. "Structure and Magnetic Properties of RF Thermally Plasma Synthesized Mn and Mn-Zn Ferrite Nanoparticles.". *J. Appl.*

Phys., 93:7495–7, 2003.

[SSZ98] D. Szabo, G. Szeghy, and M. Zrinyi. "Shape Transition of Magnetic Field Sensitive Polymer Gels.". *Macromolecules*, 31:6541–6548, 1998.

[ST90] T. Sawa and Y. Takahashi. "Magnetic Properties of Fe-Cu-(3d Transition-Metals)-Si-B Alloys with Fine-Grain Structure.". *J. Appl. Phys.*, 67:5565–5567, 1990.

[Sta84] H. H. Stadelmeier. "Structural Classification of Transition Metal Rare Earth Boride Permanent Compounds Between T and T_5R.". *Z. Metallkde*, 75:227–230, 1984.

[STC+02] S. Son, M. Taheri, V. Carpenter, V. G. Harris, and M. E. McHenry. "Synthesis of Ferrite and Nickel Ferrite Nanoparticles Using Radio-frequency Thermal Plasma Torch.". *J. Appl. Phys.*, 91:7589–7591, 2002.

[Ste84] C. P. Steinmetz. "On the Law of Hysteresis.". *IEEE Proc.*, 72:196–221, 1984.

[Sut94] R. A. Sutton. *"Irradiation Defects in Oxide Superconductors: Their Role in Flux Pinning."*. Ph.D Thesis, Carnegie Mellon Univ., Pittsburgh, PA, 1994.

[Swa05] R. Swaminathan. *"Influence of Surface Structure on the Magnetic Properties of RF Plasma Synthesized NiZn Ferrite Nanoparticles."*. Ph.D Thesis, Carnegie Mellon Univ., Pittsburgh, PA, 2005.

[TFH+99] Z. Turgut, D. E. Ferguson, M. Q. Huang, W. E. Wallace, and M. E. McHenry. "Thermal Plasma Synthesis of γ-$\mathrm{Fe}\mathrm{N}_x$ Nanoparticles as Precursors for $\mathrm{Fe}_{16}\mathrm{N}_2$ Synthesis by Annealing.". *MRS Res. Symp. Proc.*, 577:399–404, 1999.

[THG+97] Z. Turgut, M. Q. Huang, K. Gallagher, S. A. Majetich, and M. E. McHenry. "Magnetic Evidence for Structural Phase Transformations in Fe-Co Alloy Nanocrystals Produced by a Carbon Arc.". *J. Appl. Phys.*, 81:4039–4041, 1997.

[TNPM99] Z. Turgut, N. T. Nuhfer, H. R. Piehler, and M. E. McHenry. "Magnetic Properties and Microstructural Observations of Oxide Coated FeCo Nanocrystals Before and After Compaction.". *J. Appl. Phys.*, 85:4406–4408, 1999.

[Tom94] T. Tomida. "Crystallization of an fe-Si-B-Ga-Nb Amorphous Alloy.". *Mat. Sci. Eng.*, A179/180:521–525, 1994.

[TPL00] M. Tondra, M. Porter, and R. Lipert. "Model for Detection of Immobilized Superparamagnetic Nanosphere Assay Labels Using Giant Magnetoresistive Sensors.". *The Journal of Vacuum Science and Technology.*, 18:1125–1129, 200.

[Tur99] Z. Turgut. *"Thermal Plasma Synthesis of Coated FeCo-FeCoV Nanoparticles as Precursors for Compacted Nanocrystalline Bulk Magnets."*. Ph.D Thesis, Carnegie Mellon Univ., Pittsburgh, PA, 1999.

[UHK+96] K. Ullakko, J. K. Huang, C. Kantner, R. C. O'Handley, and V. V. Kokorin. "Large Magnetic-Field-Induced Strains in $\mathrm{Ni}_2\mathrm{Mn}\mathrm{Ga}$single Crystals.". *J. Appl. Phys.*, 69:1966–1968, 1996.

[VBKea99] A. N.. Vasilev, A. D. Bozhko, V. V. Khovailo, and et al. "". *Phys. Rev.*, 59:1113, 1999.

[VMCR+98] W. Van Moorleghem, M. Chandrasekaran, D. Reynaerts, J. Peirs, H. Van Brussel, J. E. Schirber, E. L. Venturini, and J. F. Kwak. "Shape Memory and Superelastic Alloys: The New Medical Materials with Growing Demand.". *Biomedical Mat. and Eng.*, 8:55–60, 1998.

[Wal60] M. G. Wallace. "Intermetallic Compounds Between Lanthonons and Transition Metals of the First Long Period 1. Preparation, Existence and Structural Studies.". *J. Phys. Chem. Sol.*, 16(1-2):123–130, 1960.

[War81] E. Warburg. "Magnetische Untersuchungen.". *Ann. Phys. (Leipzig)*, 13:14164, 1881.

[WBPea84] H. J. Weinmann, R. C. Brasch, W. R. Press, and et. al. "". *Am. J. Roentgenol.*, 142:619–624, 1984.

[Wei07] Pierre Weiss. "L'hypothese du Champ Moleculaire et la Propriete Ferromagnetique.". *J. Phys.*, 6:661, 1907.

[WFRLC99] M. Wun-Fogle, J. B. Restorff, K. Leung, and J. R. Cullen. "Magnetostriction of

Terfenol-D Heat Treated under Compressive Stress.". *IEEE Trans. Magn.*, 35:3817–3819, 1999.

[WG59] J. H. Wernick and S. Geller. "Transition Element Rare Earth Compounds with the $CaCu_5$ Structure.". *Acta Cryst.*, 12(9):662–665, 1959.

[Wil00] M. A. Willard. *"Structural and Magnetic Characterization of HITPERM Soft Magnetic Materials for High Temperature Applications."*. Ph.D Thesis, Carnegie Mellon Univ., Pittsburgh, PA, 2000.

[WLM+98] M. A. Willard, D. E. Laughlin, M. E. McHenry, K. Sickafus, J. O. Cross, V. G. Harris, and D. Thoma. "Structure and Magnetic Properties of $(Fe_{0.5}Co_{0.5})_{88}Zr_7B_4Cu_1$ Nanocrystalline Alloys.". *J. Apply. Phys.*, 84:6773–6777, 1998.

[WMMT83] A. R. Williams, V. L. Moruzzi, A. P. Malozemoff, and K. Terakura. "Generalized Slater-Pauling Curve for Tranisition Metal Magnets.". *IEEE Trans. Mag.*, 1983.

[Woh79] E. P Wohlfarth. "First and Second Order Transitions in Some Metallic Ferromagnets.". *J. Appl. Phys.*, 50:7542–7544, 1979.

[Woo00] R. Wood. "The feasibility of Magnetic Recording at 1 Terabit per Square Inch.". *IEEE Trans. Magn.*, 36:36, 2000.

[WP85] M. E. Wood and W. H. Potter. "". *Cryogenics*, 25:667, 1985.

[WST93] H. Watanabe, H. Saito, and M. Takahashi. Soft magnetic properties and structures of nanocrystalline fe-al-si-nb-b alloy ribbons. *Trans. Mag. Soc. Jpn*, 8:888–894, 1993.

[WSV+11] A. Wise, M. Saenko, M. Velazquez, D. E. Laughlin, M. Daz-Michelena, and M. E. McHenry. "Phase Evolution in the $Fe_3O_4 - Fe_2TiO_4$ Pseudo-binary System and its Implications for Remanent Magnetization in Martian Minerals.". *IEEE Trans. Mag.*, page to appear, 2011.

[XBHR06] H. Xia, A. B. A.. Baranga, D. Hoffman, and M. V. Romalis. "Magnetoencephalography with an Atomic Magnetometer.". *Appl. Phys. Lett.*, 89:211104, 2006.

[XDP+06] S. J. Xu, M. H. Donaldson, A. Pines, S. Rochester, D. Budker, and V. V. Yashchuk. "Application of Atomic Magnetometry in Magnetic Particle Detection.". *Appl. Phys. Lett.*, 89:224105, 2006.

[YBYS92] Y. Yoshizawa, Y. Bizen, K. Yamauchi, and H. Sugihara. Improvement of magnetic properties in fe-based nanocrystalline alloys by addition of si, ge, c, ga, p, al elements and their applications. *Trans. IEE of Japan*, 112A:553–558, 1992.

[YH96] W. B. Yelon and Z. Hu. "Neutron Diffraction Study of Lattice Changes in $Nd_2Fe_{17-x}Si_x(C_y)$.". *J. Appl. Phys.*, 78:7196–7201, 1996.

[YK52] Y. Yafet and C. Kittel. "Antiferromagnetic Arrangements in Ferrites.". *Phys. Rev.*, 87(2):290–294, 1952.

[YOY88] Y. Yoshizawa, S. Oguma, and K. Yamauchi. "New Fe-based Soft Magnetic Alloys Composed of Ultrafine Grain Structure.". *J. Appl. Phys.*, 64:6044–6046, 1988.

[YPZ+93] Y. C. Yang, Q. Pan, X. D. Zhang, C. L. Zhang, Y. Li, and Ge. "Structural and Magnetic Properties of $RMo_{1.5}Fe_{10.5}N_x$.". *J. Appl. Phys.*, 74:4066–4071, 1993.

[Yua09] H. Yuan. *"Study Of Composite Thin Films For Applications InHigh Density Data Storage."*. Ph.D Thesis, Carnegie Mellon Univ., Pittsburgh, PA, 2009.

[YY91] Y. Yoshizawa and K. Yamauchi. "Magnetic Properties of Fe-Cu-Cr-Si-B, Fe-Cu-V-Si-B, and Fe-Cu-Mo-Si-B Alloys.". *Mat. Sci. Eng. A*, 133:176–179, 1991.

[ZBC+03] Y. Zhang, J. S. Blazquez, A. Conde, P. J.. Warren, and A. Cerezo. "Magnetic Properties of $FeCuCrSiB$, $FeCuVSiB$, $FeCuMoSiB$, Alloys.". *Mat. Sci. Eng. A*, 353:158–16, 2003.

Index